ENERGY STORAGE PROPERTIES OF CARBON ONION-CARBON NANOFIBRE COMPOSITES CONTAINING TRANSITION METAL COMPOUNDS

UNIVERSITY OF THE
WITWATERSRAND,
JOHANNESBURG

Submitted by

Tobile N. Y. Khawula

Supervisors

Prof. K. I. Ozoemena

Prof. C. Billing

A thesis submitted to the Faculty of Science University of the Witwatersrand
in fulfilment of the requirements for the degree of Doctor of Philosophy
School of Chemistry, University of the Witwatersrand
Johannesburg, South Africa
31 August 2022

DECLARATION

I declare that this thesis is my own, unaided work. It is being submitted for the Degree of Doctor of Philosophy in Chemistry at the University of the Witwatersrand, Johannesburg. It has not been submitted before for any degree or examination at any other University.

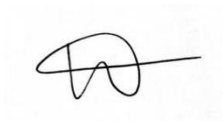

_____

(Signature of candidate)

31 August 2022 at Braamfontein, Johannesburg.

DEDICATION

To my late father

CONFERENCES

1. Khawula, T. N. Y.; Ozoemena, K. I. Energy Storage and Industry 4.0: Challenges and Prospects, Pilansberg National Park, North West, South Africa, 31 July- 2 August **2019**, Oral Presentation, Title: Electrospun iron (II) phthalocyanine (FePc) based carbon fibre hybrids as high-performance supercapacitors.

2. Khawula, T. N. Y.; Nzimande, N.; Ozoemena, K. I. 70th Annual Meeting of the International Society of Electrochemistry, Durban, Kwa-Zulu Natal, South Africa, 4-9 July **2018**, Poster Presentation, Title: Iron phthalocyanine modified carbon microfibre hybrids as high-performance supercapacitor.

3. Khawula, T. N. Y.; Ozoemena, K. I. Youth in Science and Innovation Indaba on 9-10 June **2017**, Pretoria, Gauteng, South Africa.

SCHOLARSHIPS

1. The Carnegie Ph.D. Scholarship fund. January-December 2020 Wits University, Johannesburg, South Africa.

2. Council of Scientific and Industrial Research (CSIR) Ph.D. studentship programme January-December 2017, Pretoria, South Africa.

3. European School of Materials Science, 03 November- 30 November 2016, Saarland University, Saarland, Germany.

PUBLICATIONS

A: Directly from the thesis:

[1] **Khawula, T. N. Y.;** Haruna, A.; Ozoemena, K. I. Mn_2O_3 nanoparticles embedded onto OLC-CNF composite for enhanced interfacial electrochemistry and supercapacitance, *Under review*.

[2] **Khawula, T. N. Y.**; Haruna, A.; Ozoemena, K. I. Nanostructured MoS_2/Mn_2O_3 embedded onto OLC-CNF/composites as hybrid supercapacitor electrode materials, *Under review*.

[3] **Khawula, T. N. Y.**; Haruna, A.; Ozoemena, K. I. Tetranitro-iron (II) (FeN_4) macrocycle modified carbon microfibres as a high-performance supercapacitor, *Electrochim. Acta*. *Under review*.

[4] **Khawula, T. N. Y.**; Haruna, A.; Ozoemena, K. I. Structural Modification of Electrode Materials through Fe^{2+} Vacancies in OLC-CNF@MoS_2 composites for Enhanced Electrochemical Energy Storage, *J. Electrochem. Soc. Under review*.

B: Indirectly from the thesis (*Note: Khawula and Maphumulo are both my surnames*)**:**

[5] Ozoemena, O. C.; Ehirim, T. J.; **Khawula, T. N. Y.**; Makgopa, K.; Shai, L. J.; Ozoemena, K. I. Bovine Serum Albumin-Dependent Charge-Transfer Kinetics Controls the Electrochemical Immunosensitive Detection: Vibrio cholera as a Model Bioanalyte. *Electrocatalysis*. **2021**, 12, 595-604.

[6] Ozoemena, O. C.; **Maphumulo, T. N. Y.**; Shai, J. L.; Ozoemena, K. I. Electrospun Carbon Nanofibres as an Electrochemical Immunosensing Platform for Vibrio cholera Toxin: Aging Effect of the Redox Probe. *ACS Omega.* **2020**, 5, 5762-5771.

[7] Ozoemena, O. C.; Mathebula, N. S.; Ehirim, T. J.; **Maphumulo, T. N. Y.**; Goodness Val-Ikpe, G.; Shai1, J. L.; Ozoemena, K. I. Onion-like carbon reinforced electrospun polyacrylonitrile fibres for ultrasensitive electrochemical immunosensing of Vibrio cholera toxin. *Electrochim. Acta*. **2020**, 356, 136816.

[8] Ozoemena, O. C.; Shai, J. L.; **Maphumulo, T. N. Y.**; Ozoemena, K. I. Electrochemical sensing of dopamine using onion-like carbons and their carbon nanofibre composites. *Electrocatalysis.* **2019**, 10, 381-391.

ABSTRACT

The quest for electrical energy storage has been a key driver for researchers to come up with more effective means of storing this form of energy due to the intermittent nature of renewable energy sources. Several countries have swiftly adopted the transformative potential of renewables, in particular solar energy, while others have delayed the implementation due to complex policies surrounding renewable energy projects. A way forward would be innovative regulatory approaches that encourage the pairing of solar systems with other generation technologies, and with storage, to offer a "round the clock" supply. Rechargeable batteries and supercapacitors are widely employed energy storage systems.

A rechargeable battery system offers high energy density, with lithium-ion batteries (LIBs) being the most widely used. For some applications, it is imperative that energy is delivered at a much faster rate. This characteristic feature is known as power density, and supercapacitors have proven to be much better than batteries in this case. The large-scale commercialization and adoption of a supercapacitor are hindered by its low energy density. The electrode material is a major determinant of the success of supercapacitors. Generally, these are supported on high surface area carbon materials. This study focused on the development of electrospun polyacrylonitrile (PAN) fibres embedded with onion-like carbon (OLC) and iron (II) phthalocyanine (FePc) particles, and encapsulation of the fibres with Molybdenum disulphide (MoS_2). Furthermore, composite fibres were either integrated with manganese (III) oxide (Mn_2O_3) or engineered with defects for enhanced performance in symmetric supercapacitors. The synthesis of electrode materials was divided into four phases;

In the first phase (1), OLC nanoparticles were embedded in electrospun PAN fibres and decorated with the Mn_2O_3 and evaluated as supercapacitor electrode materials. For enhanced interfacial electrochemistry and overall capacitance, the electrode material in (1) was encapsulated with MoS_2 in phase (2). In phase (3) FePc embedded in the PAN electrospun fibres were evaluated for supercapacitor applications. Limited specific capacitance and poor cycling stability were observed, thus suggesting integrating OLC and further encapsulation with MoS_2, in phase (4). The morphology of the fibres was

engineered with defects in the form of Fe^{2+} vacancies to maximize the electrochemical reactions of the OLC/MoS_2 fibre composite.

The electrochemical properties of the fibre composite materials were investigated and OLC/Mn_2O_3-CNF exhibited a specific capacitance, energy and power density of electrodes were 200 F g^{-1}, 44.63 Wh kg^{-1} and 3 235 W kg^{-1}, respectively with excellent capacitance retention. While the MoS_2 encapsulated and Mn_2O_3 decorated fibre composite, OLC/MoS_2@Mn_2O_3 displayed a specific capacitance, energy and power density of 348 Fg^{-1} 18.42 Wh kg^{-1} and 5 095 W kg^{-1}, respectively. It is pertinent to note that the capacitance of the electrodes was retained throughout the 5 000 cycles of the charge-discharge test. Upon thermal treatment at 600 °C, FePc-PAN transformed into FeN_4-CMF and exhibited a specific capacitance, energy and power density of 147 F g^{-1}, 12.48 Wh kg^{-1} and 4 320 W kg^{-1}, respectively. The vacancy-rich $(FeN_4)_d$-OLC-CNF@MoS_2 composite obtained by the removal of Fe^{2+} atoms, showed a specific capacitance, energy density and power density of 481 F g^{-1}, 76 Wh kg^{-1} 5833 W kg^{-1}, respectively. This study underscores strategic processes that can be adapted in the design, synthesis and optimization of supercapacitors-based electrodes for enhanced performance.

ACKNOWLEDGEMENTS

I would like to express my highest gratitude to my supervisor, Prof K. I. Ozoemena, I appreciate the support which has been both scientific and extramural. Mostly your patience and kindness towards me. Your support has been truly humbling. Thank you to my co-supervisor Prof C. Billing, for your kind assistance and for making sure the work becomes a success.

I am grateful for my research group, Materials Electrochemistry and Energy Technologies (MEET). A big thanks to Dr Aderemi Haruna, for his contribution and support in the characterization of the materials. In addition, I thank Nkosi Nzimande, Patrick Mwonga and Thapelo Mofokeng for the assistance in setting up the electrochemical cells for analysis. I truly appreciate your support.

Thank you to all the facility units that made their equipment available for experiments and analysis including, the Council for Scientific and Industrial Research (CSIR), National Metrology Institute of South Africa (NMISA) and Microscopy and Microanalysis Unit (MMU).

Thank you to my family for allows supporting what I do. To my mother, thank you for being my pillar of strength in difficult times. You have taught me resilience and perseverance; all my accomplishments are yours. My kids, you inspire me to be better. Your presence alone has been fulfilling and I am forever grateful to have you as ‘my gifts from God’. I do not doubt the presence of God in my life because of all of you.

TABLE OF CONTENT

LIST OF ABBREVIATIONS AND SYMBOLS

Symbols

A	Ampere, area
α	Alpha
β	Beta
C	Capacitance, coulomb
C_{sp}	Specific capacitance
C_B	Series equivalent capacitance of a cell
C_D	Diffusion capacitance
C_H	Integral capacitance of the double layer
C_{DL}	Capacitance of the double layer
ε*	Dielectric constant
cm (units)	Centimetre
D	Distance
°	Degree
ρ	Density
E	Energy
ESR	Series equivalent resistance of a cell
E^0	Standard potential of an electrode
e	Electronic charge
F	Faraday constant
f	Frequency
G	Gibbs free energy
g	Grams
H	Enthalpy
h	Planck constant
I	Current
i	Internal current
K	Equilibrium constant
kg (units)	Kilogram
L	litre
m	Mass, metres
mL (units)	Millilitre
mm (units)	Millimetre
μ	Micron
n	Stoichiometric number of electrons
Ox	Oxidized agent
P	Power
Q	Charge
R_i	Internal resistance

R	Gas constant, resistance
R_{ct}	Charge-transfer resistance
R_s	Solution resistance
Red	Reducing agent
r	Ratio
T	Temperature
t	Time
θ	Theta
W	Watt
V	Volts, voltage
V_{iR}	Voltage of internal resistance
Z	Impedance vector
Z_f	Faradaic impedance
Z′	Real part impedance
-Z″	Imaginary part impedance
Z_w	Warburg impedance

Abbreviations

AC	Activated carbon
CNT	Carbon nanotubes
CNF	Carbon nanofibre
CMF	Carbon microfibre
MWCNT	Multi-walled carbon nanotube
SWCNT	single-walled carbon nanotube
CB	Carbon black
CQD	Carbon quantum dot
GO	Graphene oxide
R-GO	Reduced graphene oxide
GQD	Graphene quantum dots
CP	Conductive polymers
PPy	Polypyrrole
PANI	Polyaniline
PT	Polythiophene
PAN	Poly acrylonitrile
POM	Polyoxymethylene
Fe	Iron
FePc	Iron (II) phthalocyanine
OLC	Onion-like carbon
MoS_2	Molybdenum disulphide
Mn_2O_3	Manganese (III) oxide
PEG	Poly ethylene glycol

PVDF	Poly vinylidene fluoride
SEM	Scanning electron microscopy
EDS	Energy dispersive x-ray spectroscopy
TEM	Transmission electron microscopy
XRD	X-ray diffraction
XPS	X-ray photoelectron spectroscopy
BET	Brunauer-Emmett-Teller
FTIR	Fourier transform infrared spectroscopy
TGA	Thermogravimetric analysis
CV	Cyclic voltammetry
GCD	Galvanostatic charge-discharge
ESR	Equivalent series resistance
EIS	Electrical impedance spectroscopy

LIST OF FIGURES

LIST OF TABLES

CHAPTER ONE

INTRODUCTION

1.1 Energy storage background

Despite the significant progress over the years to reduce the greenhouse gas (GHG) emissions, the world remains on an unsustainable path. The longer carbon emissions continue to rise, the more difficult and expensive the transition to net-zero emissions will be. According to the Statistical Review of World Energy published by British Petroleum in 2018, energy consumption will continue to increase with a concomitant increase in carbon emission levels. [1] Perhaps the single most crucial problem confronting the global energy system over the next 20 years is decarbonizing the power industry while still satisfying the rapidly growing demand for power, particularly in emerging countries. [2] To achieve energy sustainability, more efforts are needed towards the development of clean energy technology, such as energy storage and conversion. To encourage speedier deployment of new technologies, long-term energy strategies, strong political commitment, more private investment, and suitable policy and fiscal incentives are necessary. [3]

Renewable energy has an important role to play in meeting these challenges. Successively, in support of these developments, energy storage technologies must improve in order to continuously supply energy in a growing world population. Although Li-ion batteries and fuel cells have been providing energy, there is a demand for a technology with a high power density, better efficiency and longer cycle life. Supercapacitors (also known as ultracapacitors or electrochemical capacitors) have been developed to cater for these applications that Li-ion batteries and fuel cells cannot handle. [4, 5]

The first report of the electrical double layer by H. I. Becker was patented on U.S. Patent 2,800,616 in 1957 by General Electric. [6] It was impossible to demonstrate capability at the time because both electrodes needed to be submerged in an electrolyte in a battery-like configuration. [7] Robert A. Rightmire, from Standard Oil of Ohio (SOHIO) similarly detected the occurrence of a double-layer effect while working on experimental fuel cell

designs. A patent was filed in 1966 (U.S. Patent 3,536,963 subsequently licensed it to Nippon Electric (NEC). Supercapacitors were not commercially available until 1978. Since then, supercapacitors have progressed through multiple design generations. [6]

The fundamental difference between a supercapacitor and a battery is the manner in which energy is stored. Batteries depend on intercalation and de-intercalation of cations controlled by the diffusion of the electrolyte, which restricts their charging and discharging rates and ultimately the power density. [8] In supercapacitors there are two charge storage mechanisms. (i) A device that achieves electrostatic energy storage via charge accumulation at the electrode and electrolyte interface of both electrodes is called an electric double layer capacitor (EDLC). In EDLCs, ions of opposite charge diffuse through the separator and form a layer at the high surface area electrodes. The short distance between the electrodes (of the order of nanometers) coupled with non-faradaic processes results in higher power densities compared to batteries, thus allowing EDLCs to achieve faster charge-discharge rates and cycling stability. In contrast, (ii) by transferring charge between an electrode and an electrolyte solution, pseudocapacitors store charge through faradaic processes. Combining these two energy storage mechanisms leads to enhancement of capacitance and this type of a supercapacitor is referred to as a hybrid. [9]

The electrode materials play a pivotal role in determining both the type of supercapacitor and how much energy can be stored. Carbon based materials such as carbon nanotubes, activated carbon, graphene, etc., follow the mechanism of EDLCs, whereas pseudocapacitance arises when transition metal oxide such as MnO_2, RuO_2, NiO_x, etc., and conducting polymers, e.g. polyaniline, polypyrrole, etc. are used. [9] In EDLCs thousands of cycles are attainable because of their highly reversible electrostatic nature. Pseudocapacitors, on the other hand, have a high specific capacitance due to electrochemical reactions at the electrodes. Combining both of these mechanisms gives a better composite with improved energy storage properties. [10-11]

Despite the outstanding power density, supercapacitors have made less headway into energy storage applications than anticipated. At present, supercapacitors store typically 5 Wh kg^{-1}, which is significantly below that of commercialized Li-ion batteries (100-275 Wh kg^{-1}). Table 1.1 compares and lists the electrochemical characteristics of batteries and

supercapacitors. There is an apparent trade-off between power and energy density in supercapacitors which has led the research community to explore various options to try and mitigate the shortfalls. [12-13] Consequently, electrode materials have been extensively explored as they play a crucial role in defining the capacitance, energy and power density of a storage device.

Table 1.1 *Batteries vs. supercapacitors characteristics.* [12]

Function	**Supercapacitor**	**Lithium-ion (general)**
Charge time	1-10 seconds	10-60 minutes
Cycle life	1 million or 30,000 h	>500
Cell voltage	2.3 to 2.75 V	3.6 V nominal
Specific energy (Wh/kg)	5 (typical)	120-240
Specific power (W/kg)	Up to 10,000	1,000-3,000
Cost per Wh	$20 (typical)	$0,50-$1 (large system)
Service life (industrial)	10-15 years	5 to 10 years
Charge temperature	-40 to 65 °C (-40 to 149 °F)	0 to 45 °C (32° to 113 °F)
Discharge temperature	-40 to 65 °C (-40 to 149 °F)	-20 to 60 °C (-4 to 140 °F)

In this study, electrospinning was used to produce the nanofibre composite materials under investigation. Electrospinning is the preferred method because it is simple, versatile and cost-effective. [14] The flexibility of the method allowed for the preparation of electrospun fibres with diameters ranging between 10 nm and 10 µm depending on the polymer used, whilst achieving fibre continuity with a high ratio of surface area to volume. [15] During the electrospinning process, a polymer solution is subjected to a high voltage (between 10-30 kV) from the syringe needle to the collector. Electrostatic repulsion causes the polymer to elongate and deposit onto the collector plates once the electrostatic forces exceed the surface tension of the polymer fluid. The electrostatic forces, solution conductivity, flow-rate, viscosity, and distance between tip and collector are critical in determining the fibre diameter during electrospinning. [16] Electrospinning has been used to make composites with properties useful in energy related applications. [17-18]

Iron (II) phthalocyanine (FePc) was explored to provide the improved energy density in LiB and supercapacitors. [19] The interest of metallophthalocyanines (MPc) in energy storage stems from their macrocyclic nature along with extended π-systems which leads to efficient electron transfer abilities. [20] The major issues to be addressed concerning the MPc based electrodes include the very poor cycle life, poor rate capability and high solubility in liquid electrolytes. In a recent patent, Chen et al. [21] suggested the use of a protective Li-conducting layer to cover the phthalocyanine compound so that it is not in direct contact with the electrolyte. The results showed a much longer cycle life, high cathode specific capacity and best energy density for a rechargeable lithium-ion battery cell achieved to date. Jahnke et al. [22] has shown that in carbon supported transition metal porphyrins, it is possible to improve both stability and electrochemical activity by a pyrolytic heat treatment method at a temperature window of 450-900 $°C$, in an inert atmosphere.

Following these results, molybdenum disulphide (MoS_2) was investigated as a material that could potentially provide a protective layered material for the electrospun fibre composites embedded with FePc and onion-like carbons (OLC). MoS_2 is a layered-structure material, exhibiting a sheet-like morphology similar to graphene. From an energy storage perspective, the most advantageous property of this material is its centre Mo atom that possess oxidation states ranging from +2 to +6, giving it an additional capacitance via the pseudocapacitance mechanism. [23] To enhance the electrochemical storage capabilities of MoS_2, Li et al. [24] suggests doping the nano-sized MoS_2 which accelerates electronic transfer and controls phase transitions during charging and discharging. However, when the nano-size material is employed for energy storage purposes, the electronic conductivity is restricted in relation to graphite's, and its specific capacitance is still low for applications. [25-28] To increase the capacitance, manganese oxides, known for their large electrochemical storage capabilities, have been incorporated in carbon fibre composites.

To address the energy storage deficiency of MoS_2, the combination of this material with OLC offer an interesting solution. It is expected that the incorporation of OLC will play a significant role in the improvement of the surface area of the electrodes which may enable a device that can store and deliver electrical energy rapidly and efficiently.

Previously it was recognized that the use of MoS_2 on carbonaceous support, the electrolyte must permeate through the surface of carbon materials to react with the MoS_2 beneath, which reduced the electrode's rate capability. These nanocomposites typically contain a large quantity (>30 wt%) of carbon compounds that are barely active, which not only reduces the bulk loading of MoS_2 onto the electrode, but additionally causes poor accessibility of active material on the electrode, thus producing mechanical strain. As a result, the development of a superior one-dimensional MoS_2 carbon fibre composite with high specific capacity and outstanding cycling stability is most desirable. [29-30]

1.2 Research motivation

To harness the energy storage capabilities of supercapacitors, the design and development of new electrode materials that are able to kinetically facilitate more energy storage is imperative. Interest in developing efficient supercapacitors has led to the study of advanced electrodes using nanostructured composite materials to optimize performance parameters. In this study, we report the use of electrospinning to synthesize unique electrode materials that have the potential to provide the much-needed energy density in supercapacitors. To this end, composite materials are of interest, since they enable the combination of high conductivity, high capacity and stability properties, not achievable with individual materials.

1.3 Aim and objectives

The main aim of this study is to develop OLC and FePc based electrospun fibres encapsulated with MoS_2 and Mn_2O_3 as potential electrode composite materials for supercapacitor applications. The chemical and physical properties of the fibre composites is investigated prior to its fabrication as an electrode material.

To summarise, the major objectives of this thesis are as follow;

(i) To synthesize OLC based carbon nanofibres (CNF), and decorate the fibres with Mn_2O_3 nanoparticles to make OLC-CNF@Mn_2O_3 and explore its performance as a supercapacitor.

(ii) To explore the synergistic effects of the novel OLC-CNF encapsulated with MoS_2 and decorated with Mn_2O_3 i.e., OLC/MoS_2@Mn_2O_3 nanofibres as an electrode material.

(iii)To prepare electrospun FeN_4 based carbon fibres for the development of new electrode materials with improved supercapacitance.

(iv) To develop a novel electrode material engineered with defects using FePc as a source of Fe^{2+} in FeN_4-OLC-CNF@MoS_2 composite material. The etching out of the Fe^{2+} atoms was aimed at creating vacancies in the fibre composite matrix for enhanced energy storage in supercapacitors.

(v) To study the electrochemical storage capabilities of the fibre composites using a three-electrode T-type (half-cell) and a two-electrode (full-cell) symmetrical configuration in a Swagelok cell.

1.4 Hypothesis

- The synergistic effects between OLC based electrospun fibres and transitional metal complexes such as MoS_2, Mn_2O_3 and FePc enhances the performance of the electrode materials for supercapacitor applications.
- Incorporating defects into electrospun fibres further improves accessibility of the active material by the electrolyte ions, resulting in a new paradigm of energy storage limits.
- The synthesized novel electrode materials can power a light-emitting diode (LED) in a flexible pouch cell, thus demonstrating realistic energy storage capabilities of the electrode materials.

1.5 Thesis structure

The outline for the rest of the thesis is as follows;

In **Chapter two**, detailed literature review of previous studies on the energy storage principles of supercapacitors, types of electrode materials, and applications of supercapacitors, the development trends for the synthesis of supercapacitor electrode materials is also reviewed. **Chapter three** describes the materials and reagents, as well as the experimental methods for synthesis, characterisation and application testing in this study. **Chapter's four to seven** discusses the results obtained in the study and finally, **the eighth chapter** gives concluding remarks on the findings and a brief discussion on possible avenues for future research.

1.6 References

[1] Behabtu, H. A.; Messagie, M.; Coosemans, T.; Berecibar, M.; Fante, K. A.; Kebede, A. A.; Van Mierlo, J. A Review of Energy Storage Technologies' Application Potentials in Renewable Energy Sources Grid Integration. *Sustainability*. **2020**, 12, 10511.

[2] Jefferson, M. Energy policies for sustainable development. Available online: *https://www.undp.org › Environment and Energy*, [Accessed: 21 April 2020].

[3] Hadjipaschalis, I.; Poullikkas, A.; Efthimiou, V. Overview of current and future energy storage technologies for electric power applications. *Renew. Sustain. Energy Rev*. **2009**, 13, 1513-1522.

[4] Gupta, R.; Sharma, N. K.; Tiwari, P.; Gupta, Nigam, N.; Gupta, A. Application of Energy Storage Devices in Power Systems. *Int. J. Eng. Sci. Technol*. **2011**, 3, 289-297.

[5] Whittingham, M. S. Materials challenges facing electrical energy storage. *MRS Bull.* **2008**, 33, 411-419.

[6] Miller, J. R.; Simon, P. Fundamentals of electrochemical capacitor design and operation. *Electrochem. Soc. Interface.* **2008**, 17, 31-32.

[7] Miller, J. R. A brief history of supercapacitors. *Battey+energy storage technology*, ISSN521452, **2007**, 61-78.

[8] Jayalakshmi, M.; Balasubramanian, K. Simple capacitors to supercapacitors - an overview. *Int. J. Electrochem. Sci.* **2008**, 3, 1196-1217.

[9] Shin, D.; Kim, Y.; Seo, J.; Chang, N.; Wang, Y.; Pedram, M. Battery-supercapacitor hybrid system for high-rate pulsed load applications. *Design, Automation & Test in Europe*, **2011**, 1-4.

[10] Zhang, L. L; Zhao, X. S. Carbon-based materials as supercapacitor electrodes. *Chem. Soc. Rev.* **2009**, 38, 2520-2531.

[11] Choudhary, N.; Li, C.; Moore, J., Nagaiah, N.; Zhai, L.; Jung, Y.; Thomas, J. Asymmetric supercapacitor electrodes and devices. *J. Adv. Mater.* **2017**, 29, 1605336.

[12] Gidwani, M.; Bhagwani, A.; Rohra, N. Supercapacitors: the near future of batteries. *Int. J. Eng. Sci.* **2014**, 4, 22-27.

[13] Krishan, O.; Suhag, S. An updated review of energy storage systems: Classification and applications in distributed generation power systems incorporating renewable energy resources. *Int. J. Energy Res*. **2018**, 43, 1-40.

[14] Subbiah, T.; Bhat, G. S.; Tock, R. W.; Parameswaran, S.; Ramkumar, S. S. Electrospinning of nanofibres, *J. Appl. Polym. Sci.* **2005**, 96, 557-569.

[15] Teo, W. E.;Ramakrishna, S. A review on electrospinning design and nanofibre assemblies, *Nanotechnology*. **2006**, 17, R89-R106.

[16] Nataraj, S. K.; Yang, K. S.; Aminabhavi, T. M. Polyacrylonitrile-based nanofibres-A-state-of-the-art review, *Prog. Polym. Sci*. **2012**, 37, 487-513.

[17] Thavasi, V.; Singh G.; Ramakrishna, S. Electrospun nanofibres in energy and environmental applications, *Energy Environ. Sci.* **2008**, 1, 205-221.

[18] Cavaliere, S.; Subianto, S.; Savych J.; Jones, D. J.; Rozière, J. Electrospinning: designed architectures for energy conversion and storage devices, *Energy Environ. Sci.* **2011**, 4, 4761-4785.

[19] Oni, J.; Ozoemena, K. I. Phthalocyanines in batteries and supercapacitors, *J. Porphyr. Phthalocyanines.* **2012**, 16, 754-760.

[20] Ozoemena, K. I.; Nyokong, T. Surface electrochemistry of iron phthalocyanine axially ligated to 4-mercaptopyridine self-assembled monolayers at gold electrode: applications to electrocatalytic oxidation and detection of thiocyanate, *J. Electroanal. Chem*. **2005**, 579, 283-289.

[21] Chen, G.; Jang, B. Z.; Zhamu, A. Encapsulated phthalocyanine particles, high-capacity cathode containing these particles, and rechargeable lithium cell containing such a cathode. **2012** https://patents.google.com/patent/US20140072879.

[22] Jahnke, H.; Schönborn, M.; Zimmermann, G. Organic dyestuffs as catalysts for fuel cells. *Top. Curr. Chem.* **1976**, 61,133-181.

[23] Feng, C.; Ma, J.; Li, H.; Zeng, R.; Guo, Z.; Liu, H. Synthesis of molybdenum disulfide (MoS_2) for lithium ion battery applications. *Mater. Res. Bull.* **2009**, 44, 1811-1815.

[24] Li, Y.; Wang, H.; Xie, L.; Liang, Y.; Hong, G.; Dai, H. MoS_2 Nanoparticles grown on graphene: An advanced catalyst for hydrogen evolution reaction. *J. Am. Chem. Soc*. **2011**, 133, 7296-7299.

[25] Wang, T.; Chen, S.; Pang, H.; Xue, H.; Yan, Yu. MoS_2-Based nanocomposites for electrochemical energy storage, *Adv. Sci*. **2017**, 4, 1600289.

[26] Khawula, T. N. Y.; Raju, K.; Franklyn, P. J.; Sigalas, I.; Ozoemena, K. I. Symmetric pseudocapacitors based on molybdenum disulfide (MoS_2)-modified carbon nanospheres: correlating physicochemistry and synergistic interaction on energy storage. *J. Mater. Chem. A.* **2016**, 4, 6411-6425.

[27] Chen, M.; Dai, Y.; Wang, J.; Wang, Q.; Wang, Y.; Cheng, X.; Yan, X. Smart combination of three-dimensional-flower-like MoS_2 nanospheres/interconnected carbon nanotubes for application in supercapacitor with enhanced electrochemical performance. *J. Alloys Compd.* **2017**, 696, 900-906.

[28] Pan, Q.; Zhang, Q.; Zheng, F.; Liu, Y.; Li, Y.; Ou, X.; Xiong, X.; Yang, C.; Liu, M. Construction of MoS_2/C hierarchical tubular heterostructures for high-performance sodium ion batteries. *ACS Nano*. **2018**, 12, 12578-12586.

[29] Stephenson, T.; Li, Z.; Olsen, B.; Mitlin, D. Lithium ion battery applications of molybdenum disulfide (MoS_2) nanocomposites, *Energy Environ. Sci.* **2014**, 7, 209-231.

[30] Lei, Z.; Zhan, J.; Tang, L.; Zhang, Y.; Wang, Y. Recent development of metallic (1T) phase of molybdenum disulfide for energy conversion and storage. *Adv. Energy Mater*. **2018**, 8, 1703482.

CHAPTER TWO

LITERATURE REVIEW

In this chapter, a detailed review on electrochemical principles and supercapacitors is presented. A review on the basics of electrode materials is discussed with particular focus on iron (II) phthalocyanines, molybdenum disulphide and manganese oxide as electrode materials. The fundamentals for electrospinning of nanofibre composites and their applications were also briefly reviewed.

2.1 General Principles of Electrochemistry

In principle, electrochemistry is a combination of chemical and electrical phenomena caused by the passage of current. The charges are kept separate, and thus an electrostatic field is produced that leads to charge transfer. This charge transfer can either be homogenous in solution (redox reactions) or heterogeneous on electrode surface. [1-2] In simple terms, electrochemistry is concerned with the heterogeneous transfer of charge, in the form of electrons, across the interface between a solid and an adjacent solution phase. Essentially, an electrochemical reaction's overall rate is affected by three mechanisms of mass movement. [3], namely;

(i) Migration: the movement of a charged body species driven by the influence of an electric field force and thereby creating a gradient of electrical potential.

(ii) Diffusion: net movement of molecules because of a chemical concentration gradient, to achieve a homogeneous composition of the solutions.

(iii) *Convection: Fluid movement in its physical form. Natural convection (convection generated by density gradients) and forced convection (induced by stirring) enable liquids to move, and they can be distinguished by stationary zones, laminar flow, and turbulent flow.*

Mechanisms of mass transfer of species from the bulk solution to the electrode surface can occur as a reaction polarization by intermediate chemical reaction r_{ox} or r_{red} forms. Alternatively, it could also be via physical processes such as adsorption, desorption or recrystallization. A potential gradient exerts a force on a charged particle present in the solution's body. This is what propels the species toward (or away from) the electrode

surface. [2-3] When the rate of electron transfer is fast, only diffusion processes controls the electrode reaction. In this case the electrode reaction obeys the Nernst equation and it is electrochemically reversible process. In other cases, the electron transfer is slow and the reaction is non-reversible. A potential dependent charge transfer can be divided into two types of categories, namely redox reaction and ion adsorption. The Nernst equation best describes the potential, E, in a redox reaction (with an oxidant [ox], and a reductant [red], as indicated in equation (2.1)) [4];

$$Ox + ze^- \rightleftharpoons Red \tag{2.1}$$

$$E = E_0 + \frac{RT}{zF} \ln \frac{[Ox]}{[Red]} \tag{2.2}$$

in which, [Ox] refers to the concentration of the oxidized species and [Red] is the concentration of the reduced species, R is the gas constant, T is the absolute temperature, E_0 is the standard potential, and F is the Faraday constant. The amount of charge Q, is denoted by the product zF, and is a function of potential, E. [1-3]

2.2 The Electrically Charged Interface also known as the Double Layer

2.2.1 The Helmholtz Model

The physical nature of the interface is the driving force for the type of reactions that take place at the interfacial region. Helmholtz's early experiments show that at each electrode-electrolyte boundary, two layers of opposing charge are highly ordered (as shown by figure 2.1 left), such that a double layer is formed. [5] Imagine if $\Delta\phi = (\phi_M - \phi_{solution}$, where ϕ is the potential at the interface and M is a metal) in figure 2.1 (right) is positive, because of electrostatic effect, on its surface the metal possesses a positive charge (Van der Waals' forces), anions in solution diffuse to the interface, forming a negative countercharge sheet, according to Helmholtz, which would balance the charge on the electrode. Thus, a double layer exists. The parallel plate capacitor's model is comparable to the one above. However, it overlooks the interactions that take place at a distance from the electrode than the initial layer of adsorbed species, as well as any electrolyte concentration dependence. [1]

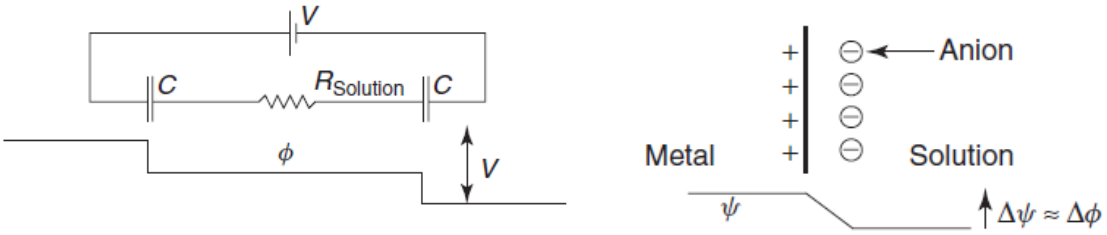

Figure 2.1 The circuit diagram of the electrode-electrolyte boundary (left) and schematic representation of the operating principle based on the Helmholtz model (right). [1]

2.2.2 The Gouy-Chapman Model

On the contrary, Gouy-Chapman proposed a model which considers the influence of the applied potential and electrolyte concentration on the double layer capacitor. Thus, from the interface to the bulk electrolyte solution, the applied potential diminishes exponentially and the ions are free to move as depicted in figure 2.2. [1]

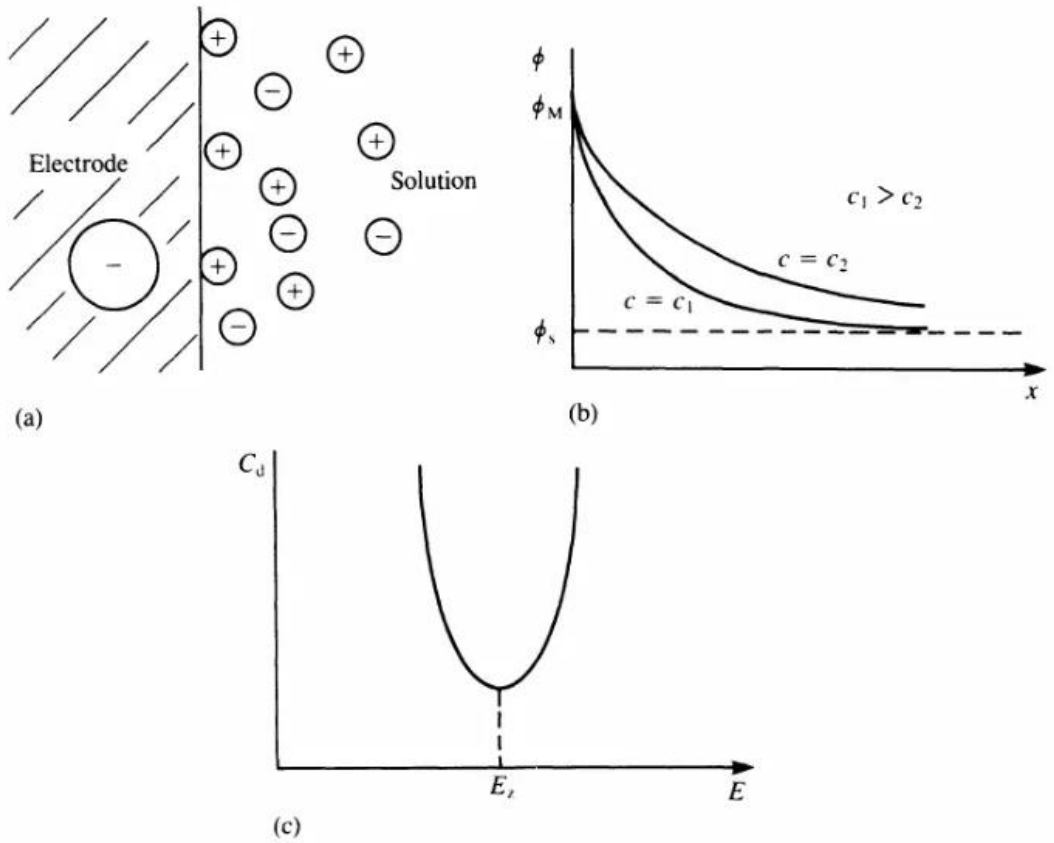

Figure 2.2 (a) The Gouy-Chapman model of the double layer showing the effects of diffusion in which the applied potential drops exponentially from the interface to the bulk electrolyte solution, the ions are arranged in a diffuse manner; (b) the electrostatic potential's fluctuation, ϕ, with distance, x from the electrode, demonstrating the influence of ion concentration, the relationship between Cd (diffuse layer capacitance) and potential, and (c) indicating the minimum at the zero charge position E_Z. [1]

2.2.3 The Stern Model

An alternative model is referred to as the Stern model, it realizes both effects of the Helmholtz and Gouy-Chapman models namely; (i) the ionic species' hydrodynamic mobility in the diffuse layer that extends into the bulk solution, and (ii) the ion accumulation near the electrode surface, see figure 2.3. [1]

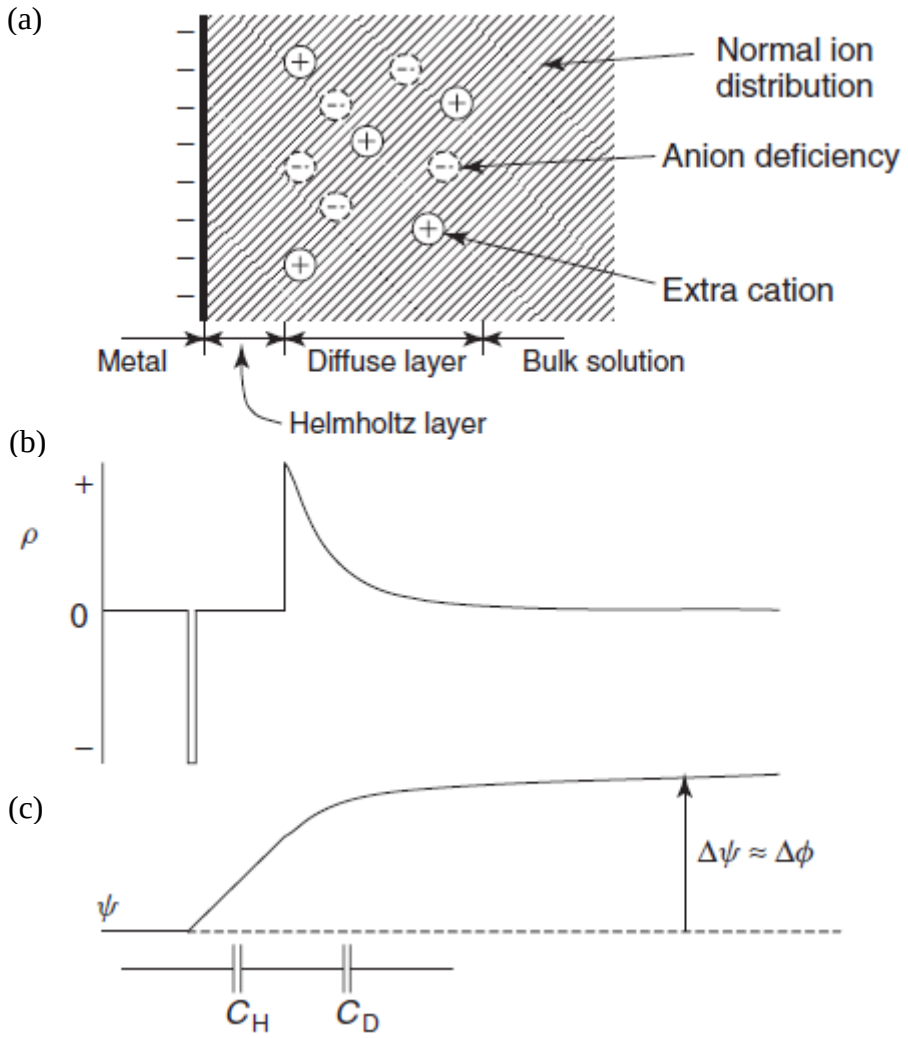

Figure 2.3 The Stern model of the double layer (a) ion arrangement (b) variation of the electrostatic potential with distance (c) variation of ψ with potential (note: Δψ is the Volta, or outer potential difference, and is the fraction of Δϕ owing exclusively to charges at the interface. [1]

The total capacitance of the double layer at the electrode C_{DL} is equal to the sum of two capacitors connected in series, where C_H denotes Helmholtz layer phenomenon and C_D denotes diffusion region capacitance. [6] The overall capacity is,

$$\frac{1}{C_{DL}} = \frac{1}{C_H} + \frac{1}{C_D} \tag{2.3}$$

2.3 Capacitor Principles

The first generation of capacitors consists of two conducting electrodes and an insulating dielectric. There are two types of capacitors, (i) electrostatic and (ii) electrolytic capacitors, as depicted in figure 2.4 (a) and (b). The difference lies in the dielectric type. Air, ceramic or polymer is used for electrostatic capacitors whilst electrolytic capacitors make use of electrolytic dielectrics. [7] In theory, a voltage is applied, and opposite charges accumulate on the electrode surfaces. Because the charges are separated by a dielectric, an electric field is created, which enables the capacitor to store energy. [5]

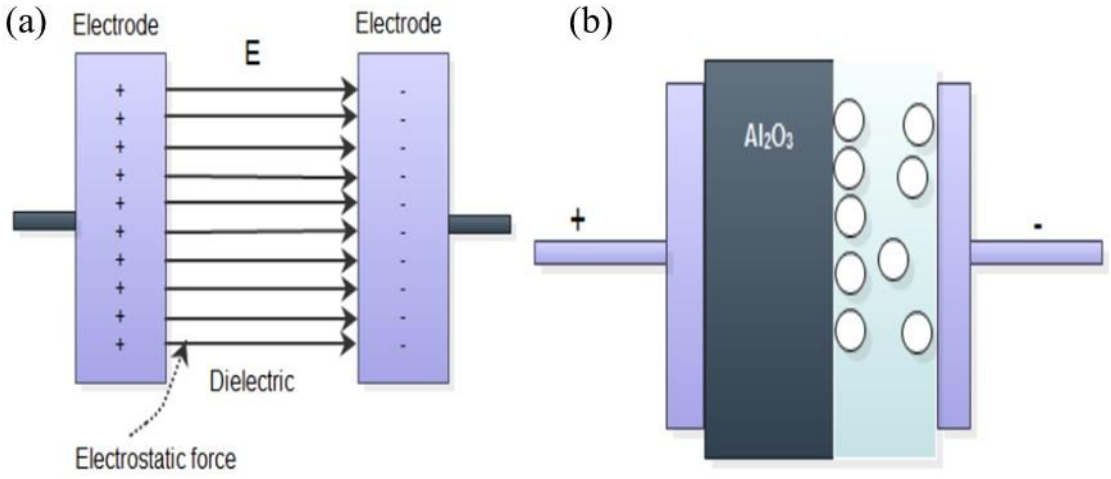

Figure 2.4 (a) Schematic diagram of conventional capacitors; electrostatic and (b) electrolytic capacitor. [6]

The following equation determines a capacitor's capacitance:

$$C = \frac{Q}{V} \tag{2.4}$$

where C denotes the capacitance [in farads, F], Q the charge [in coulombs, C] and V is the applied voltage, [in volts, V]. Each electrode has an accessible surface area A [m^2], is distanced to the other by a length D [m], and the medium between the plates has a relative dielectric constant, ε^*. As a result, the capacitance can be calculated using the equation below (2.5). [5-6]

$$C = \frac{\varepsilon^*}{D} A \tag{2.5}$$

ε* is equal to the product of the dielectric constant of free space ($\varepsilon_0 \approx 8.854 \times 10^{-12}$ F/m) and the insulating substance's dielectric constant between the electrodes (ε_r = 1 F/m). A large dielectric constant of the insulating material, a large surface area electrode, and a small distance between the electrodes can all contribute to a significant rise in capacitance value, according to this equation. [5]

Power density and energy density are two of the most critical characteristics of a capacitor. Generally, both densities are expressed in terms of a quantity per unit mass or volume. As demonstrated in equation (2.6), the maximum energy E_{max} [W h/kg] stored in a capacitor is related to its capacitance and the square of the maximum operating voltage. [6]

$$E_{max} = \frac{C{V_{max}}^2}{2} \tag{2.6}$$

Power, P [W kg^{-1}] denotes the amount of energy expended per unit of time. Capacitors are commonly depicted as a circuit in series with a "load" resistance [R] external to the circuit. The internal capacitor components, such as dielectric material, current collectors, and electrodes influence the internal resistance and are thus accounted for by a metric termed the equivalent series resistance (ESR) [Ohms, Ω]. This resistance determines the voltage that exists during discharge, as demonstrated in figure 2.5. The maximum power P_{max} equation (2.7) gives the value for a capacitor measured at matched impedance. [5]

$$P_{max} = \frac{V^2}{4 \times ESR} \tag{2.7}$$

This so-called ESR, which is also known as internal resistance, is computed as follows;

$$ESR = \frac{\Delta V_{ir}}{2i} \tag{2.8}$$

Internal resistance causes a voltage drop (V_{ir}) between the first two points of the discharge curve and a corresponding current [in ampere, A]. [5]

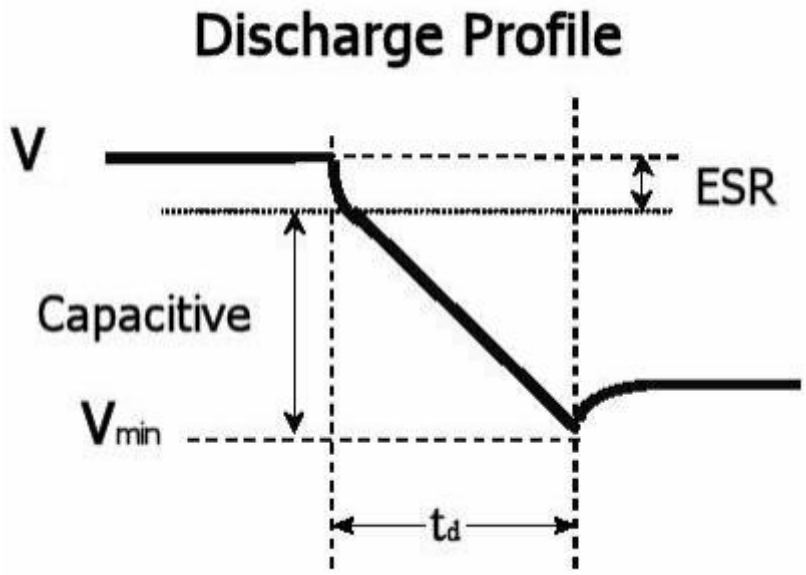

Figure 2.5 Charge-discharge tests showing different internal resistance response. [8]

Capacitors with a high power density are known as conventional capacitors. They are useful in a variety of applications that require fast charge-discharge properties. Despite having far higher power densities, they store far less energy per unit mass or volume than both batteries and fuel cells. [4] According to recent studies, supercapacitors are the third generation of capacitors, and are the most feasible for implantation. [5] Supercapacitors have high energy densities, in comparison to traditional capacitors, due to the combination of a double layer charge, an accessible electrode material surface area, and a tight charge separation distance. [6-7]

A typical supercapacitor is made up of the same fundamental components as a traditional capacitor. [9] The ions in the electrolyte of this device permeate through the separator into the pores of the electrode with opposing charges, resulting in charge accumulation at both electrodes' electrolyte interface as shown in figure 2.6. [10] The electrode material and charge accumulation mechanisms are the main differences between supercapacitors and batteries. The goal of this technology is to fill the gap between traditional capacitors and other high performing energy storage technologies. The increased specific surface area (SSA) of electrode materials combined with substantially thinner dielectrics reduce the distance (D) between the electrodes in these so-called supercapacitors. Thus, the capacitance and energy values have improved by several orders of magnitude according

to equations (2.5) and (2.6). Furthermore, supercapacitors maintain the low ESR characteristic of traditional capacitors, allowing for similar power densities. [2]

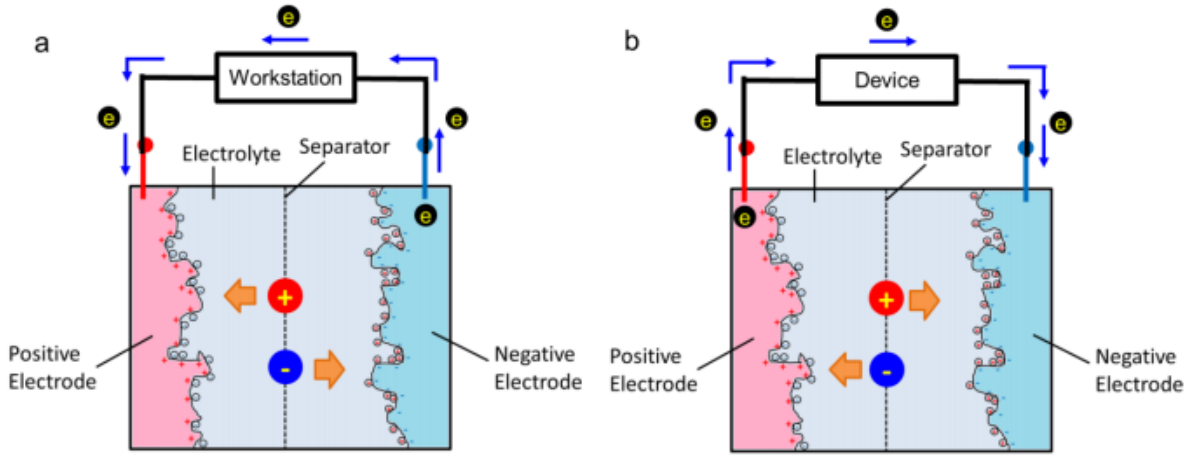

Figure 2.6 A supercapacitor schematic diagram indicating the (a) charging process, and (b) the discharging process. [10]

2.4 Supercapacitors

A supercapacitor, also known as an ultracapacitor or an electrochemical capacitor by a lot of researchers, is the most recent addition to the group of energy storage devices that use high surface area electrodes. [11] Evidently, they have received much interest because of their ability to deliver a lot of electrical power with an extended operating lifetime. The key attribute lies in the absence of active material volume changes between the charged and discharged state that is present in batteries. Consequently, the efficiency is as close as possible to 100 %. [12-15]

The Ragone plot shown in figure 2.6 best describes a supercapacitors' performance compared to other energy storage and conversion technologies such as batteries. The diagram displays energy densities versus power densities of various energy storage technologies. It is frequently used to assess and compare electrochemical energy storage device performance. Supercapacitors, according to this diagram, occupy a significant proportion of the space between batteries and traditional capacitors. While both batteries and fuel cells have high theoretical specific energy, when compared to supercapacitors, their power density falls short of what is required for application. [3, 16] In simpler terms,

they can store a vast quantity of energy but cannot distribute it quickly like capacitors. For this reason, high-power electric devices (such as supercapacitors) are routinely used to support batteries and fuel cells to compensate for the shortcomings. [9]

Supercapacitors are yet to meet the energy density requirements to replace batteries and fuel cells. This limits their competitiveness as a breakthrough energy storage system. [10] Charges are mostly kept inside the electrode active material of a battery. This means that every active atom in the bulk electrode material is charged, whereas only atoms at the particle surface are charged in the case of a supercapacitor. If the cell voltages are the same, the energy density of a battery should be substantially higher than that of a supercapacitor. In this study, the electrochemical characteristics of batteries and supercapacitors have been compared in Chapter one, Table 1.1. [16] According to the table, batteries have a high energy density and a low power density because of the faradaic processes that cause continual phase or volume changes. The cycle life of a battery is short in relation to that of a supercapacitor device. Since the charge-discharge processes in supercapacitors are exceedingly reversible, with no chemical or compositional changes they can persist 2-folds compared to batteries. In the last decade, battery power needs have grown for some applications. To this end, high-power pulse batteries were designed and developed as an alternative to supercapacitors. [11]

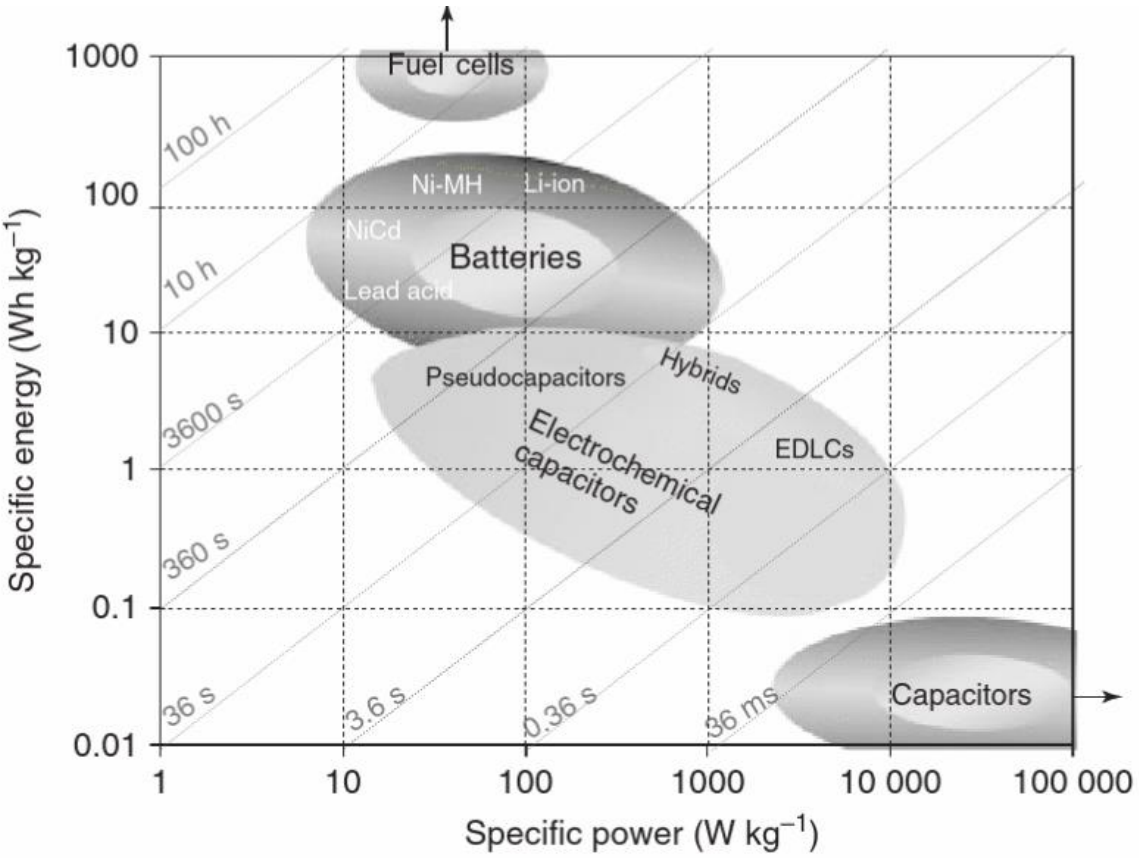

Figure 2.6 Ragone diagram for energy storage devices. [16]

2.4.1 Electrochemistry

Supercapacitors are classified based on their charge-storage mechanism. Figure 2.7 depicts different categories and their related materials.

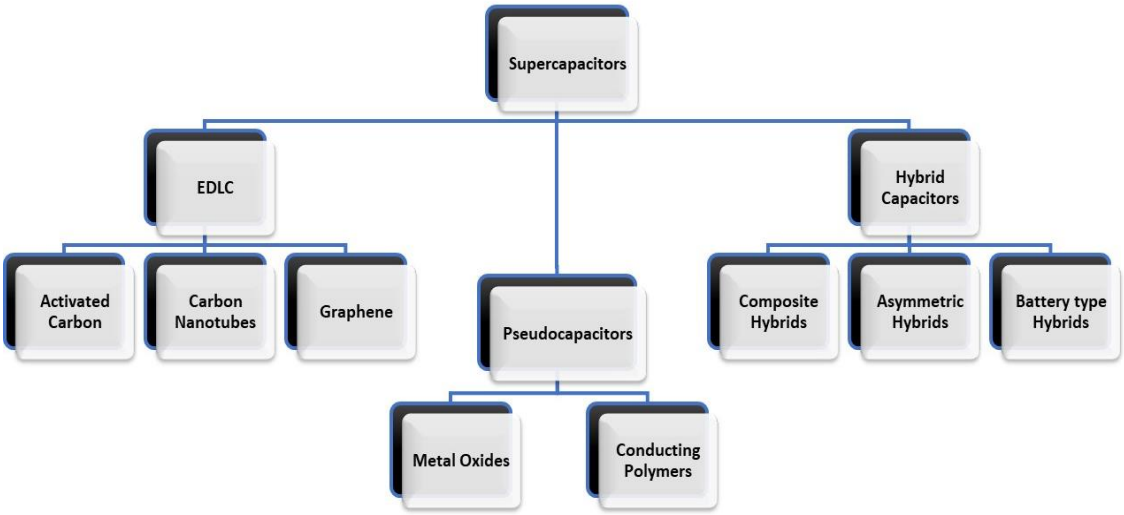

Figure 2.7 Classification flowchart of supercapacitors and related types. [3]

2.4.1.1 E electric double layer capacitors

When a potential difference is maintained across electrodes in an electrolytic cell, a current is generated and charge accumulates on the electrodes' surface. Coulomb's force causes opposing ions to diffuse over a separator and through the pores of the electrode with opposing charges. This results in a supercapacitor with two layers of charge, one at the positive electrode electrolyte interface, the other at the negative electrode electrolyte interface. This means that electric double layer capacitors (EDLCs) are supercapacitors that primarily store energy at the carbon electrolyte interface by reversible ion adsorption on the carbon surface. [3, 12] Figure 2.8 (a) shows a schematic representative of a typical EDLC. The process is fully reversible and very efficient since there are no phase or volume shifts associated with EDLC electrode materials, unlike batteries, whose performance that degrades as cells capacitance is reduced and series resistance increased over time. EDLCs made of carbon materials, have a long cycle life and highly reversible charge-discharge cycles. [11]

2.4.1.2 Pseudocapacitors

Pseudocapacitors, on the other hand, are devices that produce additional charge through transitions in active materials or conducting polymers that are faradic and easily reversible. [12] Electrosorption, reduction-oxidation, and intercalation techniques are used

to achieve this effect, as illustrated by figure 2.8 (b). The redox reaction behaves similarly to the electrochemical processes of rechargeable batteries. A pseudocapacitor electrode compromising both an electrochemically inert material like active carbon and an electrochemically active component like a redox material, two processes occur: (1) double-layer charging or discharging as described in *2.4.1.1* above, and (2) the electrochemical redox process. The charge transfer that takes place in a pseudocapacitor is voltage-dependent. The behavior of the redox process can be expressed by the Nernst equation in (2.1) and assumes that in the electrode layer both the redox material particles and reaction sites are evenly distributed, and that the oxidant and reductant are insoluble in the electrolyte. Pseudocapacitors have a significantly greater capacitance than EDLCs, but the continual volume shifts caused by solid state mass transfer restricts the supercapacitor's life. [11, 17-18]

2.4.1.3 Hybrid capacitors

Figure 2.8 (c) demonstrates a combination of an EDLC and a pseudocapacitor. This is the third and final form of supercapacitor. The most significant advantage of coupling a pseudocapacitive redox material with an EDLC material in a supercapacitor device is the increased capacitance, which improves the overall energy density. However, combining pseudocapacitive material with double-layer material poses various obstacles. For example, side reactions that occur in redox processes, may result in a reduction in the charging/discharging cycle life. Subsequently, the combination of the redox reactions and physisorption frequently occurring on the hybrid capacitor electrodes interact with or feed the electrolyte breakdown mechanisms, resulting in considerable supercapacitor performance deterioration. To optimize this combination, carbon-based materials that possess a high surface area are chosen to boost the pseudocapacitive component's deposition mass. Alternatively, an asymmetric configuration with distinct anode/cathode materials that display an increased voltage stability performance and large capacitance, appear to be a viable option. Thus, hybrid supercapacitors have reached energy and power densities levels that are unattainable in the single type supercapacitors. Composites materials, asymmetric-type, and battery electrode materials are responsible for the hybrid capacitors' exceptional performance. [3, 12]

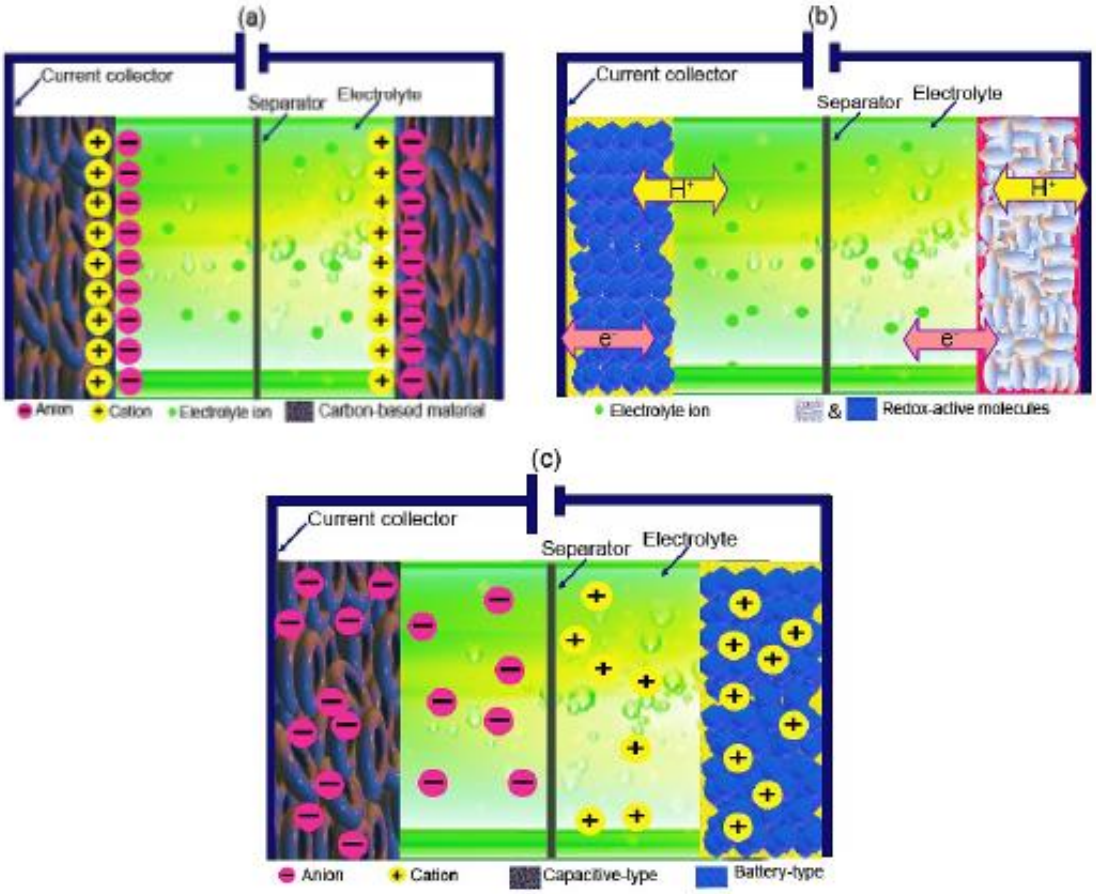

Figure 2.8 Schematic for (a) EDLCs, (b) pseudocapacitors, and (c) hybrid capacitor. [11]

2.4.2 Electrode materials

Essentially, the performance of a supercapacitor is governed by the choice of electrode materials and the corresponding mechanisms (i.e. EDLCs and pseudocapacitance) which is explained by the charge transfer and/or charge accumulation processes at the electrode-electrolyte interface. The various materials used in supercapacitor applications are depicted in figure 2.9. [19] Typically, these are classified into three main groups: carbon-based, transition metal oxides and conducting polymers. Each electrode material has its own set of properties and benefits. [11] Various carbon allotropes are leading in the market as electrode materials, while progress in the development of conducting polymers (CPs) and metal oxides as substitutes continues apace. [8]

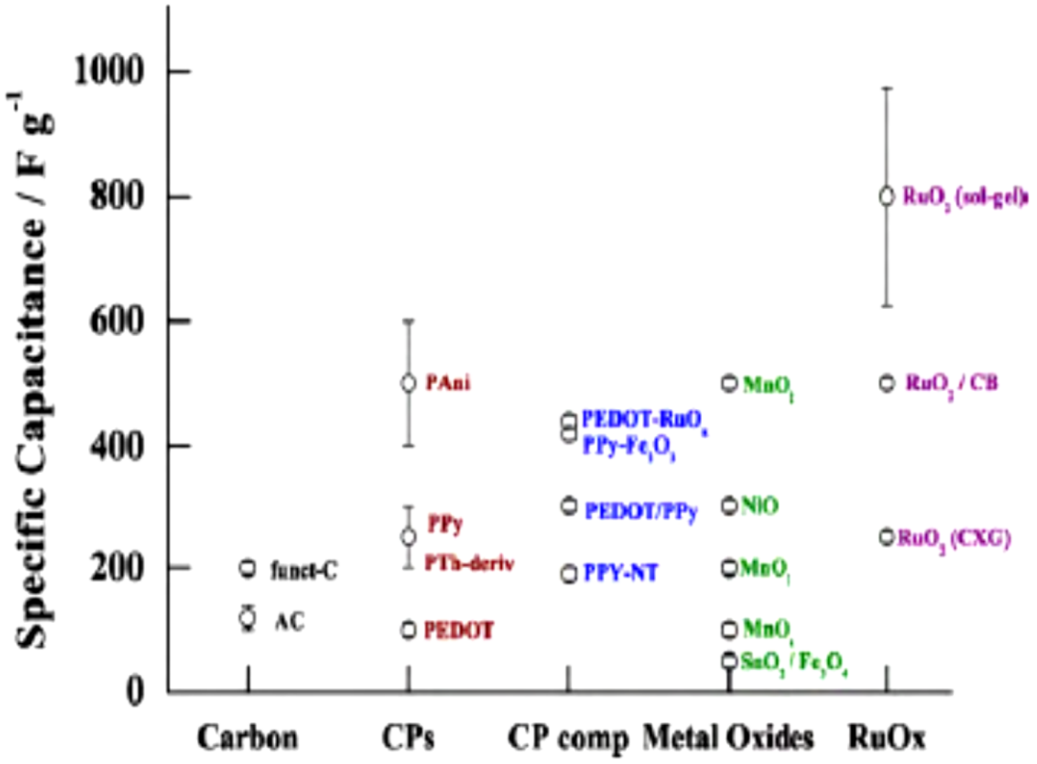

Figure 2.9 The specific capacitance of various electrode materials. [19]

2.4.2.1 Carbon-based

Carbon is a one-of-a-kind element since it can exist in a variety of structural forms, such as diamond, graphite, fullerene/nanotubes, and so on. [20] Diamond and graphite are natural minerals found in the earth's crust, whereas the others are manmade. The opportunity to build supercapacitor electrodes made entirely of carbon was explored, given that, they exhibit outstanding electrochemical stability owing to the high electrical conductivity and extraordinary chemical stability. They account for almost 80 % of the total supercapacitors developed in the period of 2020. Carbon based electrode materials are an appealing option for EDLCs because of their large surface area (up to 3 519.50 m^3 g^{-1}), versatility, low cost, and easy accessibility. [21] By changing the carbon structure, pore size, and particle size, the electrochemical characteristics of the electrodes can be varied and ultimately their specific capacitance. Pseudocapacitance in carbon-based electrodes arises due to the presence of certain electrically conductive functional groups on activated carbons. [20]

Carbon quantum dot (CQD) or Carbon dots (CDs) particles are a new family of 0D electrode materials that have found use in supercapacitor applications. [22] The nanostructures are typically less than 10 nm consisting of a nanocrystalline core and an amorphous outer layer with surface functional groups. Investigation of supercapacitor performance of hydrothermally synthesized CQD was reported by Athika et al. [23], and the results showed a specific capacitance of 95 F g^{-1} with excellent stability as well as coulombic efficiency over 1 000 cycles. Using a hydrothermal synthesis method, Zhao et al. [24] prepared CQD-decorated reduced graphene oxide (rGO) to form an interconnected 3D network morphology. The electrodes displayed a 308 F g^{-1} specific capacitance at 0.5 A g^{-1} and a capacitance retention of 92% over 20 000 cycles at 10 A g^{-1}.

Recently CDs integrated with polymers have been used to enhance the electrochemical performance of supercapacitors. In particular, a study by De et al. [25] showed GO hydrogel decorated by CD-stabilized CuS nanoparticles using the hydrothermal method. The CDs were used to bind the CuS nanoparticles to the GO inside the 3D hydrogel framework. An asymmetric configuration with the synthesized material acting as the positive electrode and rGO acting as the negative electrode was investigated as a supercapacitor. The device exhibited a considerable specific capacitance and energy density of 920 F g^{-1} and 28 Wh kg^{-1} at 1 A g^{-1}, respectively. Approximately 90% of the specific capacitance was retained after 5 000 cycles.

In-situ polymerization was used by Zhang et al. [26] to create ternary composites of CDs, polypyrrole (PPy), and GO for supercapacitor applications. It was suggested that CDs with a large specific surface area could improve the interfacial characteristics between GO, CDs, and PPy, thus enhancing the ternary composite's dielectric constant. After 5 000 cycles, a supercapacitor with symmetric GO/CDs/PPy electrodes demonstrates an energy density of 30.1 Wh kg^{-1} at a power density of 250 W kg^{-1} with good stability. The synthesized CD/PPy/GO reportedly showed a high specific capacitance at 0.5 A g^{-1} of 576 F g^{-1}.

Graphene quantum dots (GQSs) are rapidly emerging as highly stable and capacitive electrodes composites that can compete with CQDs. According to Chen et al. [27], 3D

graphene was coated with GQDs using an electrochemical process, and the resulting composite materials were then employed as electrodes for symmetrical SCs. A specific capacitance of 268 F g^{-1} was observed in the GQD/3D graphene composite, an improvement of 2-folds over the supercapacitors generated from electrodes made of pure 3D graphene (136 F g^{-1}).

Highly N and O co-doped GQDs were electro-deposited using the 3D CNT/carbon cloth (CC) network as a flexible, conductive scaffold (NeO-GQDs). A high-performance N-O-GQD/CNT/CC composite electrodes with H_2SO_4/PVA gel as the solid electrolyte were used to construct an all-solid-state flexible supercapacitor. According to figure 6 b-d, the electrodes had a 461 mF cm^{-2} area of capacitance (at 0.5 mA cm^{-2}), a 32 mWh cm^{-2} area of energy density, and an 87.5% retention of capacitance after 2 000 cycles of charging and discharging. [28]

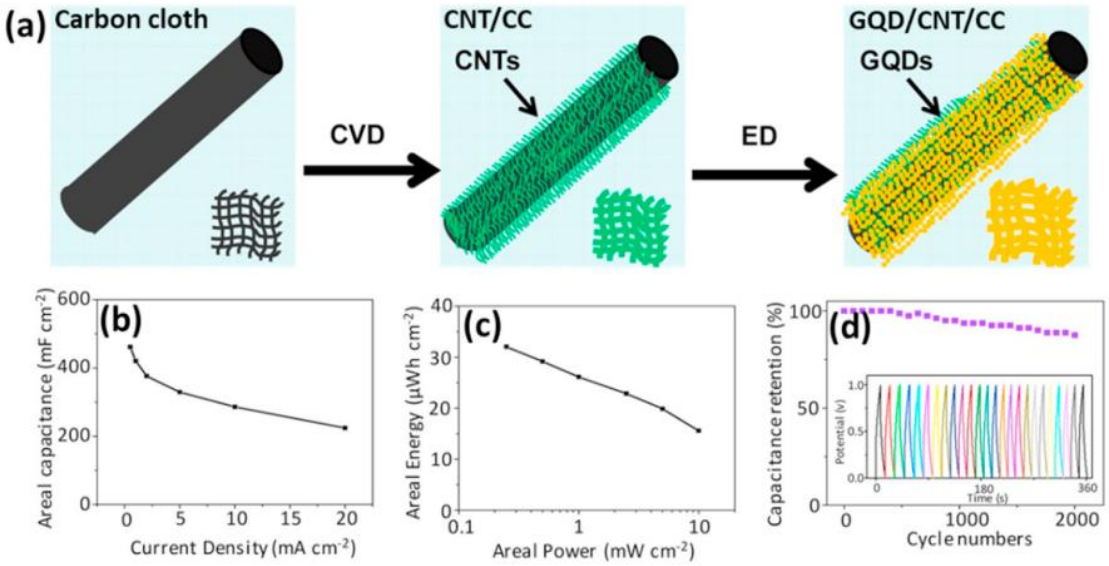

Figure 2.10 (a) Schematic diagram for the preparation of 3D NeO-GQD/CNT/CC electrodes, (b) areal capacitance of flexible electrodes as the current density changes at different current densities, (c) Ragone plot of SCs with areal energy densities and areal power densities and (d) cycle stability of the device (15 mA cm^{-2}) (Inset: galvanostatic charge/discharge curves for the 25 cycles). [28]

1D carbon-based materials such as CNTs, CFs/CNFs, carbon yarns/carbon nanoyarns, etc. have drawn much attention as electrodes in supercapacitors. [22] Superior mechanical and electrochemical qualities, as well as good electrical conductivity, are all

characteristics of CNTs. [29] In numerous studies, pure CNTs have been used as electrode materials for supercapacitors, resulting in EDLC behaviour. [30-34] Wu et al. [35] successfully produced CNTs for SCs applications by using Ni catalyst to grow them in the inner walls of carbonized wood tracheids. The capacitance values were comparable to or greater than those of supercapacitors based on wood carbon slices with pseudocapacitive materials and were roughly five folds higher than those of activated wood carbon. The specific capacitance improved to 215.3 F g^{-1} when the specific surface area increased from 365.5 to 537.9 m^2 g^{-1}. All-solid-state supercapacitors had an energy density of 39.8 Wh kg^{-1}, and 96.2% of their capacitance remained after 10 000 charging-discharging cycles. An investigation into hierarchical CNTs/N-doped porous carbon for enhanced supercapacitor performance by Zhou et al. [36] showed that the CNTs facilitate rapid ion transfer and storage during charge-discharge processes. A specific capacitance of 293.1 F g^{-1} (1 A g^{-1}) and high rate capability (207 F g^{-1} at 30 A g^{-1}) was shown by the CNTs/N-doped porous carbon composite. The symmetric supercapacitors had an energy density of 27.46 Wh kg^{-1} at a power density of 874.98 W kg^{-1}. Due to their excellent electrical and electrochemical properties, transition metal oxides and CNTs have been synthesized for use in energy storage and conversion. Co_3O_4 nanoparticles and nanostructures combined with 1D carbon-based materials are a promising option for supercapacitor electrodes. The composite nanomaterial is easily controlled in size and shape and has a high theoretical specific capacitance and good redox performance. [36] Following an acid treatment of multi-walled carbon nanotube (MWCNT) and in-situ breakdown of $Co(NO_3)_2$ in n-hexanol solution at 140 °C, Shan et al. [37] formed a MWCNT/Co_3O_4 nanocomposites. The specific capacitance of the MWCNTs/Co_3O_4 composite was 200.98 F g^{-1}, which was higher than the specific capacitance of pure MWCNTs (90.1 F g^{-1}).

Chang et al. [38] synthesized a core-shell-shaped pseudocapacitive anode material by electrochemically depositing PPy on electrochemically prepared CNT films. The volumetric energy density of the asymmetric supercapacitors with CNTs/PPy and CNTs/MnO_2 as the anode and cathode, respectively, was 3.63 mWh cm^{-3} at 13.86 mW cm^{-3} with 89.0% retention after 10 000 charge-discharge cycles. When the discharge current was increased to 40 mA cm^{-2}, the CNTs/PPy electrode maintained 75.2% of its capacitance (965.3 mF cm^{-2} at 1 mA cm^{-2}). The CNTs/PPy capacitor maintained 89.1% of its initial capacitance after 10 000 charge-discharge cycles. [38]

Activated carbon (AC) is characterized by a large surface area (2 696 m^2 g^{-1}), making it the most commonly used electrode material for supercapacitors. A number of carbon-rich raw sources, including wood and coal, are used to create AC, a carbonaceous substance. In supercapacitor application, the carbon atoms in the activated carbon are inaccessible to the electrolyte ions as shown in figure 2.11 (a), thus its specific capacitance is limited. Cheng et al. [39] described single-walled carbon nanotube (SWCNT) composite film as an excellent option for applications requiring energy-efficient materials due to their improved charge transfer channels and greater electrical conductivity. Figure 2.11 (a) shows the SWCNT stacked in bundles. The cyclic voltammogram (CVs) for different electrode materials made of CNTs, graphene, and their composite in the aqueous and organic electrolyte are illustrated in figures 2.11 (c) and (d), respectively at a scan rate of 10 mV s^{-1}. The electro-activation phenomena used to enhance the electrode surface area after charging-discharging cycles were schematically displayed. Before cycling figure 2.11 (e), graphene layers tend to restack, however, after a long cycle life, intercalated ions separated the graphene sheets figure 2.11 (f), increasing the surface area accessible for electrolyte ions and, as a result, improving the material's capacitive behaviour. [39] The fabricated graphene/CNT supercapacitor electrodes exhibited a specific capacitance of 290.4 F g^{-1} in a two-electrode system, and energy and power densities of 62.8 Wh kg^{-1} and 58.5 kW kg^{-1}, respectively, which are 23% and 31% greater than with a pristine graphene electrode in an organic electrolyte.

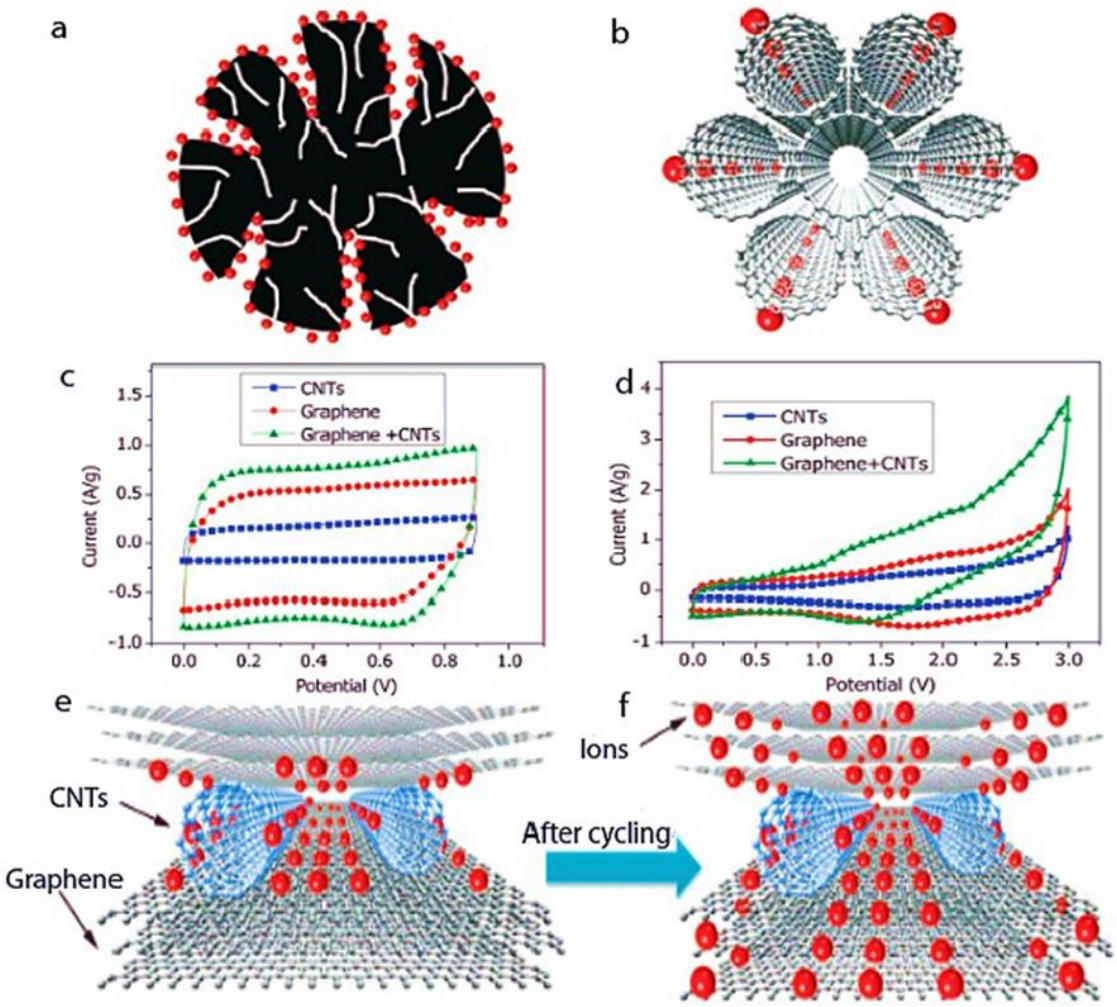

Figure 2.11 (a) AC illustrating ion adsorption at the surface of the micropores accessible to the electrolyte ions, (b) SWCNT, (c and d) cyclic voltammograms (CV) for different electrode materials made of CNTs, graphene, and their composite in the aqueous and organic electrolyte at a scan rate of 10 mV s^{-1}, respectively. (e) Before cycling, graphene layers tend to restack, (f), increasing the surface area accessible for electrolyte ions. [39]

For supercapacitor electrode materials, graphene and its porous variants provide many benefits. [40] High surface area, improved ion/electron transport, better material loading per unit area of the substrate, and higher mechanical flexibility/stability during repeated charge-discharge are some of its most essential qualities. [41] According to Xing et al. [42], humic acid can be carbonized with an oxidation-exfoliation-thermal reduction to produce high surface area graphene nanosheets. The supercapacitor electrodes displayed a specific capacitance of 272 F g^{-1} (at 50 mA g^{-1}) with an energy density of 6.47 Wh kg^{-1} and power density of 2 250 W kg^{-1}. The electrode maintained 96.5% of its initial capacitance after

8000 charge-discharge cycles. To synthesize graphene-based SCs, Xie et al. [43] combined conductive polyoxymethylene (POM) with graphene nanosheets. The cycling stability of POM/graphene nanosheets significantly increased when compared to pristine graphene nanosheets.

In-plane flexible micro-supercapacitor electrodes supported onto photographic paper via in-situ femtosecond laser reduced GO/Au nanoparticles were reported by Li et al. [44]. In a single step, the laser treatment reduced the hydrated GO and HAuCl4 while also patterning the rGO electrodes and creating the Au current collectors, as illustrated in figure 2.12 (a). A laser-written rGO/Au micro-SC with a triangle-shaped cross-sectional structure of microelectrodes is shown in the SEM image in figure 2.12 (b). Figure 2.12 (c) shows that as the scan rate of the constructed flexible micro-supercapacitor increased from 0.1 V s^{-1} to 100 V s^{-1}, the specific capacitance exhibited were 0.77 mF cm^{-2} and 0.46 mF cm^{-2}, respectively, and had a rate capability of 50%.

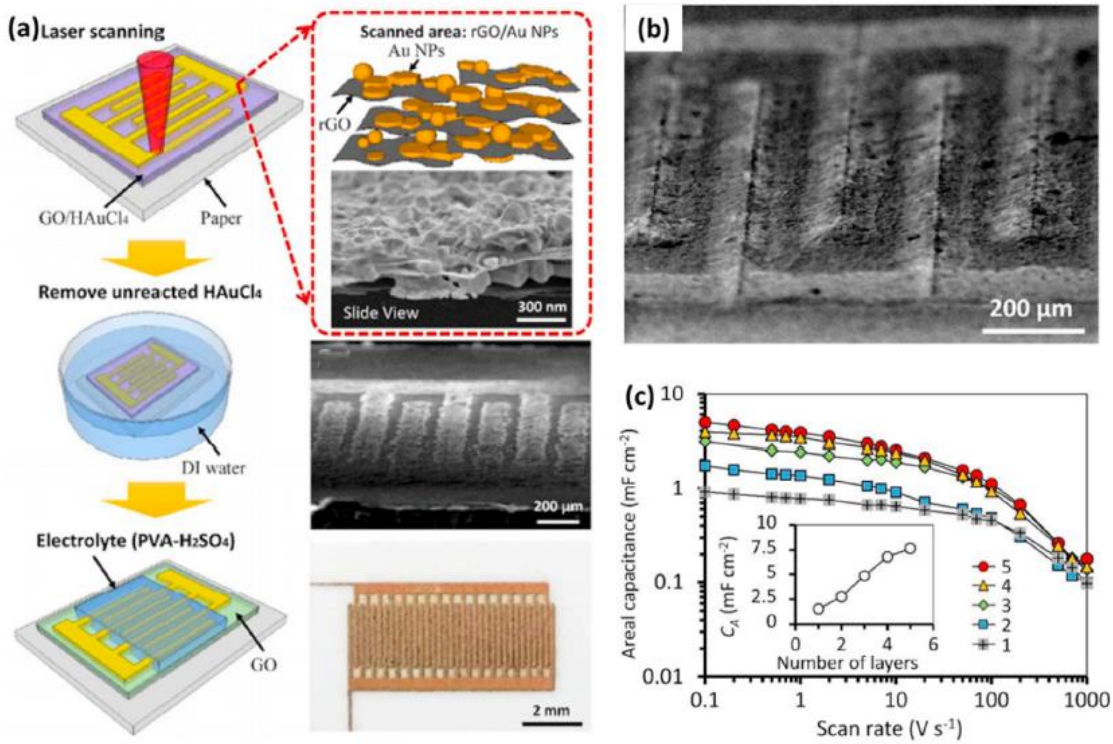

Figure 2.12 (a) Schematic illustration and images of rGO/Au micro supercapacitor fabrication. (b) SEM image of the interdigitated 5-layer rGO/Au microelectrodes and (c) areal capacitance as a function of scan rate. [44]

2.4.2.2 Metal oxides

Transition metals oxides that are originated from Ru, Co, Fe, Ti, V, Mo, and Nb have also been investigated as prospective electrode materials, with the results indicating that they store more energy than carbon-based electrodes. [13] They are pseudocapacitive in behavior i.e. there are fast and reversible faradaic reactions at the electrode surfaces, in combination with the non-faradaic electric double layer formation. Numerous oxidation states are known to exist at certain potentials in oxide materials, and choosing materials with numerous stability states within a given electrolyte's potential window enables maximal capacitance. Furthermore, the high conductivities of crystalline metal oxides allow charge propagation via the lattice structures of thin surface layers. [45]

Hydrous RuO_2 have surpassed the specific capacitance of carbon materials using EDLC charge storage mechanism. RuO_2 has a lower ESR value in comparison to carbon based and conducting polymer based compounds. This enables high reversibility, large capacitance and higher electrochemically stability. [1] However, RuO_2 has a high cost when compared to its competitors, which are largely carbon and polymer materials. The high intrinsic cost prevents these supercapacitors from reaching its market use. Substantial work has gone into developing production processes and composite materials that will lower the cost of RuO_2 while maintaining its characteristics. [8, 13, 45]

The various oxidation states displayed by RuO_2 are Ru^{4+}, Ru^{3+} and Ru^{2+} and its reversible redox reaction follows equation (2.11) below; [44]

$$RuOx\ (OH)y\ +\ \delta H+\ +\delta e-\ \rightleftharpoons\ RuOx-\delta\ (OH)y+\delta\ (0<\ \delta\ >2) \qquad (2.11)$$

Manganese oxides in their various forms **(**MnO_x or Mn_xO_y) have been heavily explored in several energy storage applications (i.e batteries and supercapcitors). Compared to other metal oxides, they are the most environmentally friendly and are easy to synthesize. In all the instances where MnO_x have been used as an electrode material in supercapacitors, it has shown improved performance. They are known to exhibit pseudocapacitance due to the redox transformations of interfacial oxycation species into different oxidation states, namely Mn^{3+} to Mn^{2+}, Mn^{4+} to Mn^{3+}, and Mn^{6+} to Mn^{4+} in a voltage window of aqueous electrolytes. [45] Charge storage for MnO_x occurs in two ways,

(1) surface adsorption of electrolyte cation (M^+= Na^+, K^+, Li^+) on MnO_x as shown by equation 2.12 and (2) through proton intercalation in equations (2.13 a and b) below; [46]

$$(MnO_2)_{surface} + M^+ + e- \rightleftharpoons (MnO_2 - M^+)_{surface} \quad (2.12)$$

Positive electrode:

$$MnOOH \rightleftharpoons H_{1-\delta}\,MnO_2 + \delta H^+ + \delta H^+ + \delta e \; (0 < \delta < 0.5) \quad (2.13a)$$

Negative electrode:

$$MnO_2 + \delta H^+ + \delta e \rightleftharpoons H_\delta MnO_2 \; (0 < \delta < 0.5) \quad (2.13b)$$

Generally, MnO_x electrodes have poor conductivity as electrode materials. Thus, a suitable component selection and reaction methods to build composite structures with the rational design is key in electrochemical properties. The synergistic effect and unique structure of the composites should be used to its full advantages. [47]

2.4.2.3 Polymers

As alternatives to transition metal oxides, pseudocapacitors also make use of conductive polymers (CPs). The most commonly used CPs include polypyrrole (PPy), polyaniline (PANI), and polythiophene (PTs). [48] The major advantages of CPs are the large specific capacitance, high conductivity, low cost and versatility of structural configurations. [49] Possible device configurations include (i) a symmetric supercapacitor based on a p-doped CP, (ii) an asymmetric supercapacitor based on two p-doped CPs that are dopable at various potential windows, or (iii) a symmetric supercapacitor with a p- and n-doped CP. In terms of energy and power density, the latter design appears to be the most promising. These electrode materials have been disadvantaged by their inability to obtain efficient, n-doped CPs. [48] The charge-discharge process of polymer electrodes is similar to that of batteries in that it involves the insertion and removal of ions (doping↔de-doping). A polymer is reversibly oxidized and reversibly reduced in this process as illustrated by the equations in figure 2.13. The cycling of the electrodes leads to a continuous change in physical structure and ultimately, a degradation in performance. These factors have hindered the wide use of CP based pseudocapacitors in application. Recently, CP

electrode material research in supercapacitor applications is directed towards the development of hybrid vehicles. [49]

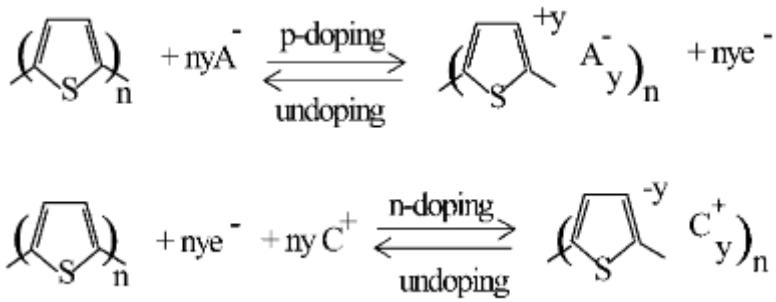

Figure 2.13 Schematic showing the p- and n-doping/de-doping processes in polythiophene. [49]

2.4.2.4 Composite

A supercapacitor from a composite material often entails a carbon related material coupled with either a conducting polymer or metal oxide in fabrication and is later cast on a single electrode. Depending on the material types, composite electrode materials effectively offer both EDLCs and pseudocapacitor energy storage mechanisms. [3]

2.4.2.5 Asymmetric

These devices employ one electrode based on a carbon material which its charge is a capacitive mechanism, while the other electrode is either a conducting polymer or metal oxide and stores charge via Faradaic processes. They offer the advantages of long-term stability and inexpensive cost. [3]

2.4.2.6 Battery type

A battery-type supercapacitor is constructed with a typical supercapacitor electrode material on one electrode, while the other is a typical battery electrode material i.e. lithium, sodium, potassium, magnesium etc. This configuration design intends to close the gap between batteries and supercapacitors with regards to energy and power density.

The achieved power and energy density range approximately between 0.1-30 kW kg^{-1} and 5-200 Wh kg^{-1}, respectively. This method incorporates the cycle life and charge-discharge times of a supercapacitor. [50]

2.4.3 Electrolytes

An electrolyte is a critical function in ion mobility and balance between the two electrodes. [51] Supercapacitor electrolytes are divided into three categories namely, ionic liquid (aqueous and non-aqueous), solid state, and organic types. Due to the low dynamic viscosity of aqueous electrolytes, their conductivity is often higher than that of non-aqueous and solid electrolytes. The concentration of free charge carriers (cations and anions) and charge transport properties are the main influences on the electrolyte conductivity. These two parameters are also influenced by the salt's solubility in the solvent and the degree of dissociation or pairing of the dissolved salt ions. Thus, the conductivity (σ) of species (i) is directly correlated to the ionic mobility (μ_i), concentration of charge carriers (n_i), elementary charge (e) and magnitude of valence of the mobile ion charges (z_i) as shown by the equation in (2.14); [51]

$$\sigma = \sum_i n_i \ \mu_i z_i e \tag{2.14}$$

Electrochemical stability of electrolytes is established through a potential window study exercise. Aqueous electrolytes are restricted by the thermodynamic electrochemical properties of water (approx. 1.23 V) and begin to decompose when the potential window exceeds 1 V. The most frequently used aqueous electrolyte solutions in supercapacitors are potassium hydroxide (KOH), sodium sulphate (Na_2SO_4) and sulfuric Acid (H_2SO_4). The hydrated cationic radius and conductivity, coupled with their effect on charge/ion exchange and diffusion are the main attributes for their common use. [52]

Solid state electrolytes strive to merge the electrolyte and separator functions into a single component, reducing the total number of components in a supercapacitor and increasing the potential window due to the matrix increased stability. When these are employed, the separator must be insoluble in the electrolyte and have sufficient ionic conductivity. The most commonly used solid state electrolytes are based on polymers such as polyethylene oxide (PEO), polyvinyl alcohol (PVA), polyethylene glycol (PEG), etc. These can be in

the following three different forms: solid polymer electrolytes (SPEs), gel polymer electrolytes (GPEs), and polyelectrolytes. [52]

As an alternative, organic electrolyte derived from a quaternary salt and dissolved in organic solvents such as acetonitrile (ACN) or propylene carbonate (PC) have been used. The operating potential window of an organic electrolyte can exceed 3.0 V which has significantly enhanced the energy density of supercapacitors by 4x folds in relation to that of aqueous electrolytes. These benefits have been the main driver for recent research to adopt organic electrolytes. However, in some cases organic electrolytes may still have low conductivity, resulting in a rise in the ESR. In applications where power density is a critical requirement, resistivity is a limiting factor. [53]

The high conductivity and adequate electrochemical stability are important to consider when selecting an electrolyte to allow the capacitor being operated to reach the highest possible voltages. The appropriate electrolyte is chosen according to the intended application of the supercapacitor. [8,11, 51]

2.4.4 Separators

The main role of a separator in an electrochemical cell is to prevent contact between both electrodes and to allow electron transfer. The type of separator used in supercapacitors contributes to its overall performance through a mechanical strength that ensures durability and limited migration of particles overtime. Separators must be compatible with the type of electrolyte. For instance, in cases where organic electrolytes have been used, polymer and paper separators are ideal. Whereas, in aqueous electrolytes, glass fibre and ceramic separators are most effective. The most favorable separator possesses chemical resistance to corrosion by the electrolyte and electrode degradation by-products. [54]

2.4.5 Applications of Supercapacitors

The applications of supercapacitors are countless because they are cost effective and environmentally friendly energy storage devices. [3] Their use ranges from small scale, for

example mobile phones or as backup power sources up to electric vehicles and industrial applications as outlined in figure 2.14.

Figure 2.14 Current applications of supercapacitors. [54]

Supercapacitors have largely penetrated the market as devices with large power capabilities for energy storage systems. They are used for uninterruptible power supply (UPS) systems (either individually or in tandem with batteries as a hybrid UPS). Other applications include transmission lines, portable electronics, renewable and off-peak energy storage, microgrid and micro-generation, adjustable speed drives (ASDs), aerospace applications, hybrid electric vehicles, medical devices, electronic fuses in the mining industry and smart weapons. Supercapacitors are most used in electric vehicles simply because of an appreciable amount of energy required during acceleration that is regained during deceleration or braking. The low ESR associated with supercapacitors enables them to be charged at a very high current. Thus, supercapacitors are suited for regenerative braking applications that require a high charging current profile to absorb braking energy. This phenomenon is unlikely for batteries with a characteristic high ESR value, in which case the current must be minimized to avoid overheating of the

electrochemical cell. The initial intent was to use supercapacitors in a combined power source configuration to boost fuel cells and batteries. Upon further developments, the device has been independently adapted in applications with high power demands which both fuel cells and electrochemical batteries are not well suited. [55-58] They considerably extend the life of batteries when used in parallel. For instance, in mobile apps, the usage of a battery-supercapacitor hybrid connection has proven advantageous for run-time expansions. [59]

2.5 MoS_2 as an electrode material

Molybdenum disulphide (MoS_2) based electrodes have demonstrated higher energy density and power capabilities, which can be ascribed to its larger theoretical capacity compared to layered graphene and higher ionic conductivity than transition metal oxides. [60] MoS_2 has been very important in improving energy storage capabilities of Li-ion batteries and supercapacitors in recent years. [61] MoS_2 is amongst the most common transition metal dichalcogenides (TMDCs) family, which are semiconductors of the type MX_2, where M is a transition metal atom (such as Mo or W) and X is a chalcogen atom (such as S, Se or Te). [62-64] TMDs arrange themselves in various crystalline forms, but only the Mo and W compounds form a 2D layered hexagonal crystal structure. As can be seen in figure 2.15 (a). MoS_2 is a layered material in which each Mo atomic layer is sandwiched between two S atomic layers, which are covalently bonded. The adjacent layers are connected through van der Waals interactions in a structurally similar manner to graphite. [9] This presents an advantage of storing energy (i) using the highly accessible high surface area for charge accumulation needed in electrical double-layer capacitors, and (ii) redox properties via intercalation of ions into MoS_2 layers at the interface accompanied by faradaic charge-transfer observed in pseudocapacitors. [64-66]

MoS_2 crystal structure can exist in three forms of atom arrangements namely, 1T-MoS_2, 2H-MoS_2, and 3R-MoS_2, see figure 2.15 (b). [67] The 2H and 3R types of MoS_2 have semiconducting properties and both of them have trigonal prismatic coordination (the stacking sequences are ABA and ABC, respectively). The vast majority of research is focused around 1T and 2H MoS_2, given that, they convert to each other by electric doping, annealing, applying strain and electron-beam irradiating, which has shown to be highly effective in most applications owing to the tunable electronic properties. [68] Despite the

mentioned advantages of MoS_2 based electrodes, their commercialization in energy storage applications is still limited by the poor cycling performance and rate capability. Increasing conductivity via additional carbon or conducting polymers to form a composite has been investigated by several researchers. [62]

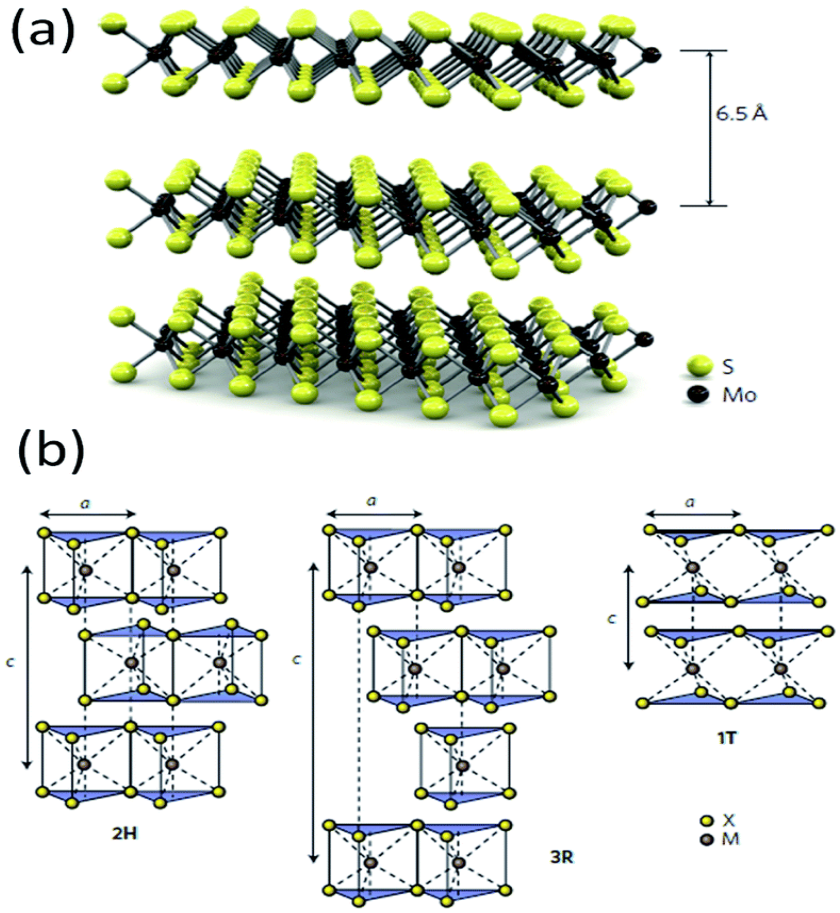

Figure 2.15 Schematic illustration of the crystal structure and optical properties of MoS_2. (a) Top view of the monolayer MoS_2. (b) Atomic arrangements of single layer MoS_2: trigonal prismatic (2H), rhombohedral symmetry (3R) and octahedral (1T). [62]

Over the past decade, research reports on MoS_2 with various morphologies as an electrode material in electrochemical energy storage have largely multiplied. [68] In order to improve the electrochemical performance of MoS_2 various synthesis strategies have been explored which have led to the discovery of nanoparticles [69], nano-flowers [70], nanotubes [71] nanoboxes [72] spheres [73] and hollow nanospheres [74-75]. Some of these morphologies are displayed in figure 2.16 together with their various synthesis methods.

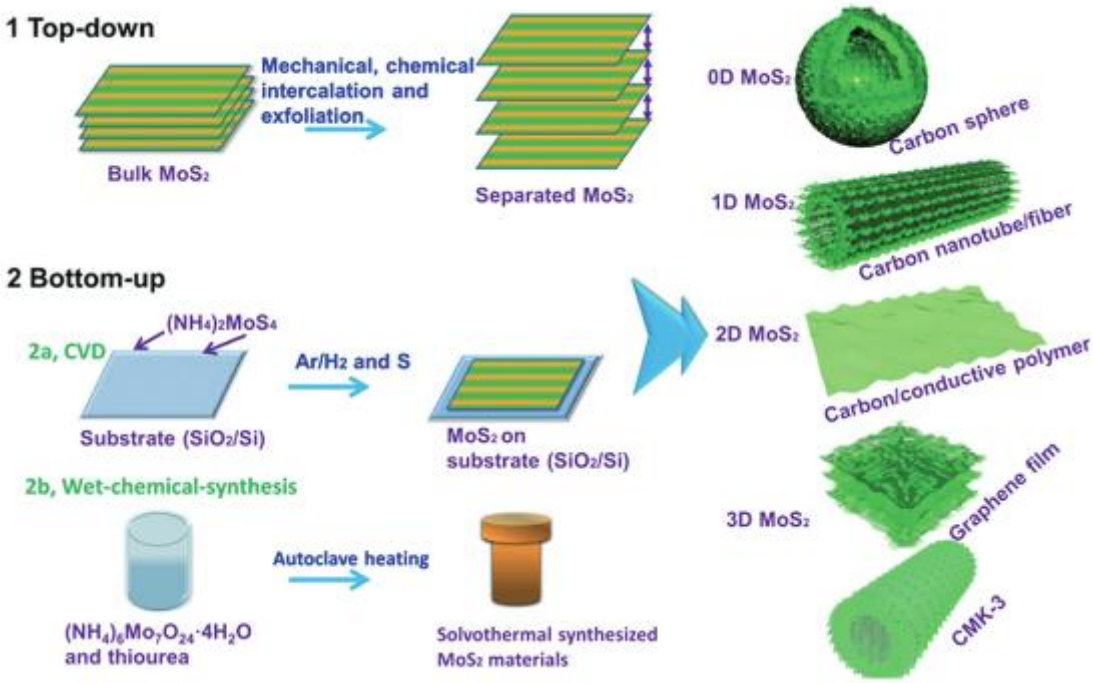

Figure 2.16 The schematic illustration of the preparation methods of MoS_2. [68]

2.6 Metallophthalocyanines (M-Pcs)

M-Pcs are the most researched macrocyclic organometallic functional materials. The metal ion is symmetrically surrounded by four nitrogen atoms in the molecules' planar geometries, commonly referenced as, transition metal N_4 macrocycles, as shown in figure 2.17. [76] Owing to their macrocyclic nature along with extended π-systems, M-Pcs exhibit unique properties that make them attractive in many fields such as electro catalysis [77] and sensing [78], electrochoursomic [79] and electroluminescent display devices [80], liquid crystal display devices [81], photodynamic therapy [82] and other photosensitisation processes [83] and in the development of energy storage and conversion systems such as fuel cells [84], oxygen reduction reaction [85], lithium battery [86] and supercapacitor development [87]. The central cavity of phthalocyanines is known to be capable of accommodating 63 different elemental ions, including hydrogens (metal-free phthalocyanine, H_2-Pc). [88]

M-Pcs were firstly studied by Yamaki et al. [8] for application in lithium batteries as a cathode material. The best capacity was reported for the FePc variant as 1440 Ah kg^{-1} by discharging at 1 mA. However, the high capacitance could not be sustained due to limited

cycle life, poor conductivity and high solubility in electrolyte solution. [89] In a recent patent, Chen et. al. [90] suggested the use of a protective Li-conducting material to cover phthalocyanine compound so that it is not in direct contact with the electrolyte. The results showed a much longer cycle life, high cathode specific capacity and best energy density for a rechargeable lithium-ion battery cell. In another study, Jahnke et al.[91] improved thermal stability as well as the electrochemical activity of transition metal porphyrins deposited on a carbon support by a pyrolytic heat treatment step in the range from 450 to 900 °C in an inert atmosphere. After the heat treatment, these centers are attached to a conductive carbon matrix as opposed to the precursor. These findings suggest that the synthesis of MPc with materials that have complementary properties to form a composite are key in achieving effective improvements on their electrochemical performance.

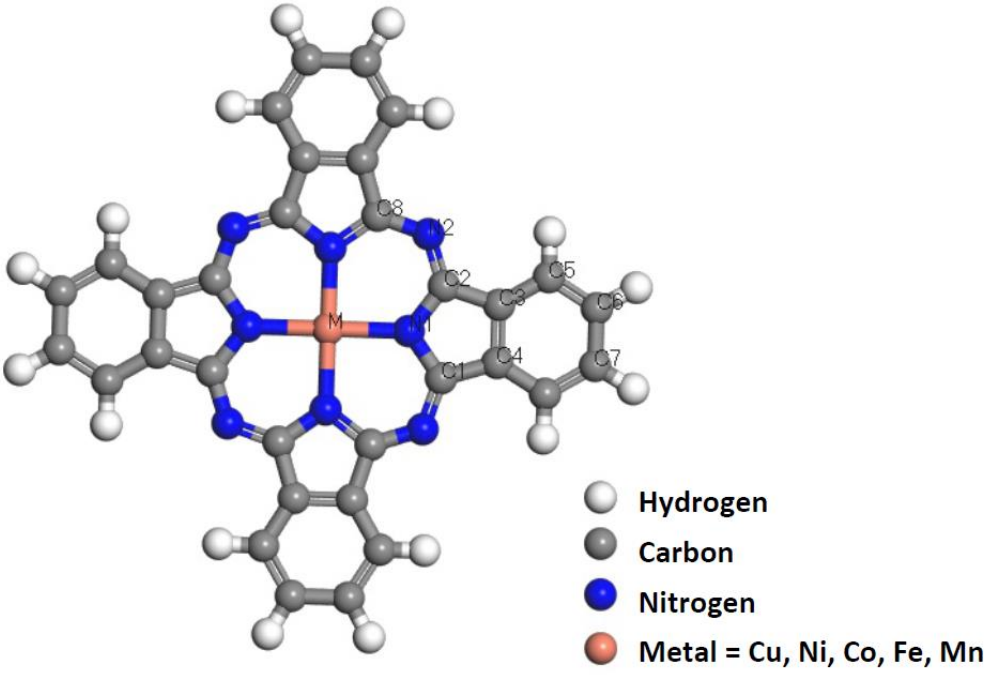

Figure 2.17 Schematic view of a molecular structure of phthalocyanine, where M in the centre of the macrocycle represents the metal ion. [78]

2.7 Fundamentals of Electrospinning

Electrospinning is perhaps the most versatile technique for the fabrication of one-dimensional nanomaterials. [92] Nanofibres obtained from the electrospinning technique

may vary in dimensions from submicron down to nanometer diameters. Nonetheless, electrospun fibres have been shown to exhibit many useful chemical and physical properties. [93] A typical electrospinning setup is shown in figure 2.18 and consists of a high voltage power supply, usually in the kV range, the syringe and the collector plate. [94-96] In principle, a potential is applied across a syringe and a collector such that the interactions of the electrical charges induce a pendant droplet on the polymer solution at the tip of the needle. The electrostatic repulsion causes the droplet to elongate and form a Taylor cone. As the intensity of the electric field increases, the repulsive electric forces overcome the surface tension and eventually a charged jet of a polymer solution is continuously stretched out. The instability in motion of the fibre resulting from the electric field causes a whipping process leading to the evaporation of the solvent. Thus, a solidified uniform thin fibre is accumulated on the grounded collector. [93] The main drivers for the diameter and morphology of the fibres are; (i) the intrinsic properties of the solution (polymer type, viscosity or concentration, solvent, elasticity etc.) (ii) the distance between the syringe and the collector, and (iii) the feed rate of the polymer solution. Moreover, humidity and temperature of the surroundings are additional variables that may also play a role in the morphology and diameter. [96-100]

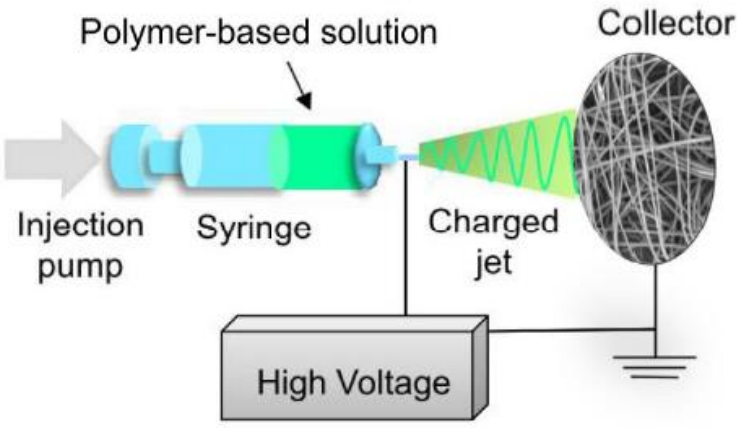

Figure 2.18 Schematic of an electrospinning apparatus with a horizontal setup. [92]

2.8 References

[1] Beguin, F.; Frackowiak, E. *Supercapacitors: Materials, Systems, and Applications*. Wiley & Sons - Technology & Engineering. Weinheim, Germany, 2013.

[2] Choo, Y.; Halat, D. M.; Villaluenga, I.; Timachova, K.; Balsara, N. P. Diffusion and migration in polymer electrolytes. *Prog. Polym. Sci*. **2020**, 103, 1010220.

[3] Bard, J. A.; Faulkner, L. R. *Electrochemical Methods: Fundamentals and Applications*, 2nd Ed. Wiley & Sons, Inc. New York, 2000, 198.

[4] Seeber, R.; Zanardi, C.; Inzelt, G. The inherent coupling of charge transfer and mass transport processes: the curious electrochemical reversibility. *Prog. Polym. Sci*. **2016**, 2, 1-18.

[5] Mclean, A. V.; Halper, M. S.; Ellenbogen, J. C. Supercapacitors: *A brief overview*, Virginia: The MITRE nanosystems group, 2006.

[6] Miller, J. R. A brief history of supercapacitors, Batteries and energy storage technologies. *Batteries and Energy Storage Technology*, 2007, 61-78.

[7] Miller, J. R.; Simon, P. Supercapaciotrs: Fundamentals of electrochemical capacitor design and operation. *Electrochem. Soc. Interface*, **2008**, 31-32.

[8] Yadav, V. K.; Bhardwarj, N. Introduction to supercapacitors and supercapacitor assisted engine starting system. *Int. J. Eng. Res*. **2013**, 4, 583-588.

[9] S. Mallika, and K. R. Saravana. Review on Ultracapacitor- Battery Interface for Energy Management System. *Int. J. Eng. Technol.* **2011**, 3, 37-43.

[10] Endo, M.; Takeda, T.; Kim, Y. J.; Koshiba, K.; Ishii, K. High power electric double layer capacitor (EDLC's); from operating principle to pore size control in advanced activated carbons. *Carbon Lett.* **2001**, 1, 117-128.

[11] Béguin, F.; Presser, V.; Balducci, A.; Frackowiak, E. Carbons and electrolytes for advanced supercapacitors. *Adv. Mater.* **2014**, 26, 2219-2251.

[12] Miller, E. E.; Hua, Y.; Tezel, F. H. Materials for energy storage: Review of electrode materials and methods of increasing capacitance for supercapacitors. *J. Energy Storage*. **2018**, 20, 30-40.

[13] Burke, A. Ultracapacitors: why, how, and where is the technology. *J. Power Sources*. **2000**, 91, 37-50.

[14] Kotz, R.; Carlen, M. Principles and applications of electrochemical capacitors. *Electrochim. Acta*, **2000**, 45, 2483-2498.

[15] Scherson, D. A.; Palencsár, A. Batteries and electrochemical capacitors. *Electrochem Soc Interface*. **2006**, 1827, 17-22.

[16] Sahin, M. E.; Blaabjerg, F.; Sangwongwanich, A. A review on supercapacitor materials and developments. *Turk. J. Biol*. **2020**, 5, 10-24.

[17] Zhang, L.; Hu, X.; Wang, Z.; Sun, F.; Dorrell, D. G. A review of supercapacitor modelling, estimation, and applications: A control/management perspective. *Renew. Sustain. Energy Rev*. **2018**, 81, 1868-1878.

[18] Pandolfo, A. G.; Hollenkamp, A. F. Carbon properties and their role in supercapacitors. *J. Power Sources*. **2006**, 157, 11-27.

[19] Frackowiak, E.; Béguin, F. Carbon materials for the electrochemical storage of energy in capacitors. *Carbon*. **2001**, 39, 937-950.

[20] Simon, P.; Gogotsi, Y. Materials for electrochemical capacitors. *Nat. Mater*. **2008**, 7, 845-854.

[21] Snook, G. a.; Kao, P.; Best, A. S. Conducting-polymer-based supercapacitor devices and electrodes. *J. Power Sources*. **2011**, 196, 1-12.

[22] Kumar, R.; Joanni, E.; Sahoo, S.; Shim, J-J.; Tan, W. K.; Matsuda, A.; Singh, R. K. An overview of recent progress in nanostructured carbon-based supercapacitor electrodes: From zero to bi-dimensional materials. *Carbon*. **2022**, 193, 298-338.

[23] Athika, M.; Prasath, A.; Duraisamy, E.; Devi, S. V.; Sharma, A. S.; Elumalai, P. Carbon-quantum dots derived from denatured milk for efficient chromium-ion sensing and supercapacitor applications. Mater. Lett. 2019, 241, 156-159.

[24] Zhao, X.; Li, M.; Dong, H.; Liu, Y.; Hu, H.; Cai, Y.; Liang, Y.; Xiao, Y.; Zheng, M. Interconnected 3 D network of graphene-oxide nanosheets decorated with carbon dots for high-performance supercapacitors. *Chem. Sus. Chem*. **2017**, 10 (12), 2626-2634.

[25] De, B.; Kuila, T.; Kim, N. H.; Lee, J. H. Carbon dot stabilized copper sulphide nanoparticles decorated graphene oxide hydrogel for high performance asymmetric supercapacitor. *Carbon*. **2017**, 122, 247-257.

[26] Zhang, X.; Wang, J.; Liu, J.; Wu, J.; Chen, H.; Bi, H. Design and preparation of a ternary composite of graphene oxide/carbon dots/polypyrrole for supercapacitor application: importance and unique role of carbon dots. *Carbon*. **2017**, 115, 134-146.

[27] Chen, X. Wang, H. Yi, H. Wang, X. Yan, X. Guo, Z. Anthraquinone on porous carbon nanotubes with improved supercapacitor performance. *J. Phys. Chem. C*. **2014**, 118 (16), 8262-8270.

[28] Li, Z.; Li, Y.; Wang, L.; Cao, L.; Liu, X.; Chen, Z.; Pan, D.; Wu, M. Assembling nitrogen and oxygen co-doped graphene quantum dots onto hierarchical carbon networks for all-solid-state flexible supercapacitors. *Electrochim. Acta*. **2017**, 235, 561-569.

[29] Yang, Z. Tian, J. Yin, Z. Cui, C. Qian, W. Wei, F. Carbon nanotube- and graphene-based nanomaterials and applications in high-voltage supercapacitor: a review. *Carbon*. **2019**, 141, 467-480.

[30] Liu, C.-F.; Liu, Y.-C.; Yi, T.-Y.; Hu, C.-C. Carbon materials for high-voltage supercapacitors. *Carbon*. **2019**, 145, 529-548.

[31] Sun, L.; Wang, Y.; Wang, Q. Zhang, Roles of carbon nanotubes in novel energy storage devices. *Carbon*. **2017**, 122, 462-474.

[32] Lota, G.; Fic, K.; Frackowiak, E. Carbon nanotubes and their composites in electrochemical applications. *Energy Environ. Sci*. **2011**, 4 (5), 1592-1605.

[33] Kumar, S.; Nehra, M.; Kedia, D.; Dilbaghi, N.; Tankeshwar, K.; Kim, K. -H. Carbon nanotubes: a potential material for energy conversion and storage. *Prog. Energy Combust. Sci*. **2018**, 64, 219-253.

[34] He, S.; Hu, Y.; Wan, J.; Gao, Q.; Wang, Y.; Xie, S.; Qiu, L.; Wang, C.; Zheng, G. Wang, B.; Peng, H. Biocompatible carbon nanotube fibers for implantable supercapacitors. *Carbon*. **2017**, 122, 162-167.

[35] Wu, M. S.; Zheng, Y. R.; Lin, G. W. Three-dimensional carbon nanotube networks with a supported nickel oxide nanonet for high-performance supercapacitors. *Chem. Commun*. **2014**, 50 (60), 8246-8248.

[36] Zhou, Y.; Song, Z.; Hu, Q.; Zheng, Q.; Jiang, N.; Xie, F.; Jie, W.; Xu, C.; Lin, D. Hierarchical nitrogen-doped porous carbon/carbon nanotube composites for high-performance supercapacitor. *Superlattice. Microst*. **2019**, 130, 50-60.

[37] Shan, Y.; Gao, L. Formation and characterization of multi-walled carbon nanotubes/Co_3O_4 nanocomposites for supercapacitors. *Mater. Chem. Phys*. **2007**, 103 (2), 206-210.

[38] Chang, Z.-H.; Feng, D.-Y.; Huang, Z.-H.; Liu, X.-X. Electrochemical deposition of highly loaded polypyrrole on individual carbon nanotubes in carbon nanotube film for supercapacitor. *Chem. Eng. J*. **2018**, 337, 552-559.

[39] Cheng, Q.; Tang, J.; Ma, J.; Zhang, H.; Shinyaa, N.; Qinc, L.-C. Graphene and carbon nanotube composite electrodes for supercapacitors with ultra-high energy density. *Phys. Chem. Chem. Phys*. **2011**, 13, 17615-17624.

[40] Kumar, R.; Singh, R. K.; Dubey, P. K.; Kumar, P.; Tiwari, R.S.; Oh, I.-K. Pressure-dependent synthesis of high-quality few-layer graphene by plasma-enhanced arc discharge and their thermal stability. *J. Nanoparticle Res*. **2013**, 15 (9), 1847.

[41] Yang, W.; Ni, M.; Ren, X.; Tian, Y.; Li, N.; Su, Y.; Zhang, X. Graphene in supercapacitor applications. *Curr. Opin. Colloid Interface Sci*. **2015**, 20 (5), 416-428.

[42] Xing, B.; Yuan, R.; Zhang, C.; Huang, G.; Guo, H.; Chen, Z.; Chen, L.; Yi, G.; Zhang, Y.; Yu, J. Facile synthesis of graphene nanosheets from humic acid for supercapacitors. *Fuel Process. Technol*. **2017**, 165, 112-122.

[43] Xie, T.; Zhang, L.; Wang, Y.; Wang, Y.; Wang, X. Graphene-based supercapacitors as a flexible wearable sensor for monitoring pulse-beat. *Ceram. Int*. **2019**, 45 (2), 2516-2520.

[44] Li, R. Z.; Peng, R.; Kihm, K. D.; Bai, S.; Bridges, D.; Tumuluri, U.; Wu, Z.; Zhang, T.; Compagnini, G.; Feng, Z.; Hu, A. High-rate in-plane micro-supercapacitors scribed onto photo paper using in situ femtolaser-reduced graphene oxide/Au nanoparticle microelectrodes. *Energy Environ. Sci*. **2016**, 9 (4), 1458-1467.

[45] Zhang, J.; Jiang, D.; Chen, B.; Zhu, J.; Jiang, L.; Fang, H. Preparation and electrochemistry of hydrous ruthenium oxide/active carbon electrode materials for supercapacitor. *J. Electrochem. Soc*. **2001**, 148 (12), A1362-A1367.

[46] Zhang S. W.; Chen G. Z. Manganese oxide based materials for supercapacitors. *Energy Mat.* **2008**, 3, 186-200.

[47] Wayu, M. Manganese Oxide Carbon-Based Nanocomposite in Energy Storage Applications. *Solids*. **2021**, 2, 232-248.

[48] Ramya, R.; Sivasubramanian, R.; Sangaranarayanan, M. V. Conducting polymers-based electrochemical supercapacitors-Progress and prospects. *Electrochim. Acta*. **2013**, 101, 109-129,

[49] Snook, G.A.; Kao, P.; Best, A.S. Conducting-polymer-based supercapacitor devices and electrodes. *J. Power Sources*. **2011**, 196,1-12.

[50] Zuo, W.; Li, R.; Zhou, C.; Li, Y.; Xia, J.; Liu, J. Battery-Supercapacitor Hybrid Devices: Recent Progress and Future Prospects. *Adv. Sci*. **2017**, 4, 1600539.

[51] Conway, B. E. Electrochemical Supercapacitors: Scientific Fundamental and Technological Applications. Kluwer Academic/Plenum: New York, 1999.

[52] Lewandowski, A.; Olejniczak, A.; Galinski, M.; Stepniak, I. Performance of carbon–carbon supercapacitors based on organic, aqueous and ionic liquid electrolyte. *J. Power Sources*. **2010**, 195, 5814-5819.

[53] Simon, P.; Gogotsi, Y. Carbon À Electrolyte Systems. Capacitive Energy Storage in Nanostructured Carbon-Electrolyte Systems. *Acc Chem Res*. **2013**, 46, 1094.

[54] Schneuwly, A.; Gallay, R. Properties and applications of supercapacitors from the state-of-the-art to future trends. Proceedings of PCIM Conference, Switzerland, 2000, 1-10.

[55] Yu, A.; Chabot, V.; Zhang, J. Electrochemical supercapacitors for energy storage and delivery: Fundamentals and applications, CRC Press-Taylor & Francis Group. London, New York, 2013.

[56] Gauthan, P. G.; Nidheesh, S.; Simran, T.; Rakshitha, K.; Bommegodwa, B. Supercapacitor technology and its applications: a review. IOP Conf. Series: Materials Science and Engineering. 2019, 561, 012105.

[57] Trasatti, S.; Kurzweil, P. Electrochemical supercapacitors as versatile energy stores. *Platin. Met. Rev*. **1994**, 38, 46-56.

[58] Chen, K.; Xue, D. Ionic supercapacitor electrode materials: A system-level design of electrode and electrolyte for transforming ions into colloids. *Colloids Interface Sci. Commun*. **2014**, 1, 39-42.

[59] Haung, S.; Zhu, X.; Sarkar, S.; Zhao, Y. Challenges and opportunities for supercapacitors. *APL Mater*., **2019**, 7, 100901.

[60] Li, Y.; Wang, H.; Xie, L.; Liang, Y.; Hong, G.; Dai, H. MoS_2 Nanoparticles Grown on Graphene: An Advanced Catalyst for Hydrogen Evolution Reaction. *J. Am. Chem. Soc*. **2011**, 133, 19, 7296-7299.

[61] Wang, T.; Chen, S.; Pang, H.; Xue, H.; Yu, Y. MoS_2-Based Nanocomposites for Electrochemical Energy Storage. *Adv. Sci*. **2017**, 4, 1600289.

[62] Li, X.; Zhu, H. Two-dimensional MoS_2: Properties, preparation, and applications. *J. Materiomics*. **2015**, 1, 33-44.

[63] Rehman, M. M.; Siddiqui, G. U.; Gul, J. Z.; Kim, S.-W.; Lim, J. H.; Choi, K. H. Resistive Switching in All-Printed, Flexible and Hybrid MoS_2-PVA Nanocomposite based Memristive Device Fabricated by Reverse Offset. *Sci. Rep*. **2016**, 6, 36195.

[64] Choudhary, N.; Patel, M.D.; Park, J.; Sirota, B.; Choi, W. Synthesis of Large Scale MoS_2 for Electronics and Energy Applications, *J. Mater. Res*. **2016**, 31, 824-831.

[65] Li, Y.; Chang, K.; Sun, Z.; Shangguan, E.; Tang, H.; Li, B.; Sun, J.; Chang, Z. Selective Preparation of 1T- and 2H-Phase MoS_2 Nanosheets with Abundant Monolayer Structure and Their Applications in Energy Storage Devices. *ACS Appl. Energy Mater*. **2020**, 3, 998-1009.

[66] Soon, J. M.; Loh, K. P. Electrochemical double-layer capacitance of MoS_2 nanowall films. *Electrochem. Solid-State Lett*. **2007**, 10, A250.

[67] Gupta, D.; Chauhan, V.; Kumar, R. A Comprehensive Review on Synthesis and Applications of Molybdenum Disulfide (MoS_2) Material: Past and Recent Developments. *Inorg. Chem. Commun*. **2020**, 121, 108200.

[68] Samy, O.; Moutaouakil, A. E. A Review on MoS_2 Energy Applications: Recent Developments and Challenges. *Energies*. **2021**, 14, 4586.

[69] Huang, K. J.; Wang, L.; Liu, Y. J.; Wang, H. B.; Liu, Y. M.; Wang, L. L. Synthesis of polyaniline/2-Dimensional Graphene Analog MoS_2 composites for High-Performance Supercapacitor. *Electrochim. Acta*. **2013**, 109, 587-594.

[70] Wang, S.; An, C.; Yuan, J. Synthetic fabrication of nanoscale MoS_2-based transition metal sulphides. *Materials*. **2010**, 3, 401-433.

[71] Song, I.; Park, C.; Choi, H.C. Synthesis and Properties of Molybdenum Disulphide: From Bulk to Atomic Layers. *RSC Adv*. **2015**, 5, 7495-7514.

[72] Krishnamoorthy, K.; Veerasubramani, G. K.; Radhakrishnan, S.; Kim, S. J. Supercapacitive Properties of Hydrothermally Synthesized Sphere like MoS_2 Nanostructures. *Mater. Res. Bull*. **2014**, 50, 499-502.

[73] Kaushik, S.; Tiwari, U.K.; Choubey, R.K.; Singh, K.; Sinha, R.K. Study of Sonication Assisted Synthesis of Molybdenum Disulfide (MoS_2) Nanosheets. *Mater. Today Proc*. **2020**, 21, 1969-1975.

[74] Gao, M.-R.; Chan, M.K.Y.; Sun, Y. Edge-Terminated Molybdenum Disulfide with a 9.4-Å Interlayer Spacing for Electrochemical Hydrogen Production. *Nat. Commun*. **2015**, 6, 7493.

[75] Tang, Q.; Jiang, D. Mechanism of Hydrogen Evolution Reaction on 1T-MoS_2 from First Principles. *ACS Catal*. **2016**, 6, 4953-4961.

[76] Ozoemena, K. I.; Nyokong, T. Surface electrochemistry of iron phthalocyanine axially ligated to 4-mercaptopyridine self-assembled monolayers at gold electrode: applications to electrocatalytic oxidation and detection of thiocyanate. *J. Electroanal. Chem*. **2005**, 579, 283-289.

[77] Yamaki, J.; Yamaji, A. Phthalocyanine Cathode Materials for Secondary Lithium Cells. *J. Electrochem. Soc*. **1982**, 129, 5-9.

[78] Sakamoto, K.; Ohno-Okumura, E. Syntheses and Functional Properties of Phthalocyanines. *Materials*. **2009**, 2, 1127-1179.

[79] Sakamoto, K.; Ohno-Okumura, E. Syntheses and Functional Properties of Phthalocyanines. *Materials*. **2009**, 2, 1127-1179.

[80] Oni, J.; KI Ozoemena, K. I. Phthalocyanines in batteries and supercapacitors. *J. Porphyrins Phthalocyanines*. **2012**, 16, 754-760

[81] Lekitima, J. N.; Ozoemena, K. I.; Jafta, C. J.; Kobayashi, N.; Song, Y.; Tong, D.; Chen, S.; Oyama, M. High performance aqueous asymmetric electrochemical capacitors based on graphene oxide/cobalt(ii)tetrapyrazinoporphyrazine hybrids. *J. Mater. Chem. A.* **2013**, 1, 2821.

[82] Madhuri, K. P.; John, N. S. Supercapacitor application of nickel phthalocyanine nanofibres and its composite with reduced graphene oxide. *Appl. Surf. Sci*. **2018**, 449, 528-536.

[83] Samanta, M.; Howli, P.; Ghorai, U. K.; Mukherjee, M.; Bose, C.; Chattopadhyay, K. K. Solution processed Copper Phthalocyanine nanowires: A promisingsupercapacitor anode material. *Physica E Low Dimens. Syst. Nanostruct*. **2019**, 114, 113654.

[84] Yang, H.; Fan, P.; Liu, S.; Wei, J.; Tan, S.; Wang, Q.; Hou, H. Electrode Characteristics and Lithiation Mechanism of FePc/GN Composites. *Int. J. Electrochem. Sci*. **2018**, 13, 2606-2616.

[85] van Veen, J. A. R.; Colijn, H. A.; van Baar, J. F. On the effect of a heat treatment on the structure of carbon-supported metalloporphyrins and phthalocyanines. *Electrochim. Acta*, **1988**, 33, 801-804.

[86] Gojkovic, S. L.; Gupta, S.; Savinell, R. F. Heat treated iron (III) tetraethoxy porphyrin chloride supported on high surface area carbon as an electrocatalyst for oxygen

reduction: Part III Detecetion of oxygen peroxide during oxygen reduction. *Electrochim. Acta*. **1999**, 45, 889-897.

[87] Sakamoto, K.; Ohno-Okumura, E. Syntheses and Functional Properties of Phthalocyanines. *Materials.* **2009**, 2, 1127-1179.

[88] Kumar, A.; Vashistha, W. K.; Das, D. K. Recent development on metal phthalocyanines based materials for energy conversion and storage applications. *Coord. Chem. Rev*. **2021**, 431, 213678.

[89] Cheng, Y.; Wu, X.; Veder, J. -P.; Thomsen, L.; Jiang, S. P.; Wang, S. Tuning the Electrochemical Property of the Ultrafine Metal-oxide Nanoclusters by Iron Phthalocyanine as Efficient Catalysts for Energy Storage and Conversion. *Energy Environ. Mater*. **2019**, 2, 5-17.

[90] Chen, G.; Jang, B. Z.; Zhamu, A. Encapsulated phthalocyanine particles, high-capacity cathode containing these particles, and rechargeable lithium cell containing such a cathode. US13/573,298 https://patents.google.com/patent/US20140072879.

[91] Jahnke, H.; Schönborn, M.; Zimmermann, G. Organic dyestuffs as catalysts for fuel cells. *Top. Curr. Chem*. **1976**, 61, 133-181.

[92] Santangelo, S. Electrospun Nanomaterials for Energy Applications: Recent Advances. *Appl. Sci*. **2019**, 9, 1049.

[93] Shi, X.; Zhou, W.; Ma, D.; Bridges, D.; Ma, Y.; Hu, A. Electrospinning of nanofibres and their applications for their applications for energy devices. *J. Nanomater*. **2015**, 2015, 1-20.

[94] Li, D.; Xia, Y. Electrospinning of nanofibre: Reinventing the wheel? *Adv. Mater*. **2014**, 16, 1151-1170

[95] Thavasi, V.; Singh, G.; Ramakrishna, S. Electrospun nanofibres in energy and environmental applications. *Energy Environ. Sci*. **2008**, 1, 205-221.

[96] Cavaliere, S.; Subianto, S.; Savyeh, I.; Jones, J. D.; Roziere, J. Electrospinning: Design architectures for energy conversion and storage devices. *Energy Environ. Sci*. **2011**, 4, 4761-4785.

[97] Subbiah T., Bhat G. S.; Tock R. W. Electrospinning of Nanofibres, *J. Appl. Polym. Sci*. **2005**, 96, 557-569.

[98] Teo W. E.; Ramakrishna S. A review on electrospinning design and nanofibre assemblies. *Nanotechnology.* **2006**, 17, R89-R106.

[99] Nataraj S. K.; Yang K. S.; Aminabhavi T. M. Polyacrylonitrile-based nanofibres-A state-of-the-art review, *Prog. Polym. Sci*. **2012**, 37, 487-513.

[100] Thavasi V.; Singh G.; Ramakrishna S. Electrospun nanofibres in energy and environmental applications. *Energy Environ. Sci*. **2008**, 1, 205-221.

CHAPTER THREE

EXPERIMENTAL APPROACH

This chapter describes the experimental apparatus, precursor materials, synthesis, structural/chemical modification pathways in depth, and provides background information on performance testing methods. A comprehensive description of experiments for studies presented from chapter four through to seven. The experiments for this study were conducted at the University of the Witwatersrand, Johannesburg and at the Council for Scientific and Industrial Research (CSIR) in Pretoria, SA.

3.1 Materials

3.1.1 Precursor materials

The purchased chemicals are listed in table 3.1 and they all had a purity above 98.99%. Distilled deionised water (18 MΩ.cm) was used for the synthesis and fabrication of the electrode materials.

Table 3.1 *Chemical used for material synthesis and device fabrication.*

Category	**Chemical Name**	**Source**
Synthesis of fibres	Polyacrylonitrile (PAN)	Sigma Aldrich
	Dimethylformamide (DMF)	Sigma Aldrich
Conductive carbon	Nanodiamond (ND)	NaBond Technologies
FePc synthesis	Iron (II) Phthalocyanine (FePc)	Sigma Aldrich
Mn_2O_3 synthesis	Potassium permanganate ($KMnO_4$)	Sigma Aldrich
MoS_2 synthesis	Sodium molybdate dihydrate ($Na_2MoO_4 \cdot 2H_2O$)	Analytical Reagent
	Polyethylene glycol 1000, (PEG-1000)	Fluka Analytical
	Thiourea (CH_4N_2S)	Sigma Aldrich
Fe vacancies	Hydrochloric acid (HCl)	Associated Chemical Enterprises

Washing	Absolute ethanol (C_2H_6O)	Associated Chemical Enterprises
Fabrication of active electrode material	N-methyl-2-pyyolidone (NMP)	Sigma Aldrich
	Carbon Black	PRINTEX XE-2-B
	Polyvinylidene Fluoride (PVDF)	MTI Corp
Electrolyte	Sodium sulphate (Na_2SO_4)	Sigma Aldrich
Current collector	Aluminium foil	GELON
	Carbon paper	GELON

3.2 Material Synthesis

The set-up and geometry used in the electrospinning process of fibres is demonstrated in figure 3.1. The distance between the needle-tip to collector was kept constant at 15 cm for all polymer solution. Other parameters such as voltage and feed rate, varied between 8-10 kV and 0.4-1 mL/hours, respectively, depending on the effect of the polymer solution properties. These were (i) concentration, (ii) molecular weight, (iii) viscosity, (iv) surface tension, and finally (v) conductivity. The method of electrospinning is therefore discussed in detail for each of the polymer solutions.

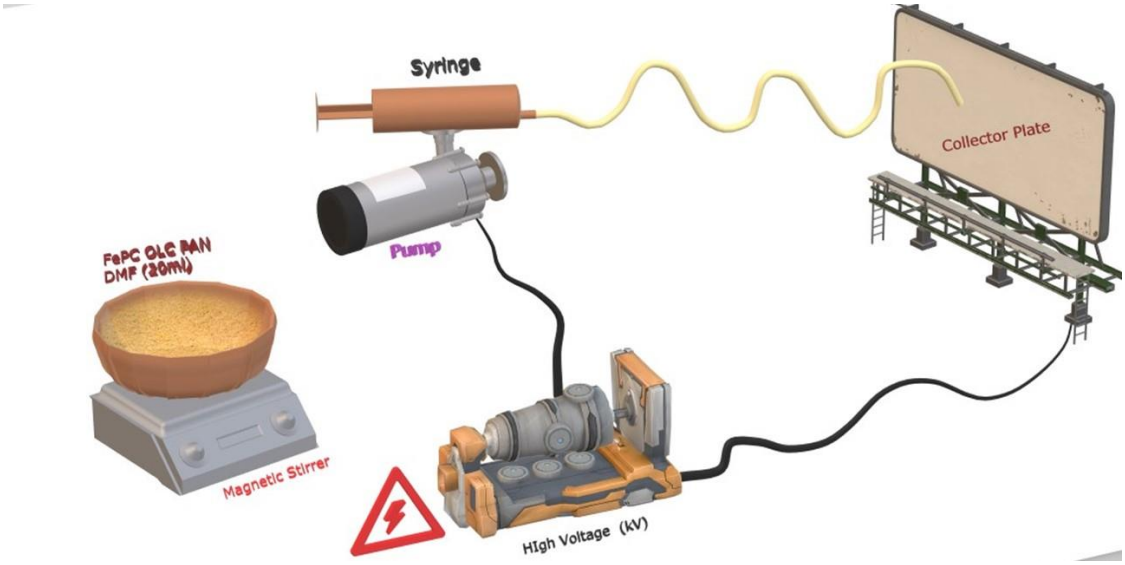

Figure 3.1 Schematic showing electrospinning setup used for synthesis of fibres (OLC-PAN, FePc-PAN and FePc-OLC-PAN).

3.2.1 Synthesis of OLC, OLC-PAN, OLC-CNF and OLC-CNF@Mn_2O_3 composites

This section describes the synthesis of the fibre composite material discussed in chapter four.

3.2.1.1 OLC synthesis

Nano diamond (ND) powder was poured into a closed lid cylindrical graphite crucible (10 cm in diameter and 20 cm in height) and thermally treated in a water-cooled high temperature vacuum furnace with tungsten heaters (Model: 1100-3580-W1, Thermal Technology Inc.). The ramp up and ramp down rates were both 15 °C/min and the chamber pressure ranged within 10 and 100 mPa. ND powder synthesis was performed at 1300 °C for 3 hours in an argon flow of 1 L/min resulting in OLC nanoparticles with an average diameter of 5 nm. Microstructural analysis was completed prior to subsequent use in electrospinning experiments.

3.2.1.2 Electrospinning OLC-PAN

OLC-PAN nanofibres were synthesized as follows. Firstly, 2g of OLC and 2g of PAN were dissolved separately in 15 mL of N,N-Dimethylmethanamide (DMF), then mixed together and stirred for 2 hours at room temperature. The mixture was further sonicated for 20 minutes in a bath ultrasonicator (30 kHz) to allow for homogenous dissolution. The resulting polymer solution was filled in the syringe to carry out electrospinning. The electrospinning was carried out at a feed rate of 0.4 mL/hours and 15 cm distance from tip to collector plate. The potential difference between the tip and the grounded plate was 10 kV. The collected fibres were immersed in water overnight (~12 hours) to remove/extract the solvent (DMF) and finally dried in oven at ~60 ^{o}C for 2 hours.

3.2.1.3 Stabilization and carbonization of fibres

The electrospun material was annealed in a horizontal furnace with a quartz tube filled with argon gas at a rate of 100 mL/min, firstly at 260 °C for 3hours for stabilization and secondly at 600 °C for 4 hours for carbonization to obtain OLC-CNF.

3.2.1.4 Synthesis of OLC-CNF@Mn_2O_3

Integration of Mn_2O_3 nanoparticles with the OLC-CNF was achieved by dispersion of the fibres into $KMnO_4$ solution at 60 °C. The weight ratio of OLC-CNF to $KMnO_4$ was 1:1 (1 g each) in 30 mL of de-ionized water. The reaction was vigorously stirred until the residual solution turned golden brown. The resulting Mn_2O_3 decorated OLC-CNF composites were rinsed with water three times followed by ethanol to remove by product. Finally, OLC-CNF@Mn_2O_3 composite material was obtained by vacuum drying in the oven at 60 °C overnight.

3.2.2 Synthesis of OLC-CNF/MoS_2 and OLC-CNF/MoS_2@Mn_2O_3 composites

This section describes the synthesis of the fibre composite material discussed in chapter five.

3.2.2.1 Encapsulation of MoS_2 on the OLC-CNF fibre support

Approximately 50 mg of the stabilized and carbonized OLC-CNF material (refer to 3.2.2.3) were immersed in 70 mL of deionized water containing 0.2 g sodium molybdate ($Na_2MoO_4 \cdot 2H_2O$), thiourea (0.4 g) and PEG-1000 (0.1 g). The solution was left to soak for 12 hours to allow proper soaking. The mixture was transferred to a Teflon-lined stainless-steel autoclave and heated at 180 C for 24 hours. OLC-CNF/MoS_2 fibre was collected by centrifugation and dried in the vacuum oven at 60 ° C.

3.2.2.2 Mn_2O_3 integration on OLC-CNF@MoS_2

The decoration of OLC-CNF/MoS_2 with Mn_2O_3 nanoparticles was achieved by dispersing the fibres in a $KMnO_4$ solution at 60 °C. The weight ratio of OLC-CNF/MoS_2 to $KMnO_4$ was 1:1 in 30 ml of de-ionized water. The reaction was vigorously stirred until the residual solution turned golden brown. The resulting Mn_2O_3 coated OLC/MoS_2-CNF composites were rinsed with water three times followed by ethanol to remove any by product. Finally, OLC-CNF/MoS_2@Mn_2O_3 fibre composite was obtained by vacuum drying in the oven at 60 °C overnight.

3.2.3 Synthesis of FePc-PAN and FeN_4-CMF

This section describes the synthesis of the fibre composite material discussed in chapter six.

3.2.3.1 Electrospinning FePc-PAN fibre

FePc-PAN nanofibres were synthesized as follows. Firstly, 2g of FePc powder was dissolved in 15 ml of DMF and in another beaker 2g of PAN was dissolved in 15 mL of DMF. Upon stirring each of the solutions for 2 hours these were mixed together and sonicated for 30 minutes in a bath ultrasonicator (30 kHz) at room temperature to allow for homogeneous dissolution. The resulting solution was then filled in the syringe to carry out electrospinning, as shown in figure 3.1. The electrospinning was carried out at a feed rate of 0.4 mL/hours and 15 cm distance from tip to collector plate. The potential difference between the tip and the grounded plate was 8 kV. The collected fibres were immersed in water overnight (~12 hours) to remove/extract the solvent (DMF) and finally dried in oven at ~60 °C for 2 hours.

3.2.3.2 Stabilization and carbonization of FePc-PAN fibre

The as-electrospun material was annealed using a multi-step heat-treatment in a horizontal furnace with a quartz tube filled with argon gas at a flow rate of 100 mL/min for 7 hours. Multi-step heat treatment consisted of stabilization step at 260 °C at a rate of 1 °C/min for 3 hours, followed by carbonization at 600 °C for 4 hours to induce microspores and form FeN_4-CMF.

3.2.4 Synthesis of FeN_4-OLC-CNF@MoS_2 and $(FeN_4)_d$-OLC-CNF@MoS_2 fibre composites

This section describes the synthesis of the fibre composite material discussed in chapter seven.

3.2.4.1 Electrospinning of FePc-OLC-PAN fibre

Firstly, a FePc-OLC-PAN nanofibre was synthesized. 2g of OLC, 2g FePc and 2g of PAN were dissolved in separate beakers with 15 mL of DMF solvent. Each solution was stirred for 2 hours at room temperature before mixing into one slurry of OLC, FePc and PAN in DMF solvent. The mixture was further sonicated for 30 minutes to allow for homogenous

dissolution. The resulting polymer solution was filled in the syringe to carry out electrospinning. The electrospinning was carried out at a feed rate of 1 mL/hours and 15 cm distance from tip to collector plate. The potential difference between the tip and the grounded plate was 9 kV. The collected fibres were immersed in water overnight (~12 hours) to remove/extract the solvent (DMF) and finally dried in oven at ~60 ^{o}C for 2 hours.

3.2.4.2 Stabilization and carbonization

The electrospun material above was thermally treated in a horizontal furnace with a quartz tube filled with argon gas at a rate of 100 mL/min for 7 hours. Multi-step heat treatment consisted of 260 °C, 3 hours for stabilization and 600 °C, 4 hours for carbonization to obtain FeN_4-OLC-CNF composite.

3.2.4.3 Synthesis of FeN_4-OLC-CNF@MoS_2 and $(FeN_4)_d$-OLC-CNF@MoS_2

A 0.41g of the heat treated FeN_4-OLC-CNF was sonicated in 40 ml de-ionised water for 30 minutes and sodium molybdate ($Na_2MoO_4 \cdot 2H_2O$, 1.21 g), thiourea (1.56 g) and PEG-1000 (0.28 g) were added. This solution was transferred to a Teflon insert of a stainless-steel autoclave and heated for 24 hours at 180 ºC. After cooling to room temperature, the sample was collected by centrifugation to obtain the FeN_4-OLC-CNF@MoS_2 composite. FeN_4-OLC-CNF@MoS_2 sample was immersed in concentrated HCl and ultrasonicated at 30 kHz for 30 minutes to remove Fe. During which, Fe reacted with Cl to form $FeCl_3$ as evidenced by the solution turning yellow. The final product was centrifuged, and dried in an oven at 60 °C for 24 hours. The final product was expected to be highly porous and defect rich thus is denoted as $(FeN_4)_d$-OLC-CNF@MoS_2.

3.3 Characterization techniques for supercapacitor electrode materials

3.3.1 X-Ray Diffraction (XRD)

XRD had been used to assess the structural properties of fibre composite materials using a Bruker Lynxeye PSD diffractometer. Typically, X-ray is useful for unit cell dimension and ascertaining the level of crystallinity on materials. The analysis is based on constructive interference of monochromatic X-rays with a sample. [1] During analysis a sample is bombarded with X-rays and a constructive interference of X-ray radiation occurs in the material, as described by Bragg's law in equation (3.1)

$$n\lambda = 2d \sin\theta \,; n = 1, 2, 3 \qquad (3.1)$$

where n is an integer, λ is the wavelength of the incident wave, d is the distance between two planes in the atomic lattice, and θ is the angle between the incident beam and the scattering planes. [2]

With a mortar and pestle, the fibre composite samples were gently crushed and carefully placed into a Si sample holder. Each sample was flattened with a glass slide prior to being placed inside the instrument. The XRD patterns were produced throughout the 2θ range of 10-90° at room temperature using a Co radiation with λ= 1.78897 Å. The OriginPro 8.5 program was used for qualitative phase analysis.

3.3.2 Brunauer-Emmett-Teller (BET)

The surface area and pore size distribution of the fibre composites were measured using the Micromeritics Tristar 3000 of the Brunauer Emmett Teller (BET) instrument. BET technique relies on the adsorption of nitrogen gas onto the surface particles homogenously at a given pressure. [3] Prior to analysis, samples were degassed in order to remove unwanted vapours and gases adsorbed on the surface for at least four hours at 150 $°C$ in a heating mantle.

The surface area was determined by the fundamental BET equation (3.2);

$$1/W * ((P/P0) - 1) \; = \; 1/\mathrm{W_m}C + C - 1/\mathrm{W_m}C \; * (P/P0) \qquad (3.2)$$

W_m represents the weight of the adsorbate creating a monolayer of surface coverage, W, is the weight of the gas adsorbed at a relative pressure, P/P_0, and C, is the BET constant and is related to the energy of adsorption in the first adsorbed layer and hence, its value indicates the magnitude of the adsorbent-adsorbate interactions. [3] The findings from BET analysis are crucial for understanding the electron-ion current density effects and diffusion at the electrode electrolyte interface. [4]

3.3.3 Scanning Electron Microscopy (SEM) and Energy Dispersive X-ray Spectroscopy (EDS)

The SEM was useful in recording the morphology displayed by the fibre composites. Fundamentally, an SEM instrument makes use of a beam of electrons that hit the atoms in the sample and forms an image with the secondary and backscattered electrons. [5] In this study, the powder samples were homogeneously dispersed on a double-sided carbon tape and supported on a metallic disc stub. Subsequently, the fibres composites were encapsulated with a 10 nm layer thickness of a gold-palladium and carbon coat to reduce charging interference while imaging in the SEM. The instrument model used for this study is the Ziess Ultra Plus 55 field Emission Scanning Electron Microscope (FE-SEM) and is operated at 20 kV.

The elemental composition of the samples was quantified using the Oxford INCA EDS software attached to the SEM instrument. Briefly, elemental composition was attained due to the electron beam interaction with the sample and X-rays with similar properties of the elements presented by the sample. The chemical composition data was qualitatively and quantitatively obtained from both the area map and point scan analysis.

3.3.4 Transmission Electron Microscopy (TEM)

In TEM analysis, a fraction of an electron beam is transmitted after it is focused on a specimen and forms an image, as illustrated in figure 3.3. The instrument's tailored capabilities enable for significantly better resolution directed pictures of nanomaterials than light microscopy. Particle size distribution and crystallographic information are examples of additional data obtained using the TEM. Prior to analysis, samples were sonicated in an ethanol solution for dispersion and dried onto the lacey copper grid. Each sample was put on a sample holder and inserted into the apparatus using tweezers. This study made use of the FEI Tecnai T12 model operated at an acceleration voltage of ~120 kV.

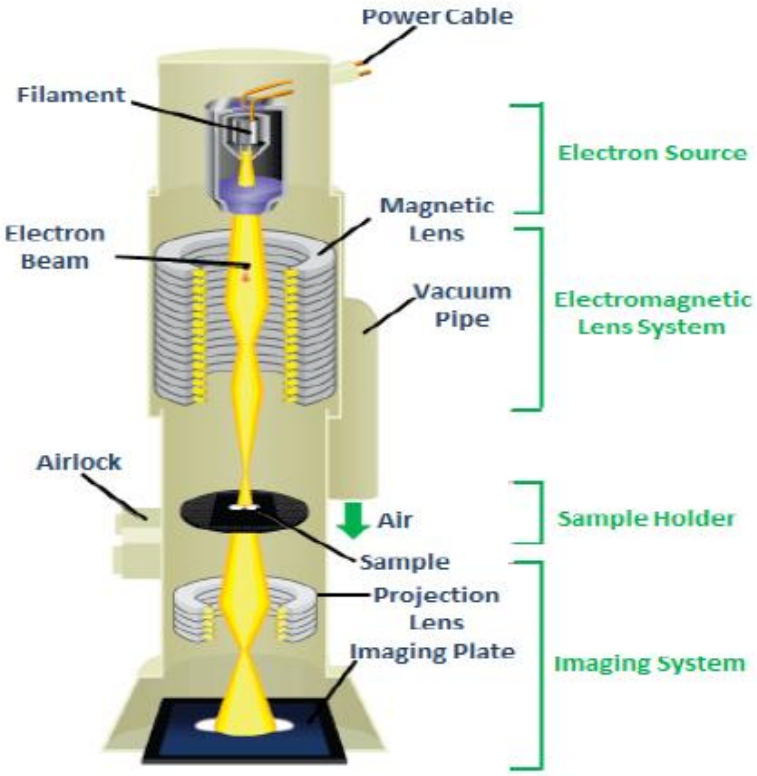

Figure 3.3 Schematic diagram of a typical TEM. [6]

3.3.5 Thermogravimetric Analyzer (TGA)

TGA determines the thermal stability i.e. the strength of the material at a given temperature, and the oxidative stabilities i.e. the oxygen absorption rate of materials, and the compositional properties (e.g. solvents, fillers, polymer resin etc.) of a sample. This is done by measuring the quantity and the frequency of the weight variation of the samples against temperature and time in a controlled atmosphere. Temperature in a TGA instrument can increase up to about 1600 $°C$ whereas the heating rate can be set from a range between 1 and 20 $°C$/min. The material being examined could be either in liquid, solid or gel forms and have weight variations from as small as 1 to 100 mg, up to 100 g. Graphical data is usually plotted with a derivative thermogram (DTG) curve to aid better understanding or resolution of successive weight changes. The DTG curve can be extracted from the TGA curve data by deriving the weight data as a function of temperature. The schematic in figure 3.4 illustrates the set-up of the instrument and the information extracted. [7] For this study, Perkin Elmer TGA 6000 instrument was used, and test was conducted under high-purity nitrogen at a heating rate of 10 °C/min and gas flow rate of 10 mL/min.

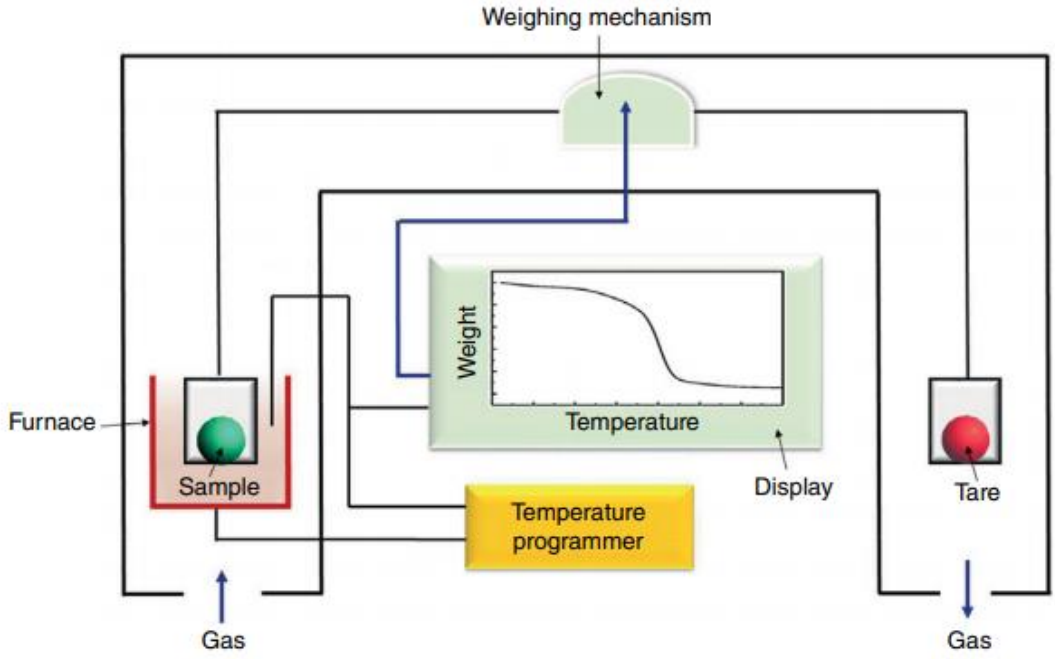

Figure 3.4 Schematic diagram of TGA instrument. [7]

3.3.6 Raman spectroscopy and Fourier Transform Infrared spectroscopy (FT-IR)

Raman and FT-IR spectroscopies have both shown to be effective non-destructive characterization methods for studying amorphous and crystalline substances in detail. [8]

Raman measurements were obtained using the Bruker Raman Senterra spectrometer, equipped with a 532 nm excitation laser. The incident beam was focused onto the sample using a 100 objective (NA = 0.90), and the backscattered light was dispersed onto a fluid nitrogen cooled charge coupled device (CCD) camera through 600 lines per millimeter grating. The information was captured utilizing LabSpec v5 software. The method works by scattering monochromatic light from a laser in an inelastic manner. The energy of the laser photons is pushed up or down as a result of the interaction of light with molecular vibrations in a specific system. This unique shift in energy is what generates information about a system's vibrational modes.

FT-IR spectra of the fibre composites were produced using the Bruker Tensor 27 equipped with ZnSe crystal. The data was collected in the wavelength range of 550-4000 cm^{-1}. Prior to running an actual sample for a single beam measurement, a background spectrum is obtained. FT-IR used the same fundamental concepts as Raman analysis to provide precise information on bonding and coordination of the fibre composite materials. Raman analysis provided information on the vibration of S-Mo-S atoms and approximate layer thickness that is largely dependent on the E_{2g} and A_{1g} peak frequencies, intensities and widths on MoS_2 containing samples. [8] Mn-O-Mn asymmetric and symmetric stretching out-of-plane bending modes were identified in the Mn_2O_3 nanoparticle containing samples. [9] The typical D and G vibrations demonstrated by the carbon fibres and OLC were also detected in the spectra. The area ratios of the D and G (I_D/I_G) peaks were used to measure the extent of structural defects and disorder in the carbons for the carbonaceous samples. [10]

3.3.7 X-Ray Photoelectron Spectroscopy (XPS)

XPS also commonly referred to as Electron Spectroscopy Chemical Analysis (ECSA), is a commonly used tool for analyzing the surface elemental composition and a chemical or an electronic state analysis of each element in the sample surface. In this technique, the sample is bombarded with soft X-rays usually comprised of k-alpha X-rays. The X-rays are focused on the sample (typically 1–3 keV) in a vacuum, and the energy of electrons are emitted. The energy emitted by these photoelectrons is used to deduce the atom being bombarded thus allowing identification of elements. [9] See figure 3.4 below.

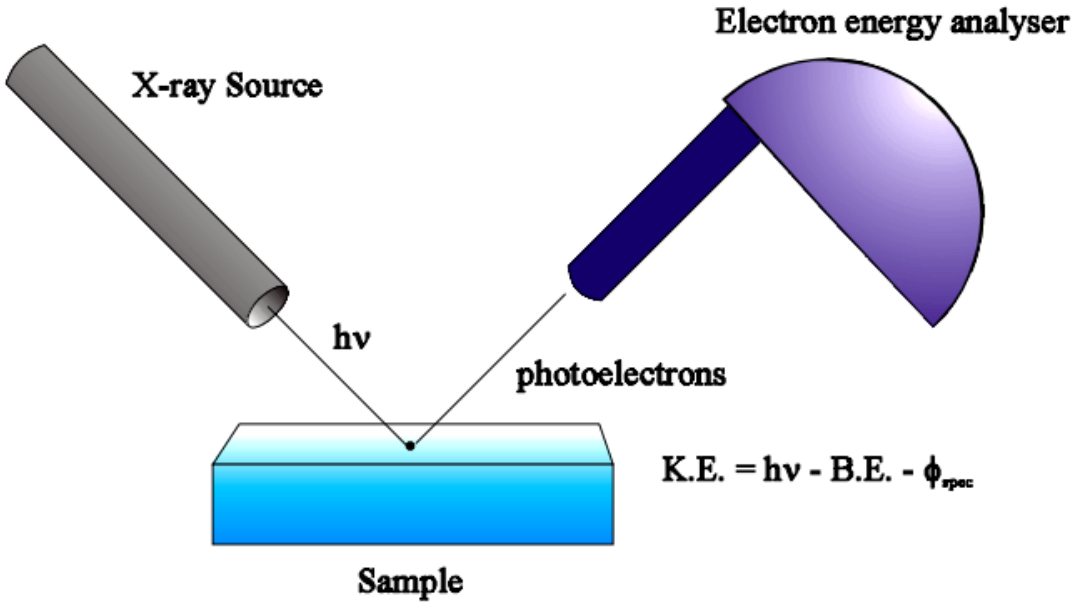

Figure 3.4. Schematic diagram of a principle operation of XPS. [9]

The core electrons are ejected by incident X-ray with a kinetic energy of photoelectron, which according to Einstein's photoelectric effect can be expressed as in equation (3.3) [10];

$$E_K = hv - E_B - \varphi_{sp} \qquad (3.3)$$

where E_K, is the kinetic energy of the photoelectron. E_b, is the binding energy of electron to the nucleus relative to the Fermi level, h is Planck's constant, ν is the photon frequency of X-rays and φ_{sp} the spectrometer work function. [10]

XPS analysis for this study was performed with the K-Alpha + XPS spectrometer using monochromatic Al Kα (1486.6 eV) X-ray source leading to a very shallow escape depth (or inelastic mean free path, IMPF), λ, of photoelectrons. In this energy range, λ is approximately 0.3-4 nm depending on E_k. The E_b scale was calibrated by measuring the reference peak of C1s ($E_b = 284.6\ eV$) and a Shirley function was used to subtract the background. [10]

3.4 Electrochemical Characterization Techniques for Supercapacitors

This section gives details on the basic principles of all electrochemical methods used for the primary characterisation of all electrode materials in supercapacitors.

3.4.1 Cyclic Voltammetry (CV)

CV is a powerful technique used to study redox processes in electrode materials. In supercapacitor electrodes, this is an integral part for the charge storage mechanism. In principle, the voltage applied to an electrode is scanned linearly between two voltage limits (V_1 and V_2) and plotted as a function of the measured current response. The current depends on two things, firstly, the movement of the electrode surface electroactive species and secondly, the electron transfer reaction. The current-voltage curve is referred to as a voltammogram and an example is depicted in figure 3.5. According to equation (3.3);

$$Q = CV\ (C) \tag{3.4}$$

The slope of the curve may be used to compute the value of the capacitance, C [F]. However, this is not always the case, especially in pseudocapacitor materials where the Q-V curve is not so linear. Practically, they adopt a pattern of a parallelogram with prominent peaks as depicted in figure 3.5. According to Frackowiak and Beguin at al. [11] the prominent peaks are associated with faradic reactions of pseudocapacitor electrode materials and their porous nature. Thereby, the capacitance is dependent on the applied voltage and the accuracy of the linear regression is unsatisfactory. In which case, the expression in (3.4) is applied;

$$C = I \frac{\partial t}{\partial V} \ (F) \qquad (3.5)$$

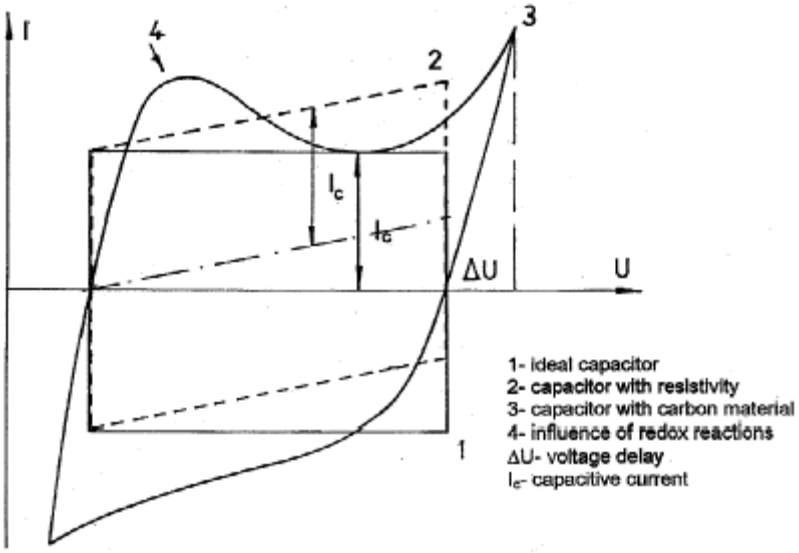

Figure 3.5 Typical voltammograms for capacitors and supercapacitors. [12]

The scan rate is the pace at which potential changes (ν). In this study, CV curves were recorded at various scan rates between 5 and 200 mV s^{-1} to understand the influence of scan rate on the capacitance of the electrodes. The specific capacitance drops as the scan rate increases, which is explained by the fact that at low scan rates, electrolyte ions have more time to diffuse and enter into the electrode pores, thus enabling the creation of double layer charge storage. At low scan rate this mechanism adds substantially to the total capacitance of a supercapacitor. An additional characteristic feature determined from the CV analysis is the reversibility of the reactions on the surface of an electrode. In the case where reactions are reversible, the curves display a mirror image. Whereas irreversible reactions will result in different charge to discharge asymmetrical profiles.

3.4.2 Galvanostatic charge-discharge

This is the most efficient test in comparison with the CV. The current is controlled and the voltage is measured as a function of time. It is the most useful electroanalytical technique especially because it can be extended from a laboratory scale to an industrial one. It is also used to estimate the relationship between power and energy densities in a device. The voltage variation is explained by equation (3.5);

$$V\,(t) = IR + \ It\,(V)/C \tag{3.6}$$

In supercapacitors the capacitance can be calculated from the slope of the V *vs* t curve presented in figure below.

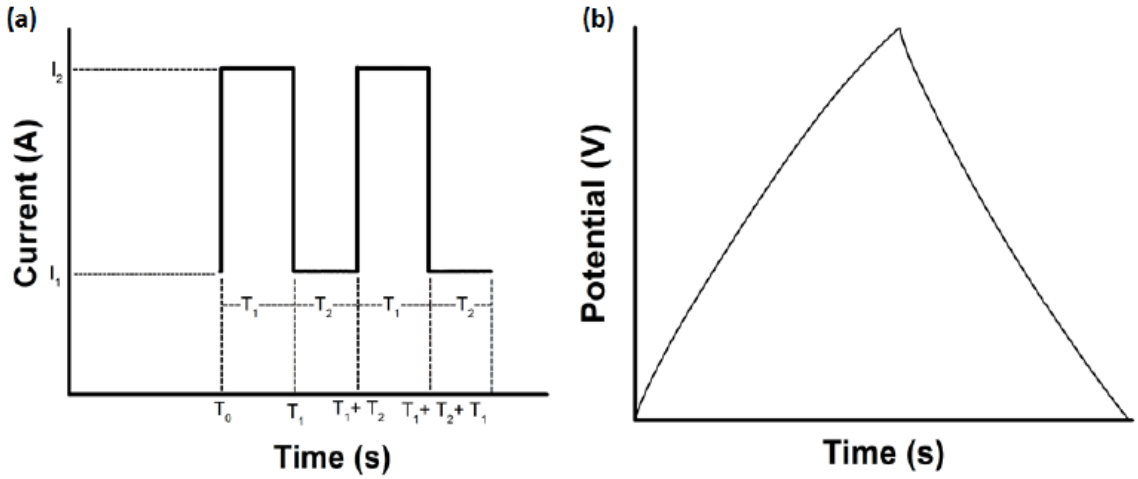

Figure 3.6 Graphical representation of current versus time profile (a) and potential versus time profile (b), during galvanostatic charge-discharge in supercapacitors. [13]

For a pseudocapacitor, the V *vs* t curve is not linear therefore, the capacitance is calculated by integrating the current over the discharge time charge time.

$$C = \frac{\int_{V1}^{V2} idt}{\int_{V1}^{V2} Vdt}\,(F) \tag{3.5}$$

where V_1 to V_2 is the voltage window, C is the capacitance, i the current, t time and V is the voltage. It is common practise to calculate the capacitance using the backward scan (discharge).

Specific capacitance of a symmetrical cell is calculated using; and power density

$$C_{sp}\,(F\,g^{-1}) = \frac{4C}{m} \tag{3.6}$$

Furthermore, the internal resistance is determined from the voltage drop (V_{ir}) occurring over the current inversion (Δi) at the beginning of each discharge. This resistance, also referred to as an equivalent series resistance (ESR), is linked with ion diffusion

obstruction in the electrodes. ESR is key to gaining insight on the internal chemistry and is determined using the equation below;

$$R_{ir} = \frac{V_{ir}}{\Delta I} \tag{3.7}$$

$$E\left(\frac{1}{3.6}\ W\ h\ k\ g^{-1}\right) = \frac{CV^2}{2m} \tag{3.8}$$

$$P_{max}(10^3 W\ kg^{-1}) = \frac{V^2}{4mR_{ir}} \tag{3.9}$$

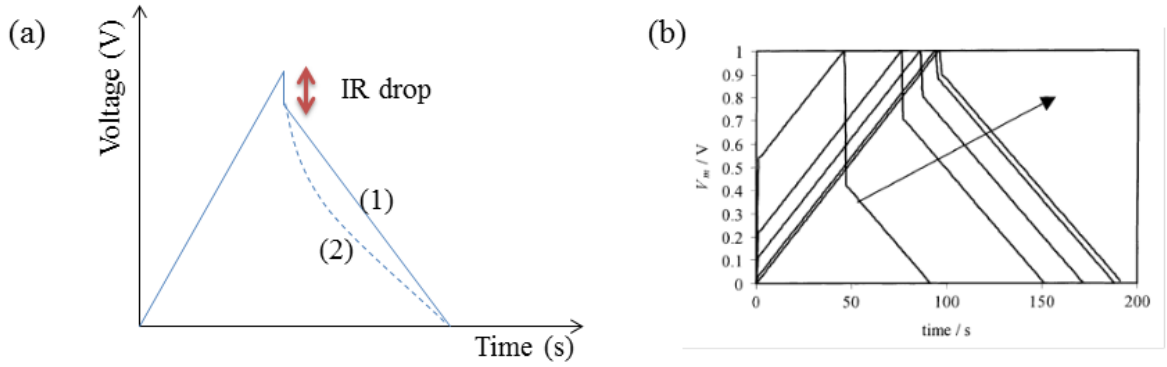

Figure 3.7 (a) Charge-discharge curves of EDLCs (1) and pseudocapacitors (2), and (b) charge-discharge experiments revealing varying internal resistance behaviour. [14]

3.4.3 Electrochemical impedance spectroscopy (EIS)

The tendency of a circuit to resist the flow of electrical current is measured by its impedance. Compared with resistance, which obeys Ohm's law and is present in DC circuits, impedance has zero phase angle, and considers the capacitive and resistive effects at a particular frequency. Simply, EIS analysis is useful for the behavioural study of the electrode in the frequency domain. A mathematician, Oliver Heaviside deduced real values of impedance in a temporal space. [12] He reviewed in detail the operational impedance as the complex ratio of the voltage and current in an AC circuit, which is now defined as [12];

$$Z(j\omega) = \frac{V(j\omega)}{I(j\omega)} \tag{3.10}$$

where Z denotes the impedance, I is the current, V is the voltage, j is the imaginary component and ω is the angular frequency. Z (ω) is composed of real and imaginary, (Z') and (Z'') impedance parts, respectively. When $Z'$is plotted on the X-axis and Z'' on the Y-axis of a chart, a "Nyquist Plot" shown in figure 3.8 is obtained. This diagram can be grouped into three segments. First, the high frequency region, which is interpreted to deduce solution resistances (Rs). Second, the medium frequency region that shows a semi-circle, reflecting charge transfer resistance (R_{ct}) at the electrode-electrolyte interface and electric double layer capacitance (C_{DL}). Third, is the low frequency region of impedance, which relates diffusional electrochemical systems reported by Warburg. EIS principles are robust, and thus have been implemented beyond research application to large scale production for the purpose of electrode material quality control. [14]

There are two fundamental equations used to evaluate the real and imaginary impendences of an EIS experiment. These are presented in equations (3.11) and (3.12) and are representative of the Nyquist plot shown in figure 3.8. [15]

$$Z' = R_s + \frac{R_{ct}}{1+ \omega^2 {R_{ct}}^2 {}_{ct} {C_{DL}}^2} \tag{3.11}$$

and

$$Z'' = \frac{{R_{ct}}^2 C_{dl} \omega}{1+ \omega^2 {R_{ct}}^2 {}_{ct} {C_{DL}}^2} \tag{3.12}$$

where

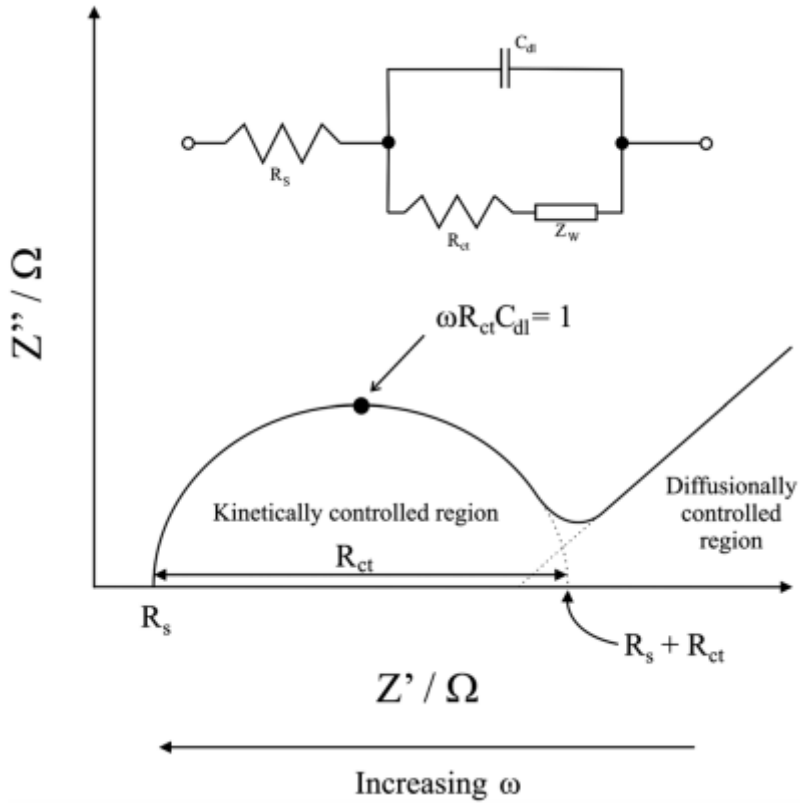

Figure 3.8 Nyquist plot and Randles equivalent circuit of an electrochemical cell. [15]

When the frequency of an ideal capacitor increases, ion diffusion transport in the electrolyte decreases, lowering the resistance and capacitance. Adversely, in some cases EIS has exhibited capacitance discrepancies between concentrated and diluted electrolyte solutions. To overcome these deficiencies, a bode plot with phase angle vs frequency is used to determine the capacitive or inductive effects of electrochemical systems. [16]

3.5 Fabrication and testing of electrochemical cells

All electrochemical measurements (CV, GCD and EIS) were done using a multi-channel Potentiostat/Galvanostat Bio-Logic SP300 work station driven by EC-Lab® v10.40 software. EIS measurements were carried out in the frequency range from 10 kHz to 10 mHz at the open circuit voltage with AC voltage amplitude of 1.5 mV. The following details how the electrochemical cells were assembled for both three-electrode (half-cell) and two-electrode (full cell) systems.

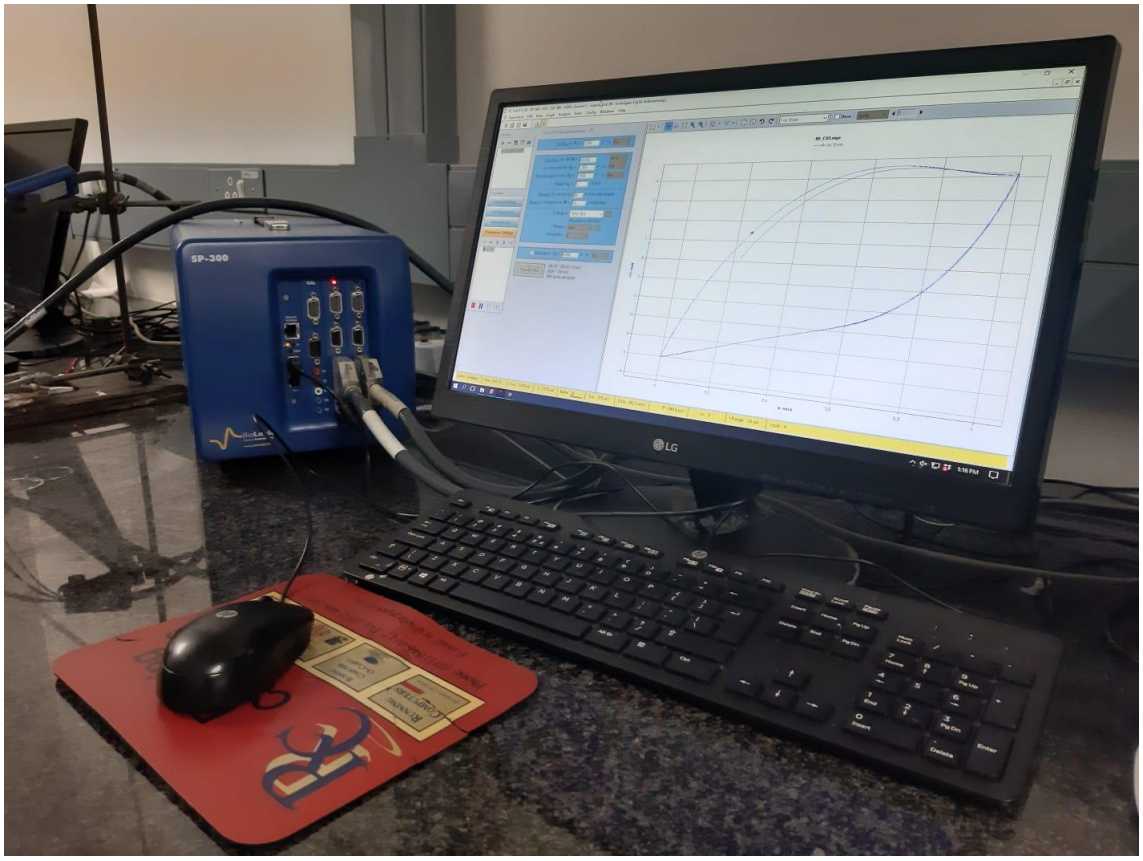

Figure 3.9 Image of multi-channel Potentiostat/Galvanostat Bio-Logic SP300.

3.5.1 Three-electrode system

3.5.1.1 Screen-printed electrodes

As a preliminary trial, the electrochemical behavior was initially obtained from the three-electrode system of screen-printed carbon electrodes (SPCEs). These were purchased from Metrohm SA (Pty) Ltd. The electrochemical cell was composed of a 4 mm diameter carbon nanotube (CNT) working electrode, carbon auxiliary electrode and silver/silver chloride (Ag/AgCl) paste as a reference electrode. An example of a SPCE is shown in figure 3.10. Approximately 2 mg of the active material was dispersed in 2 drops of DMF and the mixture sonicated for 15 minutes. A glass pipette was used to deposit 2 drops of the mixture onto the working electrode followed by drying in an oven for 2 minutes at 60 °C. The electrodes were then connected to a DSC box from DropSens, working as an interface between SPE and the potentiostat.

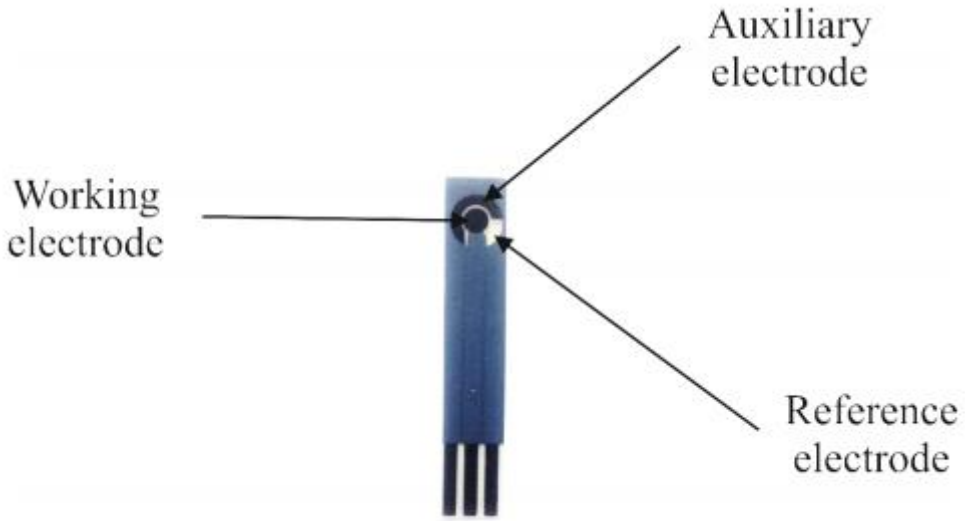

Figure 3.10 Typical screen-printed electrode characterized by the following dimensions: 12 mm width; 41 mm length; 2.54 mm pitch; 4 mm working electrode diameter.

3.5.1.2 T-type cell

Further three-electrode measurements were done on the T-type cell shown in figure 3.10 The working electrode was prepared by thoroughly mixing the active materials (i.e fibre composites) with carbon black (CB) as a conducting agent and polyvinylidene fluoride (PVDF) as a binder material in a ratio of 80:10:10. To produce homogeneous slurry-like paste, a few drops of anhydrous N-methyl-2-pyrrolidone (NMP) were added followed by vigorous mixing using a mortar and pestle. In this case, the counter electrode for the t-type cells is titanium. Aluminium foil was used as current collector in the fabrication of the working. Before use, the Al foil was thoroughly cleaned with acetone to ensure removal of unwanted residues. Using a glass pipette, a slurry containing the active material was carefully deposited onto the foil and distributed with a blade or doctor blade. The electrode was then dried at 90 ℃ overnight in a vacuum oven. The mass of the active materials in working electrodes was within a 0.5 to 10 mg range. All three-electrode measurements used a porous glass fibre (whatman grade GF/D glass microfibre filters) as a separator and 1M Na_2SO_4 aqueous solution as an electrolyte. For complete impregnation the cells were left for 30 minutes prior to testing.

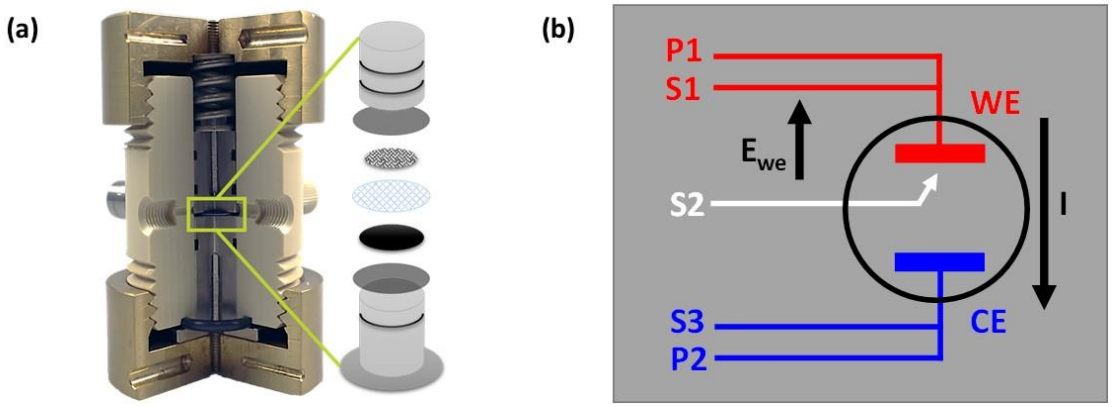

Figure 3.10 Schematic diagram representing (a) three-electrode T-type cell and its components setup and (b) how the cells are connected to the SP300 Biologic

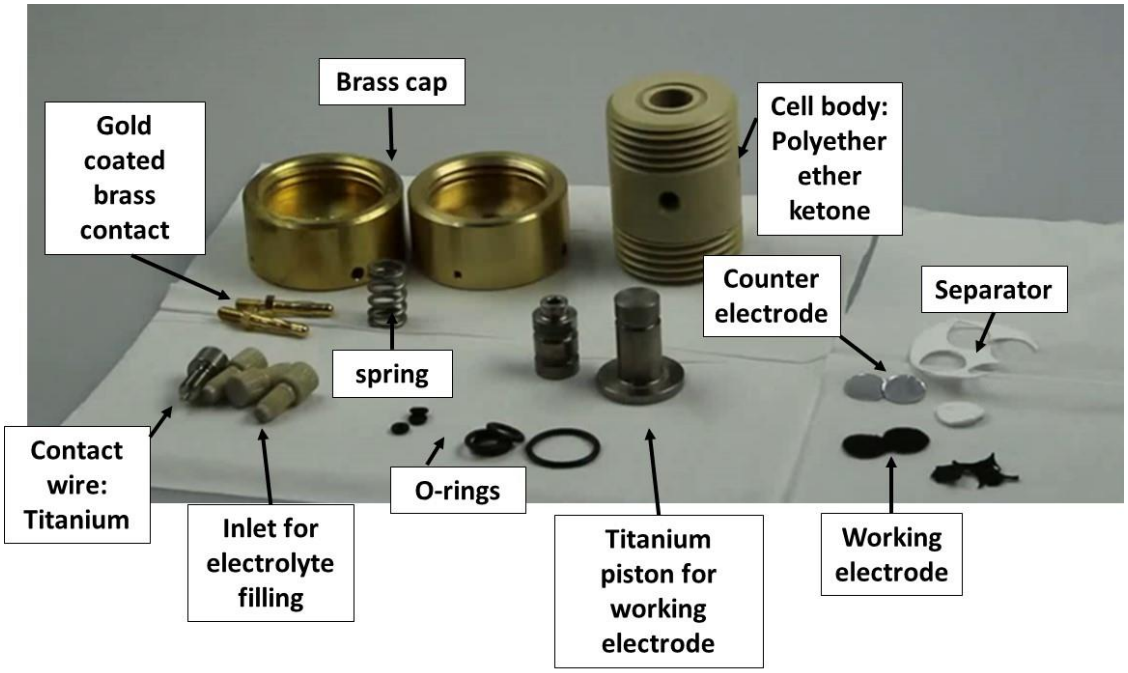

Figure 3.11 Image showing all the components in a T-type cell for three-electrode measurement.

3.5.2 Two-electrode symmetrical cells

For the two-electrode system, nickel (Ni) foam with the following dimensions was used as a substrate in the fabrication of the electrodes. Typically, the specifications of the foam are as follows; celmet: thickness = 1.6 mm, surface area 7500 m^2, cell size = 0.5 mm, 48-52 cells per inch. Prior to being used, the Ni foam was thoroughly cleaned by sonicating in 1 M HCl solution for 30 min, washing with copious amount of distilled water, and

finally drying under vacuum. Symmetric supercapacitor properties of the materials were investigated using the Swagelok cells (MTI, Inc., USA) shown in figure 3.12a and the cells were assembled according to the configuration displayed in figure 3.12b. The cells already consist of two cylindrical current collectors, made of stainless steel on the anode and cathode sides.

A few drops of an aqueous electrolyte solution (1M Na_2SO_4) were added to the prepared electrode with an active material within the bottom split of the stainless steel split test cell. Subsequently, a separator made out of porous glass fibre material was placed on the surface of the first electrode followed by an O-ring made of Teflon. More drops of the electrolyte solution were added before the second electrode with active material was placed facing downward towards the separator. A spacer was added to maintain contact with the upper split while the stack is horizontal. Finally, the upper split was sealed with the bottom, using the bolts and the cap. The assembled electrochemical cells were given 12 hours to rest prior to testing, to ensure thorough impregnation of the electrolyte solution into the electrodes and separator.

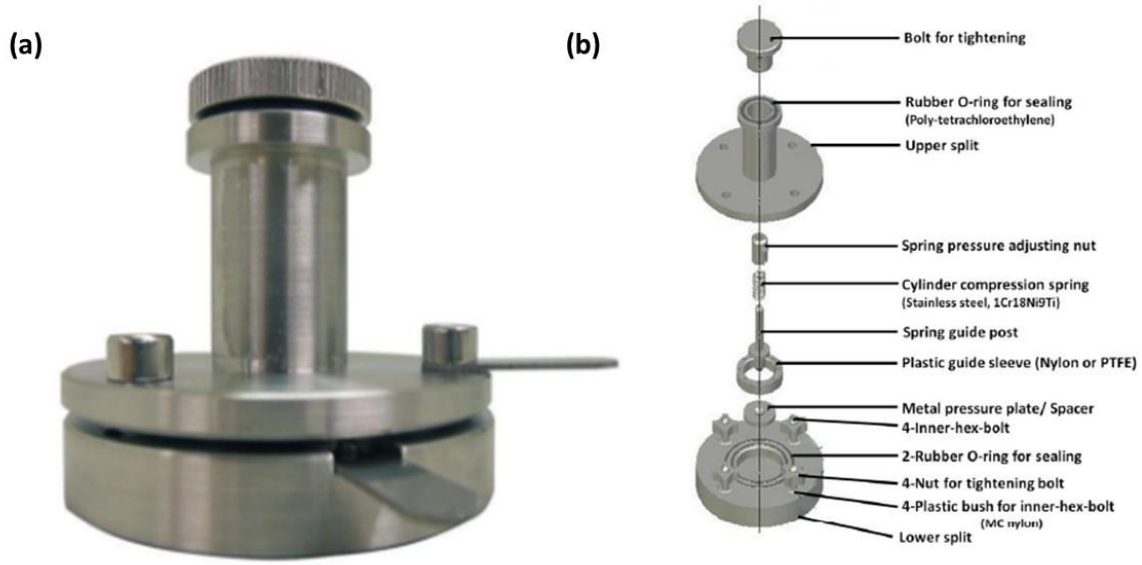

Figure 3.12 Swagelok cell configuration used for fabrication of two-electrode symmetrical systems of supercapacitors.

3.5.3 Pouch cell fabrication for the light emitting diode (LED)

Pouch cells were fabricated for the materials that gave the best performance as supercapacitors and were connected in series to light an LED 1.67 V bulb. The slurry consisting of the 80:10:10 weight ratio of the active material: PVDF: carbon black, was prepared similarly to the electrodes tested in the two and three cells above. Subsequently, the slurry was coated on the carbon paper and dried at 90 °C overnight. Copper strips were cut sufficiently long and pasted with silver paste on the base of the current collector i.e. carbon paper and given few minutes to dry. The electrode with a copper strip attached to it, was placed at the centre of a laminate piece cut to a square shape of 35 mm by 35 mm. A porous glass fibre filter separator was added on top of the electrode before the second coated electrode was placed facing towards the separator. The laminate was sealed using an impulse heat sealer on three sides of the laminate. The fourth side was used to inject the 1 M Na_2SO_4 aqueous electrolyte and sealed afterwards. For connection purpose, the long copper strips outlets from the two electrodes were facing in opposite direction and were later connected to a cell on either ends in series. The outer cells were attached to the Bio-logic for charging and attached to the light bulb for discharging. The charge-discharge measurements of the cells were done at a 0° angle in a planar state, flexibility and bendability of the device was not tested for this work.

3.6 References

[1] Cullity, B. D.; Stock, S. R. *Elements of X-ray diffraction*, 3rd Ed.; New York: Prentice Hall, 2001.

[2] Moore, D. M.; Reynolds, R. C. *X-ray diffraction and the identification and analysis of clay minerals*, 2nd Ed. Oxford University Press, 1989.

[3] Bae, Y. S.; Yazaydin, A. O.; Snurr, R. Q. Evaluation of the BET method for determining surface areas of MOFs and Zeolites that contain ultra-micropores. *J. Am. Chem. Soc*. **2010**, 26, 5475-5483.

[4] Mohammed, A.; Abdullah, A. Scanning Electron Microscopy (SEM): A Review. Proceedings of 2018 International Conference on Hydraulics and Pneumatics – HERVEX, Băile Govora, Romania, November 2-9, 2018, 77-85.

[5] Bassani, G.; Liedl, G.; Wyder, P. *Enyclopedia of Condensed Matter Physics*, 1st Ed. Academic Press, 2005, 240-247.

[6] "Basic principles of transimission electron microscope' http://www.hk-phy.org/atomic_world/tem/tem02_e.html [Accessed June 2018].

[7] Toxqui-Teran, A.; Leyva-Porras, C.; ruiz-Cabrera, M. A.; Cruz-Alcantar, P.; Saavedra-Leos, M. Z. *Polymers*, **2018**, 10, 467.

[8] Stiles, P. L.; Dieringer, J. A.; Shah, N. C.; Van Duyne, R. P. Surface-Enhanced Raman Spectroscopy. *Annu. Rev. Anal. Chem.* **2008**, 1, 601-626.

[9] Berthomieu, C.; Hienerwadel, R. Fourier transform infrared (FTIR) spectroscopy. *Photosynth. Res.* **2009**, 101, 157-170.

[10] Watts, J. F.; Wolstenholme, J. An Introduction to Surface Analysis by XPS and AES, 2nd Ed. Wiley Journal of Surface and Interface Analysis, 2020.

[11] Suroveic, A. H. Introduction to Electrochemistry. *J. Lab. Chem. Educ*. **2013**, 3, 45-48.

[12] Kumar, R. V.; Sarakonsri, T. Introduction to Electrochemical Cells. High Energy Density Lithium Batteries: Materials, Engineering, Applications. *Wiley-VCH*, **2010**, 1-25.

[13] Shu, D.; Lv, C.; Cheng, F.; He, C.; Yang, K.; Nan, J.; Long, L. Enhanced Capacitance and Rate Capability of Nanocrystalline VN as Electrode Materials for Supercapacitors. *Int. J. Electrochem. Sci.* **2013**, 8, 1209-1225.

[14] Frackowiak, E.; Béguin, F. Carbon Materials for the Electrochemical Storage of Energy in Capacitors. *Carbon*, **2001**, 39, 937–950.

[15] Ko, R.; Carlen, M. Principles and Applications of Electrochemical Capacitors, *Electrochim. Acta*. **2000**, 45, 2483–2498.

[16] Yoo, H. D.; Jang, J. H.; Ryu, J. H.; Park, Y.; Oh, S. M. Impedance Analysis of Porous Carbon Electrodes to Predict Rate Capability of Electric Double-Layer Capacitors. *J. Power Sources.* **2014**, 267, 411-420.

[17] Randviir, E. P.; Banks, C. E. Electrochemical impedance spectroscopy: an overview of bioanalytical applications, *Anal. Methods*, **2013**, 5, 1098-1115.

CHAPTER FOUR

Mn_2O_3 nanoparticles embedded onto OLC-CNF composite for enhanced interfacial electrochemistry and supercapacitance

4.1 Introduction

Manganese oxides have captured a lot of attention due to their high theoretical capacitance of up to 1300 F g^{-1} and stable cycling performance. [1-5] Nonetheless, what is still of concern is its low electrical conductivity. [6-8] To mitigate these shortfalls, Mn-based materials have been synthesized in carbon supports with a higher degree of carbon ordering leading to higher conductivity and higher electrochemical stability. [9-10] In addition, nanostructured Mn-based oxides are synthesized to affect an increase in surface area relative to its bulk contour part. Generally, nanostructured electrodes are known to enhance the electrochemical kinetics by reducing the diffusion pathway for electronic and ionic transport. [11-12] Recently electrospun carbon nanofibres (CNFs) have gained interest for energy storage related applications due to their excellent combination of properties previously discussed in chapter two. [13] Their potential is most realized in cases where they become substrates for active materials that possess electrical double layer capacitance (EDLC) and pseudocapacitance behaviour. In a review by Zeiger et al. [9] onion-like-carbon (OLC) were described as the most interesting form of carbon due to their high electrical conductivity, large external surface area and nanoscopic size. [14-17] The capacitance of OLCs are typically 3x greater than that of activated carbon (AC) which is attributed to the high surface area of up to 2 000 m^2g^{-1}. [14]

The objective of this study was to explore the properties of OLC based nanofibres and determine whether the integration of manganese oxide nanoparticles could improve their performance as an electrode material for supercapacitors. The fibre composites were synthesized by electrospinning a polymer solution with previously prepared OLC powder. Followed by a thermal treatment for stabilization and carbonization. Finally, Mn_2O_3 nanoparticles were embedded on the surface of the fibres resulting in the desired

OLC-CNF@Mn_2O_3 composite material. Figure 4.1 provides a schematic diagram of the synthesis procedure of the OLC-CNF@Mn_2O_3 composite material.

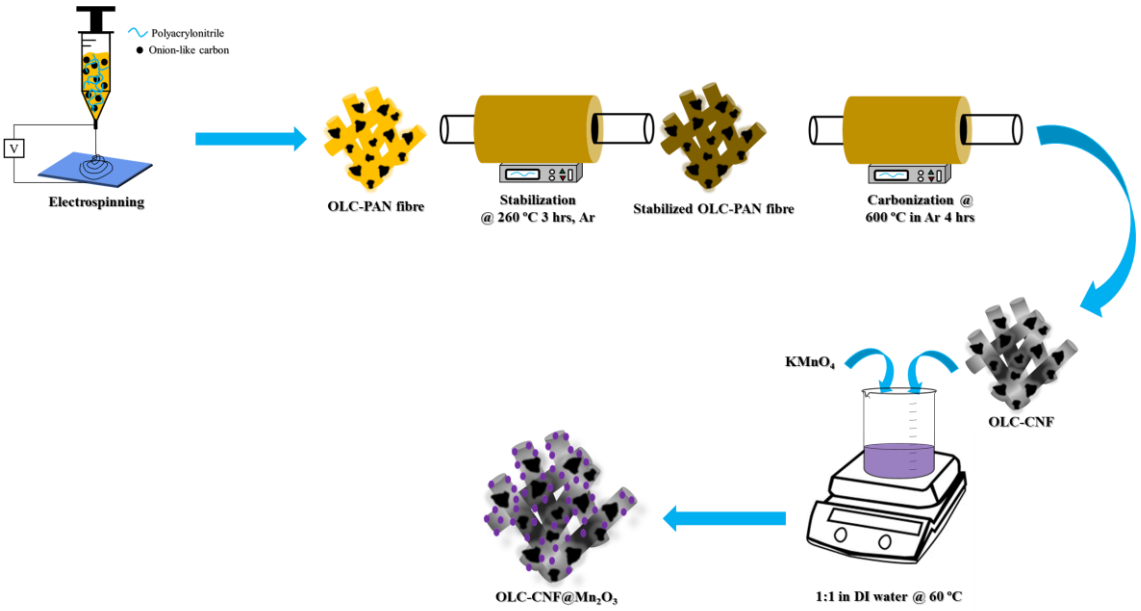

Figure 4.1 Schematic for synthesis of OLC-CNF@Mn_2O_3 composite electrode material.

4.2 Results and discussions

4.2.1 Material characterization

Prior to electrospinning, OLC powders were pre-synthesized from the Nano diamond powder and analyzed. The diameter of the sintered OLC nanoparticles ranged between 5 and 10 nm, which is in good agreement with Zeiger et al. [6], Weingarth et al. [17] and Makgopa et al. [18]. OLCs exhibit concentric layered morphology of spherical particles with a tendency to form agglomerated flower-like structures as demonstrated in the SEM and TEM in figure 4.2 a and b, respectively. The mechanism of phase transformation of OLC morphology from the initial ND powder has been extensively discussed in the literature. [6] The formation of OLC was confirmed by the onion-like layers visibly displayed on the surfaces of the clustered particles in the TEM micrograph (figure 4.3 b). In some cases, closed concentric graphite shells could be observed completely enveloping small diamonds. The partial to complete covering of ND in a few graphitic layers is consistent with the ordering of carbon atoms on the surfaces of individual ND once the surface groups (consisting of C, H, N, O) have thermally decomposed. [17]

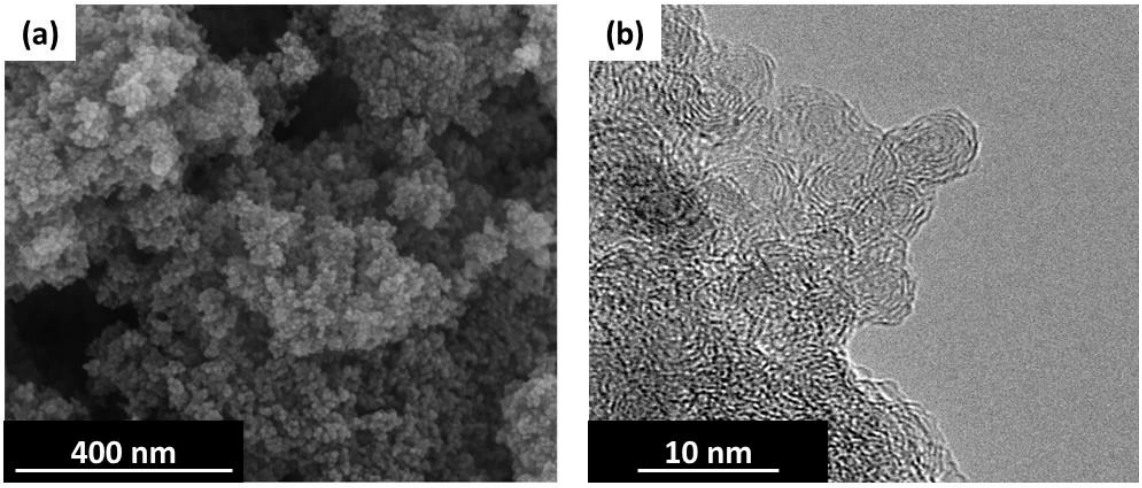

Figure 4.2 (a) SEM and (b) TEM image of OLC nanoparticles.

The morphology of as-electrospun PAN fibres are shown in figure 4.3 from both SEM and TEM. Firstly, the SEM micrograph in figure 4.3 a at high magnification revealed that the as-electrospun PAN fiber morphology were characterized by a uniform nano diameter with continuous length at random orientations. The low magnification SEM and TEM images in figure 4.3 b and c, respectively show a fibre morphology with solid interior and a noticeably rough/wrinkled surface. The rough nature is attributed to the buckling instabilities and stretching of the polymer solution by electrical forces. [15] Based on SEM micrographs, the fibres are characterized by a random 3-D network with a diameter ranging between 475-800 nm and an average diameter of 569 nm, this agrees with findings by Mao et al. [16].

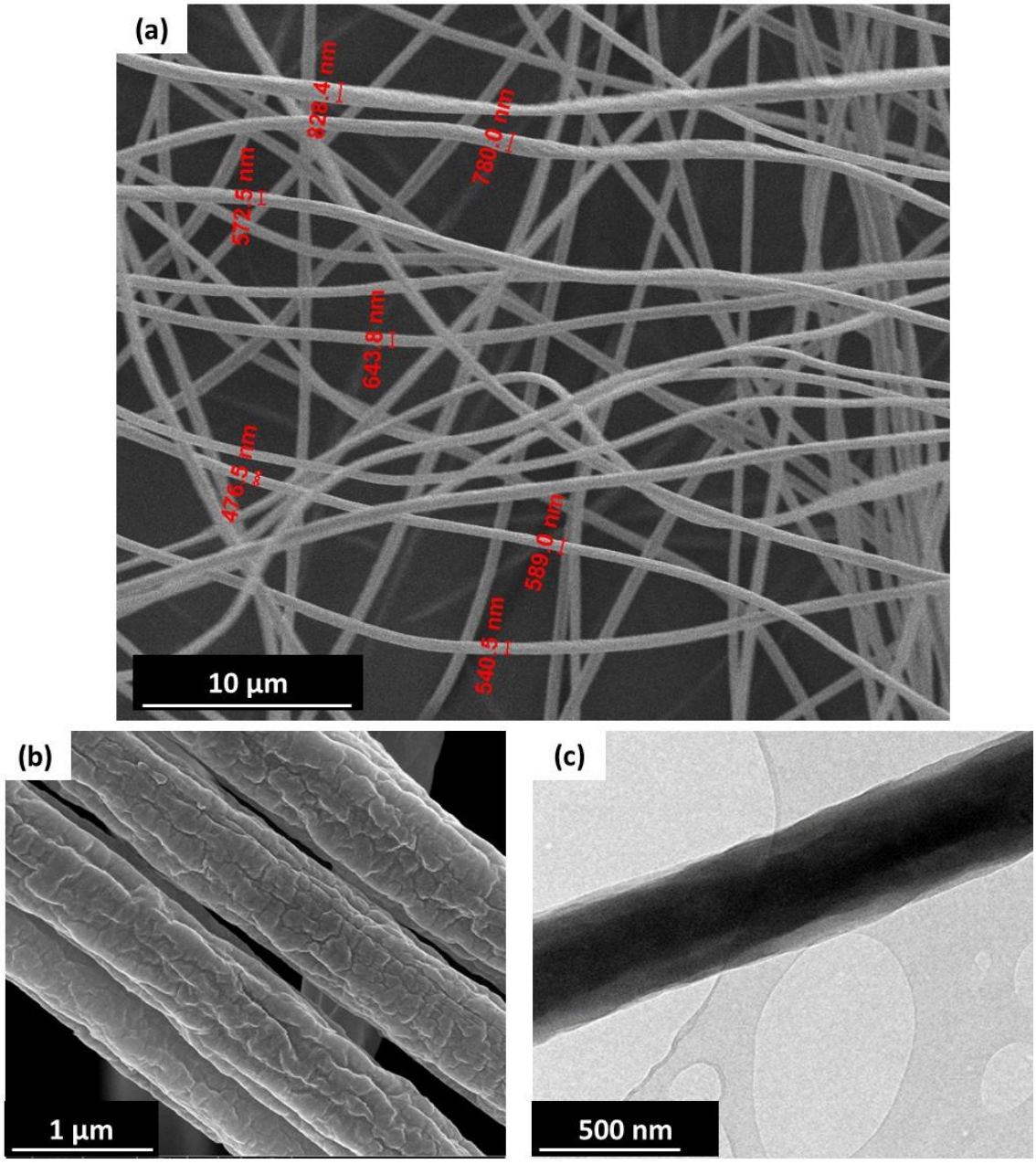

Figure 4.3 (a) SEM and (b) TEM image of as-electrospun PAN fibres.

SEM and TEM images of OLC-PAN fibres are shown in figure 4.4 a and b, respectively. When the OLC was added to the polymer solution, the surface morphology of the PAN fibre became beaded with an irregular fibre diameter due to the OLC nanoparticles embedded therein. The average diameter of OLC-PAN increased to ~895 nm from its original 630 nm average in PAN and had a larger distribution ranging from 200 nm up to 1.2 µm. This was explained by the change in polymer solution key properties (i.e. viscosity, surface tension and conductivity) of the polymer slurry. [19] These are critical

factors that ultimately determine the morphology of a fibre. The viscosity of the OLC-PAN in DMF solution was higher compared to that of PAN alone in DMF. One of the contributing factors was the additional concentration resulting from OLC addition to the polymer solution. Another was the tendency of OLC nanoparticles to self-assemble into clusters in solutions (i.e. PAN and DMF) despite vigorous sonication owing to their high surface area and π-π interactions. The use of vigorous sonification could not counteract this effect. Thus, in the fibre there are scattered agglomerates of OLC along the PAN fibre that fused together during electrospinning process. [20] This is also evident on the micrographs. Contrary to expectation a multi-step heat treatment in an argon atmosphere had to be employed to maintain the fibrous structure of the OLC-CNF. This consists of an initial heat treatment step aimed at stabilization of the fibres at a relatively low temperature of 260 °C for 3 hours. To affect the conversion of OLC-PAN (figure 4.4 a and b) into OLC-CNF (figure 4.4c and d) via carbonization, the second heat treatment step was performed at higher temperatures of 600 °C for 4 hours. The evolution of the fibre morphology is clearly visible in the low magnification micrograph, figure 4.4 d. The diameter of the OLC-CNF significantly reduced from an average of 895 nm to 269 nm as measured from the SEM image and had a smoother appearance on the outer surface in comparison to the electrospun OLC-PAN. These observations suggest that carbonization may greatly influence the surface morphology of the fibres due to weight and density changes associated with heat treatment.

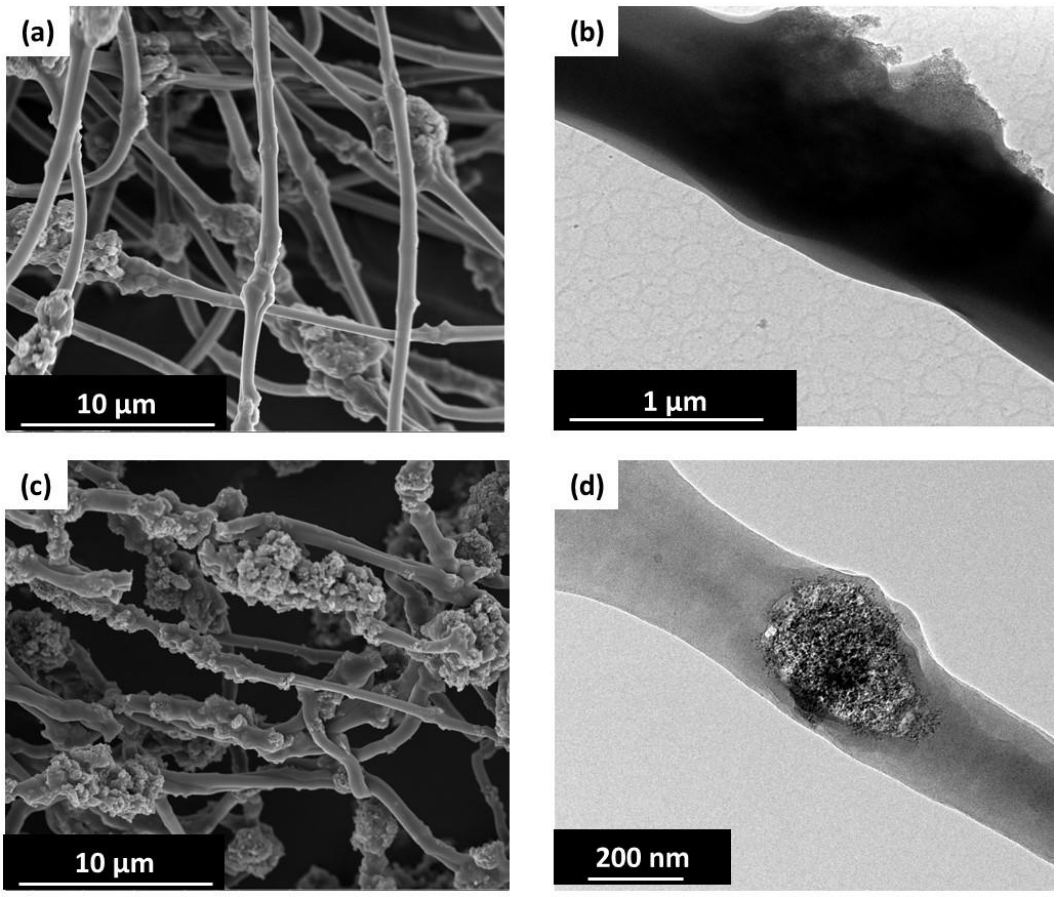

Figure 4.4 (a, c) SEM and (b, d) TEM micrographs of OLC-PAN fibres and OLC-CNF, respectively.

The final composite was denoted OLC-CNF@Mn_2O_3 after chemical treatment of OLC-CNF with $KMnO_4$ and the morphology is shown in figure 4.5 a and b under SEM and TEM, respectively. The micrographs reveal a good dispersion of the Mn_2O_3 nanoparticles. Seemingly incorporation of the Mn_2O_3 played a key role in de-agglomeration of OLC nanoparticles in the fibre structure, thus making it easier for electrolyte ions to diffuse into the composite structure for charge accumulation.

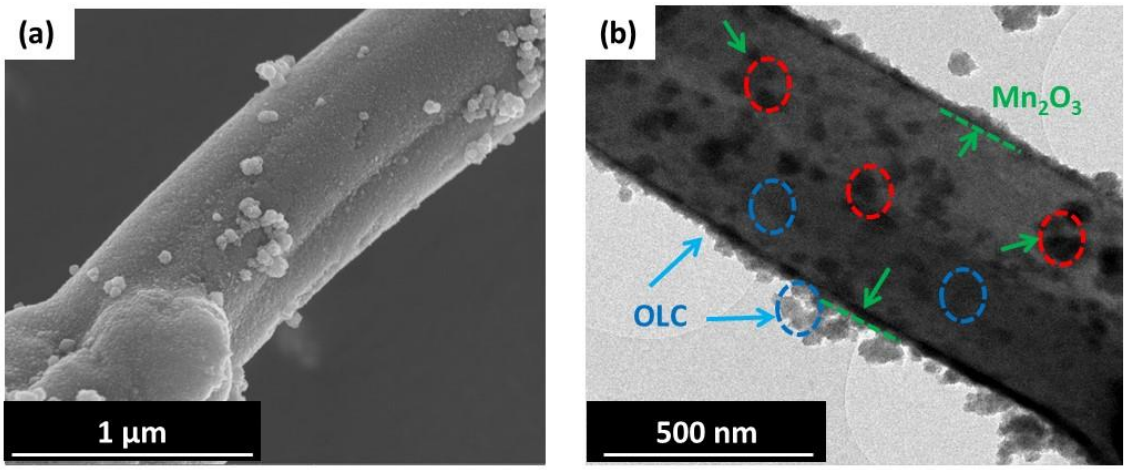

Figure 4.5 (a) SEM and (b) TEM image of as-electrospun OLC-CNF@Mn_2O_3 composite, indicating the presence of both OLC and Mn_2O_3 on the surface of the fibres.

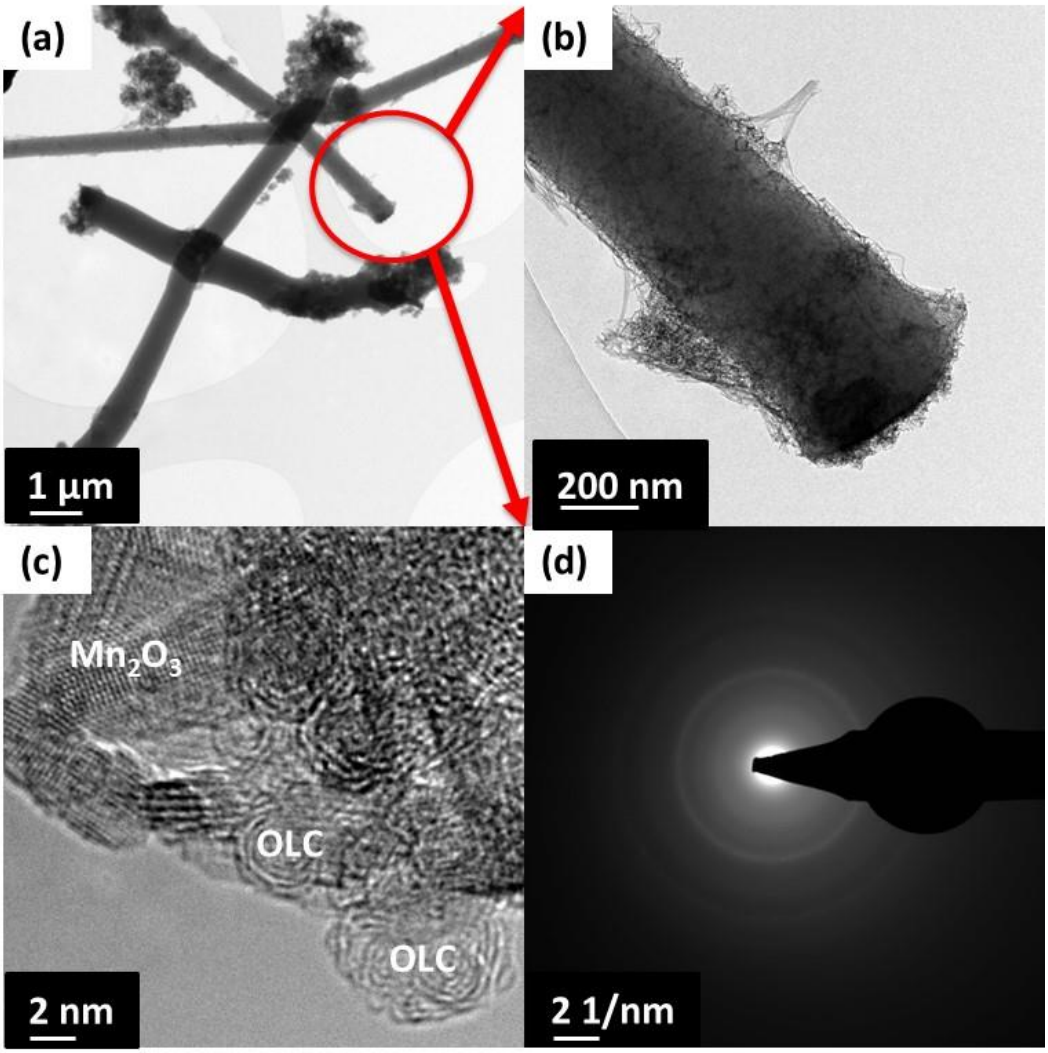

Figure 4.6 (a) HR-TEM images for OLC-CNF@Mn_2O_3 fibre composite with selected area aperture marked with a red circle, (b-c) a higher magnification of selected area, and (d) the radial intensity parallel and perpendicular to the fibre axis after background subtraction.

Fibre diameter size distributions have been shown using a bar chart in figure 4.7a and b for OLC-CNF and OLC-CNF@Mn_2O_3, respectively. The results show an overall increase in the fibre diameter when Mn_2O_3 is incorporated which agrees with observations in the TEM micrographs of an additional outer layer on the CNF's. It was also observed that the diameter of the fibre was uneven, ranging from hundreds of nanometres to micron levels in size. The shift on the diameter of the majority of the fibres from the highest frequency at 200-400 nm on OLC-CNF to 600-800 nm for OLC-CNF@Mn_2O_3 suggested successful

integration and encapsulation of CNF with Mn_2O_3 thin layer, corresponding with the SEM and TEM images in the previous figure 4.5a and b.

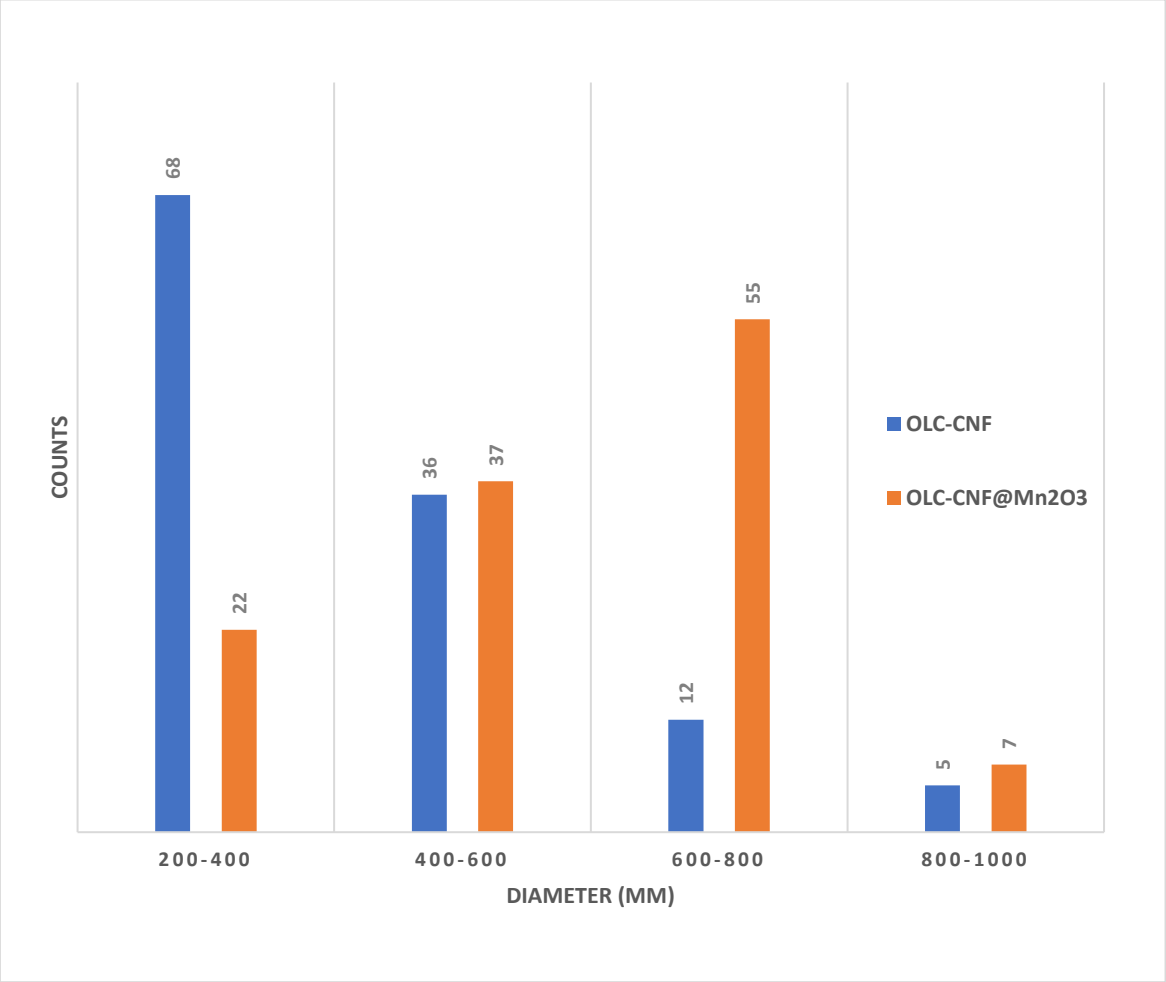

Figure 4.7 Fibre diameter distribution of OLC-CNF and OLC-CNF@Mn2O3 composites from SEM images.

Investigation of the bulk carbon structure in OLC-PAN using XRD, indicates the presence of an amorphous peak at 2θ = 17° attributed to PAN and another peak near 2θ = 27° corresponding to the (002) layers of graphite (figure 4.8). The peak corresponding to the 002 plane became narrower and intensified after thermal treatment. This is characteristic of an ordered graphite lattice structure. An additional peak at 2θ = 44° (100) indicating presence of partially graphitized carbon in the nanofibres. These XRD results support the electron microscope evidence that the conversion of PAN to CNF via heat treatment is incomplete. This also agrees with the observations made on SEM and TEM

results in figure 4.4. The carbon onion to diamond ratio increases from OLC-PAN to OLC-CNF also indicating an increase in sp^2 hybridized carbon. A higher degree of sp^2 hybridized carbon is desirable to enhance the electrical conductivity and intrinsic conductivity due to the π-electrons dangling bonds. [9] The six major XRD peaks observed at 2θ equals 18.8, 36.6, 38.23, 55.18, 65.79 and 81.8 ° for OLC/Mn_2O_3-CNF can be indexed to (002), (211), (004) (044) (226) and (008) planes, respectively and matched those of the cubic *I a -3-unit* cell, corresponding to the cubic Bixbyite structure with lattice constant, 9.4080 Å. The 2θ values and their corresponding d-spacing values have been summarized in table 4.1. In accordance with Mykhailiv et al., [21] two types of interstitial sites can be envisaged. These are (i) tetrahedral (8a) and (ii) octahedral (16c). The presence of these sites helps promotes the diffusion of charge carriers for ion intercalation pseudocapacitance, as shown by electrochemical performance studies.

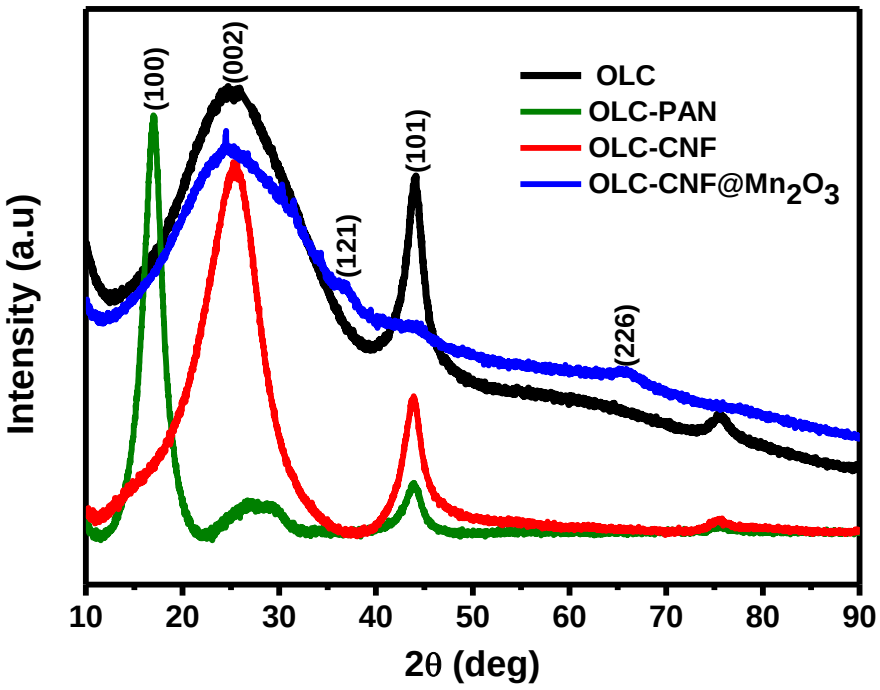

Figure 4.8 Powder X-ray diffraction patterns, of OLC, OLC-PAN, OLC-CNF and OLC-CNF@Mn_2O_3 composites materials.

Table 4.1 *Peak list of Mn_2O_3*

h	k	l	d [Å]	2θ [°]
0	0	2	4.70400	18.850
1	1	2	3.84080	23.139
2	2	2	2.71586	32.954
2	1	1	2.51439	36.679
0	0	4	2.35200	38.235
2	3	3	2.00579	45.168
0	4	4	1.66312	55.183
2	2	6	1.41831	65.791
0	0	8	1.17600	81.842

*hkl are symbols for the planes, where h, j, and l are all integers.

Raman spectroscopy is a powerful probing technique used to investigate the surface and electronic structure of materials. Particularly for this work, the degree of carbonization of the thermally treated fiber composites was estimated from Raman spectroscopy. Figure 4.9 depicts the Raman scattering spectra for OLC, OLC-PAN, OLC-CNF and OLC-CNF@Mn_2O_3 samples. It is well known that for carbon-based materials one has to focus on the relative Raman scattering at ~1357 and 1574 cm^{-1} which correspond to D and G bands (R_I), respectively. [21] The G band detected in all four samples is related to sp^2-hybridized carbon and originates from phonons at the Γ (0, 0, 0) point in the first Brillouin zone. [21] Generally, the strongest peak in the Raman scattering of OLC based materials is the D band which is naturally related to structural defects and often used to assess the degree of disorder in carbon-based systems via the I_D/I_G ratio. The intensity of the D and G peaks greatly increased by a factor of ~30 in the argon annealed OLC-CNF sample in relation to the OLC-PAN, this is an indication that the annealing process contributed to increase in ordering in the carbon system, similar results were previously reported. [9, 22]

The Gaussian deconvolution of the Raman spectrum of OLC-CNF sample revealed that the D band accounts for 55.37 % while G band represents 32.08 % of the total Raman scattering. More importantly, figure 4.7 shows a blue shift of the D band from 1348 cm^{-1} in the OLC-PAN to 1352 cm^{-1} in the OLC-CNF sample while the G band appeared at 1576 and 1580 cm^{-1} for OLC-PAN and OLC-CNF respectively. This G band red-shift suggests the formation of defects, inducing a change in the electronic band structure and may also be related to the dispersion change in the Raman-active-phonon. [9, 23-26] The calculated relative intensity ratio I_D/I_G for OLC-PAN and OLC-CNF were found to be 1.97 and 1.47. This decrease in I_D/I_G ratio confirms that OLC-CNF produced is highly graphitized. [23] The significant decrease of I_D/I_G ratio with annealing indicates the transformation of disordered carbon into graphitic carbon with a lower defect density. This structural transformation is known to have a positive impact on the storage capability. [24, 25]

The presence of cubic structure Mn_2O_3 nanoparticles was confirmed by the presence of a weak band at 344 cm^{-1} representing the deformation vibration of Mn-O-Mn symmetric and symmetric stretching. A characteristic vibration peak observed at 636 cm^{-1} was assigned to the motions of oxygen in Mn-O, representative of the α-/γ-Mn_2O_3. [26] The

broad nature of the Raman peaks for the final OLC-CNF@Mn_2O_3 composite material is indicative of a greater amorphous carbon content than the OLC-CNF starting material (figure 4.9). This is further supported by the shift of the D and G bands in the spectra to 1348 and 1576 cm^{-1}.

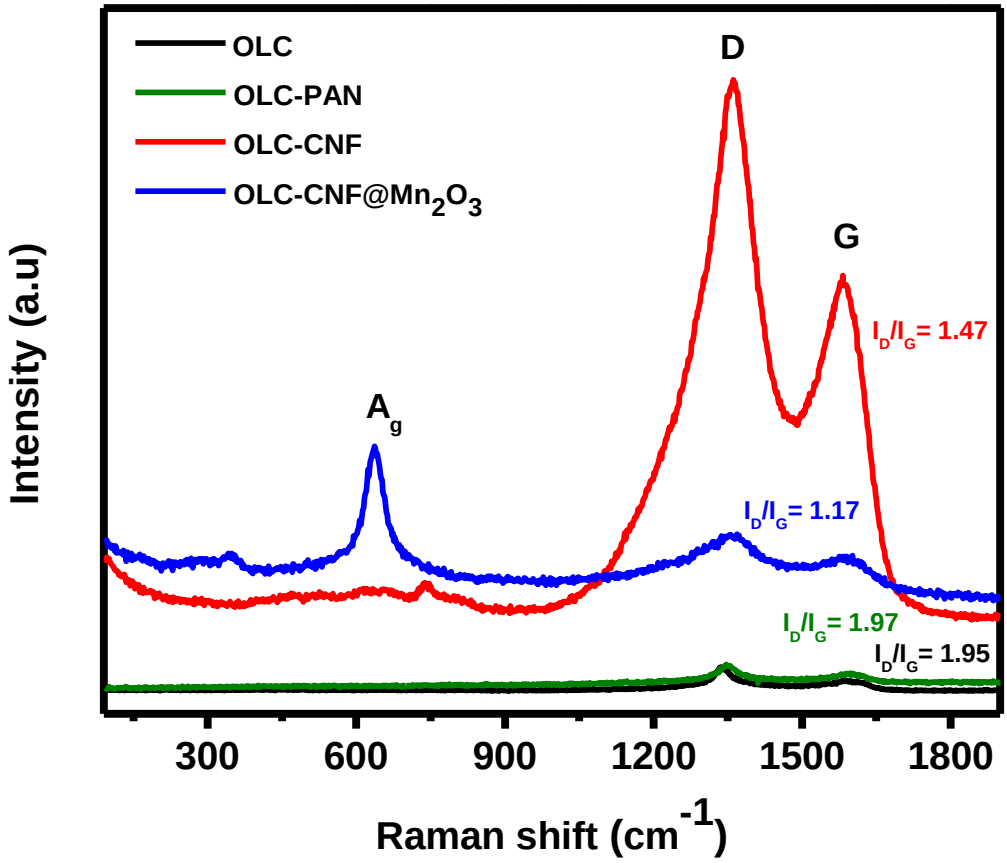

Figure 4.9 Raman spectra of OLC, OLC-PAN, OLC-CNF, and OLC-CNF@Mn_2O_3 composites.

Table 4.2 *Comparative Raman analysis of the electrode materials.*

Electrode Material	D	FWHM	G	FWHM	I_D/I_G	A_g	FWHM
OLC	1341.42	104	1564.52	66	1.95		
OLC-PAN	1348.18	167	1576.01	82	1.97		
OLC-CNF	1352.61	199	1580.65	110	1.47		
OLC-CNF@Mn_2O_3	1348.18	166	1575.98	82	1.17	636.44	68

*D and G represent disordered carbon and G graphitic carbon, respectively.

*I_D/I_G represents the degree of graphitization.

*FWHM represents the full width at half maximum.

The surface area and pore volume of the different materials produced were analyzed by N_2 adsorption and desorption. The BET specific surface areas (SSA) were calculated and are shown in Table 4.3. The synthesized OLC nanoparticles showed a high SSA value and a relatively low corresponding pore size. On the other hand, OLC-PAN showed a decrease in SSA due to the polymer interaction with OLC leading to the formation of agglomerated OLC nanoparticles embedded on the PAN, as evident from the SEM images. The pore size distribution of the OLC-CNF is broader than that of OLC-PAN due to high temperature employment which enables high porosity and thermal decomposition of PAN that impede the OLC outer surface area. When OLC-PAN undergoes heat treatment to produce the OLC-CNF, partial graphitization occurs and oxygen-containing functional groups from the PAN fibres are reduced to carbon/graphite leading to a relatively high surface area and high carbon ordering. The incorporation of Mn_2O_3 in the fibre provided an increase in the SSA and pore size of the fibre composite, which is likely to maximize the electrochemical performance of the electrodes.

Table 4.3 *Comparative BET surface area parameters of potential electrode materials.*

Electrode Material	SSA_{BET}	Pore Volume	Pore Size
	m^2/g	cm^3/g	nm
OLC	279.05	1.2	17.11
PAN	17.87	0.08	387.08
OLC-PAN	117.69	0.54	22.89
OLC-CNF	80.96	0.36	44.51
OLC-CNF@Mn_2O_3	129.98	0.35	51.78

*SSA is the specific surface area calculated from the BET analysis

X-ray photoelectron spectroscopy (XPS) was used for a surface chemical composition comparative analysis on OLC-PAN and OLC-CNF samples. The survey scan spectra presented in figure 4.10 and figure 4.11 demonstrated the co-existence of C 1s, O 1s and N 1s core levels in both as electrospun and argon annealed samples namely OLC-PAN and OLC-CNF, respectively. The graphitic structure of the samples was confirmed in both samples which exhibited more than 70 % carbon. The survey scan revealed an obvious increase in the carbon content of the OLC-CNF sample, this increase from C 1s core level is related to the higher degree of graphitization of OLC-CNF resulting from heat treatment in an argon atmosphere at 600 °C. Moreover, the concentration of oxygen decreased from 9.03 % in OLC-PAN to 7.45 % in OLC-CNF. In contrast, the nitrogen content remains relatively unchanged for both samples at approximately 19.15 %. A detailed comparative summary of the atomic percentage of the elements are shown in table 4.2.

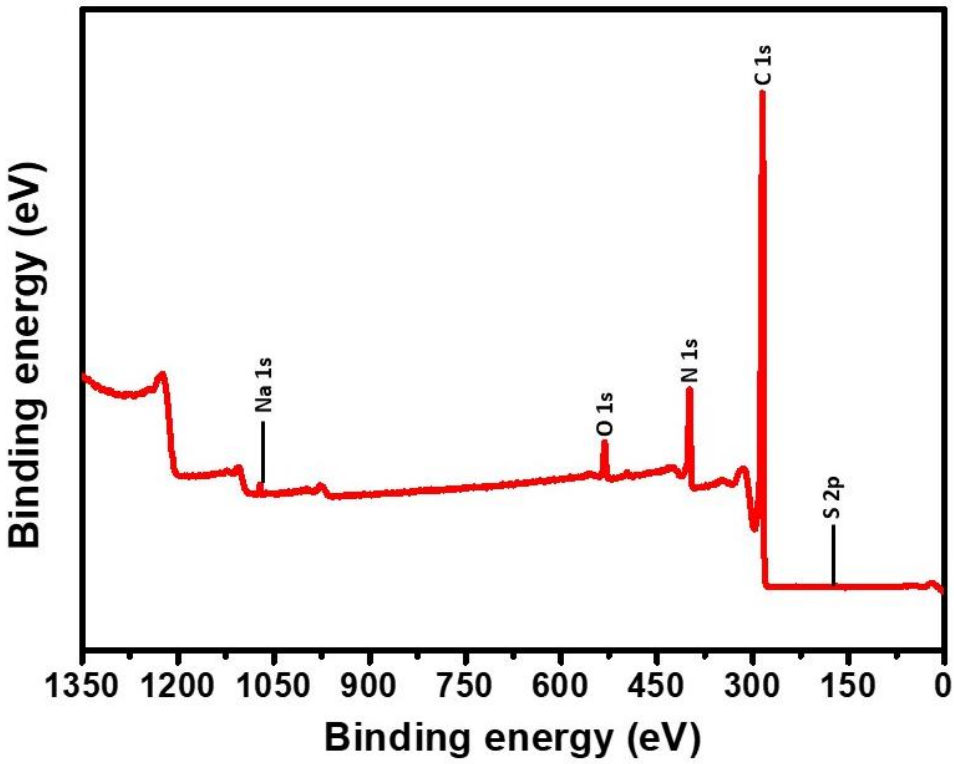

Figure 4.10 XPS Survey Scan spectra of OLC-PAN.

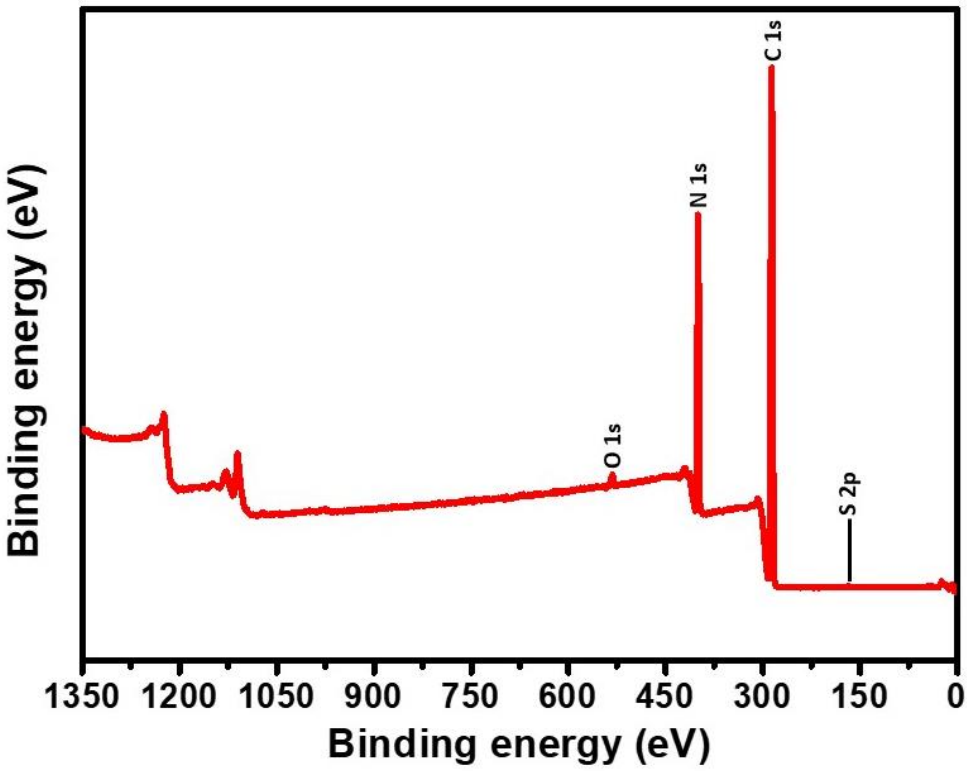

Figure 4.11 XPS Survey Scan spectra of OLC-CNF.

Table 4.4 *Comparative XPS data of OLC-PAN and OLC-CNF.*

	OLC-PAN		**OLC-CNF**	
Name	Atomic conc [%]	Mass [%]	Atomic conc [%]	Mass [%]
C 1s	71.81	67.63	73.40	69.47
O 1s	9.02	11.32	7.45	9.39
N 1s	19.16	21.05	19.15	21.14

Further XPS analysis were carried out on the manganese oxide doped composite fibres, OLC-CNF@Mn_2O_3. Figure 4.12 represents a survey scan of the fibre composite which showed characteristic peaks of C 1s O 1s, Mn2p, N 1s and K2p3 with corresponding binding energies. The values of binding energies and atomic concentration are summarized in Table 4.5 and were in good agreement with those in literature.

Table 4.5 *XPS data of OLC-CNF@Mn_2O_3.*

Name	Peak	Atomic concentration [%]
C 1s	284.7	49.2
O 1s	530.2	31.2
Mn2p	642.0	9.6
N 1s	398.7	6.3
K 2p3	292.2	3.7

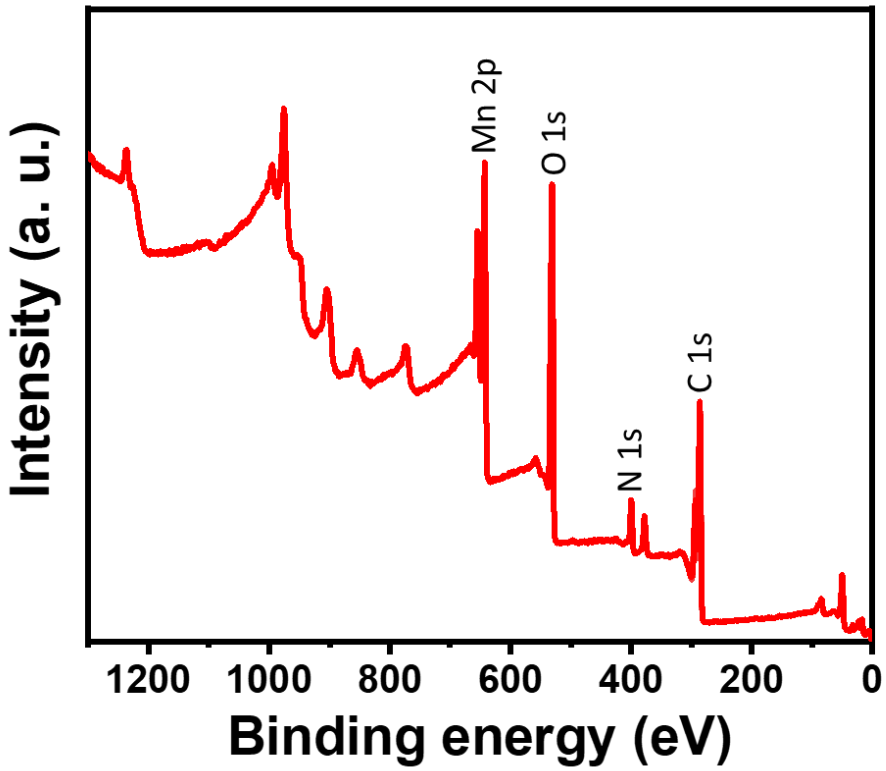

Figure 4.12 XPS Survey Scan spectra of OLC-CNF@Mn_2O_3.

The C 1s core levels were deconvoluted in a doublet of Gaussian. The dominant Gaussian component of the C 1s core level revealed a relative broadening of the full width at half maximum (FWHM) for the OLC/Mn_2O_3-CNF composite (FWHM=1.85 eV) compared to that of OLC-CNF precursor (FWHM=1.84 eV) indicating the superior ordered structure of a fullerene-like layer in OLC-CNF@Mn_2O_3 sample composite as a result of the formation of more carbon bonds due to high temperature treatment in an argon atmosphere (see figure 4.13). [26] The O 1s core levels illustrated in figure 4.13 were fitted using two Gaussian functions which revealed the coexistence of quinines or pyrone at 529 eV and the carbon-oxygen single bonds at 532 eV. [26] The amount of carbon-oxygen single bonds was found to have increased in the OLC-CNF@Mn_2O_3 (93 %) relative to that of OLC-CNF (91.36 %), this finding is consecutive to the relative increase of graphitization. More importantly, contrary to earlier reports where thermal treatment increased the surface nitrogen content [8], it was found that the atomic concentration of nitrogen remained nearly unchanged after thermal annealing in argon gas. The XPS results are in accordance/good agreement with the Raman analysis presented.

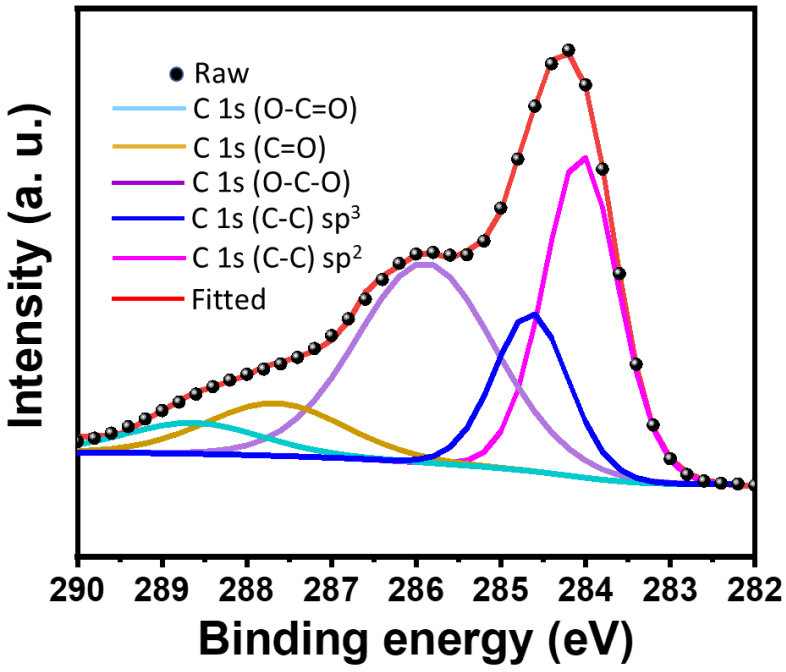

Figure 4.13 High resolution XPS spectra of C 1s core levels for OLC-CNF@Mn_2O_3.

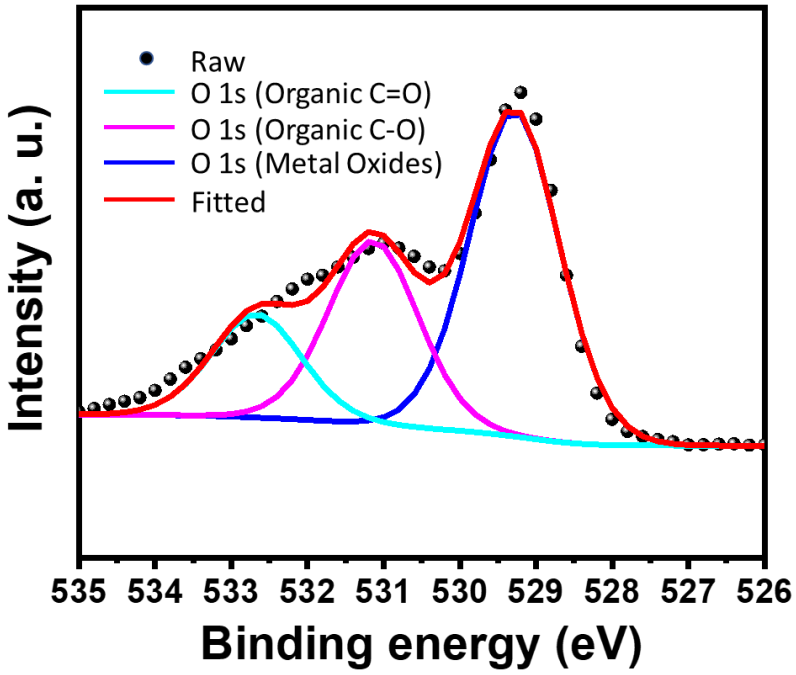

Figure 4.14 High resolution XPS spectra of O 1s core levels for OLC-CNF@Mn_2O_3.

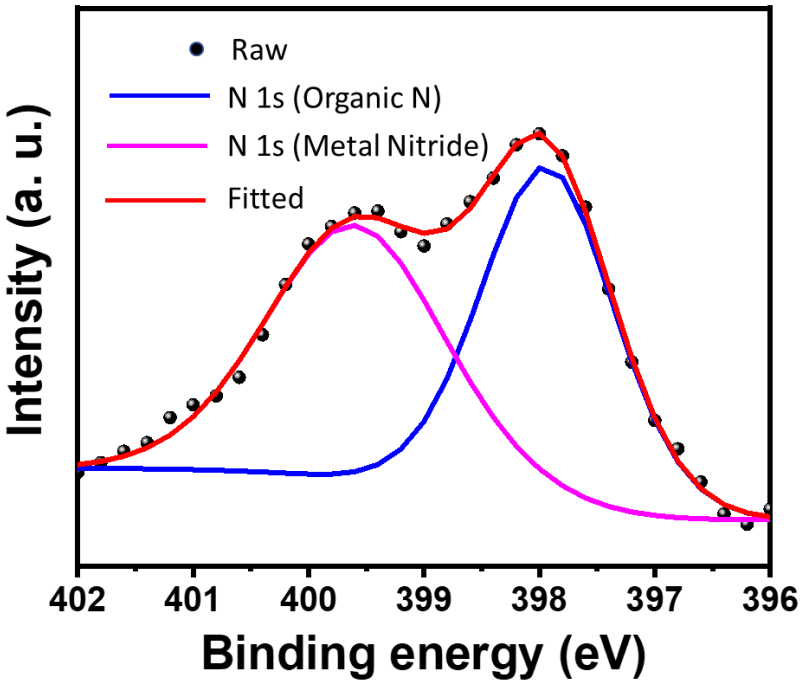

Figure 4.15 High resolution XPS spectra of N 1s core levels for OLC-CNF@Mn_2O_3.

Figure 4.16 shows the XPS spectrum of Mn2p. The peaks located at 653.4 and 641.7 eV can be assigned to Mn2p1/2 and Mn2p3/2, respectively and the calculated Mn 2p separation energy ΔE2p = 11.7eV. [10] This result compares favorably with that reported by Chen et al.[11] and other researchers who have reported similar binding energies for Mn and confirmed that the oxidation state is +3. [12-13] Thus, it can be proposed that the Mn exists as Mn^{3+} in the OLC-CNF@Mn_2O_3 composite.

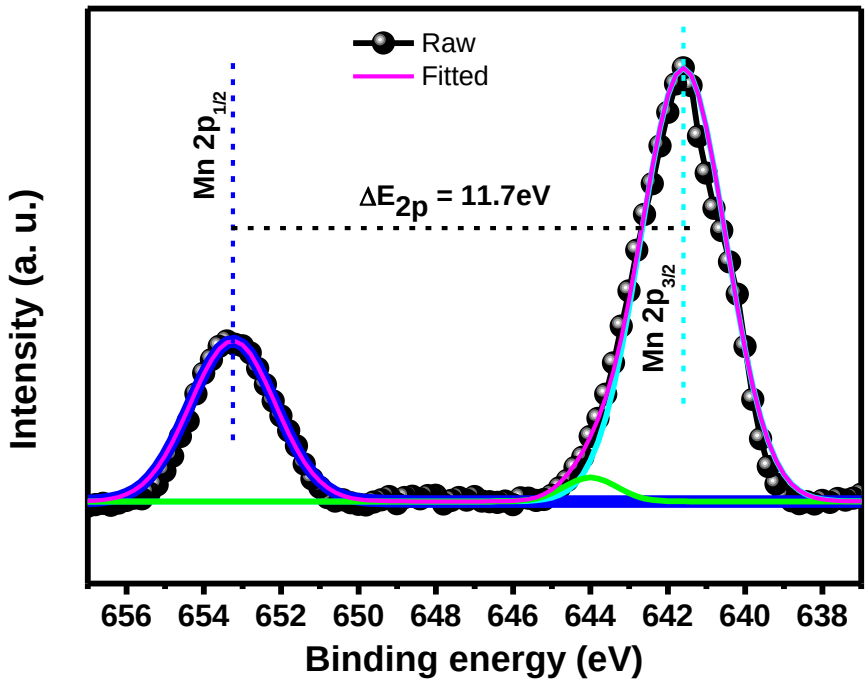

Figure 4.16 High resolution XPS spectra of Mn 2p core levels for OLC-CNF@Mn_2O_3.

The two peaks detected at 83 and 89 eV are attributed to multiplet splitting in the 3s shell and confirmed the Mn^{3+} oxidation state. As shown in Figure 4.17, the splitting width was 5.75 eV, which is in accordance with a previous report on the XPS spectrum of Mn_2O_3. [14]

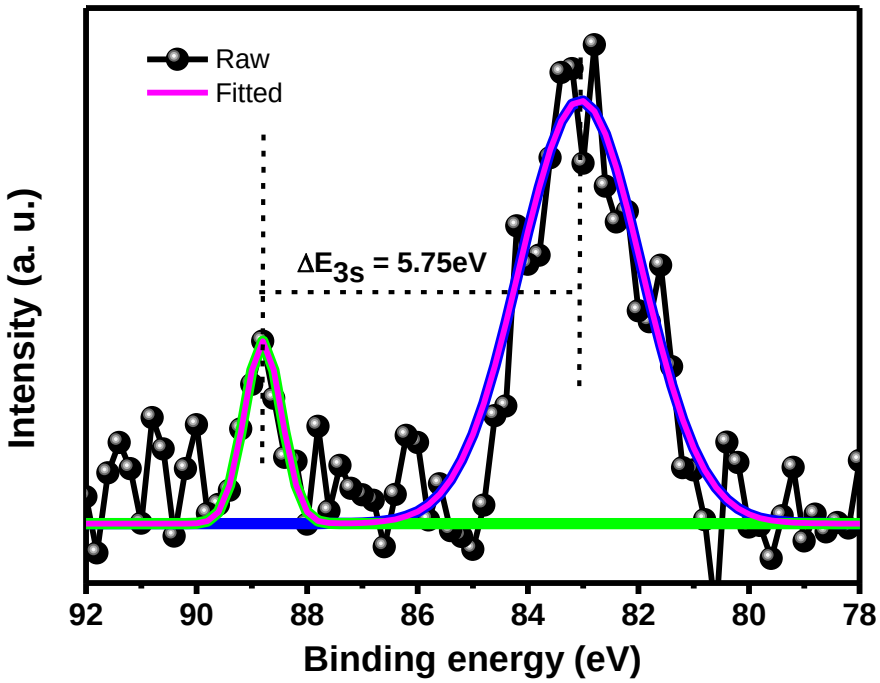

Figure 4.17 High resolution XPS spectra of Mn 3*s* core levels for OLC-CNF@Mn_2O_3.

4.2.2 Electrochemical performance

In this study, a three-electrode configuration of the screen-printed carbon electrodes (SPCEs) was used to qualitatively confirm the capacitive behavior of the carbon-based electrospun fibres. Figure 4.18 displays three-electrode CV graphs obtained from the SPCEs of OLC-PAN and OLC-CNF, in which current density is reported as a function of cell voltage. The shape of the voltammograms displayed by OLC-PAN and OLC-CNF in figure 4.18 a and b, respectively, suggests ideal capacitor type behavior by the electrode materials. At a higher scan rate, the rectangular shape for both materials began to deviate as a result of the carboxylic functional groups from the PAN. This effect suggests poor rate capability of the electrodes. Figure 4.18 c and d show CV graphs at a constant scan rate of 25 mV s^{-1}, at various potential windows (between 0.6 and 1.6 V) for OLC-PAN and OLC-CNF, respectively. The CV graphs of the electrodes have retained their shape between 0.6 and up to 1.4 V indicating excellent stability within the typical aqueous electrolyte potential range.

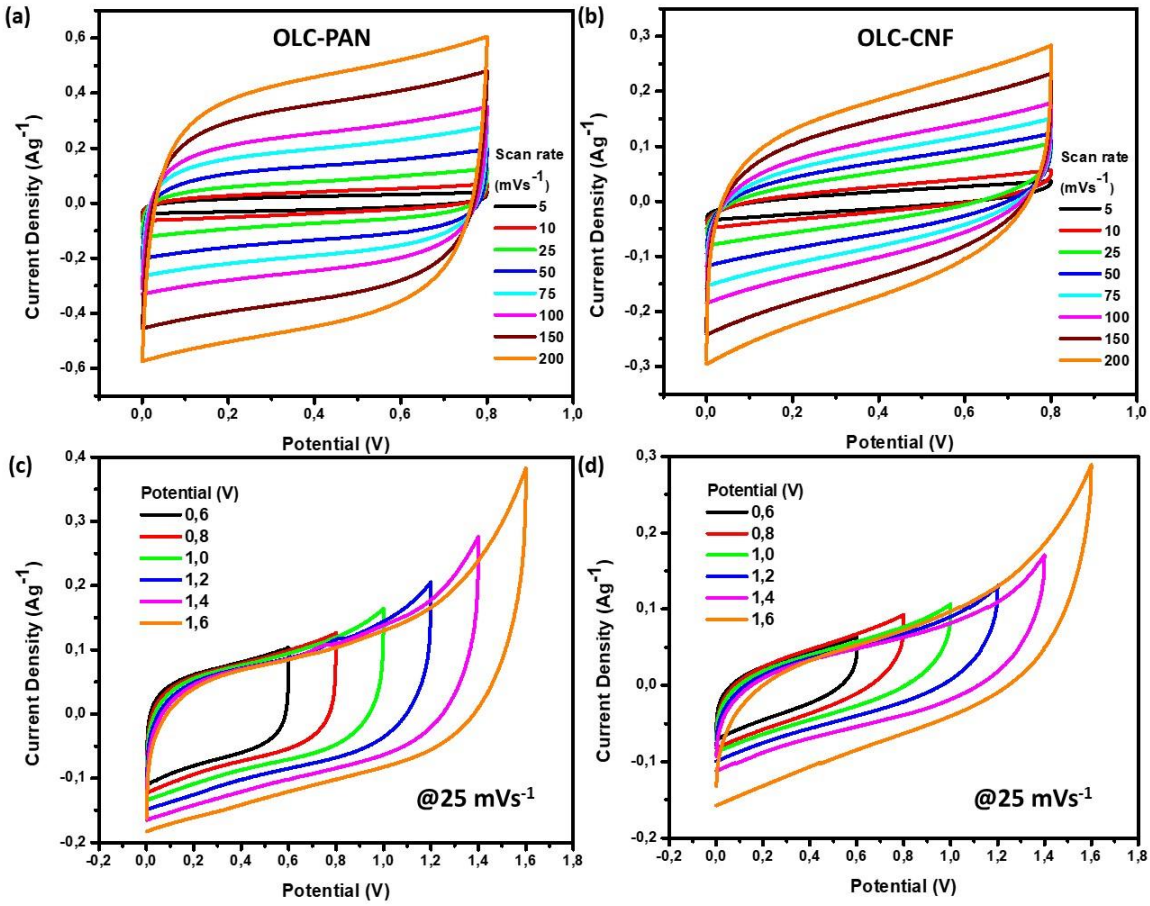

Figure 4.18 Three-electrode CV plots of the OLC-PAN and OLC-CNF fibre composites between 5-200mV s^{-1} in 1 M Na_2SO_4 electrolyte.

Galvanostatic charge-discharge curves were recorded at various current densities and are presented in figure 4.19. The potential drop in the OLC-PAN fibre (figure 4.19 a) is higher than that of the OLC-CNF composite (figure 4.19 b), suggesting electronic resistance in this electrode, as expected for high surface area containing electrode materials. [15] Since the area under the potential curve represents the total amount of energy delivered to a load, it is obvious that OLC-CNF variant is able to deliver more energy than OLC-PAN at the same current density. The higher potential window of the OLC-CNF electrodes (figure 4.19 d) induces strain in comparison to the OLC-PAN fibre equivalent (figure 4.19 c), which suggest that the electrodes are likely to self-discharge at potential windows above 1.0 V.

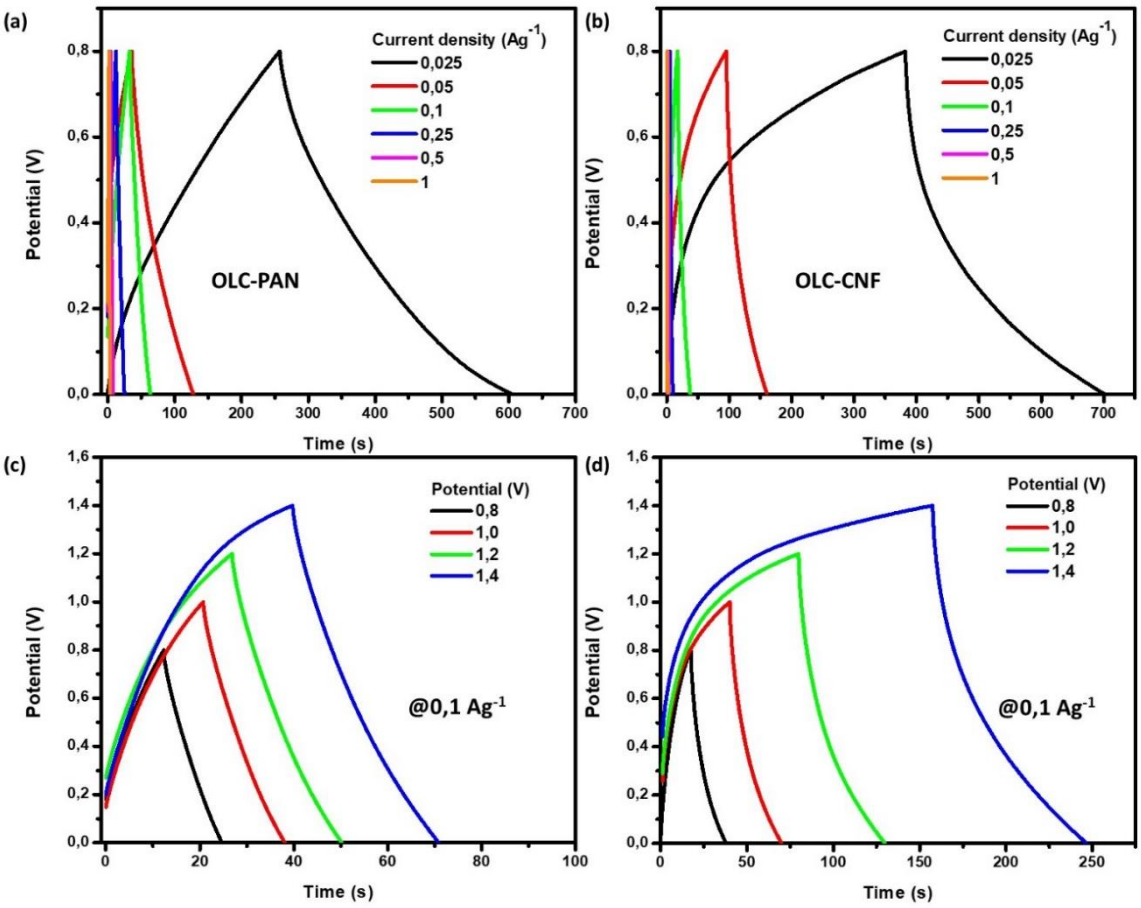

Figure 4.19 Galvanostatic charge-discharge curves for OLC-PAN and OLC-CNF fibre composites in a three-electrode SPCE system.

The three-electrode data was obtained from a T-cell arrangement with titanium as the counter electrode, a 1 M Na_2SO_4 electrolyte solution and a Ag/AgCl reference electrode with Nickel as a counter electrode. The OLC-PAN, OLC-CNF and OLC-CNF@Mn_2O_3 electrode performances were compared in a CV test at 30 mV s^{-1} (figure 4.20). These results show that OLC/Mn_2O_3-CNF is more capacitive due to its higher current response compared to the fibres without Mn_2O_3 nanoparticles. The ideal capacitive nature of the OLC-PAN and OLC-CNF is visible from the rectangular shape of their CV curves. In the case of OLC-CNF@Mn_2O_3 composite, an additional charge storage was achieved through the faradaic reactions from the incorporation of Mn_2O_3.

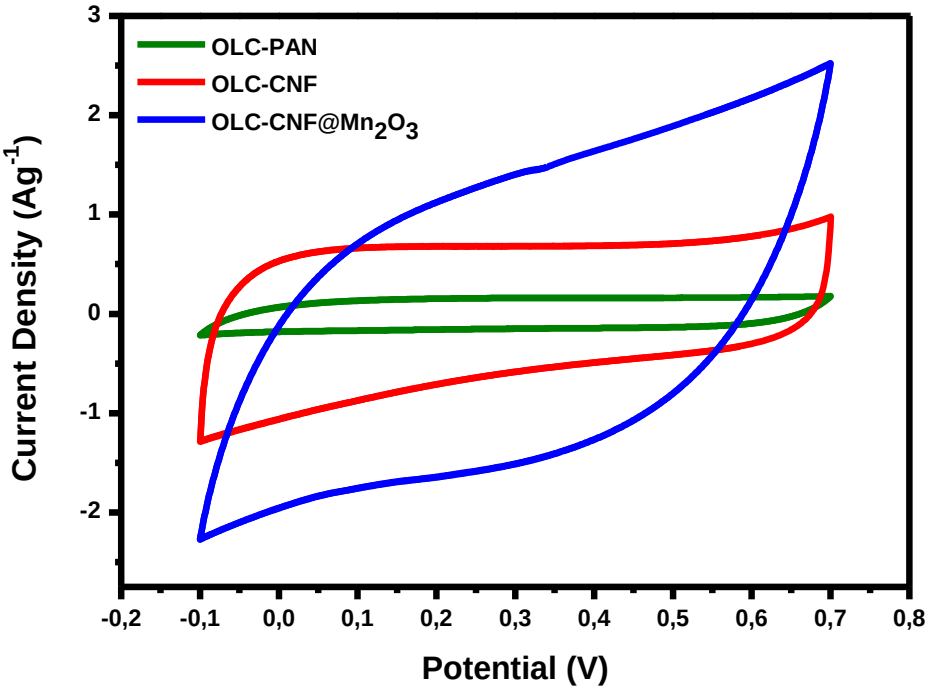

Figure 4.20 Comparative three electrode CV at 30 mV s^{-1} for OLC-PAN, OLC-CNF, and OLC-CNF@Mn_2O_3 composites.

Charge-discharge curves shown in figure 4.21 at 0.25 A g^{-1} resemble those of supercapacitors with dominant capacitive behaviour. The difference lies in the discharge time for OLC-CNF@Mn_2O_3 composite, which was more than double that of the original OLC-PAN, suggesting an enhancement in capacitance as indicated by the CV data. The curves had a small potential drop at the start of discharge cycle, reflecting the effect of the internal resistance on the electrodes. Although the electrodes were cycled at 1 A g^{-1} for 200 cycles to assess their stability, no capacitance calculations were deduced as these were half cells and do not represent how supercapacitors are used in applications.

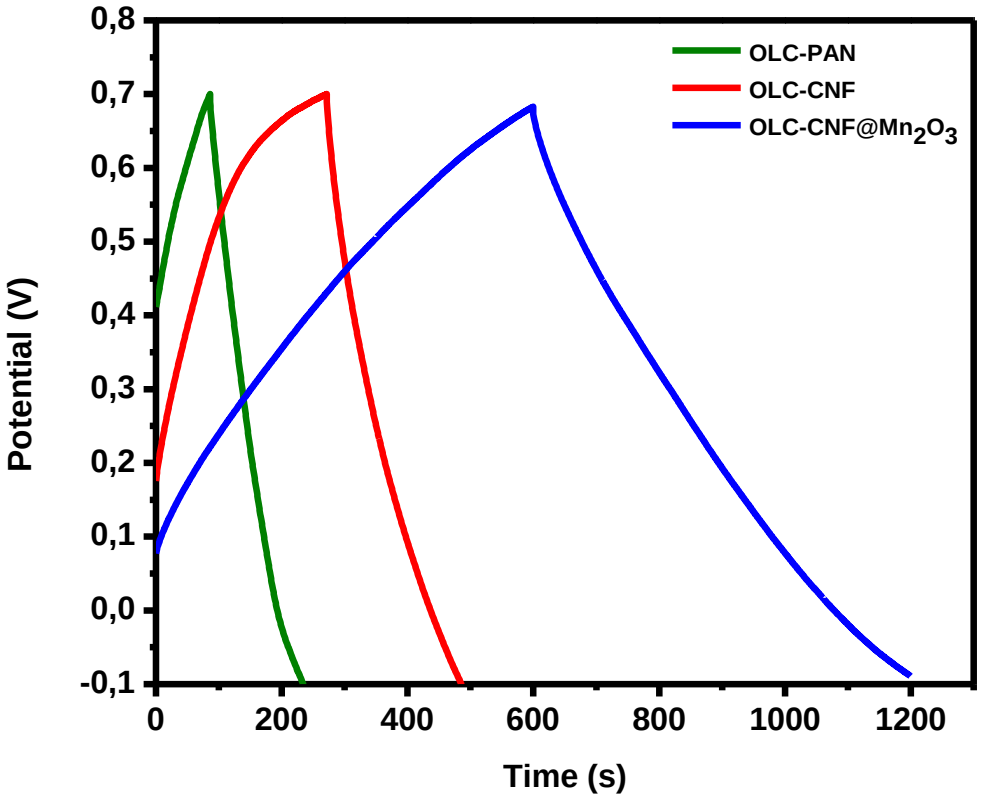

Figure 4.21 Comparative three electrode galvanostatic charge-discharge curves at 0.25 A g^{-1} for OLC-PAN, OLC-CNF, and OLC-CNF@Mn_2O_3 composites.

Figure 4.22 and 4.23 show Nyquist plots obtained from the EIS analysis for the three electrode materials before and after cycling to understand the effect of Mn_2O_3 addition in the composite fibres. The circuits used to fit the Nyquist plots are presented in figure 4.24 for OLC-PAN, OLC-CNF and OLC-CNF@Mn_2O_3. Although they exhibited low R_s values, OLC-PAN demonstrated the highest R_{CT} in a high frequency regime but nearly ideal linear shape with a phase angle of 78 ° at 0.01 Hz representative of a low frequency regime. This is explained by the dense morphology of the fibres in which the ions were not able to penetrate through the electrode material, thus increasing the resistance. In addition, the surface area associated with OLC-PAN fibres was small which adversely affected the exposure to the electrolyte solution. The OLC-CNF electrodes showed better electron transfer due to the porous nature of the highly carbonaceous fibres which subsequently led to increased conductivity. When Mn_2O_3 were incorporated into the fibres of the OLC-CNF, the $R_S$increased slightly whilst the R_{CT} improved by twofold.

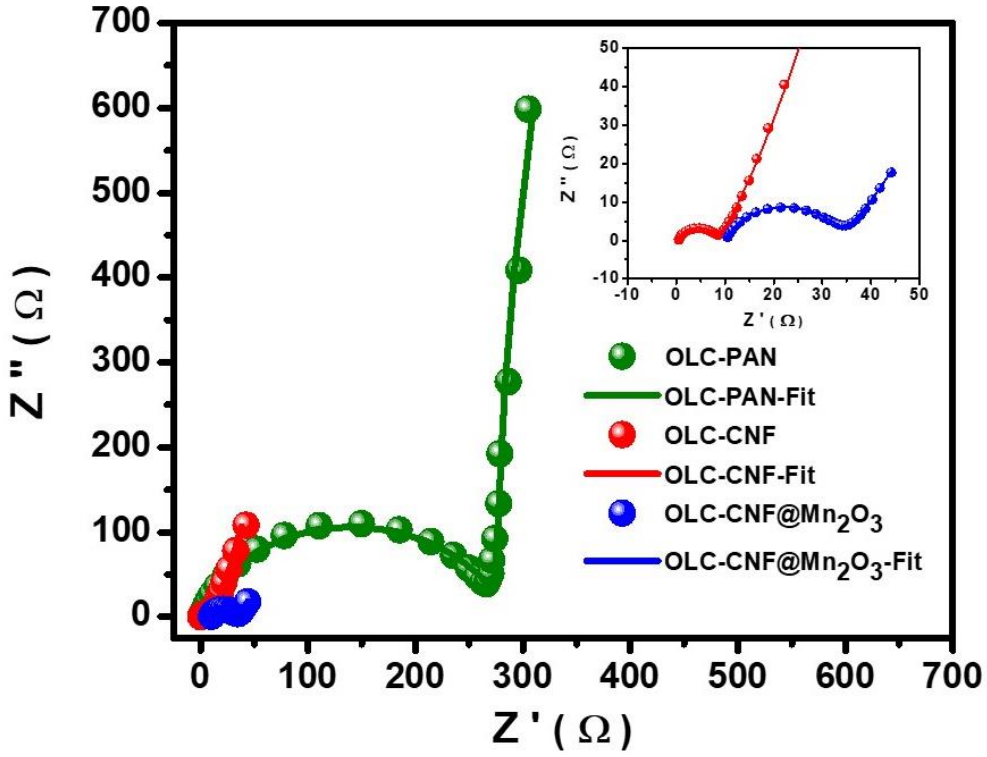

Figure 4.22 Comparative Nyquist plots for OLC-PAN, OLC-CNF, and OLC-CNF@Mn_2O_3 composites before charge-discharge cycles.

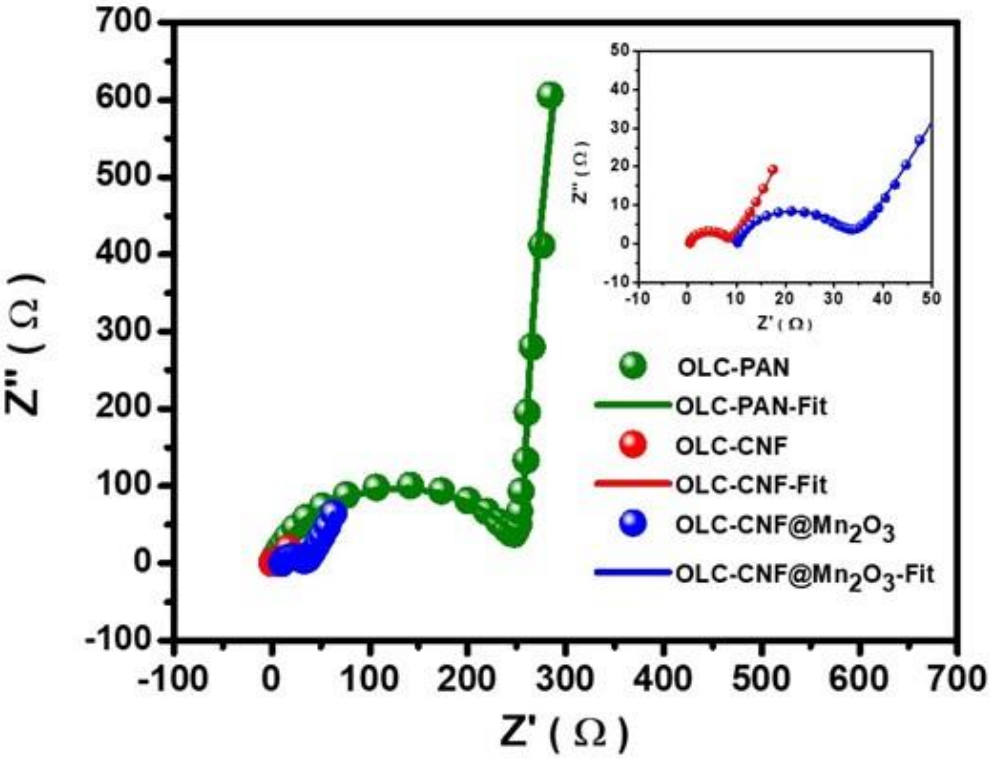

Figure 4.23 Comparative Nyquist plots for OLC-PAN, OLC-CNF, and OLC-CNF@Mn_2O_3 composites after charge-discharge cycles.

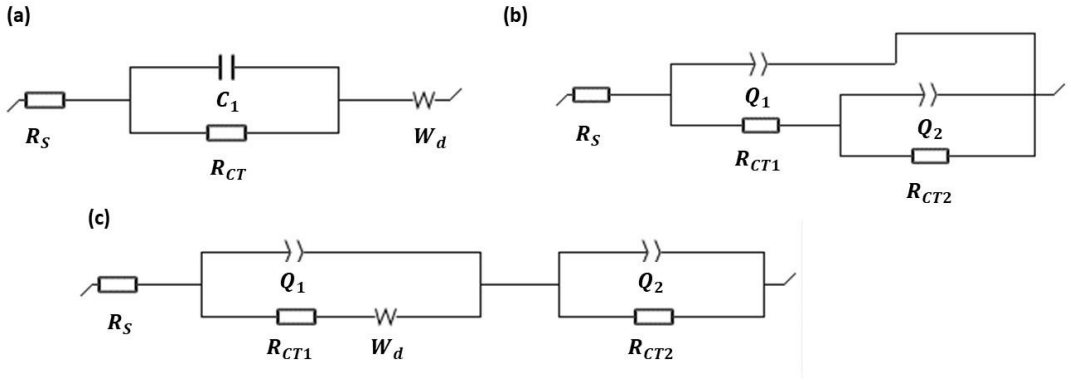

Figure 4.24 The electrical equivalent circuit used in fitting the Nyquist plots of OLC-PAN (a) OLC/CNF and (b) OLC-CNF@Mn_2O_3 (c).

A capacitance contribution study was done for the OLC-CNF@Mn_2O_3 electrodes and the corresponding CV plots are presented in figure 4.25 a and b at 10 and 100 m Vs^{-1}, respectively. The graphs indicate that at low scan rates, the capacitance is largely driven by diffusion-controlled processes, whereas at a high scan rate both surface and diffusion-controlled processes occur. Figure 4.26 a and b presents the b-values for the anodic and cathodic currents, respectively. The b values were 0.67/0.72 V for the anode peaks, and 0.66/0.73 for cathodic peaks, respectively. This confirms that the charge storage mechanism in the OLC-CNF@Mn_2O_3 electrode is based on diffusion controlled or pseudocapacitive mechanism.

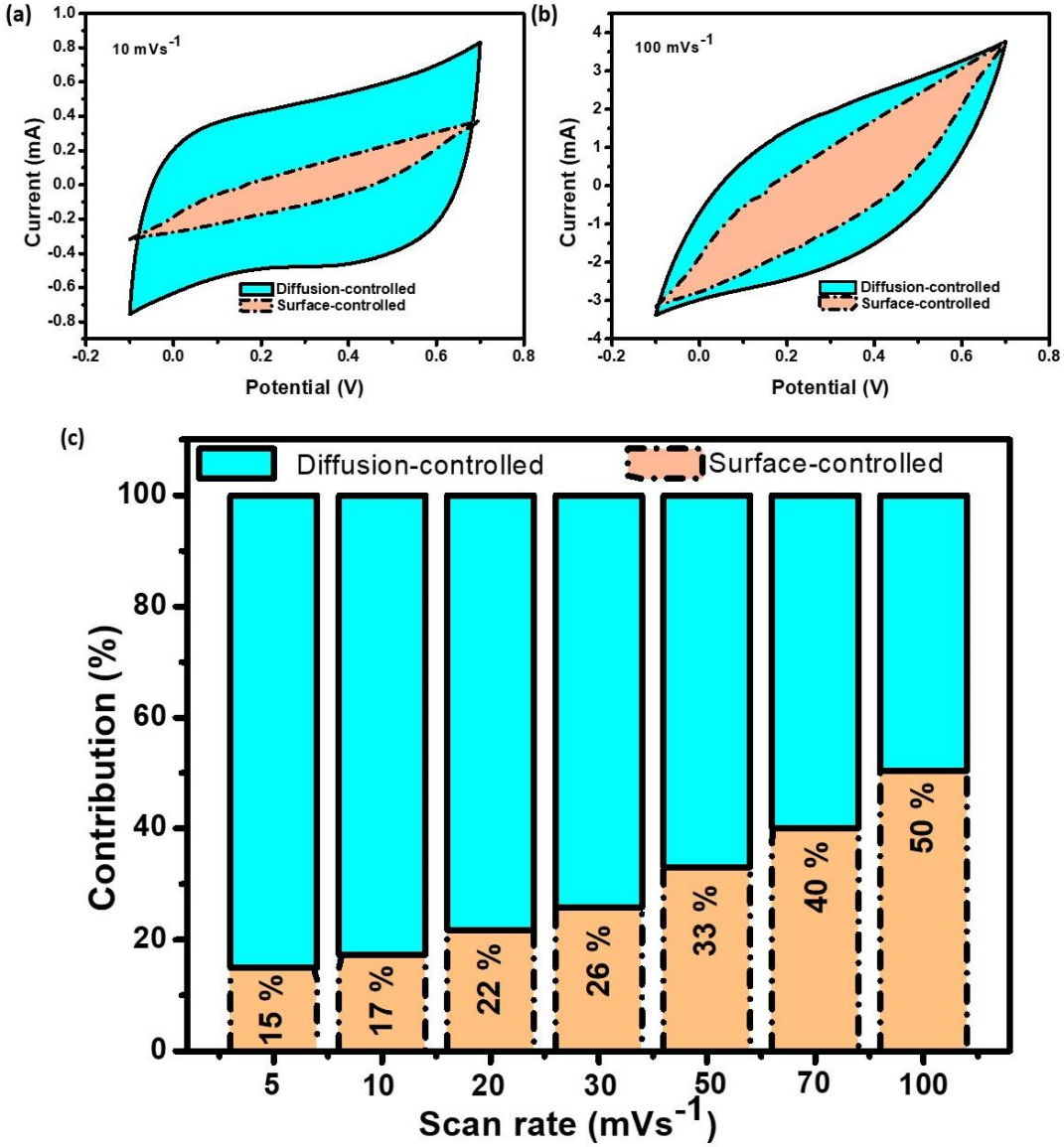

Figure 4.25 (a) Comparison of the capacitive contribution and the diffusion-controlled contribution fraction for OLC-CNF@Mn_2O_3 at (a) 10 m Vs^{-1} versus at 100 m Vs^{-1}, and (c) histograms of the percentage contributions at varying scan rate between 5 and 100 mV s^{-1}.

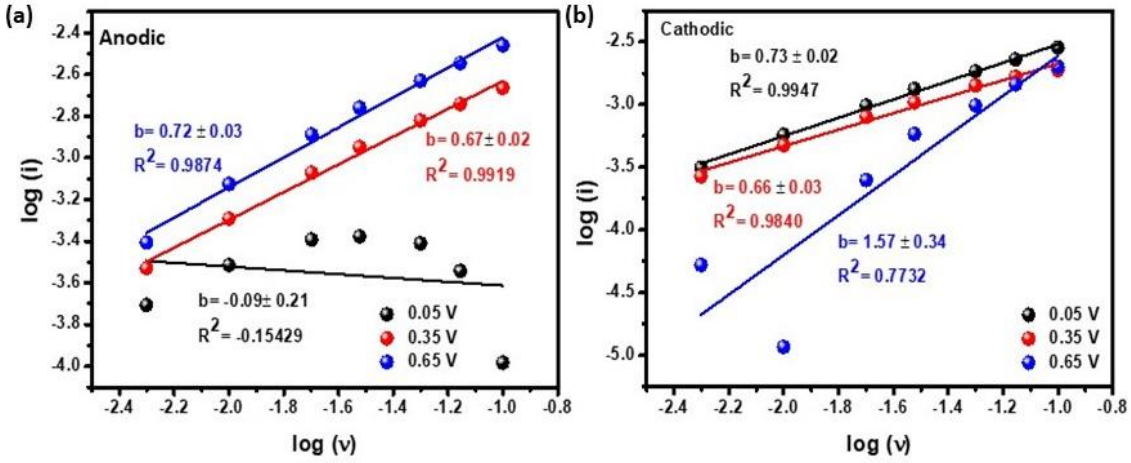

Figure 4.26 Log peak current vs log scan rate for (a) anodic and (b) cathodic electrodes of OLC-CNF@Mn_2O_3.

Figure 4.27 presents the CV and charge-discharge results of a two-electrode system obtained from a Swagelok cell for OLC-PAN, OLC-CNF and finally OLC-CNF@Mn_2O_3 composites, respectively. The CV analysis discussed were conducted at various scan rates between, 5 and 100 mV s^{-1} to establish the current response of the composites in a full cell and compare the improvements from as-electrospun OLC-PAN to heat-treated OLC-CNF and finally, with that of the OLC-CNF@Mn_2O_3 composite. All the electrode materials had a potential window between 0 and 0.8 V. The distinguishing feature was the accessibility of ions to the electrolyte for charge accumulation, which was quantified from the current response. The CV and GCD curves for the two-electrode measurements of the OLC-PAN fibres were similar to those of ideal capacitors. As the fibres were thermally treated, they began to show pseudocapacitive behaviour, i.e. a slight deviation from the original rectangular shape of the CV and triangular shape of the GCD was observed. The results agree with those obtained from the three-electrode system.

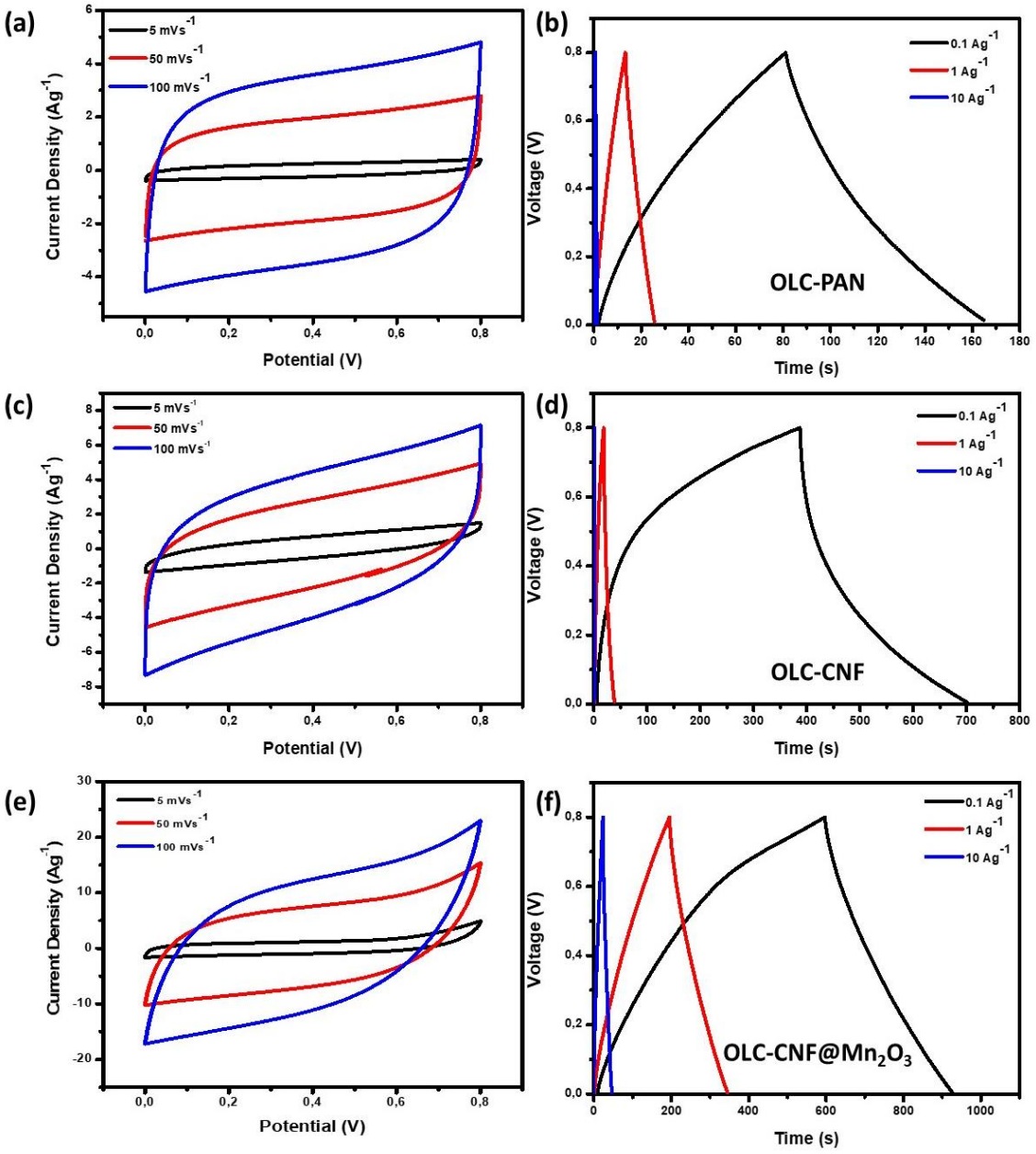

Figure 4.27 Comparative two-electrode CV plots at 10, 50 and 100 mV s^{-1} (a), and galvanostatic charge-discharge curves 0.1, 1 and 10 A g^{-1} for OLC-PAN in (a and b), OLC-CNF in (c and d) for OLC-CNF@Mn_2O_3 in (e and f), respectively.

The fitted Nyquist plot shown in figure 4.28 represents the impedance response associated with the two-electrode symmetrical supercapacitor cell for the OLC-CNF@Mn_2O_3 composites. From the Nyquist plot, R_s is 0.84 Ohms before cycling and 0.79 Ohms after cycling. The semi-circle was reduced after cycling and since a pseudocapacitance-generating reaction is absent, as suggested by the three-electrode capacitive study, this deformed semicircle was not assigned to an electrochemical process. Thus, it is believed

that this semi-circle comes from the interface between the OLC-CNF@Mn_2O_3 composite and Ni foam.

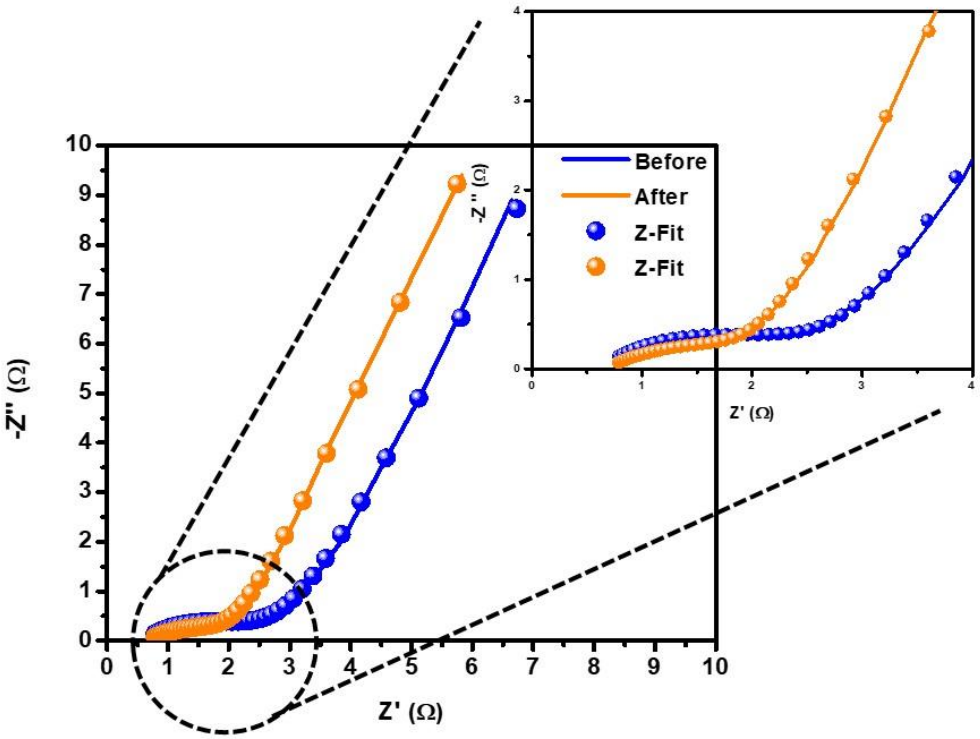

Figure 4.28 Nyquist plots before and after cycling of the OLC-CNF@Mn_2O_3 two-electrode system.

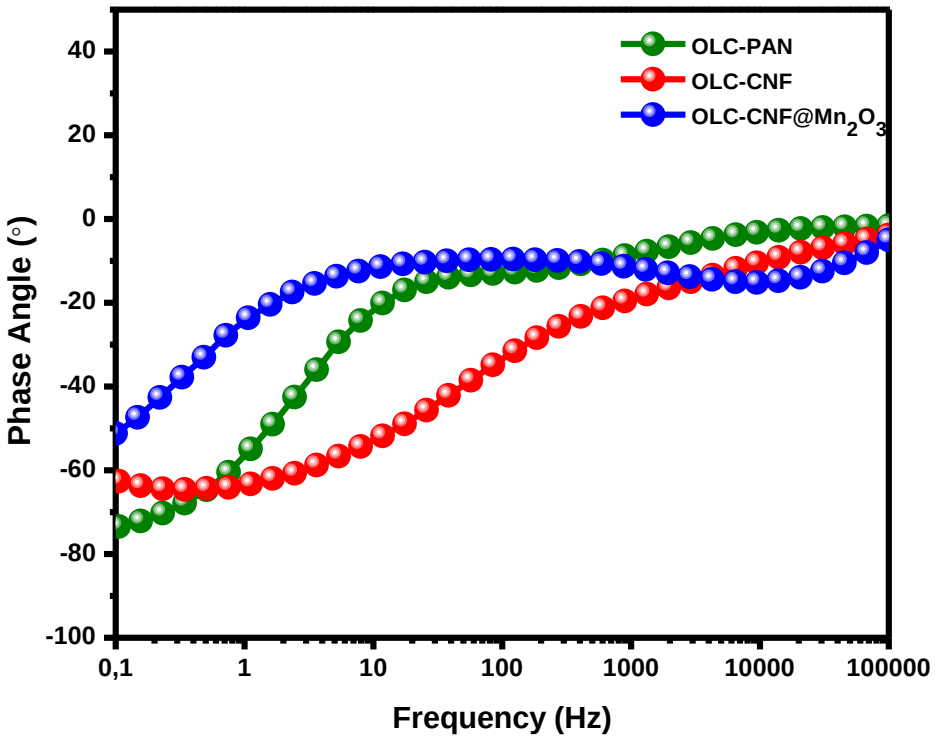

Figure 4.29 Comparative Bode plots for OLC-PAN, OLC-CNF, and OLC-CNF@Mn_2O_3 composites.

The maximum specific capacitance measured in this study was 40.36 F g^{-1} and 10.75 F g^{-1} for the OLC-CNF and OLC-PAN fibres, respectively. Unfortunately, these are not sufficient for supercapacitors applications. Hence, the development of state-of-the-art OLC-CNF@Mn_2O_3 electrodes was key to achieving greater capacitance values. The Mn_2O_3 serves as an active site for redox reactions and thus accelerates the kinetics of surface reactions which enhances the capacitance. Consequently, a specific capacitance of 200 F g^{-1} at 1 A g^{-1} was achieved as shown in figure 4.30a in a two-electrode symmetrical system in 1M Na_2SO_4 electrolyte solution. Figure 4.30b shows the Ragone plot for the OLC-CNF@Mn_2O_3 electrodes. According to this diagram, there is a direct correlation between specific power density and current density, whilst for specific energy density the inverse is true. OLC-CNF@Mn_2O_3 electrodes exhibit a specific energy density and power density of 44.63 Wh kg^{-1} and 3 235 kW kg^{-1}, respectively.

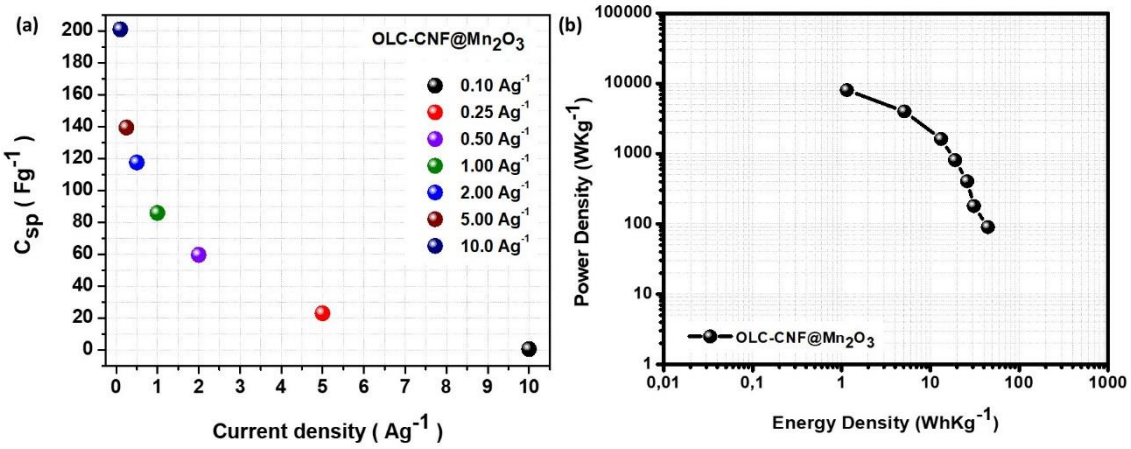

Figure 4.30 (a) Specific capacitance vs current density and (b) Ragone plot for OLC-CNF@Mn_2O_3 electrodes.

The long-term stability of the electrochemical performance of the OLC-CNF@Mn_2O_3 composite was investigated at 1 A g^{-1} for 10 000 cycles. In the beginning of the cycle, the specific capacitance was 80 F g^{-1} and by the 1000th cycle it had increased to 82 F g^{-1} and finally reduced to 81.2 Fg^{-1} at the 10 000th cycle (figure 4.31). The low capacitance values at the start of the cycling is attributed to the fact that the electrolyte ions had not diffused into the pores of the electrodes for charge accumulation. However, as the cycles progressed the surface area became accessible for electrolyte ions and the insertion of Na^+ ions in the Mn_2O_3 with various possible oxidation state enhanced the overall capacitance retention of by approximately 102 %.

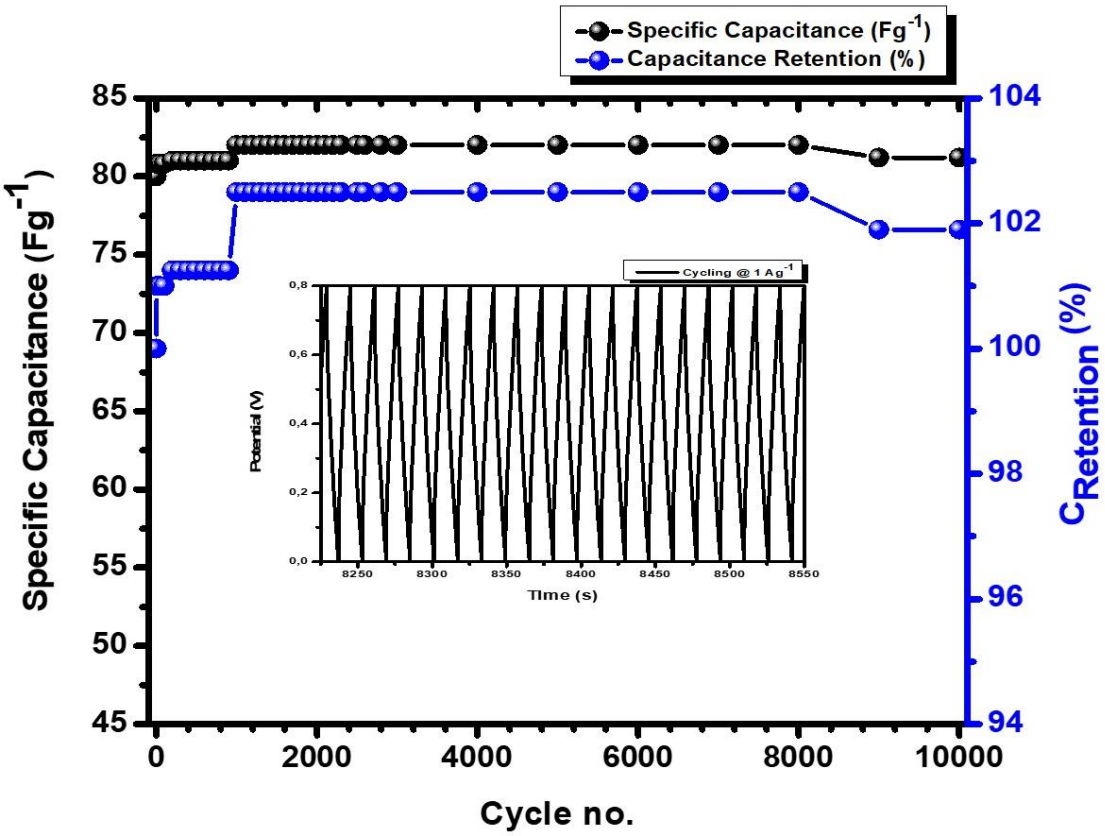

Figure 4.31 Cycling stability study showing specific capacitance and capacitance retention for 10 000 cycles for the OLC-CNF@Mn_2O_3 composite on a two-electrode system.

A typical demonstration for supercapacitor electrode capabilities in research, is to power an LED that provides a highly efficient and quickly rechargeable safety lights. Figure 4.32(a) shows the GCD curve of three cells connected in series as shown by figure 4.32(b). The overall potential window was 3.6 V and the applied current density was 1 A g^{-1}. The representative circuit for the application of OLC-CNF@Mn_2O_3 electrodes is displayed by figure 4.32(c).

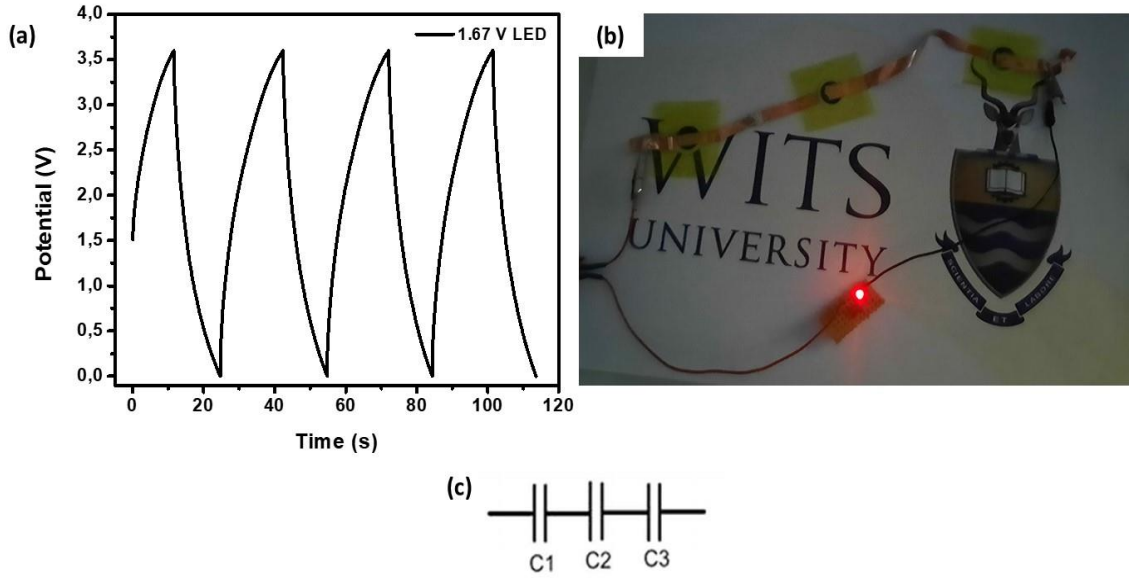

Figure 4.32 (a) Charge-discharge profiles of OLC-CNF@Mn_2O_3 composite electrodes giving 3.6 V, (b) a photograph of electrodes lighting up a 1.67 V LED at a 0° bending angle and (c) electrical circuit representative of the electrodes connected in series.

4.3 Conclusions

Thermally treated OLC-CNF had a higher degree of carbon ordering, high specific capacitance, better conductivity and higher electrochemical stability than their OLC-PAN counterparts. The electrochemical behaviour of OLC-CNF can be ascribed to a higher degree of carbon ordering leading to a more graphitic and electronically conductive electrode material.

In conclusion, the preparation of the OLC-CNF@Mn_2O_3 composite was relatively simple and inexpensive. The OLC-CNF@Mn_2O_3 composites showed an increase in surface area to approximately 129 m^2/g compared to its OLC-CNF counterpart due to the inclusion of Mn_2O_3 nanoparticles, which increased the accessibility of the active material to electrolyte ion diffusion. The specific capacitance, energy and power density of OLC-CNF@Mn_2O_3 composite electrodes were 200 F g^{-1}, 1.63 Wh kg^{-1} and 3 235 W kg^{-1}, respectively. Electrochemical stability of the electrodes was verified through a cycling test which demonstrated 102% capacitance retention after 10 000 cycles. This composite had remarkable differences in terms of its surface area and functional groups, which are reflected by the electrochemical properties. This composite did not, as had been initially expected, yield energy density values comparable to batteries.

4.4 References

[1] Krishan, O.; Suhag, S. An updated review of energy storage systems: Classification and applications in distributed generation power systems incorporating renewable energy resources. *Int. J. Energy Res.* **2018**, 15, 1-40.

[2] Gu, J.; Fan, X.; Liu, X.; Li, S.; Wang, Z.; Tang, S.; Yuan, D. Mesoporous manganese oxide with large specific surface area for high-performance asymmetric supercapacitor with enhanced cycling stability. *Chem. Eng. Sci*., **2017**, 324, 35-43.

[3] Toupin, M.; Brousse, T.; Bèlanger, D. Charge storage mechanism of MnO2 electrode used in aqueous electrochemical capacitor. *Chem. Mater*., **2004**, 16, 3184-3190.

[4] Wei, W.; Cui, X.; Chen, W.; Ivey, D. G. Manganese oxide-based materials as electrochemical supercapacitor electrodes. *Chem. Soc. Rev*., **2011**, 40, 1697-1721.

[5] Zhang, G.; Ren, L.; Yan, Z.; Kang, L.; Lei, Z.; Xu, H.; Shi, F.; Liu, Z-H. Mesoporous-assembled MnO_2 with large specific surface area. *J. Mater. Chem. A*., **2015**, 3, 14567-14572.

[6] Zhao, Y.; Ran, W.; He, J.; Huang, Y.; Liu, Z.; Liu, W.; Tang, Y.; Zhang, L.; Gao, D.; Gao, F. High-performance asymmetric supercapacitors based on multilayer MnO_2/graphene oxide nanoflakes and hierarchical porous carbon with enhanced cycling stability. *Small*., **2015**, 11, 1310-1319.

[7] Gallaway, J. W.; Hertzberg B. J.; Zhong Z.; Croft, M.; Turney, D. E.; Yadav, G. G.; Steingart, D. A.; Erdonmez, C. K.; Banerjee, S. Operando identification of the point of $[Mn_2]O_4$ spinel formation during γ-MnO_2 discharge within batteries. *J. Power Sources.* **2016**, 321, 135-142.

[8] Zhang, S. W.; Chen, G. Z. Manganese oxide based materials for supercapacitors. *Energy Materials.* **2008**, 3, 186-200.

[9] Wayu, M. Manganese oxide carbon-based nanocomposite in energy storage applications. *Solids*. **2021**, 2, 232-248.

[10] Xu, C.; Kang, F.; Li, B.; Du, H. Recent progress on manganese dioxide based supercapacitors. *J. Mater. Res*. **2011**, 25, 1421-1432.

[11] Amade, R.; Muyshegyan-Avetisyan, A.; González, J. M.; del Pino, A. P; Gyorgy, E.; Pascual, E.; Andujar, J. L.; Serra, E. B. Super-capacitive performance of manganese dioxide/graphene nano-walls electrodes deposited on stainless steel current collectors. *Materials*. **2019**, 12, 483-495.

[12] Raymundo-Piñero, E.; Khomenko, V.; Frackowiak, E.; Béguin, F. Performance of manganese oxide/CNTs composites as electrode materials for electrochemical capacitors. *J. Electrochem. Soc.* **2005**, 152, A229-A235.

[13] Lee, C. Y.; Tsai, H. M.; Chuang H. J.; Li, S. Y.; Lin, P.; Tseng, T. Y. Characteristics and electrochemical performance of supercapacitors with manganese oxide-carbon nanotube nanocomposite electrodes. *J. Electrochem. Soc.* **2005**, 152, A716-A720.

[14] Zeiger, M.; Jäckel, N.; Mochalin, V. N.; Presser, V. Review: carbon onions for electrochemical energy storage. *J. Mater. Chem.* **2016**, 4, 3172-3196.

[15] Zheng, Z.; Su, Q.; Zhang, Q.; Ye, H.; Wang, Z. Onion-like carbon microspheres as long-life anodes materials for Na-ion batteries. *J. Mater. Sci.* **2018**, 53, 12421-12431.

[16] Makgopa, K.; Ejikeme, P. M.; Jafta, C. J.; Raju, K.; Zeiger, M.; Presser, V.; Ozoemena, K. I. A high-rate aqueous symmetric pseudocapacitor based on highly graphitized onion-like carbon/birnessite-type manganese oxide nanohybrids. *J. Mater. Chem. A.* **2015**, 3, 3480-3490.

[17] Zeiger, M.; Jäckel, M.; Aslan, M.; Understanding structure and porosity of nanodiamond-derived carbon onions. *Carbon*. **2015**, 84, 584-598.

[18] Mao, X.; Hatton, T.; Rutledge, G. A review of electrospun carbon fibres as electrode materials for energy storage. *Curr. Org. Chem.* **2013**, 17, 1390-1401.

[19] Abouali, S.; Akbari, M.; Zhang, B.; Xu, Z-L.; Heidari, E. K.; Haung, J-Q.; Haung, J.; Kim, J-K. Electrospun carbon nanofibres with in situ encapsulated Co_3O_4 nanoparticles as electrodes for high performance supercapacitors. *ACS Appl. Mater. Interfaces.* **2015**, 7, 13503-13511.

[20] Zhi, M.; Manivannan, A.; Meng, F.; Wu, N. Highly conductive electrospun carbon nanofibres/MnO_2 coaxial nano-cables for high energy and power density supercapacitors. *J. Power Sources*, **2012**, 208, 345-353.

[21] Mao, X.; Hatton, T.; Rutledge, G. A review of electrospun carbon fibres as electrode materials for energy storage. *Curr. Org. Chem.* **2013**, 17, 1390-1401.

[22] Weingarth, D.; Zeiger, M.; Jackel, N.; Aslan, M.; Feng, G.; Presser, V. Graphitization as a universal tool to tailor the potential-dependent capacitance of carbon supercapacitors. *Adv. Energy Mater.* **2014**, 4, 1400316.

[23] Makgopa, K.; Ejekeme, P. M.; Jafta, C. J.; Raju, K.; Zeiger, V. P.; Ozoemena, K. I. A high rate aqueous symmetric pseudocapacitor based on highly graphitized onion-like carbon/birnessite-type manganese oxide nanohybrids. *J. Mater. Chem. A.* **2015**, 3, 3480-3490.

[24] Cavaliere, S.; Subianto, S.; Savych, I.; Jones, D. J.; Rozière, J. Electrospinning: designed architectures for energy conversion and storage devices, *Energy Environ. Sci.* **2011**, 4, 4761-4785.

[25] Wei, M.; Kang, B.; Sung, C.; Mead, J. Core-sheath structure in electrospun nanofibres from polymer blends. *Macromol. Mater. Eng*. **2006**, 291, 1307-1314.

[26] Naeem, R.; Mansoor, M. A.; Munawar, K.; Adnan, A.; Zaharinie, T.; Zubir, M. N. M. Versatile Fabrication of Binary Composite SnO_2-Mn_2O_3 Thin Films by AACVD for Synergistic Photocatalytic Effect. *J. Electron. Mater*. **2021**, 50, 3897-3906.

[27] Mykhailiv, O.; Zubyk, H.; Brzezinski, K.; Gras, M.; Lota, G.; Gniadek, M.; Romero, E. L.; Plonska-Brzenzinska, M. E. Improvement of the structural and chemical properties of carbon nano-onions for electrocatalysis. *Chem. Nano. Mat*. **2017**, 3, 583-590.

[28] Beams, R.; Cancado, L. G.; Novotny, L. Raman characterization of defects and dopants in graphene. *J. Condens. Matter Phys.* **2015**, 27, 083002-083027.

[29] Bhalerao, G. M.; Singh, M. K.; Sinha, A. K.; Ghosh, H. Optical redshift in the Raman scattering spectra of Fe-doped multiwalled carbon nanotubes: Experiment and theory. *Phys. Rev. B.* **2012**, 86, 1254191-1254196.

[30] Van Aken, K. L.; Maleski, K.; Mathis, T. S.; Breslin, J. P.; Gogotsi, Y. Processing of onion-like carbon for electrochemical capacitors. *ECS J. Solid State Sci. Technol.* **2017**, 6, M3103-M3108.

[31] Jang, W.; Jeon, D-Y.; Lee, Y-S.; Koo, H. Y. Effect of potassium ions on the formation of mixed-valence manganese oxide/graphene nanocomposites. *Materials*. **2019**, 12, 1245.

[32] Ameen, S. Vertically arranged Mn_2O_3 nanosheets as smart sensing electrode for highly sensitive N-hydroxysuccinimide. *Microchem. J*. **2021**, 163, 105912.

[33] Li, C.; Zhang, X-Q.; Zhang, B.; Zou, S-R.; Hu, N.; Sun, D-W.; Lei, C-X. Facile synthesis of porous Mn_2O_3/TiO_2 microspheres as anode materials for lithium-ion batteries with enhanced electrochemical performance. Qian-Zhi Gou, *J. Mater. Sci. Mater. Electron*. **2018**, 29, 16064-16073.

[34] Chen, X. Q.; Lin, H. B.; Zheng, X. W.; Cai, X.; Xia, P.; Zhu, Y. M.; Li, X. P.; Li, W. S. Fabrication of core-shell porous nanocubic $Mn_2O_3@TiO_2$ as high-performance anode for Lithium Ion Battery. *J. Mater. Chem. A*. **2015**, 3, 18198-18206.

[35] Zhu, J.; Chen, C.; Lu, Y.; Ge, Y.; Jiang, H.; Fu, K.; Zhang, X. Nitrogen-doped carbon nanofibres derived from polyacrylonitrile for use as anode material in sodium-ion batteries. *Carbon*. **2015**, 94, 189-195.

[36] Hong, K-L.; Qie, L.; Zeng, R.; Yi, Z-Q.; Zhang, W.; Wang, D.; Yin, W.; Wu, C.; Fan, Q-J.; Zhang, W-X.; Huang, Y-H. Biomass derived hard carbon used as a high-performance anode material for sodium ion batteries. *J. Mater. Chem. A*. **2014**, 2, 12733-12738.

[37] Wu, G.; Nelson, M.; Ma, S.; Meng, H.; Cui, G.; Shen, P. K. Synthesis of nitrogen-doped onion-like carbon and its use in carbon-based CoFe binary non-precious-metal catalysts for oxygen-reduction. *Carbon*. **2011**, 49, 3972-3982.

[38] Pech, D.; Brunet, M.; Durou, H.; Huang, P.; Mochalin, V.; Gogotsi, Y.; Taberna, P.; Simon, P. Ultrahigh-power micrometre-sized supercapacitors based on onion-like carbon. *Nat. Nanotechnol.* **2010**, 5, 651-654.

[39] Kovalenko, I.; Bucknall, D. G.; Yushin, G. Detonation nanodiamond and onion-like-carbon-embedded polyaniline for supercapacitors. *Adv. Funct. Mater.* **2010**, 20, 3979-3986.

[40] Bushueva, E. G.; Galkin, P. S.; Okotrub, A.; Bulusheva, L.; Gavrilov, N.; Kuznetsov, V. L.; Moiseekov, S. I. Double layer supercapacitor properties of onion-like carbon materials. *Phys. Status Solidi B.* **2008**, 245, 2296-2299.

[41] Portet, C.; Yushin, G.; Gogotsi, Y. Electrochemical performance of carbon onions, nanodiamonds, carbon black and multiwalled nanotubes in electrical double layer capacitors. *Carbon*. **2007**, 45, 2511-2518.

[42] Gao, Y.; Zhou, Y. S.; Qian, M.; He, X. N.; Redepenning, J.; Goodman, P.; Li, H. M.; Jiang, L.; Lu, Y. F. Chemical activation of carbon nano-onions for high-rate supercapacitor electrodes. *Carbon*. **2013**, 51, 52-58.

[43] Wang, Y.; Yu, S. F.; Sun, C. Y.; Zhu, T.; Yang, H. MnO_2/onion-like carbon nanocomposites for pseudocapacitors. *J. Mater. Chem.* **2012**, 22, 17584-17588.

[44] Azhagan, M. V. K.; Vaishampayan, M. V.; Shelke, M. V. Synthesis and electrochemistry of pseudocapacitive multilayer fullerenes and MnO_2 nanocomposites, *J. Mater. Chem. A*, **2014**, 2, 2152-2159.

[45] Borgohain, R.; Li, J.; Selegue, J. P.; Cheng, Y. T. Electrochemical Study of Functionalized Carbon Nano-Onions for High-Performance Supercapacitor Electrodes. *J. Phys. Chem. C.* **2012**, 116, 1506-15075.

[46] Zhi, M.; Manivannan, A.; Meng, F.; Wu, N. Highly conductive electrospun carbon nanofibre/MnO_2 coaxial nano-cables for high energy and power density supercapacitors. *J. Power Sources.* **2012**, 208, 345-353.

CHAPTER FIVE

Nanostructured MoS_2@Mn_2O_3 embedded onto OLC-CNF composites as hybrid supercapacitor electrode materials

5.1 Introduction

Energy density is an inherent problem for carbon-based supercapacitors, thus systems based on metals are fundamental for the commercialization of this technology. [1-3] MoS_2 are increasingly used as electrode materials in energy storage applications, due to the great boost of specific capacitance resulting from its unique properties. [3-6] MoS_2 offers an advantage of storing energy using the highly accessible high surface area for charge accumulation needed in electrical double-layer capacitors and redox properties via intercalation of ions into MoS_2 layers at the interface accompanied by faradaic charge-transfer reactions of pseudocapacitors. The layered structure increases the specific surface area for the electrolyte ions, while simultaneously decreasing the electron transfer and ion diffusion paths, which ultimately leads to better power performance. A specific capacitance of ~ 230 F g^{-1} can be obtained with MoS_2 and such high values are pivotal for power sources in portable electronics and electric vehicles. [7]

The main concern with MoS_2 based electrode materials has been its poor electronic conductivity and cycling stability. [8-10] To tackle these deficiencies, nanostructured MoS_2 have been synthesized to minimize the strain upon cycling. In our previous study, MoS_2 sheets were synthesized on carbon nanosheres (CNS). [11] The combination of MoS_2 with a highly conductive material (such as R-Gr, CNT, C, etc.) has shown diverse functionality via synergistic effects. [12-18] However, the excessive amounts of carbon composition present difficulties through the following mechanisms, (i) the diffusion process, (ii) the loading of MoS_2, and (iii) confines the entry sites of the active material. [19] Consequently, with this study, an electroactive species namely, manganese (III) oxide (Mn_2O_3) was integrated in between MoS_2 sheets as a strategy for efficient electrochemical kinetics. It was expected that a three-dimensional pathway of nanosized Mn_2O_3, enables efficient electrolyte ion diffusion in the structure to ensure high capacitance values.

For this study, the electrospun fibres produced in chapter four were thermally treated and subject to a hydrothermal treatment reaction for the MoS_2 sheet growth on the surface of the fibres. Subsequently, the dispersion of the fibres in a $KMnO_4$ solution resulted in a composite electrode material ideal for enhanced energy storage capabilities. The fibres were encapsulated with MoS_2 sheets and embedded with the Mn_2O_3 nanoparticles resulting in the composite material OLC-CNF/MoS_2@Mn_2O_3. Figure 5.1 illustrates the synthesis schematic of how the fiber composite material was made.

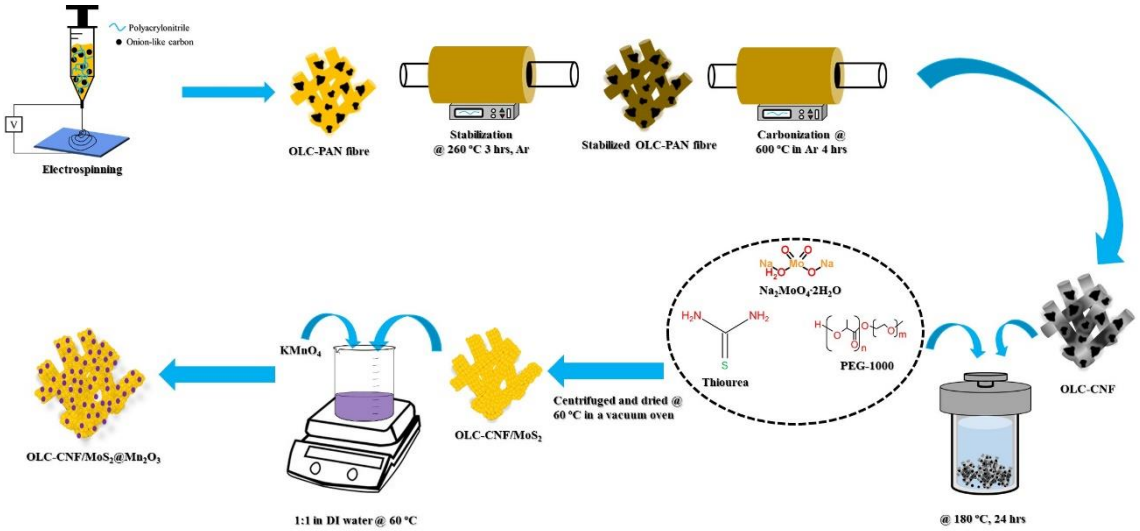

Figure 5.1 Schematic for synthesis of OLC-CNF/MoS_2@Mn_2O_3 composite electrode material.

5.2 Results and discussion

5.2.1 Material characterization

SEM and TEM micrographs of the electrospun OLC-PAN fibres are presented in chapter four after electrospinning in figure 4.4 (a) and (b). It was observed that the fibres had an irregular wrinkled surface with much thicker diameters (i.e. ~800 nm on average). The formation of OLC related beads on the PAN fibres could be related to the tendency of OLC to form agglomerated clusteres in the polymer solution which presents high resistance against the electrical force and thus enables stretching during electrospinning process.

The OLC-PAN fibres were subjected to a mulit-step heat treatment in an argon environment, first for stabilization followed by carbonization. The resulting composite's morphology, OLC-CNF morphology were shown in figure 4.4 (c) and (d) in chapter four.

It is clear that the fibre morphology was still maintained after heat treatment and the diameter of the fibre reduced significantly, indicating removal of residual polymer and evaporation of the carboxylic groups resulting in a highly porous structures. After thermal treatment the fibres were porous and more irregular in shape due to the openess around the OLC nanoparticles. This is also apparent on their TEM micrograph. The heat treated fibres were subjected to a hydrothermal treatment for MoS_2 sheet growth on the existing OLC-CNF matrix. The images in figure 5.2 (a) show an additional layer formation on the outer diameter of the fibres which signifies encapsulation by MoS_2 sheets on the original OLC-CNF matrix. The fibres were a nucleation site for MoS_2 sheets to originate and grow their typical hierarchical structure as shown by the high magnification image in figure 5.2 (b).

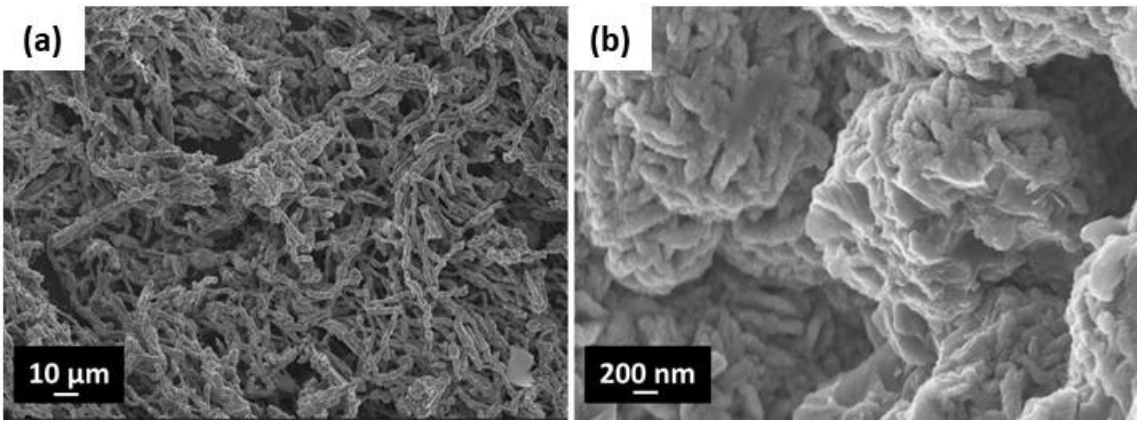

Figure 5.2 SEM images MoS_2 encapsulated OLC-CNFs; OLC-CNF/MoS_2 composite material at (a) low and (b) high magnifications.

Figure 5.3 shows the morphology exhibited by OLC-CNF/MoS_2 after the incorporation of Mn_2O_3 nanoparticles at various magnifications under SEM. The composite material displays a similar outer layer formation to that observed in the OLC-CNF@Mn_2O_3 material, suggesting succesful integration of Mn_2O_3 with MoS_2 encapsulated OLC-CNF. The final product was denoted as OLC-CNF/MoS_2@Mn_2O_3. The homogeneity distribution of the Mn_2O_3 is considered ideal for the robustness of the electrode material manufacturing. Furthermore, the 3D structural morphology of the fibres were retained as shown in figure 5.3. The average diameter of the final composite ranged between 600-800 nm according to the TEM images, which is lower than the diameter of the initial OLC-PAN counterpart.

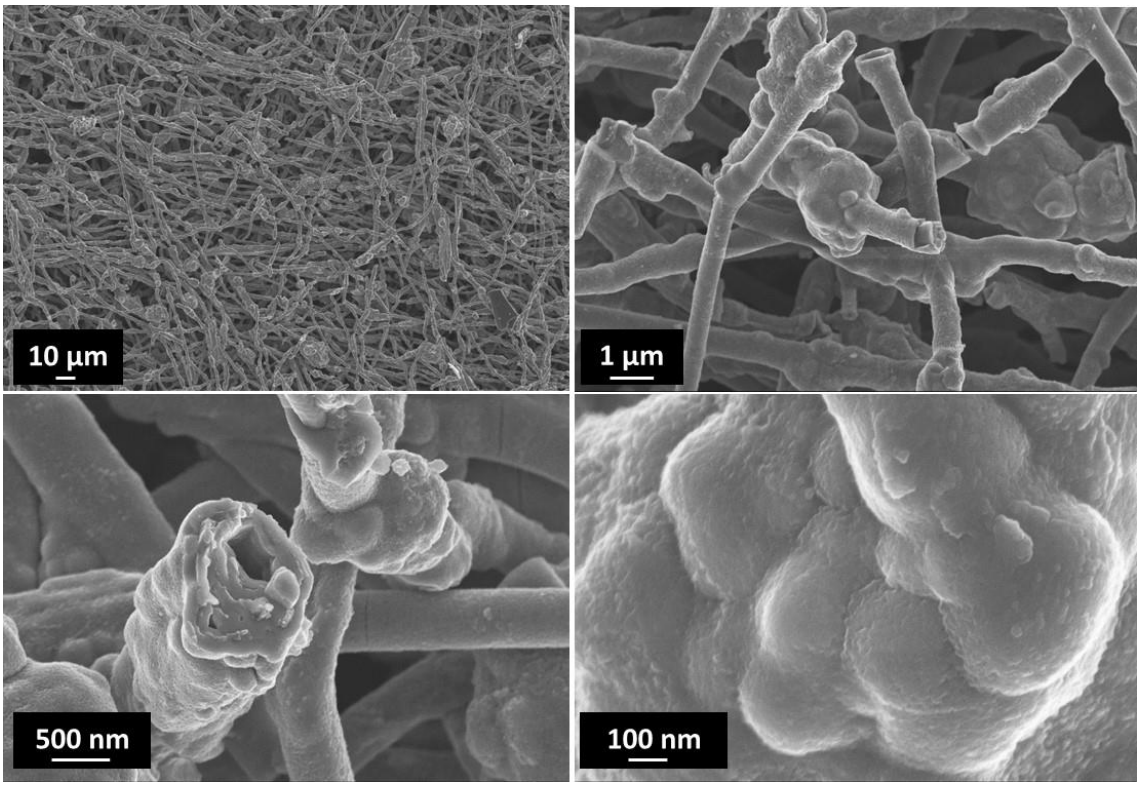

Figure 5.3 SEM images of Mn_2O_3 integrated with OLC-CNF/MoS_2; OLC-CNF/MoS_2@Mn_2O_3 composite at various magnifications.

The elemental analysis of the two main nanofibre composites namely, OLC-CNF/MoS_2; OLC-CNF/MoS_2@Mn_2O_3 were analyzed with EDS software under the SEM. Table 5.1 shows the summary of the main elements with their respective contents in weight % ratios. The data confirms the presence of Mo and S elements. Intuitively, the content ratios suggest a stoichiometry for MoS_2 that is $MoS_{1.75}$ for the OLC-CNF/MoS_2 composite and $MoS_{1.53}$ for the OLC-CNF/MoS_2@Mn_2O_3 composite. Both values are within the limits of errors and satisfactorily confirm the stoichiometry of the MoS_2. Mn was detected for the OLC-CNF/MoS_2@Mn_2O_3 composite, as expected after the incorporation of $KMNO_4$, suggesting successful synthesis of Mn_2O_3 and integration to the final composite. The observed stoichiometry for the composite was $MnO_{3.76}$. Other additional elements, N, Na and K were attributed to the starting precursors namely, $Na_2MoO_4{\cdot}2H_2O$ and $KMNO_4$. Whereas, Al originated from the sample holder. EDS spectra for OLC-CNF/MoS_2 and OLC-CNF/MoS_2@Mn_2O_3 are illustrated in figure 5.4 and 5.5, respectively.

Table 5.1 *Comparison of elemental composition between OLC-CNF/MoS_2 and OLC-CNF/MoS_2@Mn_2O_3 composite materials.*

	OLC-CNF/MoS_2		**OLC-CNF/MoS_2@Mn_2O_3**	
Element	**Wt.%**	σ	**Wt.%**	σ
O	41,5	0,4	35,8	0,2
S	32,6	0,3	31,5	0,1
Mo	18,6	0,2	20,5	0,3
N	5,4	0,3	NA	NA
Mn	NA	NA	9,4	0,1
K	NA	NA	2,6	0
Na	1,8	0	0.1	0
Al	0,1	0	0.1	0

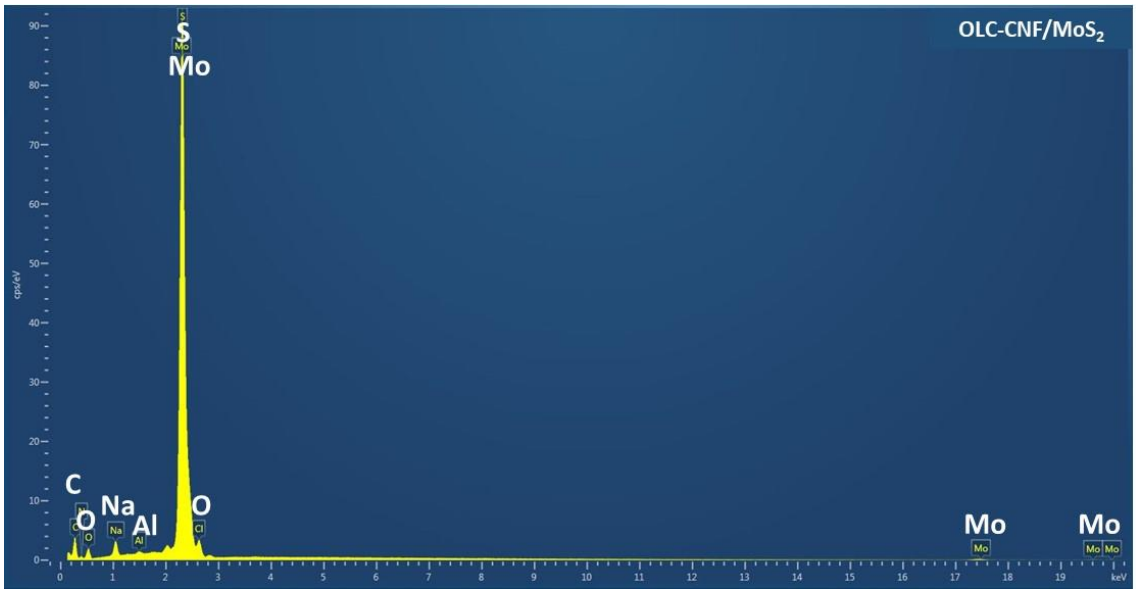

Figure 5.4 SEM-EDS spectra of OLC-CNF/MoS_2.

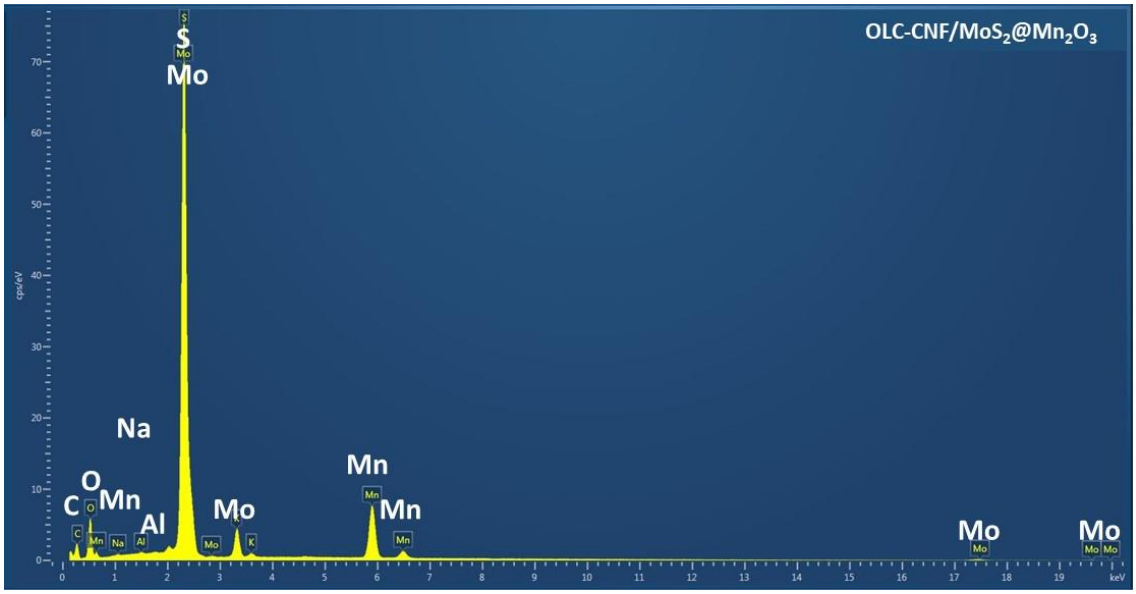

Figure 5.5 SEM-EDS spectra of OLC-CNF/MoS_2@Mn_2O_3.

HR-TEM analysis of OLC-CNF/MoS_2@Mn_2O_3 composites was completed and figure 5.6 confirms the integration of the OLC, MoS_2 with Mn_2O_3 components. According to figure 5.6 c, the composite consists mainly of MoS_2 patterns that display a hexagonal structural morphology, onion shaped OLC and Mn_2O_3 nanoflakes.

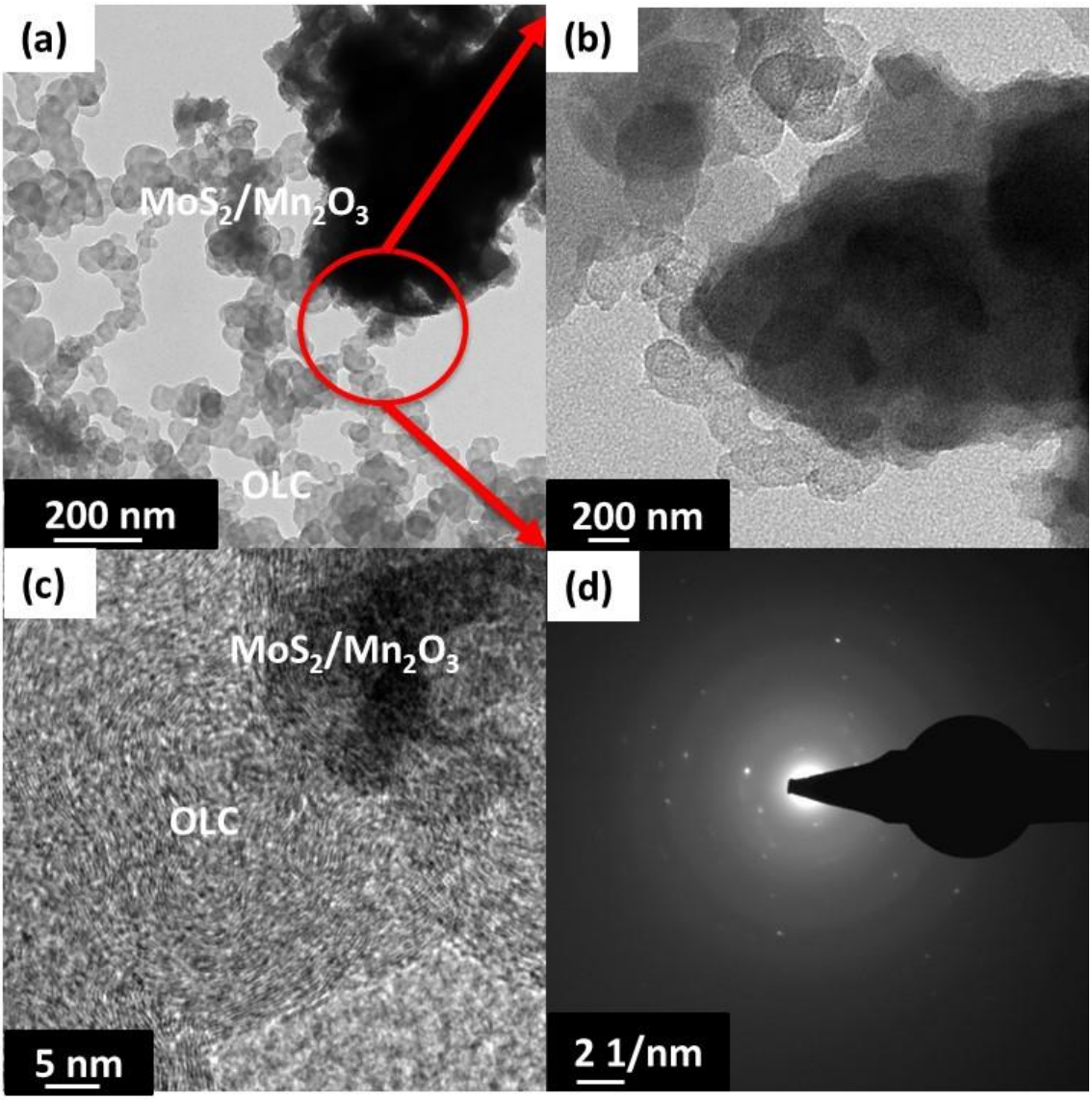

Figure 5.6 (a) HR-TEM images for the OLC-CNF/MoS_2@Mn_2O_3 fibre composite with selected area aperture marked with a red circle (b-c) higher magnification of selected area (d) radial intensity parallel and perpendicular to the fibre axis after background subtraction.

The crystalline structure of OLC-CNF/MoS_2 and OLC-CNF/MoS_2@Mn_2O_3 was further verified by XRD and the results are shown in figure 5.7. The MoS_2 in the OLC-CNF/MoS_2 fibre composite is a hexagonal crystal system with layered structures, a $R3m$ space group and a space group number that equates to 160. The cell parameter values were a (Å): 3.1600, b (Å): 3.1600, and c (Å): 18.4500. Whereas in the final composite, MoS_2 is a layered hexagonal crystal system with $R3$ crystal sysetm and 148 space group number. The cell parameters here were; a (Å): 9.2200, b (Å): 9.2200, and c (Å): 10.8310.

The increase in the cell parameters can be explained by Bragg's equation where $d = 0{,}5\lambda / \sin\theta$, which indicates that the lattice d spacing undergoes a distortion as a result of the intercalation of Mn^{3+} atoms into the spacing between the Mo-S layers. The XRD diffraction peaks for OLC-CNF/MoS_2 at 2θ equals 14.39, 33.06, 38.21, 41.03 47.88, 58.35 and 60.44, correspond well to (002) (101) (103) (015) (107) (110) and (113) planes, respectively and were attributed to amorphous MoS_2. [23-24] An additional peak at 2θ 27.25° was assigned to carbonecous (002) plane emerging from OLC and CNF in the fibre composite. These results confirmed the sucessful encapsulation of OLC-CNF fibres with MoS_2 sheets. It is also important to point out that during high temperature treatment, not all of the PAN fibre were accesible for carbonization due to the nature of the framework structure which prevented complete transformation, and thus some residual PAN could be detected through XRD in the final structure.

The amorphous and low intensity peak for the (002) plane in the OLC-CNF/MoS_2 nanofibre structural morphology, reflects the degree of ordered hexagonal MoS_2 sheets in comparison to (002) MoS_2 plane of OLC/MoS_2@Mn_2O_3 nanofibres. After incorporation of Mn_2O_3 nanoparticles the typical hexagonal diffraction peaks of MoS_2 were observed at 13.77, 30.72, 33.98, 34.96, 41.59, 43.24, 46.72, 52.71 and 61.02 ° 2θ corresponding to (002), (101) (103) (105) (223) (532) and (324) for OLC/MoS_2@Mn_2O_3. It is likely that the incorporation of Mn_2O_3 nanoparticles in between the MoS_2 sheets resulted in structural transformation from an amorphous nature to a more ordered hexagonal structure. The peaks at 19, 33, 38, 45, 55. 66 and 69 ° 2θ were assigned to (002), (222), (004), (233), (044) (226) and (444) Mn_2O_3. [26] These were in agreement with those of the cubic spinel manganese oxides. An amorphous carbonaceous peak were detected at 9.86, 19.79, 21.11 29.88 and 32.59 ° 2θ were attributed to the (002), (004), (221), (006) and (332) planes as a result of the combination of OLC and carbon fibre matrix. The addition of Mn_2O_3 nanoparticles positively contributed to the electrochemical performance of the electrodes given the interstitial sites that cause lattice distortion and subsequently influence band structure. These create new electronic states near the Fermi level and increase the quantum capacitance. [27]

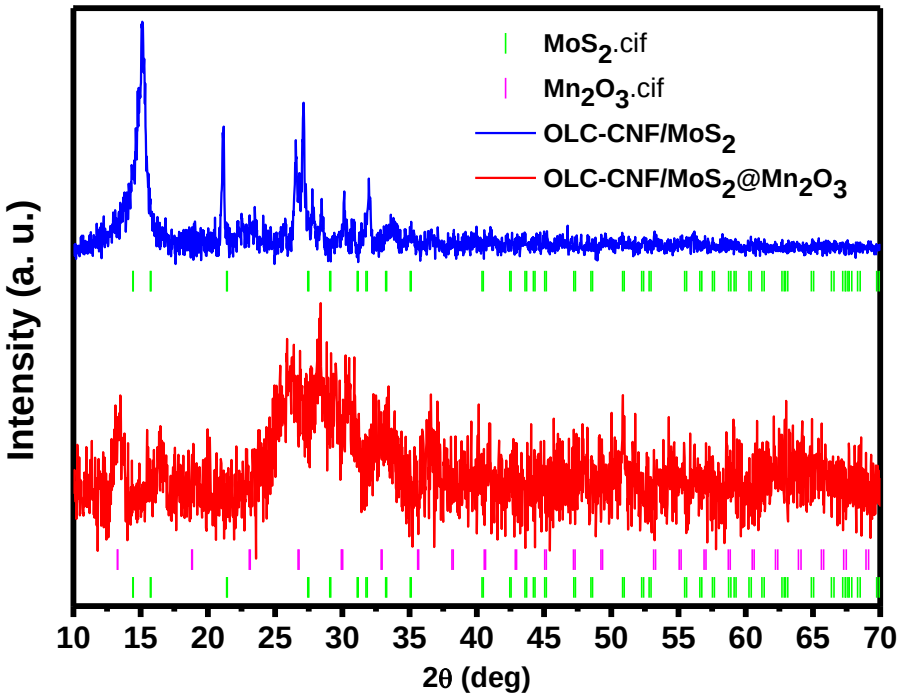

Figure 5.7 XRD spectra of OLC-CNF/MoS_2 vs. OLC-CNF/MoS_2@Mn_2O_3 nanofibre composite.

Figure 5.8 shows a comparison of the FT-IR spectra of the fibres with absorption peaks and their assignement. The vibrational bands were observed as follows, the band at 1114 cm^{-1} to $C-H$, 1646 $C=O$, 2105 cm^{-1} to $C-C$ stretching, 2330 cm^{-1} to $C\equiv N$, 2440 cm-1 to $O-H$ to 2659 cm^{-1} correspond to the CNFs and Mo-S, C-S at 797, 921 and finally OLC-CNF/MoS_2 at 605 cm^{-1}. [10] OLC-CNF/MoS_2@Mn_2O_3 composite showed similar bands as OLC-CNF/MoS_2 with the exception of an additional peak at 825 cm^{-1} corresponding to $Mn-O$ vibrations, suggesting succesful incorporation of Mn_2O_3 nanoparticles int the fibre matrix.

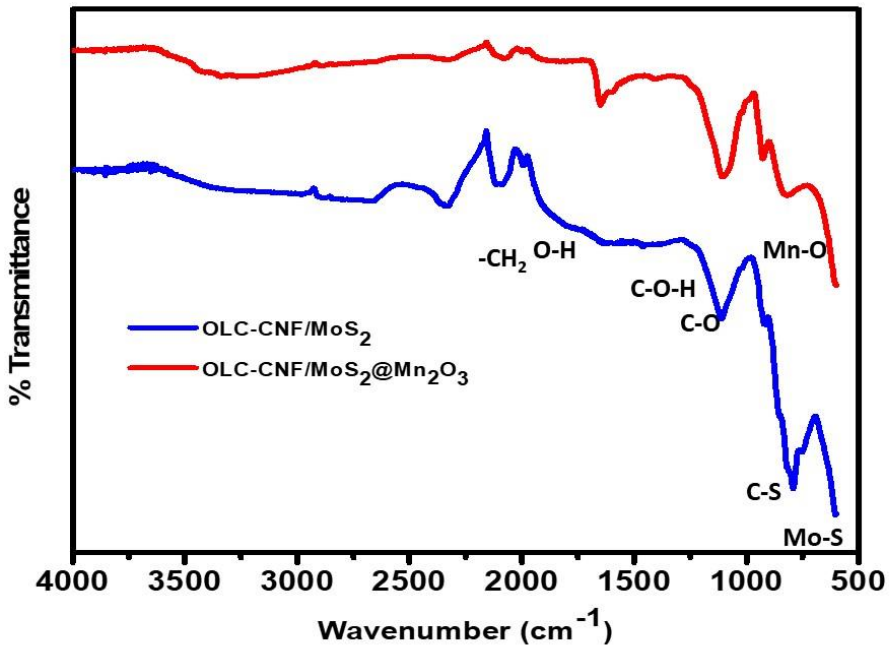

Figure 5.8 FT-IR spectra of OLC-CNF/MoS_2 vs. OLC-CNF/MoS_2@Mn_2O_3 composite materials.

Figure 5.9 shows the Raman scattering spectra for both OLC-CNF/MoS_2 and OLC-CNF/MoS_2@Mn_2O_3 samples. The Raman active modes corresponding to D and G bands of carbon structures and E_{2g}^1 (in-plane) and A_{1g}(out-of-plane) bands for MoS_2 vibrations were observed and their values summarized in table 4.2. Since Raman is a surface measurement technique and in this case most of the fibre surface were encapsulated with MoS_2 sheets during the hydrothermal process and further covered with Mn_2O_3 nanoparticles. The typical D and G intensity bands have dramatically reduced for the OLC-CNF/MoS_2@Mn_2O_3 composite. Whereas in the case of OLC-CNF/MoS_2 the bands have greater visibility and higher intensity. Nonetheless, this is an indication that the OLC-CNF were successfully encapsulated with MoS_2 and further decorated with Mn_2O_3 nanoparticles, in agreement with the observations from XRD and FT-IR analysis.

Table 5.2 *Comparison of Raman peaks for OLC-CNF/MoS_2 and OLC-CNF/MoS_2@Mn_2O_3.*

Electrode Material	D	G	I_D/I_G	E^1_{2g}	A_{1g}	$\lvert E^1_{2g} - A_{1g} \rvert$
OLC-CNF/MoS_2	1332.81	1592.82	1.63	402.35	425.71	23.36
OLC-CNF/MoS_2@Mn_2O_3	2692.27	2940.44	1.06	377.07	401.10	24.03

*D and G represent disordered carbon and G graphitic carbon, respectively.

*I_D/I_G represents the degree of graphitization.

*A_{1g} and E^1_{2g} represents in-plane and out-of-plane vibrations for bands for MoS_2 vibrations.

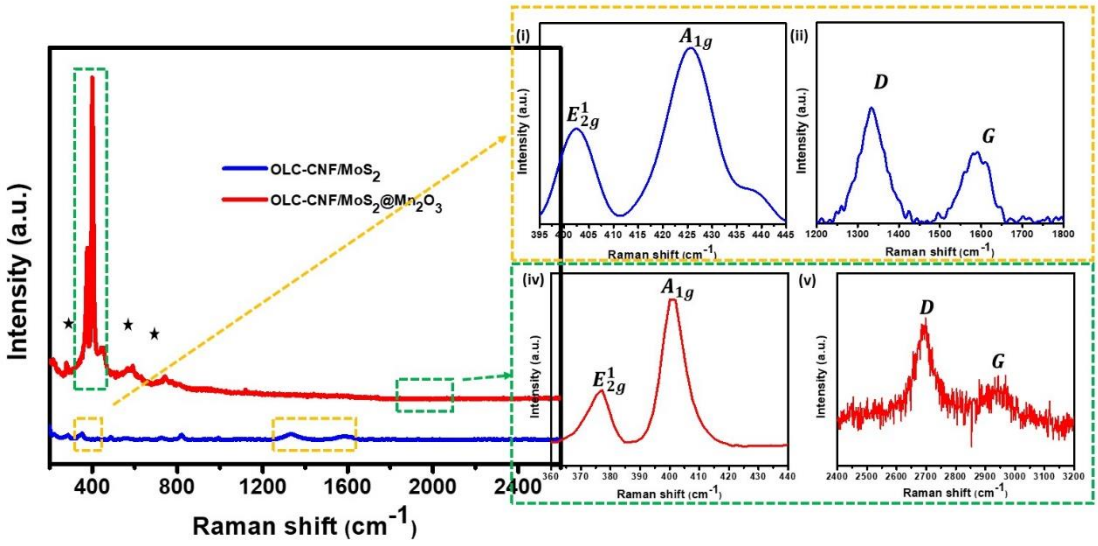

Figure 5.9 Raman spectra of OLC-CNF/MoS_2 and OLC-CNF/MoS_2@Mn_2O_3 with mangified views of E^1_{2g} and A_{1g} for MoS_2 and D and G bands for carbon.

XPS analysis was conducted on the OLC-CNF/MoS_2@Mn_2O_3 nanofibre composites to verify its chemical states and composition. Peaks for O 1s C 1s Mn 2p S2p K 2p Mo 3d and Na 1s were obtained as shown in figure 5.10 and their quantitative analysis shown in table 5.3. This data confirms the presence of Mn_2O_3 nanoparticles in MoS_2 encapsulated fibres and agrees with previous results from XRD, FT-IR and Raman. There are minor residual impurities of K and Na, from $KMnO_4$ and $Na_2MoO_4 \bullet 2H_2O$ precursors.

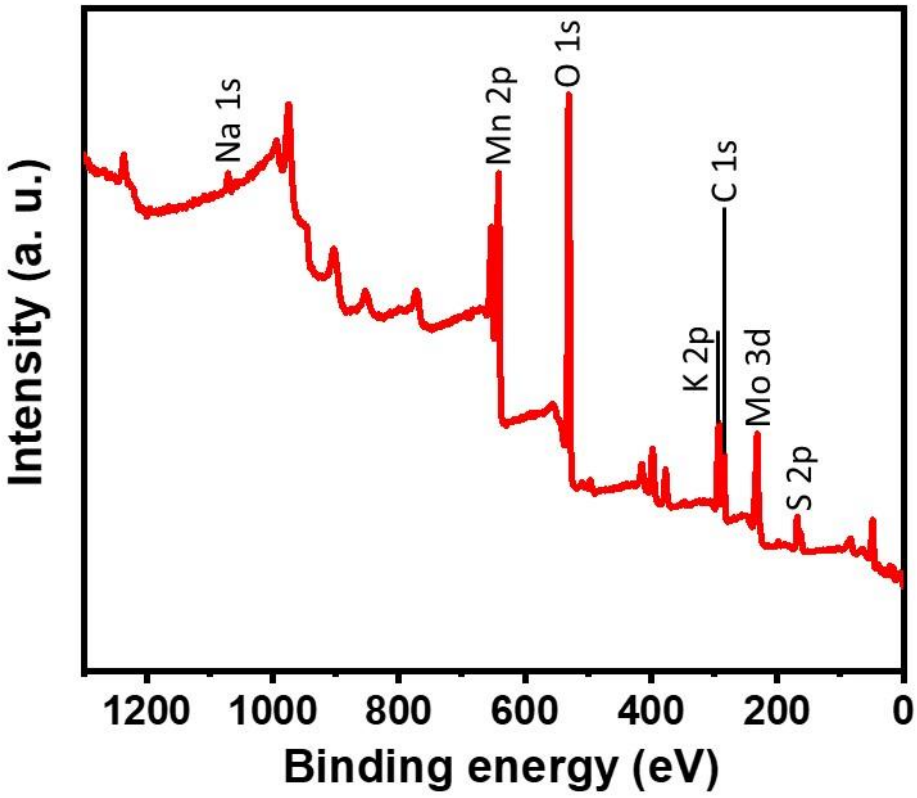

Figure 5.10 XPS Survey Scan spectra of OLC-CNF/MoS_2@Mn_2O_3 composite.

Table 5.3 *XPS data of OLC-CNF/MoS_2@Mn_2O_3 nanofibres.*

Name	Peak	Atomic conc [%]
O1s	530.7	52.3
C1s	284.7	14.4
Mn2p	642.1	13.0
S2p	168.3	8.3
K2p	293.1	6.7
Mo3d	232.2	4.4
Na1s	1071.2	0.8

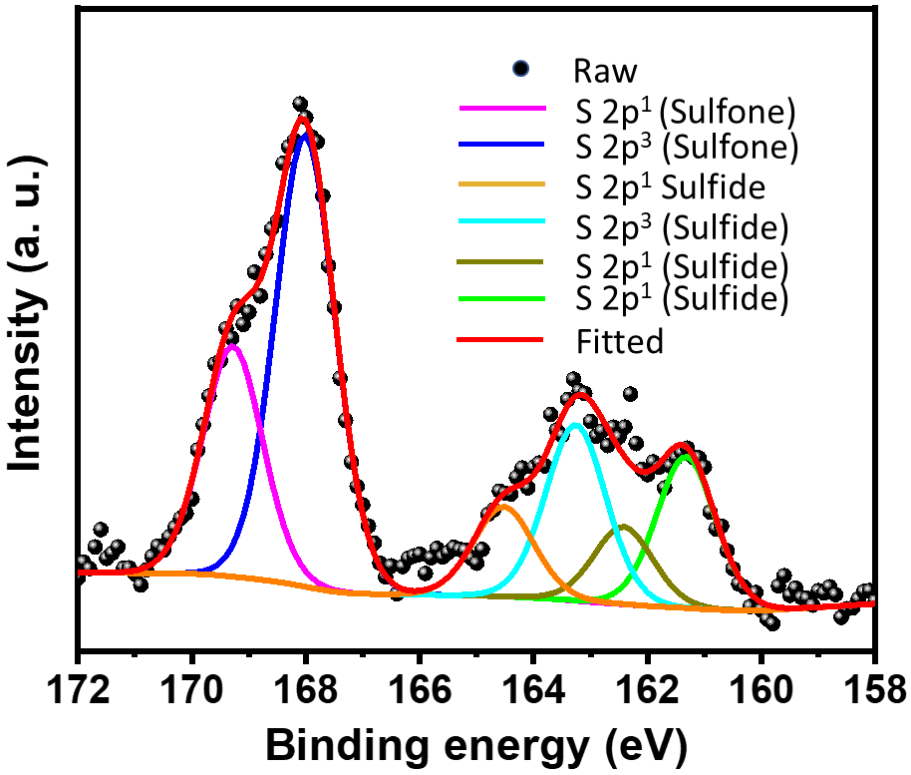

Figure 5.11 High resolution XPS spectra of S 2*p* core levels for OLC-CNF/MoS_2@Mn_2O_3.

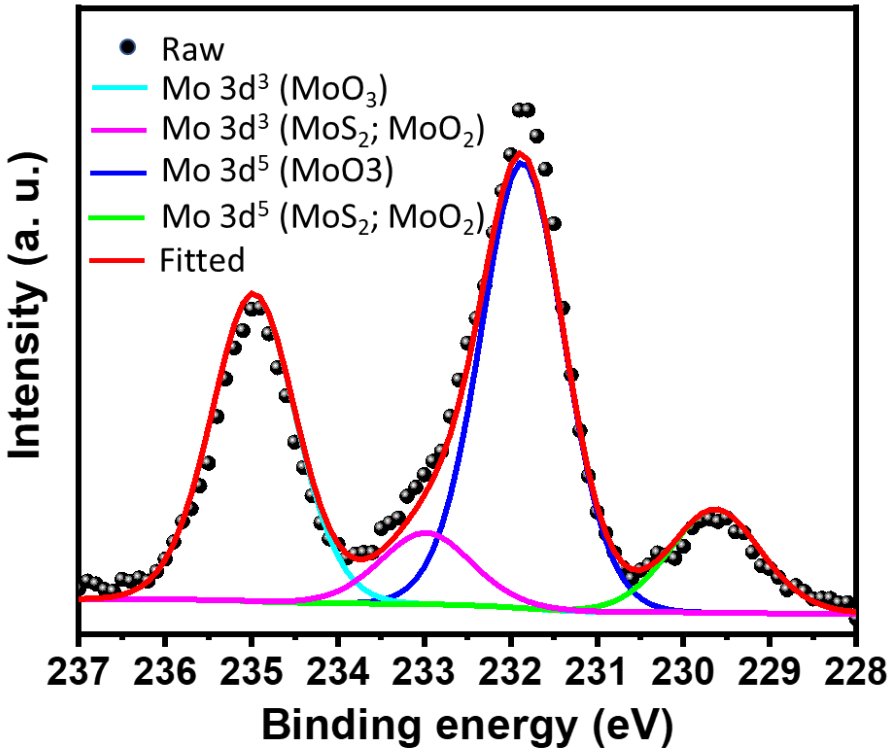

Figure 5.12 High resolution XPS spectra of Mo 3*d* core levels for OLC-CNF/MoS_2@Mn_2O_3.

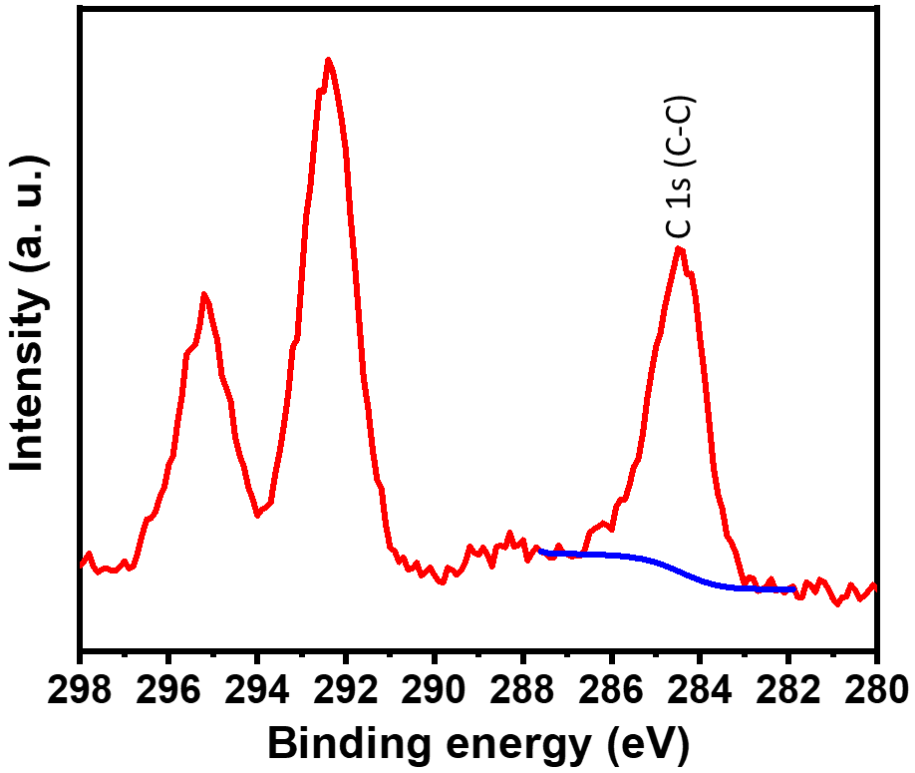

Figure 5.13 High resolution XPS spectra of C 1*s* core levels for OLC-CNF/MoS_2@Mn_2O_3.

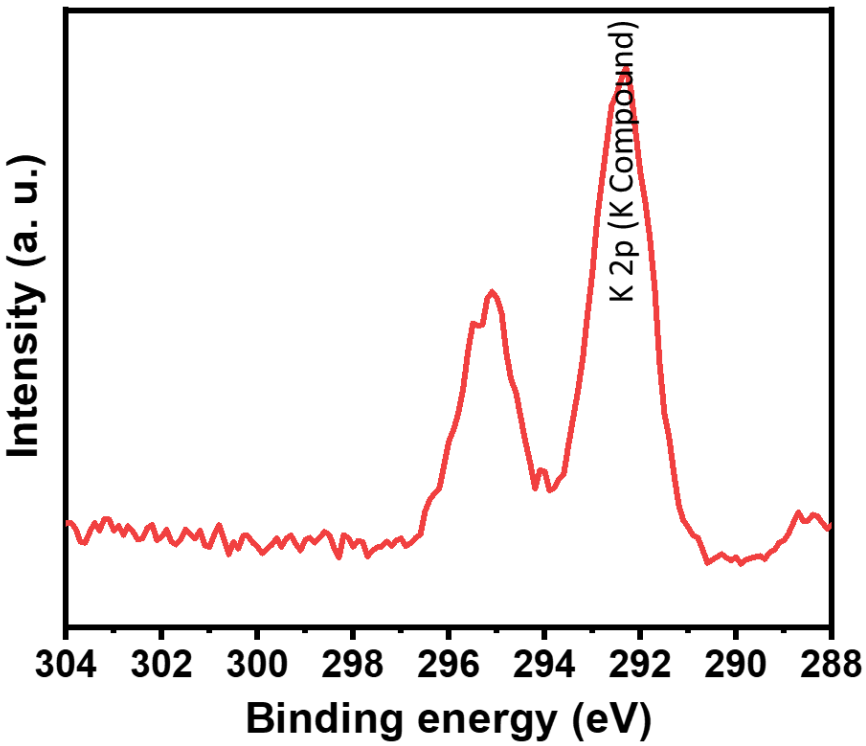

Figure 5.14 High resolution XPS spectra of K 2*p* core levels for OLC-CNF/MoS_2@Mn_2O_3.

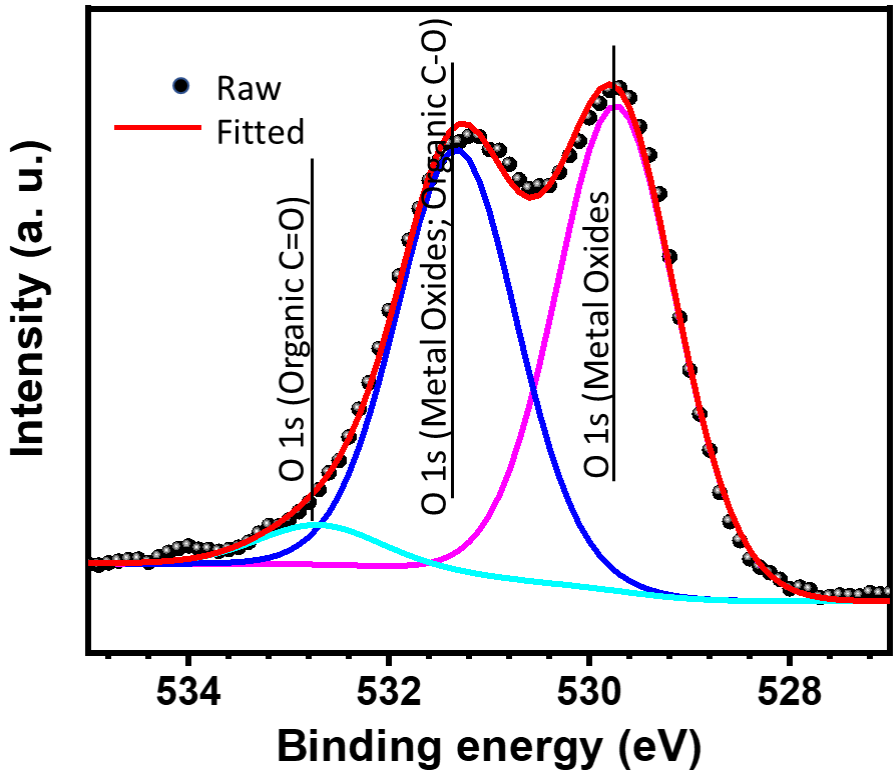

Figure 5.15 High resolution XPS spectra of O 1s core levels for OLC-CNF/MoS_2@Mn_2O_3.

As indicated in figure 5.16, the peaks at 653.7 eV and 641.6 eV were assigned to Mn 2p1/2 and Mn 2p3/2, respectively. The bonding energies at the Mn 2p1/2 and Mn 2p3/2 peaks agree well with the reported values of Mn_2O_3 in literature, indicating that manganese mainly exists in the Mn^{3+} in the OLC-CNF/MoS_2@Mn_2O_3 composite. [28-29] The energies positioned between Mn 2p3/2 and Mn 2p1/2 are displayed with binding energy separation of ~11.7 eV, and these values are well-matched with Mn_2O_3. [30]

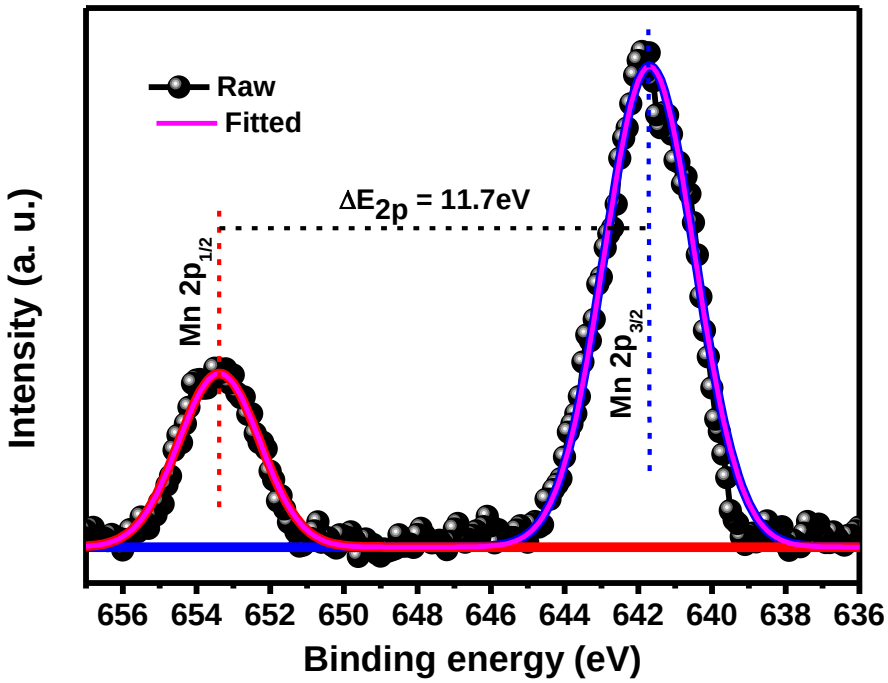

Figure 5.16 High resolution XPS spectra of Mn 2*p* core levels for OLC-CNF/MoS_2@Mn_2O_3.

Moreover, the fitted binding energies in figure 5.17 at ~83.3 eV and ~89 eV again confirm the origin of Mn3+ species in OLC-CNF/MoS_2@Mn_2O_3. [31] The ΔE_{3s} = 5.49 eV and based on the conventional linear equation (V_{Mn} = 7.875 − 0.893 ΔE_{3s}), the average oxidation state of Mn is 3.0. [32]

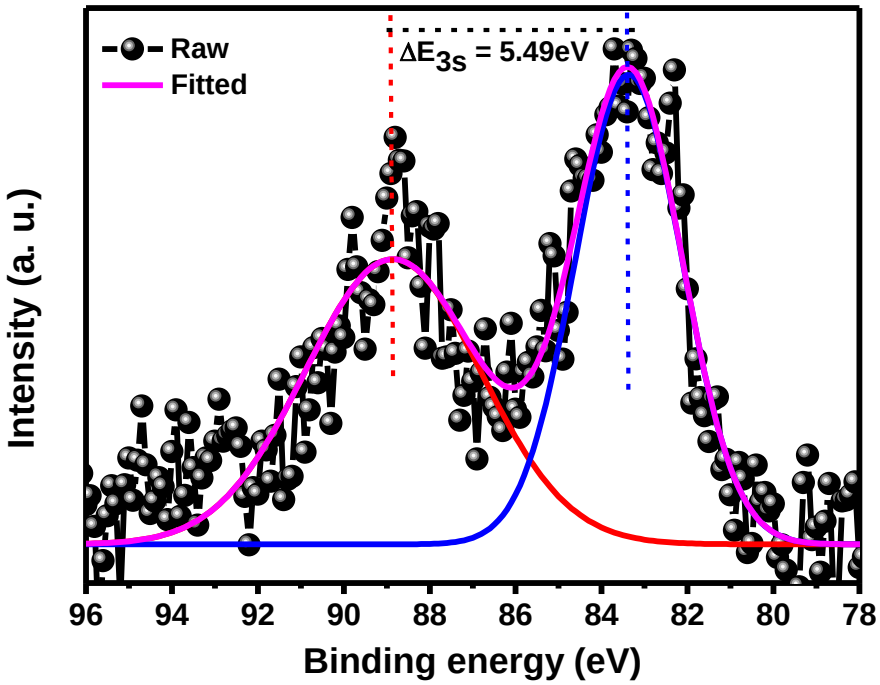

Figure 5.17 High resolution XPS spectra of Mn 3*s* core levels for OLC-CNF/MoS_2@Mn_2O_3.

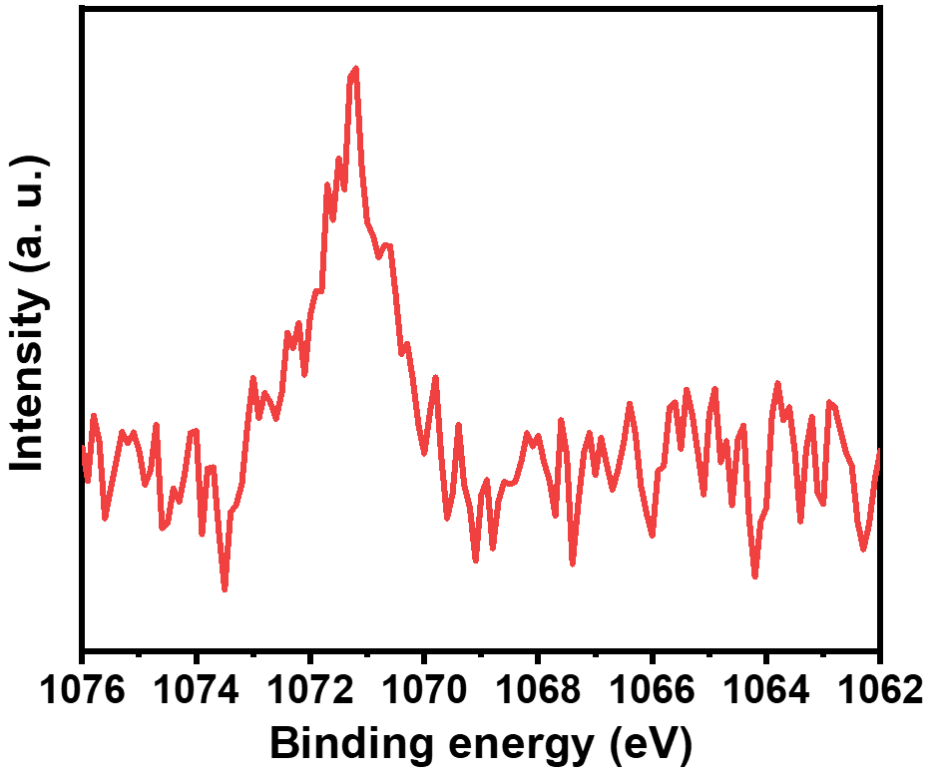

Figure 5.18 High resolution XPS spectra of Na 1*s* core levels for OLC-CNF/MoS_2@Mn_2O_3.

5.2.2 Electrochemical properties

Preliminary electrochemical study was performed in a three-electrode setup consisting of a 1 M Na_2SO_4 aqueous electrolyte solution. The examined working electrodes were OLC-CNF/MoS_2 and OLC-CNF/MoS_2@Mn_2O_3. It is worth noting that the CV curves of the two variants at 25 m Vs^{-1} are quite distinctive as shown in figure 5.19 a. Firstly, it was observed that the area of the curves varies slightly owing to a higher current response on the OLC-CNF/MoS_2@Mn_2O_3 composite. The difference is most probable due to higher surface area and the presence of the manganese oxide component in the OLC-CNF/MoS_2@Mn_2O_3 composite leading to a better overall capacitance than its counterpart. In the case of OLC-CNF/MoS_2, the voltammograms were more rectangular in shape and symmetrical resembling a typical EDLC shape which enables the high power characteristic in supercapacitors. Whereas, the OLC-CNF/MoS_2@Mn_2O_3 composite material electrodes showed a deviation from the typical rectangular CV response shape. The redox characteristic peaks visible at voltages, 0 V and -0.3 V, are an indication of pseudocapacitance behavior. The presence of an additional redox active material such as

Mn_2O_3 to an OLC-CNF/MoS_2 matrix, has seemingly enhanced the energy storage capabilities by displaying faradaic based mechanisms. The galvonostatic charge-discharge curves are shown in figure 5.19 b at similar current density as a comparison. OLC-CNF/MoS_2@Mn_2O_3 has longer charging and discharging times in comparison to OLC-CNF/MoS_2.

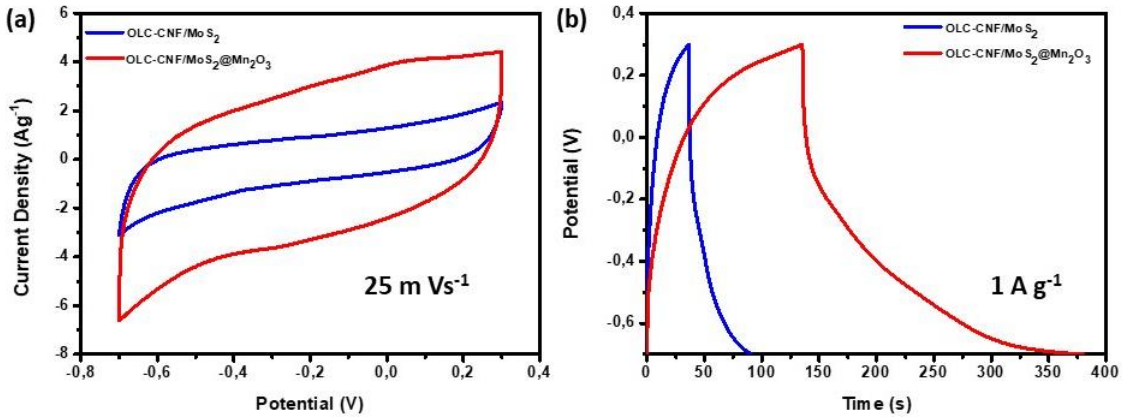

Figure 5.19 Comparative three-electrode results of OLC-CNF/MoS_2 in comparison to OLC-CNF/MoS_2@Mn_2O_3 in Na_2SO_4 electrolytes (a) CV at 25 mV s^{-1} (b) Charge-discharge at 1 A g^{-1}.

EIS spectra before and after cycling were fitted and are presented in figure 5.20 for OLC-CNF/MoS_2 and figure 5.21 for OLC-CNF/MoS_2@Mn_2O_3. The limitation of an electrode material in supercapacitors is best explained by electrical equivalent circuit obtained from the fitted raw EIS data. As seen in table 5.4 below the series resistance (R_s) values for OLC-CNF/MoS_2 and OLC-CNF/MoS_2@Mn_2O_3 composites were 5.288 and 0.164 Ω, respectively. In the case of charge-transfer resistance (R_{ct}) the obtained values were 723.6 Ohm and 218.7 Ω, respectively. Given that the charge transfer reduced from OLC-CNF/MoS_2 to OLC-CNF/MoS_2@Mn_2O_3 alludes to enhanced electrode transfer kinetics from the composite. This clearly proves that the presence of Mn_2O_3 in OLC-CNF/MoS_2 nanofibres has enhanced the electrochemical processes in the electrode. The presence of the semi-circle suggests localized charge transfer between OLC-CNF/MoS_2 and Mn_2O_3 nanoparticles could also be attributed to the higher surface area of the composite. However, the slope at the low frequency region suggest that the electrodes from the OLC-CNF/MoS_2 composite had lower diffusive resistance of the electrolyte in the electrode pores. Nonetheless, the interaction between MoS_2 and Mn_2O_3 is showing better

conductivity and facilitates the charge transfer process with increased accessibility of charge carrier ions.

Table 5.4 *EIS data comparison of 3 electrode system fitted with Voigt equivalent circuit*

Parameter	**OLC-CNF/MoS_2**	**OLC-CNF/MoS_2@Mn_2O_3**
R_s/Ω Ω	5,288	0,164
C/F	8,52E-03	2,89E-03
R_{ct}/Ω	723,6	218,7
$W/\Omega.s^{-\frac{1}{2}}$	125,1	124

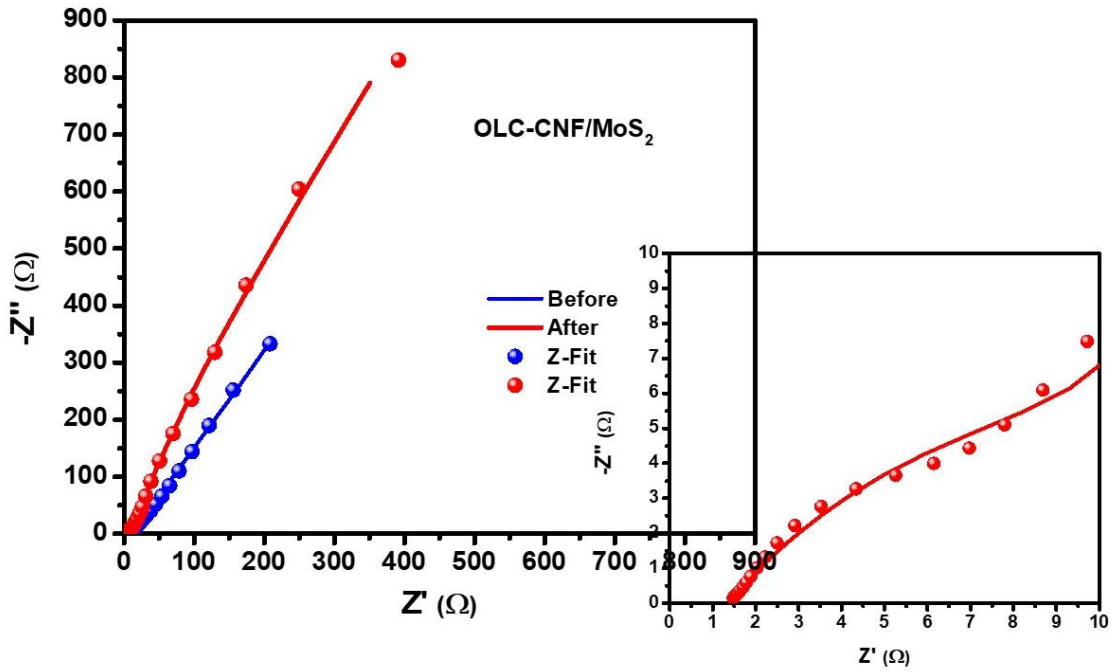

Figure 5.20 Nyquist plots with Z-fits for OLC-CNF/MoS_2 before and after 2000 charge-discharge cycles at 1 A g^{-1} cycling.

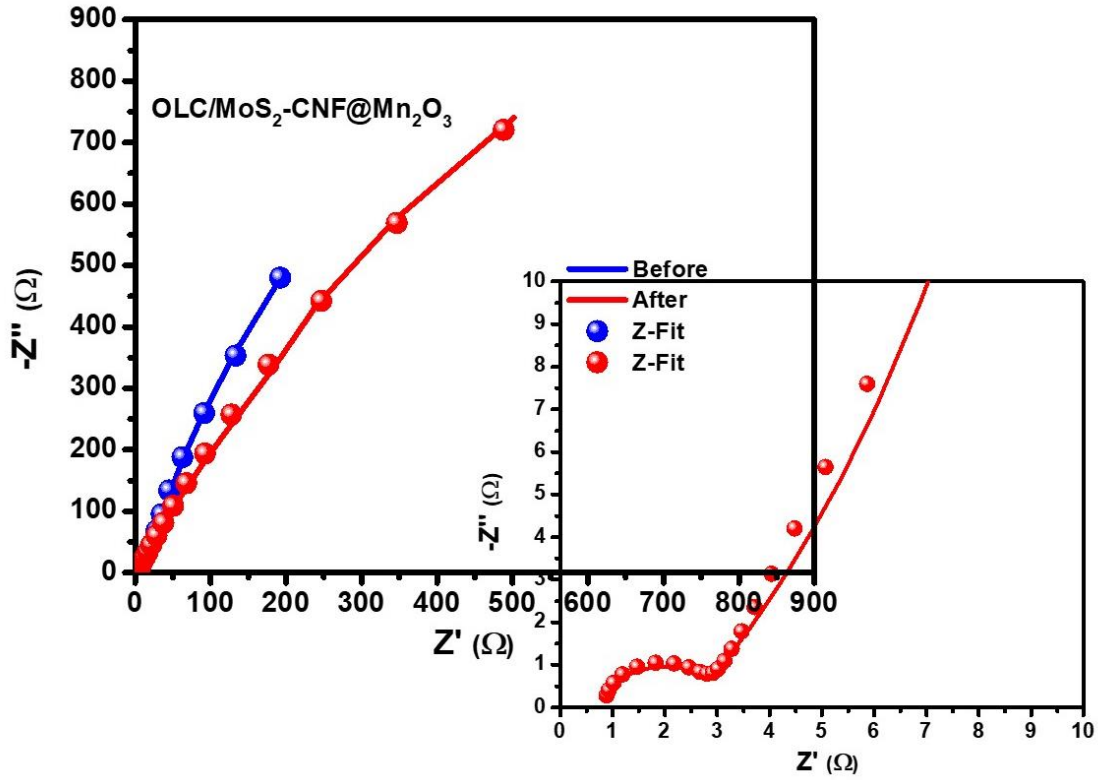

Figure 5.21 Nyquist plots with Z-fits for OLC-CNF/MoS_2@Mn_2O_3 before and after 2000 charge-discharge cycles at 1 A g^{-1} cycling.

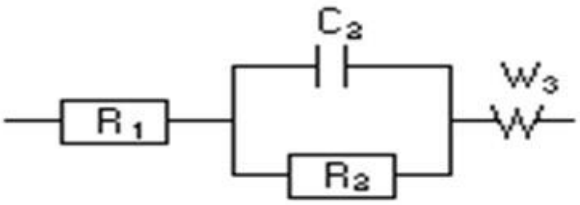

Impedance

$$Z(f) = R_1 + \frac{R_2}{1 + j2\pi f R_2 C_2} + \frac{\sqrt{2}\,\sigma_3}{\sqrt{j2\pi f}}$$

Nyquist Diagram (-Im(Z) vs. Re(Z))

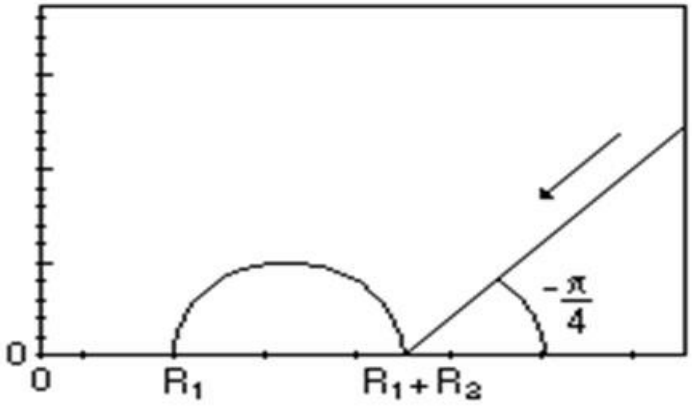

Figure 5.22 The electrical equivalent circuit used in fitting the Nyquist plots of OLC-CNF/MoS_2@Mn_2O_3 supercapacitor device is also shown together with the equation describing the real impedance from the EIS experiment where R_1 is the solution resistance, R_2 is the charge-transfer resistance, f is the angular frequency, π is the time domain for pulse modulation and C_2 a double layer capacitance. [33]

Figure 5.23 a below illustrates the kinetic information obtained from the CV curves of the OLC-CNF/MoS_2@Mn_2O_3 composites that was used to determine the capacitance contribution. In a redox reaction where, semi-diffusion peak is limited, generally the peak current i varies as $v^{1/2}$, whereas for capacitive process, it varies as v. Conventionally this relationship is explained by the equation below [34]

$$i = av^b \tag{5.1}$$

$$\log j = b \log v + \log a \quad (5.2)$$

where j represents the current density, whilst a and b represent adjustable parameters which can easily be obtained from the plot of $\log j$ and $\log v$. b value gives insight on the dominant charge storage mechanism that the dominant energy storage mechanism, $b = 1$ is surface-controlled, pure capacitive (i.e., non- Faradaic) process. On the other hand, a value of $b = 0{,}5$ means that storage mechanism is diffusion-controlled (i.e., Faradaic) process. For mixed charge-storage mechanisms (i.e., both Faradaic and non-Faradaic processes in operation) the b value is greater than 0.5 but less than 1. [26] In the case of OLC-CNF/MoS_2@Mn_2O_3 nanofibres the b value was 0.65 and 0.79 V for both anodic and cathodic currents, respectively suggesting a combination of supercapacitive mechanisms. However, figure 5.23 b with various scan rates (5-100 mV s^{-1}) confirms non-faradic process to be the most dominating and increases with increasing scan rate. This is characteristic of a capacitance behavior and has a potential to offer excellent reversibility as an electrode material.

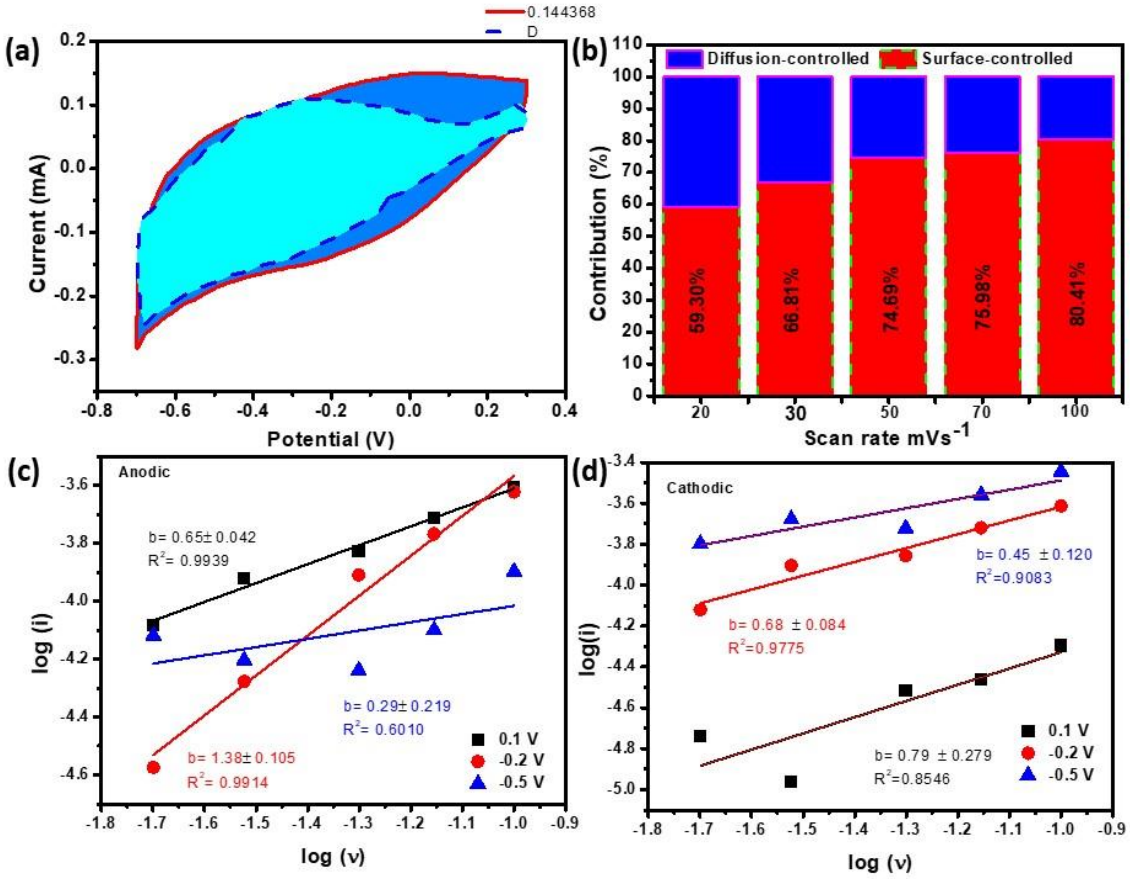

Figure 5.23 CV plot at 50 mV s^{-1} with capacitive contribution fraction displayed (a), kinetics histogram showing comparison of the EDLC contribution vs diffusion controlled of OLC-CNF/MoS_2@Mn_2O_3 electrodes with increasing scan rate (50-100 mV s^{-1}) (b), and finally (a) Log peak current vs log scan rate (b) Log peak current vs log scan rate for OLC-CNF/MoS_2@Mn_2O_3.

CV and charge-discharge methods were employed in a two-electrode symmetrical configuration between 0-0.8 V potential window. The resulting curves for OLC-CNF/MoS_2 and OLC-CNF/MoS_2@Mn_2O_3 composites are presented in figure 5.24 a and b, respectively. The shape of these curves is typical for supercapacitors possessing a combination of EDLC and pseudocapacitive storage mechanisms. Seemingly, at various scan rates (5-100 mV s^{-1}) the OLC-CNF/MoS_2@Mn_2O_3 composite in figure 5.24 b is more capacitive compared to OLC-CNF/MoS_2 in figure 5.24a. It is expected that the charge/voltage ratio is somewhat larger for charging electrodes as opposed to discharging. This phenomenon is referred to as Coulomb efficiency (CE) and was investigated, where under a fixed potential window, the CE of a device is the ratio between charge and

discharge capacity. It was a critical parameter to establish the kinetics and resistance issue associated with the electrode materials presented in this work. In the case of OLC-CNF/MoS_2 electrodes, both CV and charge-discharge curves showed a charge capacity significantly different to the discharge capacity, and thus efficiency would be a limiting factor in supercapacitor applications. Whereas in OLC-CNF/MoS_2@Mn_2O_3 composite electrodes, the demonstrated CE is higher.

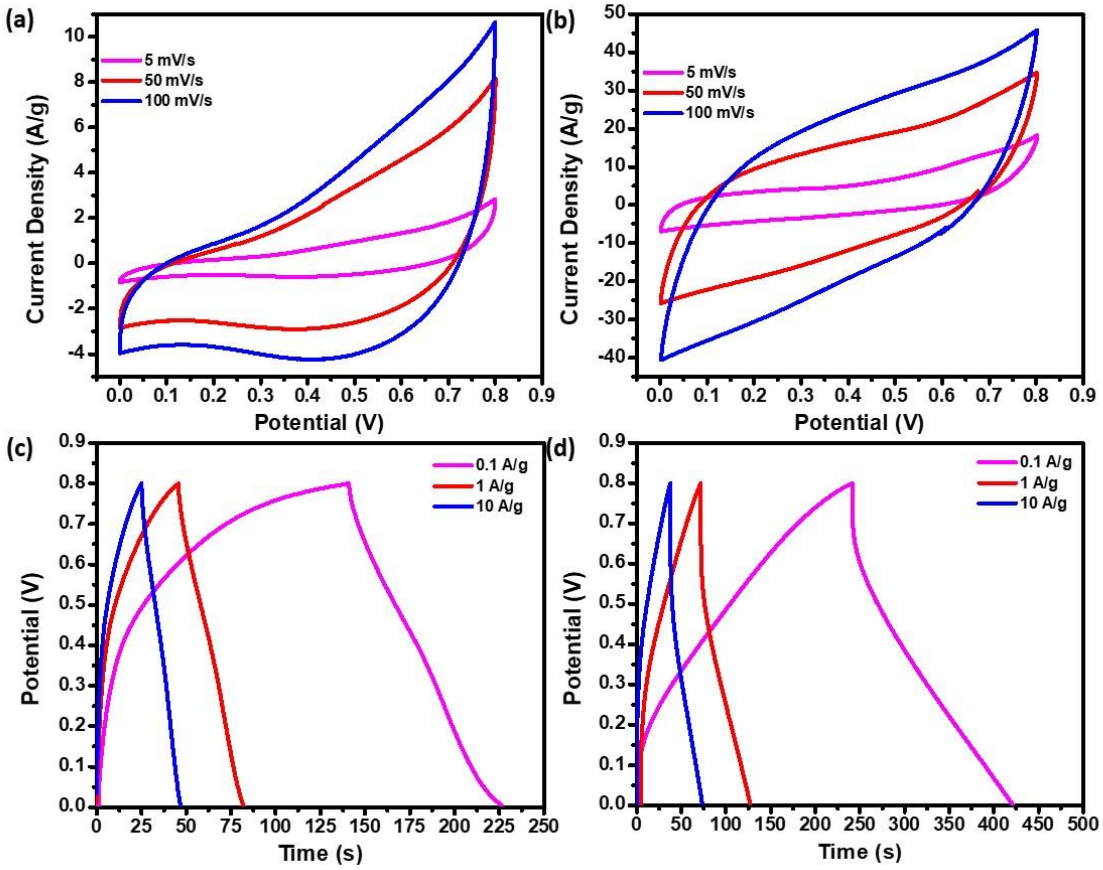

Figure 5.24 CV (5, 50, 100 mV s-1) and GCD (0.1, 1, 10 A g-1) curves of the two-electrode system for the OLC-CNF/MoS_2 (a, c) and OLC-CNF/MoS_2@Mn_2O_3 (b, d) electrodes, respectively.

Specific capacitance was calculated using the GCD plots and a comparison was plotted in figure 5.25a. The specific capacitance of OLC-CNF/MoS_2 and OLC-CNF/MoS_2@Mn_2O_3 was 107 F g^{-1} and 348 F g^{-1} at 0.1 A g^{-1}, respectively. As the current density increased, the specific capacitance reduced gradually in the case of OLC-CNF/MoS_2@Mn_2O_3 electrodes, which indicates good rate capability for the composite.

This confirms the enhancement of electrochemical properties through incorporation of Mn_2O_3 nanoparticles in the OLC-CNF/MoS_2 fibre matrix. The increase in capacitance was explained by the redox active sites that are on the surface on the fibres, making it easy for the electrolyte ions to store charge. The performance of OLC/MoS_2 and OLC-CNF/MoS_2@Mn_2O_3 CNF supercapacitors was summarized using a Ragone plot and compared as illustrated in figure 5.25 b. The power density of OLC-CNF/MoS_2 was 6 537 W kg^{-1} when the optimal energy density was 37 Wh kg^{-1} compared with power density of 1 098 W kg^{-1} and energy density of 92 Wh kg^{-1} at 0,1 A g^{-1} for OLC-CNF/MoS_2@Mn_2O_3 electrodes. The amount of energy density for the latter electrodes is applicable for technologies required to harvest energy and powering devices.

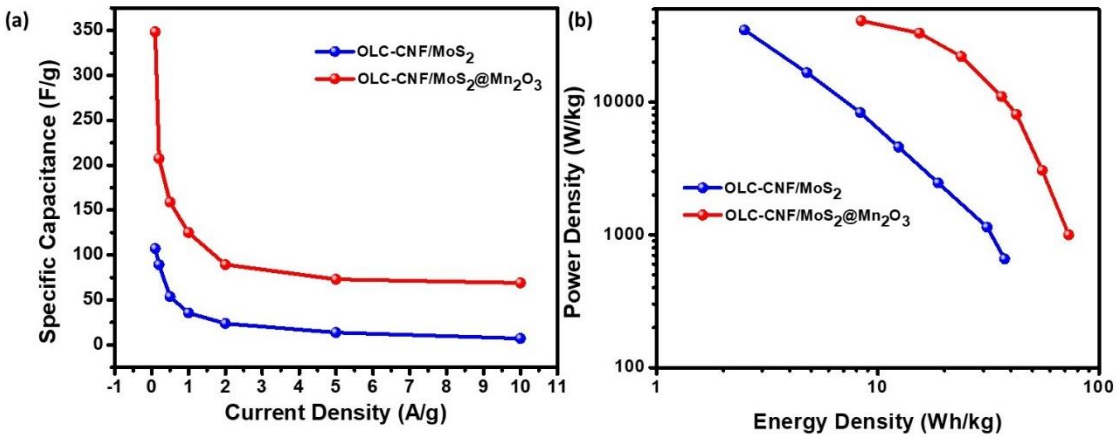

Figure 5.25 Specific capacitance at various current densities (0.1, 0.5, 1, 2, 5 and 10 A g^{-1}) (a), and Ragone plot for OLC-CNF/MoS_2 and (b) OLC-CNF/MoS_2@Mn_2O_3 supercapacitors electrodes.

To understand the specific role of electrode kinetics in a two-electrode setup, EIS experiments were carried out with voltage amplitudes ranging between 5 mV and 8 mV corresponding to 0.01 Hz to 100 kHz. Nyquist plots of OLC-CNF/MoS_2 and OLC-CNF/MoS_2@Mn_2O_3 supercapacitors are presented in figure 5.26 and 5.27 respectively. Generally, these plots consist of three regions namely, high frequency (i.e. greater than 10^4 Hz) followed by the medium frequency (10^4-10^1 Hz) and finally low frequency (< 1 Hz). The data relating to the Voigt RC elements is summarized in table 5.5. The R_s values of OLC-CNF/MoS_2 before and after 5000 charge discharge cycles were 1.189 and 1.729

Ω respectively. In comparison to, OLC-CNF/MoS_2@Mn_2O_3 where these were as low as 0.579 and 0.595 Ω, respectively before and after 5000 charge discharge cycles. Further the Rct values before and after cycling for OLC-CNF/MoS_2 were 3.309 and 7.933 Ω. Whereas for OLC-CNF/MoS_2@Mn_2O_3 these were 4.124 and 4.645 Ω, respectively. These slight differences in Rct before and after cycling of the OLC-CNF/MoS_2@Mn_2O_3 electrodes suggests improved stability compared to its counterpart. The improvement in conductivity of the electrodes upon Mn_2O_3 integration in a two electrode configuration are in agreement with the results from the three electrode configuration. The results clearly indicate the presence of Mn_2O_3 nanoparticles in the fibre matrix has enhanced the conductivity and consequently increased the capacitance of OLC/MoS_2 electrodes. The impedance of the CPE (ZCPE) is related to the frequency-independent constant (Q) and radial frequency (w) according to the equation (5.3) [28]

$$Z_{CPE} = \frac{1}{[Q\ (jw)^n]} \tag{5.3}$$

Where n (with values in the $-1 \leq n \leq 1$ range) is obtained from the slope of $\log Z$ vs. $\log f$. When n = 0, 1, −1 or 0.5, the CPE describes a pure resistor, a pure capacitor, an inductor, or Warburg impedance (Zw), respectively, due to the diffusion of the ions. [29] For all the cells, the n values observed for these electrodes are generally greater than 0.5, which confirms the typical pseudocapacitive properties of the MoS_2-based symmetric cells, corroborating the CV capacitive contribution study done on the three-electrode system. The phase angle before and after cycling were lower than - 75° which is expected for pseudocapacitors systems. It is also important to note that the knee frequency $f_0, \emptyset = 45°$ relating to the rate or power capability of the supercapacitor is higher for OLC-CNF/MoS_2@Mn_2O_3 based electrode in comparison to OLC-CNF/MoS_2 suggesting faster charge-discharge capabilities.

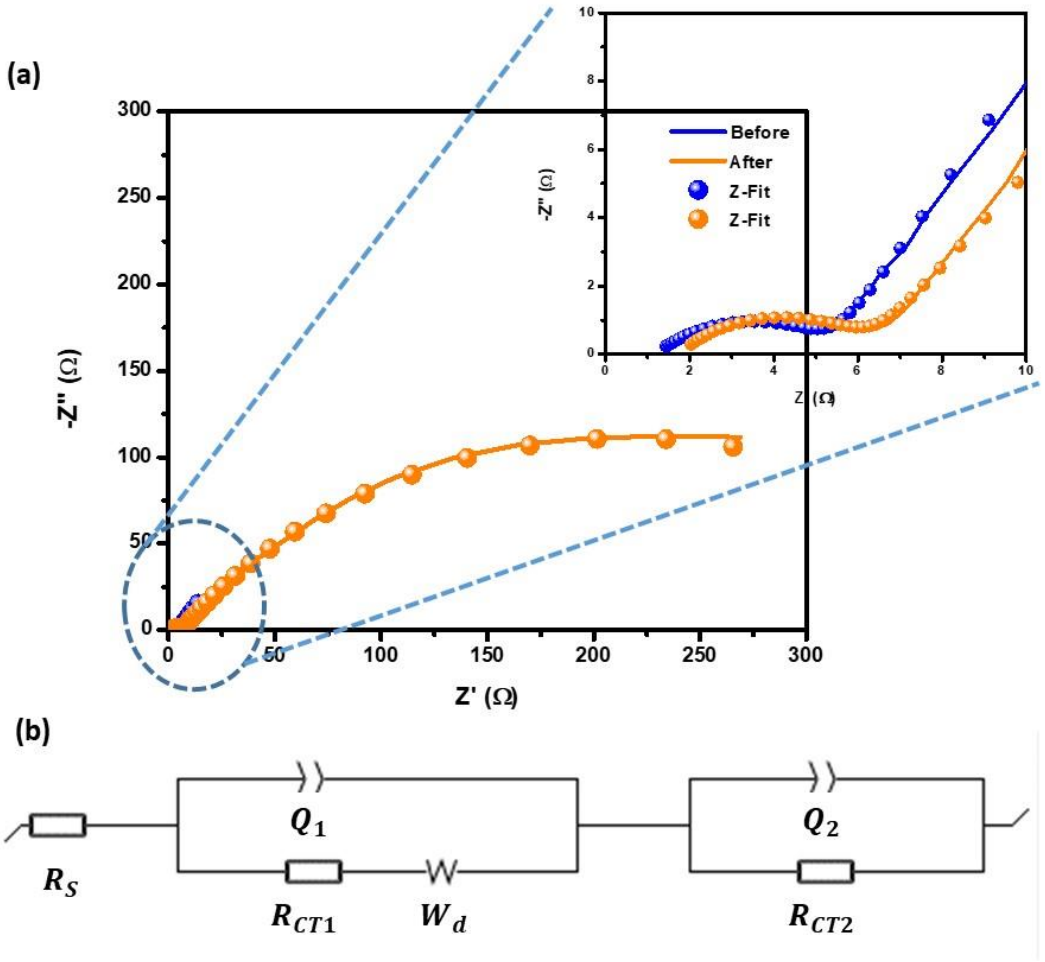

Figure 5.26 (a) Nyquist plots for symmetric two-electrode cells of OLC-CNF/MoS_2 with Z-fits before and after 5000 charge-discharge cycles at 1 A g^{-1} (b) The electrical equivalent circuit used in fitting the Nyquist plots are also demonstrated.

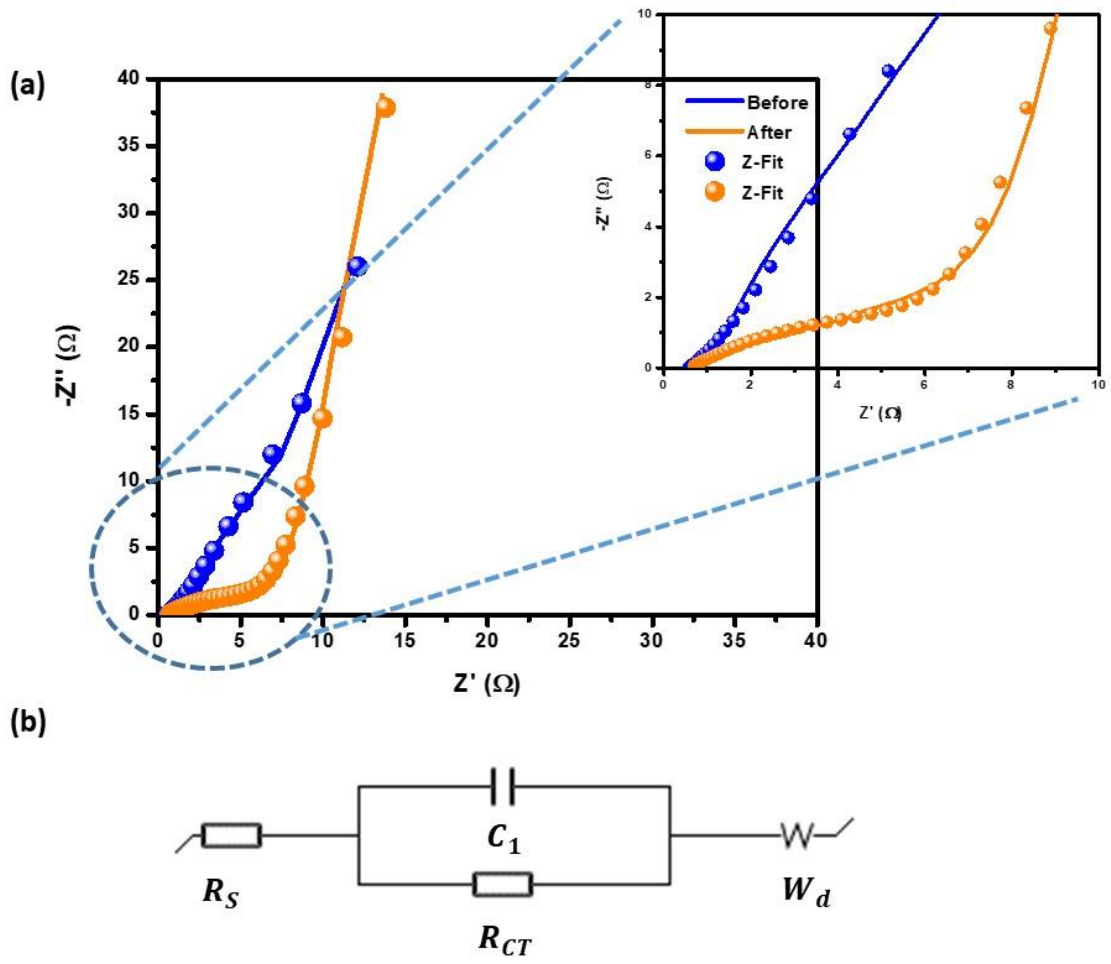

Figure 5.27 (a) Nyquist plots for symmetric two-electrode cells of OLC-CNF/MoS_2@Mn_2O_3 with Z-fits before and after 5000 charge-discharge cycles at 1 A g^{-1} (b) The electrical equivalent circuit used in fitting the Nyquist plots are also demonstrated.

Table 5.5 *Electrochemical performance OLC-CNF/MoS_2 and OLC-CNF/MoS_2@Mn_2O_3 fibre composites.*

	OLC-CNF/MoS_2		**OLC-CNF/MoS_2@Mn_2O_3**	
	Before Cycling (@ 0 cycle)	**After Cycling (@ 5000 cycles)**	**Before Cycling (@ 0 cycle)**	**After Cycling (@ 5000 cycles)**
Rs/Ohm	0.579	0.595	1.189	1.729
Q1/ F.s^(a - 1)	0.665	0.04	0.09	1.81E-03
n1	1	0.389	0.737	0.532
Rct	3.302	7.933	4.124	4.645
Q2	1.189	0.309	1.10E-02	0.076
n2	1	0.89	0.518	0.619
Rct2	25.27		0.11	419.3
s/Ohm.s^-1/2	2.207		1.462	
Phase angle	-65.84	-70.68	-48.53	-22.54

5000 charge-discharge cycles were done to evaluate the reversibility of the OLC-CNF/MoS_2@Mn_2O_3 composite electrodes. The specific capacitance was analyzed at different points of the charge-discharge cycles. More data points were collected at shorter intervals up to 2000 cycles as compared to between 2000 and 5000 cycles. The irreversible degradation caused by phase transformations, physical relaxation, or dissolution was not apparent during cycling as displayed by the capacitance retention plot. Instead the electrodes proved to be stable throughout and retained the same capacitance as shown in figure 5.28. This result agrees with the supercapacitive study from the three-electrode, suggesting EDLC as the dominant storage mechanism for the OLC-CNF/MoS_2@Mn_2O_3 composite electrodes. Figure 5.29 demonstrates the ability of the electrodes to light up a 1.68 V LED when symmetrical cells are connected in series. Interestingly, the light stayed on for more than three minutes, when charged for a minute and few seconds.

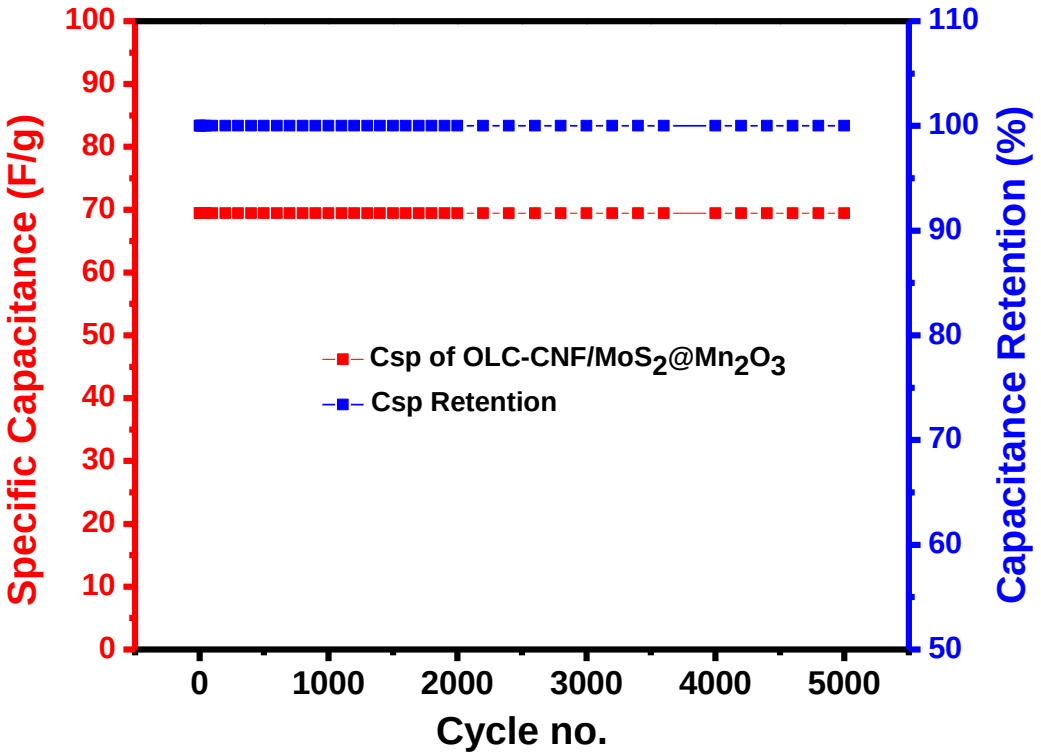

Figure 5.28 Cycle stability of OLC-CNF/MoS_2@Mn_2O_3 electrodes.

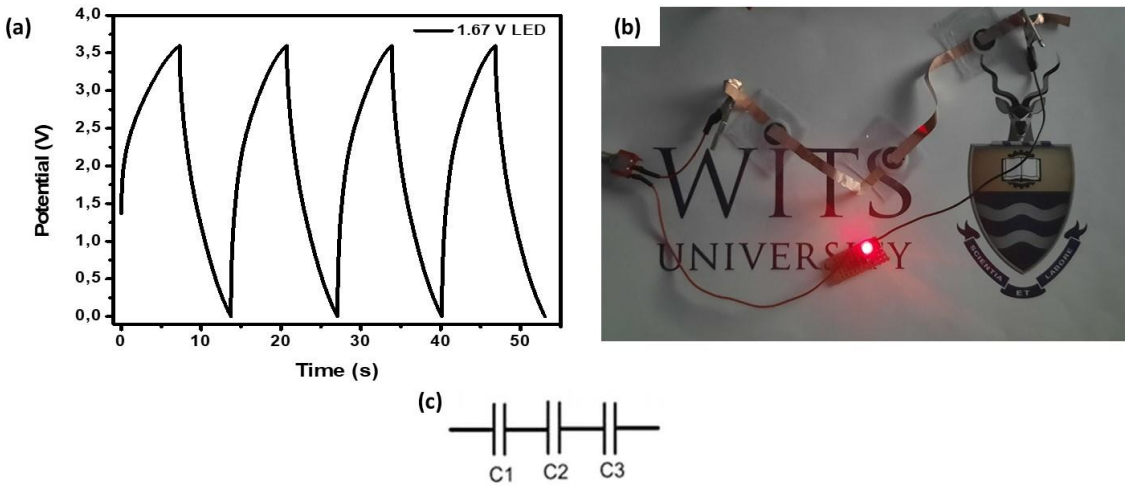

Figure 5.29 (a) charge-discharge profiles of OLC-CNF/MoS_2@Mn_2O_3 fibre composite electrodes giving 3.6 V, (b) a photograph of OLC-CNF/MoS_2@Mn_2O_3 electrodes lighting up a 1.67 V LED at a 0° bending angle, and (c) electrical circuit representative of the electrodes connected in series.

5.3 Conclusions

OLC nanoparticles were successfully imbedded in electrospun fibres and hydrothermally synthesized for the encapsulation with MoS_2. For the first time, MoS_2 sheets were successfully synthesized on electrospun carbon nanofibres in the absence of an existing template due to the multi-step thermal treatment of the OLC-PAN, which significantly improved their stability even under harsh conditions associated with hydrothermal synthesis method. Finally, an OLC-CNF/MoS_2@Mn_2O_3 composite material was synthesized using a simple and cost-effective method. The synergistic effects of the OLC-CNF/MoS_2@Mn_2O_3 composites led to a capacitance of 348 F g^{-1} in comparison to that of OLC/MoS_2 which was 107 F g^{-1} in a symmetrical configuration at 1 A g^{-1} in 1 M Na_2SO_4 electrolyte solution. Improved cycling stability in the OLC-CNF/MoS_2@Mn_2O_3 composite was attributed to the increase of the electrochemical active sites in the active material and hence the limited internal resistance of the electrodes. The addition of Mn_2O_3 nanoparticles/flakes positively contributed to the electrochemical performance by influencing the physicochemical properties of the electrodes given the electrodes benefited with higher capacitance values, improved rate capability and cycle life.

5.4 References

[1] Chen, H.; Cong, T. N.; Yang, W.; Tan, C.; Li, Y.; Ding, Y. Progress in electrical energy storage system: A critical review. *Prog. Nat. Sci.* **2009**, 19, 291-312.

[2] Iro, Z. S.; Subramani, C.; Dash, S.S. A Brief Review on Electrode Materials for Supercapacitor. *Int. J. Electrochem. Sci.* **2016**, 11, 10628-10643.

[3] Muzaffara, M.; Ahamed, M. B.; Deshmukh K. A review on recent advances in hybrid supercapacitors: Design, fabrication and applications. *Renew. Sust. Energ. Rev.* **2019**, 101, 123-145.

[4] Abdah, M. A. A.; Azman, N. H. N.; Kulandaivalu S.; Sulaiman, Y. Review of the use of transition-metal-oxide and conducting polymer-based fibres for high-performance supercapacitors. *Mater. Des.* **2020**, 186, 1-20.

[5] Huang, K. J.; Wang, L.; Liu, Y. J.; Liu, Y. M.; Wang, H. B.; Gan, T.; Wang, L. L. Layered MoS_2-Graphene composites for supercapacitor applications with enhanced capacitive performance. *Int. J. Hydrog. Energy*. **2013**, *38*, 14027-14034.

[6] Wang, S.; An, C.; Yuan, J. Synthetic fabrication of nanoscale MoS_2-based transition metal sulfides. *Materials*. **2010**, *3*, 401-433.

[7] Huang, K. J.; Wang, L.; Zhang, J. Z.; Wang, L. L.; Mo, Y. P. One-step preparation of layered molybdenum disulfide/multi-walled carbon nanotube composites for enhanced performance supercapacitor. *Energy*. **2014**, *67*, 234-240.

[8] Hu, B.; Qin, X.; Asiri, A. M.; Alamry, K. a.; Al-Youbi, A. O.; Sun, X. Synthesis of porous tubular C/MoS_2 nanocomposites and their application as a novel electrode material for supercapacitors with excellent cycling stability. *Electrochim. Acta*. **2013**, 100, 24-28.

[9] Chen, Y. M.; Yu, X. Y.; Zhen, L.; Paik, U.; Wen X. Hierarchical MoS_2 tubular structures internally wired by carbon nanotubes as a highly stable anode material for lithium-ion batteries. *Sci. Adv.* **2016**, 2, 1-8.

[10] Khawula, T. N. Y.; Raju, K.; Franklyn, P. J.; Sigalas, I.; Ozoemena K. I. Symmetric pseudocapacitors based on molybdenum disulfide (MoS_2)-modified carbon nanospheres: Correlating physico-chemistry and synergistic interaction on energy storage. *J. Mater. Chem. A.* **2016**, 4, 6411-6425.

[11] Chen, Q.; Zhang, Z.; Awaga, K. Electrochemical Tuning-Induced Magnetic Transitions in Geometrically Frustrated Spinel $LixMn_2O_4$ ($0.07 \leq x \leq 0.93$), *J. Phys. Chem. C.* **2021**, 125, 7763-7771.

[12] Zeng, Y-X.; Zhong, X-W.; Liu, Z. Q.; Chen, S.; Li, N. Preparation and Enhancement of Thermal Conductivity of Heat Transfer Oil-Based MoS_2 Nanofluids, *J. Nanomater*. **2013**, 1, 1-6.

[13] Acerce, M.; Voiry, D.; Chhowalla M. Metallic 1T phase MoS_2 nanosheets as supercapacitor electrode materials. *Nat. Nanotechnol.*, **2015**, 10, 313-318.

[14] Zieger, M.; Jackel, N.; Mochalin, V. N.; Presser, V. Review: carbon onions for electrochemical energy storage. *J. Mater. Chem. A.* **2016**, 4, 3172-3196.

[15] McDonough, K.; Gogotsi, Y. Carbon onions: Synthesis and Electrochemical applications. *Electrochem. Soc. Interface.* **2013**, 22, 61-66

[16] Weingarth, D.; Zeiger, M.; Jackel, N.; Aslan, M.; Feng, G.; Presser, V. Graphitization as a universal tool to tailor the potential-dependent capacitance of carbon supercapacitors. *Adv. Energy Mater*. **2014**, 4, 1400316.

[17] Shi, X.; Zhou, W.; Ma, D.; Bridges, D.; Ma, Y.; Hu, A. Electrospinning of nanofibres and their applications for their applications for energy devices. *J. Nanomater*. **2015**, 2015, 1-20.

[18] Gao, Y.; Zhou, Y. S.; Qian, M.; He, X. N.; Redepenning, J.; Goodman, P.; Li, H. M.; Jiang, L.; Lu Y. F. Chemical activation of carbon nano-onions for high-rate supercapacitor electrodes. *Carbon*. **2013**, 51, 52-58.

[19] Bushueva, E. G.; Galkin, P. S.; Okotrub, A. V.; Bulusheva, L. G.; Gavrilov, N. N.; Kuznetsov, V. L.; Moiseekov, S. I. Double layer supercapacitor properties of onion-like carbon materials. *Phys. Status Solidi B.* **2008**, 245, 2296-2299.

[20] Nataraj, S. K.; Yang, K. S.; Aminabhavi, T. M. Polyacrylonitrile-based nanofibres:A-state-of-the-art-review. *Prog. Polym. Sci.* **2012**, 37, 487-513.

[21] Cavaliere, S.; Subianto, S.; Savych, I.; Jones, D. J.; Rozière. Electrospinning: designed architectures for energy conversion and storage devices. *Energy Environ. Sci.* **2011**, 4, 4761-4785.

[22] Wei, M.; Kang, B.; Sung, C.; Mead, J. Core-Sheath Structure in Electrospun Nanofibres from Polymer Blends. *Macromol. Mater. Eng.* **2006**, 291, 1307-1314.

[23] Sahu, T. S.; Mitra, S. Exfoliated MoS_2 sheets and reduced Graphene Oxide-An excellent and fast anode for sodium-ion battery, *Sci. Rep*. **2015**, 5, 12571.

[24] Wang, M.; Fei, H.; Zhang, P.; Yin, L. Hierarchically Layered MoS_2/Mn_3O_4 Hybrid Architectures for Electrochemical Supercapacitors with Enhanced Performance, *Electrochim. Acta*. **2016**, 209, 389-398.

[25] Liu, T. C.; Pell, W. G.; Conway, B. E.; Roberson, S. L. Behavior of molybdenum nitrides as materials for electrochemical capacitors: comparison with ruthenium oxide. *J. Electrochem. Soc.* **1998**, 145, 1882.

[26] Chen, X-B.; Chen, Z-L.; Li, J. Critical electronic structures controlling phase transitions induced by lithium ion intercalation in molybdenum disulphide. *Chin. Sci. Bull.* **2013**, 58, 1632-1641.

[27] Kim, S.; Gupta, N. K.; Bae, J.; Kim, K. S. Fabrication of coral-like Mn_2O_3/Fe_2O_3 nanocomposite for room temperature removal of hydrogen sulfide. *J. Environ. Chem. Eng*. **2021**, 9, 105216.

[28] Naeem, R.; Mansoor, M. A.; Munawar, K.; Adnan, A.; Zaharinie, T.; Zubir, M. N. M. Versatile Fabrication of Binary Composite SnO_2-Mn_2O_3 Thin Films by AACVD for Synergistic Photocatalytic Effect. *J. Electron. Mater*. **2021**, 50, 3897-3906.

[29] Li, J.-Y.; Lü, H.-Y.; Zhang, X.-H.; Xing, Y.-M.; Wang, G.; Guan, H.-Y.; Wu, X.-L. P2-type $Na_{0.53}MnO_2$ nanorods with superior rate capabilities as advanced cathode material for sodium ion batteries. *Chem. Eng. J*. **2017**, 316, 499-505.

[30] Haruna, A. B.; Mwonga, P.; Barrett, D.; Rodella, C. B.; Forbes, R. P.; Venter, A.; Sentsho, Z.; Flether, P. J.; Marken, F.; Ozoemena, K. I. Defect-Engineered β MnO2−δ Precursors Control the Structure− Property Relationships in High-Voltage Spinel LiMn1.5Ni0.5O4−δ, *ACS Omega*. **2021**, 6, 25562-25573.

[31] Ameen, S. Vertically arranged Mn_2O_3 nanosheets as smart sensing electrode for highly sensitive N-hydroxysuccinimide. *Microchem. J*. **2021**, 163, 105912.

[32] Li, C.; Zhang, X-Q.; Zhang, B.; Zou, S-R.; Hu, N.; Sun, D-W.; Lei, C-X. Facile synthesis of porous Mn_2O_3/TiO_2 microspheres as anode materials for lithium-ion batteries with enhanced electrochemical performance. Qian-Zhi Gou, *J. Mater. Sci. Mater. Electron*. **2018**, 29, 16064-16073.

[33] Mclean, A. V.; Halper, M. S.; Ellenbogen, J. C. Supercapacitors: *A brief overview*, Virginia: The MITRE nanosystems group, 2006.

[34] Randviira, E. P.; Banks, C. E. Electrochemical impedance spectroscopy: an overview of bioanalytical applications, Anal. Methods, **2013**, 5, 1098-1115.

CHAPTER SIX

Tetranitro-iron (II) (FeN_4) macrocycle modified carbon microfibers as high-performance supercapacitor

6.1 Introduction

Phthalocyanines are characterized by an excellent combination of properties which make them attractive in application such as, optical materials[1-2], molecular semiconductors[3-4], gas sensors[5-6] and molecular electronic devise[7-8], to name a few. Recently they have also been examined as potential electrode materials for batteries due to the nitrogen active centres and metal centres capable of redox reactions which benefits energy storage capabilities. [9-10] Poor cycle life, poor rate capability and high solubility in liquid electrolytes are some of the challenges reported on MPc as electrode materials. To address these concerns, Chen et. al [12] proposed encapsulations of MPc's with a protective Li-conducting material so that it is not in direct contact with the electrolyte. A comparative study showed a much longer cycle life, high cathode specific capacity and best energy density for a rechargeable lithium-ion battery cell. In another study, Jahnke et al.[13] improved thermal stability as well as the electrochemical activity of transition metal porphyrins deposited on a carbon support by a pyrolytic heat treatment step in the range from 450 to 900 ℃ in an inert atmosphere. [13]

This study presents the use of electrospinning technique to prepare tetranitro-iron (II) (FeN_4) macrocycle modified carbon microfibers as illustrated by the schematic in figure 6.1. Contrary to the precursor (FePc) the centres are bonded to a conducting carbon matrix after the thermal treatment in the FeN_4-CMF. The final product has potential as a supercapacitor electrode material based on its efficient electron transfer abilities of the active centre FeN_4, that offers electron transition and reversibility of the Fe^{3+} and Fe^{2+} redox coupled with the conductive carbon network providing π to π interactions for further enhanced electrochemical properties.

Figure 6.1 Schematic for synthesis of FeN_4-CMF composite electrode material.

6.2 Results and discussions

6.2.1 Material characterization

The SEM micrographs of the as-electrospun FePc-PAN fibre are shown in figure 6.2a and b at high and low magnifications, respectively. From the previous study in chapter four, the PAN diameter increased with the integration of other components in the polymer solution. In this case, the average diameter of the fibres increased with FePc addition in the original PAN fibre from 569 nm to 1.6 µm for FePc-PAN. This was explained by; (i) the significant reduction in viscosity of the slurry solution which required a slower feed rate and subsequently drawing fibres with a thicker diameter. In support of this, several authors have also noted that generally thick fibres are less dense and therefore have less orientation than thin fibres because they are formed at lower feed rates and a slower solvent operation during electrospinning.[14-16] (ii) during the stretching of the polymer fluid process the FePc with a rod like morphology became oriented along the fiber axis thus widening the overall diameter. Evidently, the as-electrospun fibres exhibited fibrous continuous morphology with an increased surface roughness (grainy) and irregularities after the addition of FePc.

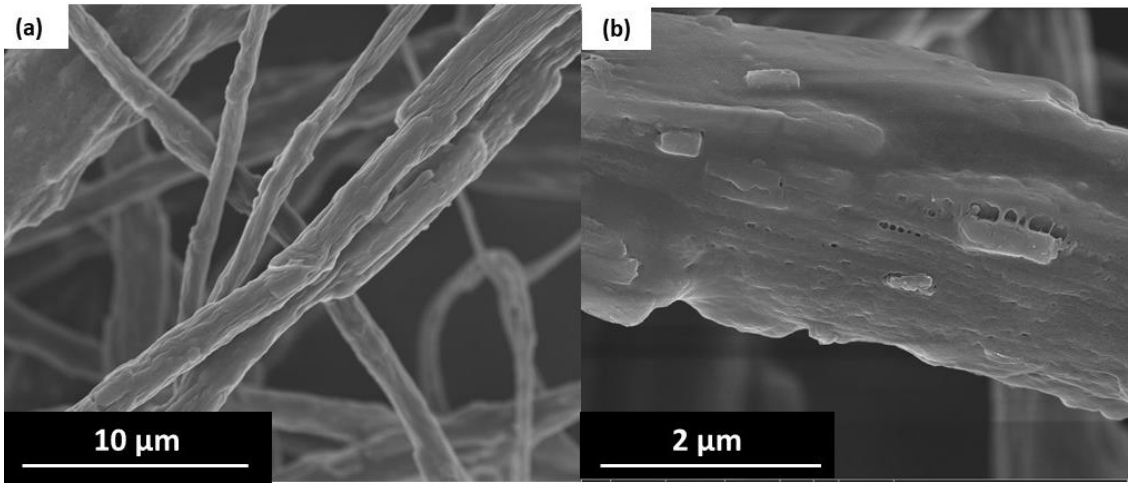

Figure 6.2 (a, b) SEM micrographs of electrospun FePc-PAN fibres at high and low magnifications.

Figures 6.3a and b display the micrographs of stabilized and carbonized FeN_4-CMF with the 1D microstructure of the fibres preserved after thermal treatments. According to Peng et. al., [33] PAN undergoes cyclization reaction and crosslinking of chains during stabilization, which prevents melting during subsequent carbonization. This entails the conversion of the nitrile groups (C≡N) into a double bond structure (C=N), leading to a six-membered cyclic pyridine ring. These processes cause the PAN nanofibres to release a variety of gases, such as CO_2, CO, NH_3, and H_2O, which aided the shrinkage of the nanofibres. Given that the 1D morphology of the fibres was preserved after thermal treatment, suggests successful carbonization of PAN and improved thermal stability of fibres.

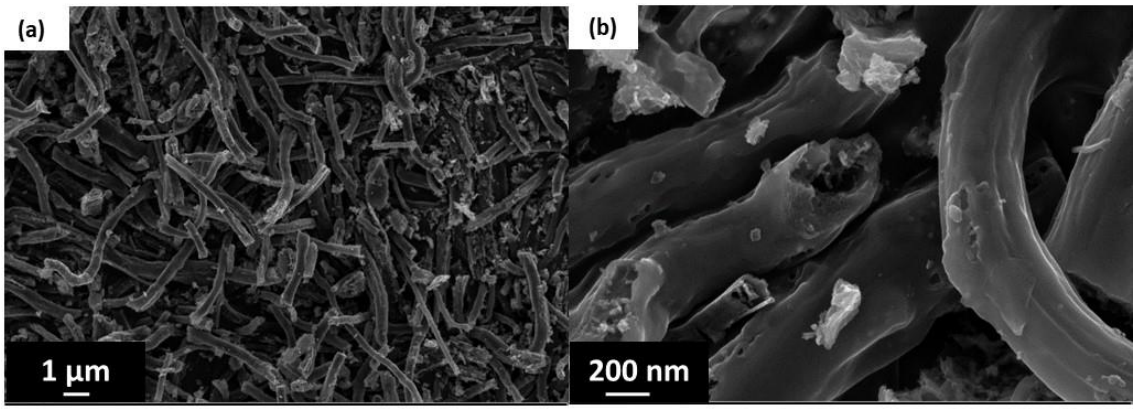

Figure 6.3 (a, b) SEM images thermally treated FeN_4-CMF at high and low magnification, respectively.

TEM images shown in Figure 6.4 demonstrate the porous micro-fibres with the crystalline FeN_4 particles embedded on the surface of the pristine micro-fibres after carbonization and stabilization heat treatments at various magnifications. Meso- and macro-porous structure of FeN_4-CMF was expected to play an effective role in optimization of energy storage capabilities for supercapacitors

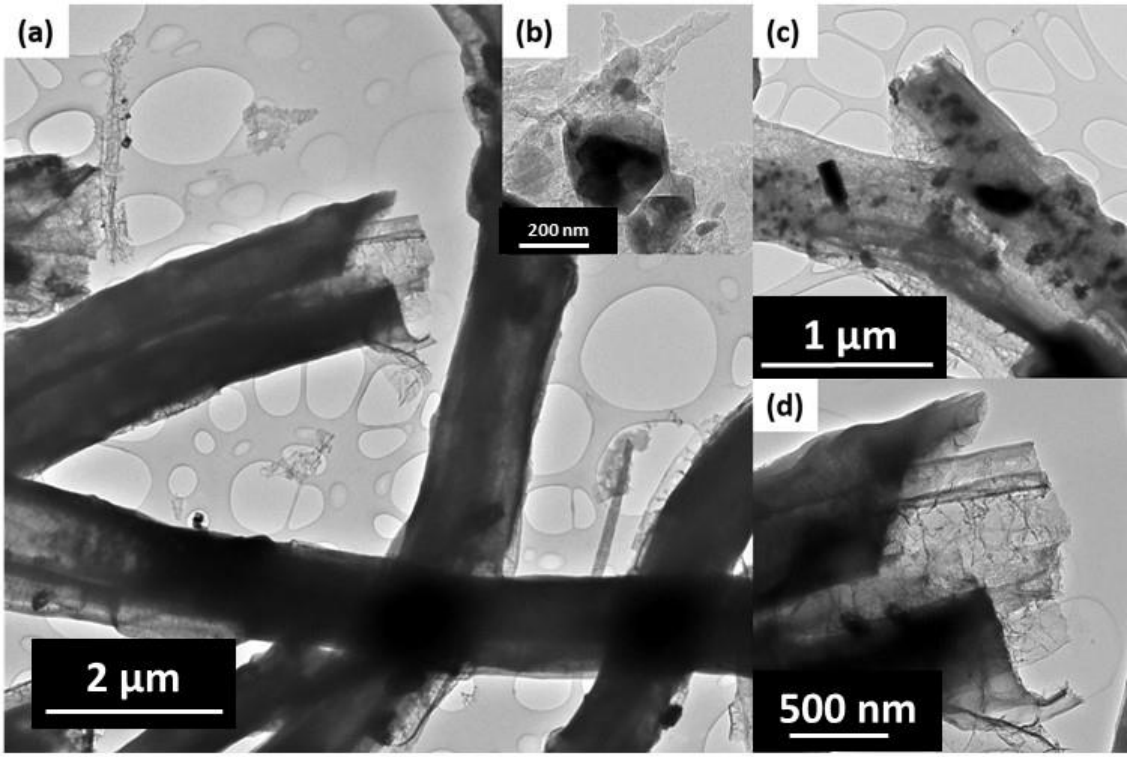

Figure 6.4 TEM images of porous FeN_4-CMF.

BET analysis of the fibres was done to ascertain the changes in surface area and pore volume changes from FePc-PAN and FeN_4-CMF. The results are summarised in Table 6.1. The non heat-treated PAN and FePc-PAN fibres were entangled and densily packed resulting in inaccessible surface area. On the other hand, FeN_4-CMF had a higher surface area as well as pore volume due to stabilization and carbonization heat treatments. During which the evolution of gases created pores and volume shrinkage as a consequence of carbon densification. It is expected that for FeN_4-CMF fibres there are more accessible electrolyte ions when used as an energy storage material due to their micro porous granuar surface observed in TEM.

Table 6.1 *BET Surface Area parameters of FePc-PAN and Fe-N_4-CMF.*

Name	Surface area/m^2g^{-1}	Pore volume /cm^3g^{-1}
FePc-PAN	37.56	0.20
FeN_4-CMF	419.23	1.21

Figure 6.5 a shows the N_2 adsorption isotherms of the carbon nanofibres. The relative low-pressure region (<0.05 P/P_o) was attributed to the micropore adsorption whereas the relative high-pressure region (>0.02 P/P_o) was explained by the mesopore adsorption. The pore size distribution based on the Barrett-Joyner-Halenda (BJH) method is presented in figure 6.5 b where the pore volume increased with decreasing fibre diameter.

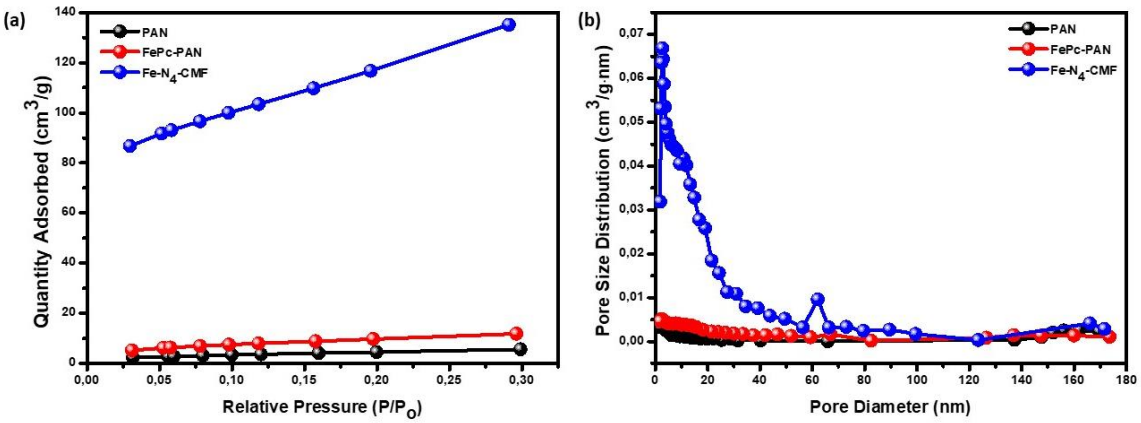

Figure 6.5 (a) N_2 adsorption of the electrospun nanofibres (b) Pore size distribution obtained from the N_2 adsorption data after applying the BJH equation.

Figure 6.6 shows XRD traces of FePc-PAN and FeN_4-CMF. According to Harmish et al. [14] materials containing arrays of single metal ions coordinated to four nitrogen atoms (M-N_4) were produced by heat treatment at 600 ℃. At higher temperatures (between 800-900 ℃) the metal species become carbon supported. Typical broad diffraction peak centered at 24.8° 2θ angle represents the X-ray reflection of (002) crystallographic plane in FePc-PAN nanofibres. Additional peaks were observed at 43.2 and 61.7° 2θ which were attributed to (101) and (112) crystallographic planes. The peak was due to the amorphous nature and the hexagonal packing of rod like chains in the sample. The intensity of the peaks of the fibres increased after stabilization and carbonization

treatments and further shifted to higher 2θ angle values to 25.4, 44.1 and 76 ° for (002) (101) and (112) planes, respectively. The peak shifts suggest that the atoms were re-arranged into an increasingly aligned form (graphitic phase), resulting in an enhancement of the crystallinity of electrospun fibres.

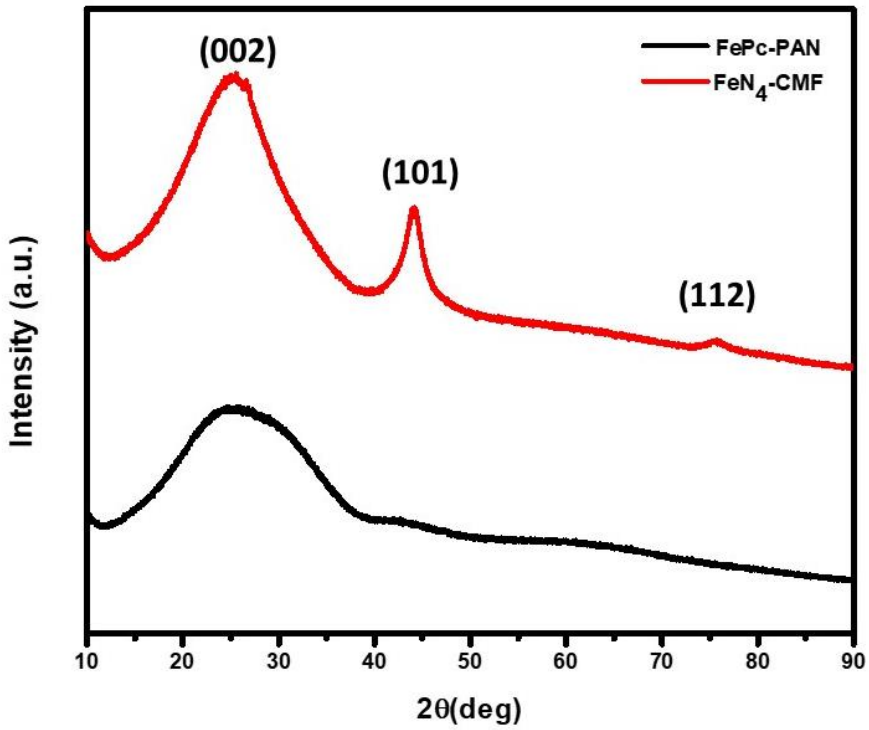

Figure 6.6 Comparative XRD analysis for FePc-PAN and FeN_4-CMF.

Figure 6.7 shows the Raman spectra for as-electrospun FePc-PAN and heat-treated FeN_4-CMF. Generally, carbon fibres show two peaks, the D and G peaks around 1360 cm^{-1} and 1580 cm^{-1}, respectively. In this study, the D peak of the FePc-PAN was found at 1592 cm^{-1} and the G peak appeared at 1607 cm^{-1}. The presence of the G peak in the spectrum of FePc-PAN indicated the presence of Raman active sp^2 carbon network. For the stabilized and carbonized fibres the G and D peaks were observed at 1355 an1587 cm^{-1} which are attributed to the existence of a disordered structure and stretching of the C−C bond, respectively.

Typically, the higher the D-band intensity, the larger the number of defects, and from the double resonance theory, crystal defects scatter the excited electrons resulting in the wave vector condition, making the intensity of the D-band defect dependent. A narrow G-band

is an indication of higher structural ordering and crystallinity. Therefore, the intensity ratio of the D- and G-bands and the shape of these bands can be used to determine the structural ordering in the CMFs. [15]

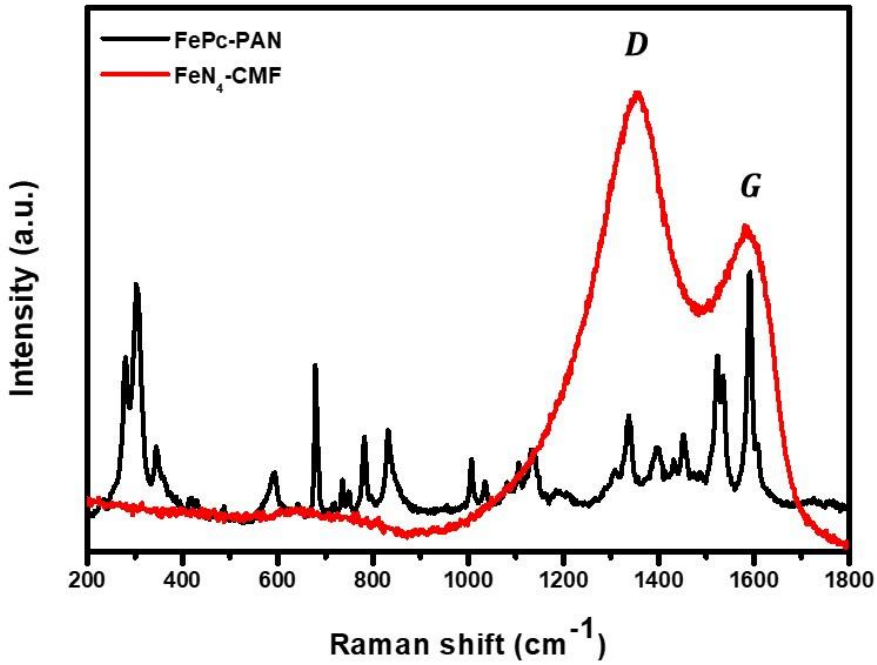

Figure 6.7 Raman spectra of as-electrospun FePc-PAN and heat-treated FeN_4-CMF.

FT-IR spectra are displayed in figure 6.8. A typical IR spectrum for FePc-PAN is characterized by the strong absorption peaks at 721 cm^{-1} for C-H out-of-plane bending vibration and at 750 cm^{-1} for benzene and isoindole in-plane deformation and Fe–N stretching. The bands at 1084 cm^{-1} were attributed to the C–N stretching and vibration in the polymer backbone. Whereas those at 1117 and 1304 cm^{-1} were assigned to Fe–N vibration of pyrrole and C–H in-plane bending vibrations, respectively. The bands exhibited at 1330 cm^{-1} and 1467 cm^{-1} are associated with C=C or C=N stretching of pyrrole ring and isoindole stretching in the plane of FePc macrocycle, respectively. This supports the claim that FePc-PAN fibres were indeed composites of FePc and PAN materials. Similar bands were also detected in the spectrum of Fe-N_4-CMF with an

addition of a new band at 1695 cm^{-1}, which is attributed to Fe–N metal-axial ligands of the diagonally stacked Fe-N_4 molecules on the carbon surface.

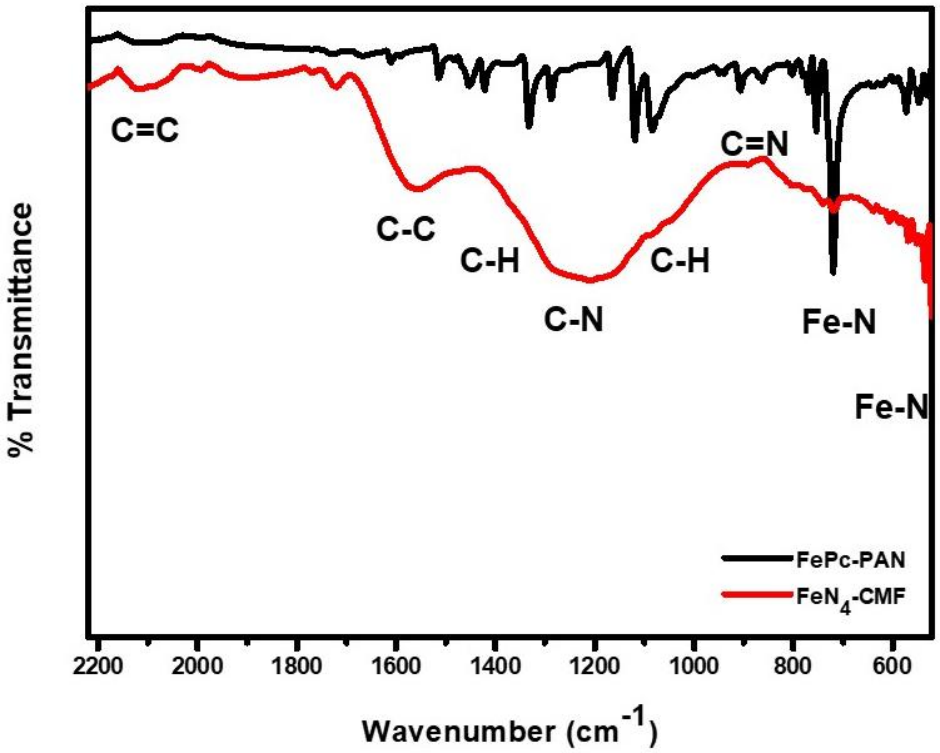

Figure 6.8 FT-IR analysis of as-electrospun FePc-PAN and heat-treated FeN_4-CMF.

With the aim to understand the surface atomic composition and electronic structure of the fibres, XPS analysis was performed for the as-electrospun FePc-PAN and heat-treated FeN_4-CMF and a wide spectrum is shown in figure 6.8 and 6.9, respectively for the different samples taken at the C 1s, N 1s, O 1s and Fe 2p binding energy regions.

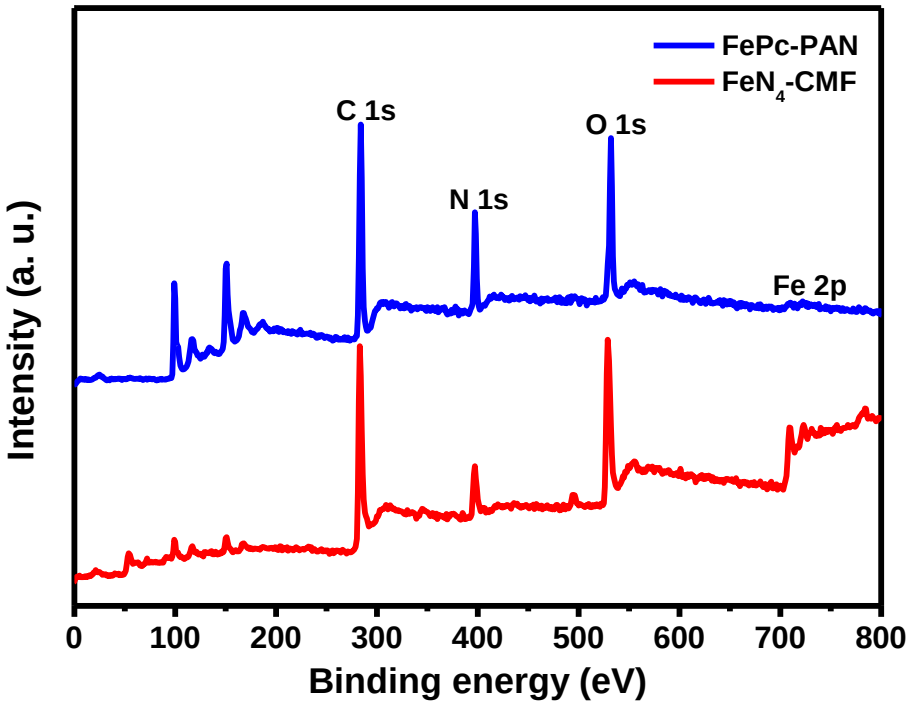

Figure 6.8. XPS spectra of as-electrospun FePc-PAN and FeN_4-CMF fibre.

Seemingly, there are three contributions to the C 1s spectrum for FePc-PAN in figure 6.9 a. The highest peak at approximately 282.4 eV stems from the 24 carbon atoms in the benzene rings. The second highest peak is observed at about 283.6 eV and comes from the eight pyrrole carbons. At around 285.5 eV we see the third contribution to the spectrum, a low intensity structure that as explained by Åhlund et al.[18] is due to shake-up electron transitions mostly from pyrrole carbons. The C1 intensity of FeN_4-CMF, slightly deviated from that of FePc-PAN as revealed in figure 6.9 b. This was explained by the different molecular structure and/or to different geometric organizations of the molecules causing a different kind of molecule-molecule interactions. In figure 6.9 c, O 1s spectra has a characteristic peak at 528.8 eV associated with surface COOH or OH groups and adsorbed water. This contribution is still present after heat treatment as shown in figure 6.9 d. The N1s spectra peak at about 400 eV is more pronounced for FeN_4-CMF than its FePc-PAN counterpart, see figure 6.10 a and b**.** This shows that carbonization and stabilization treatments do not affect the N atoms in the molecules. Figure 6.10 c and d shows comparative fibre Fe^{2+} spectra with corresponding binding energy.

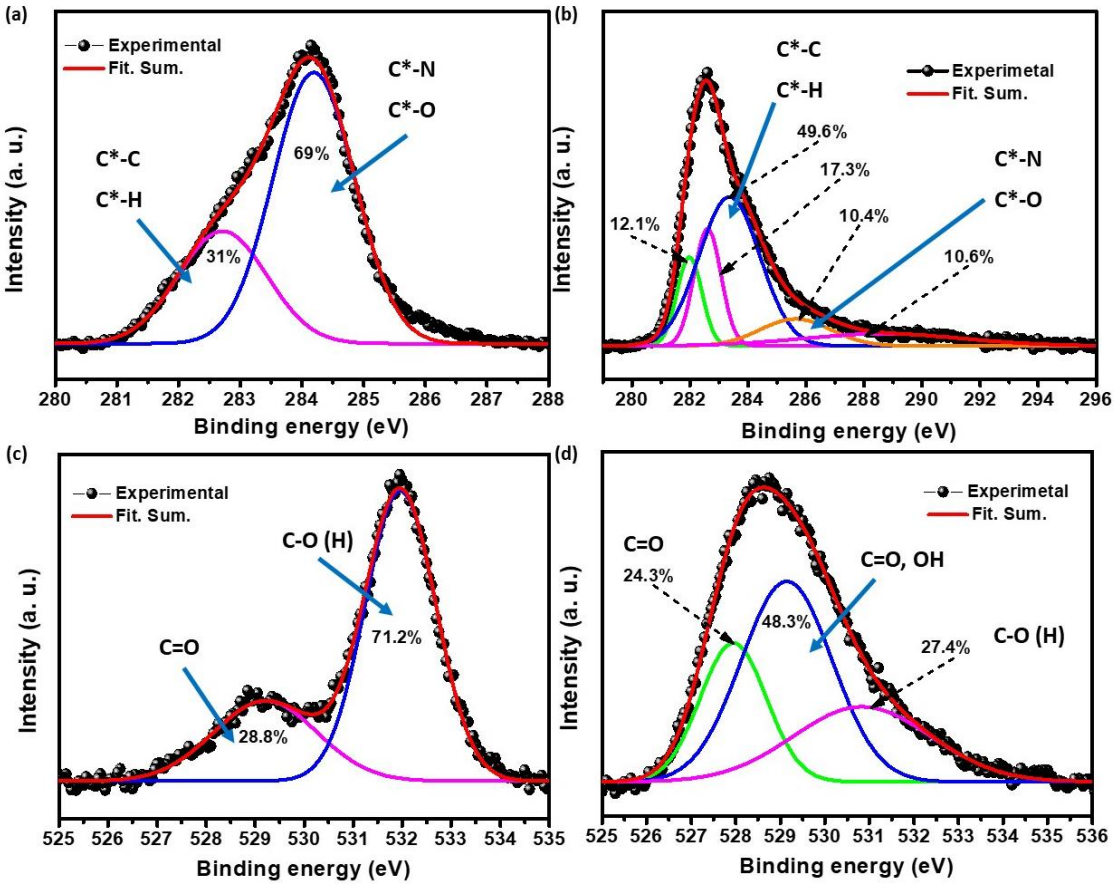

Figure 6.9 Comparative XPS spectrum of (a, b) as-electrospun FePc-PAN and (c, d) thermally-treated FeN_4-CMF for C 1s and O 1s, respectively.

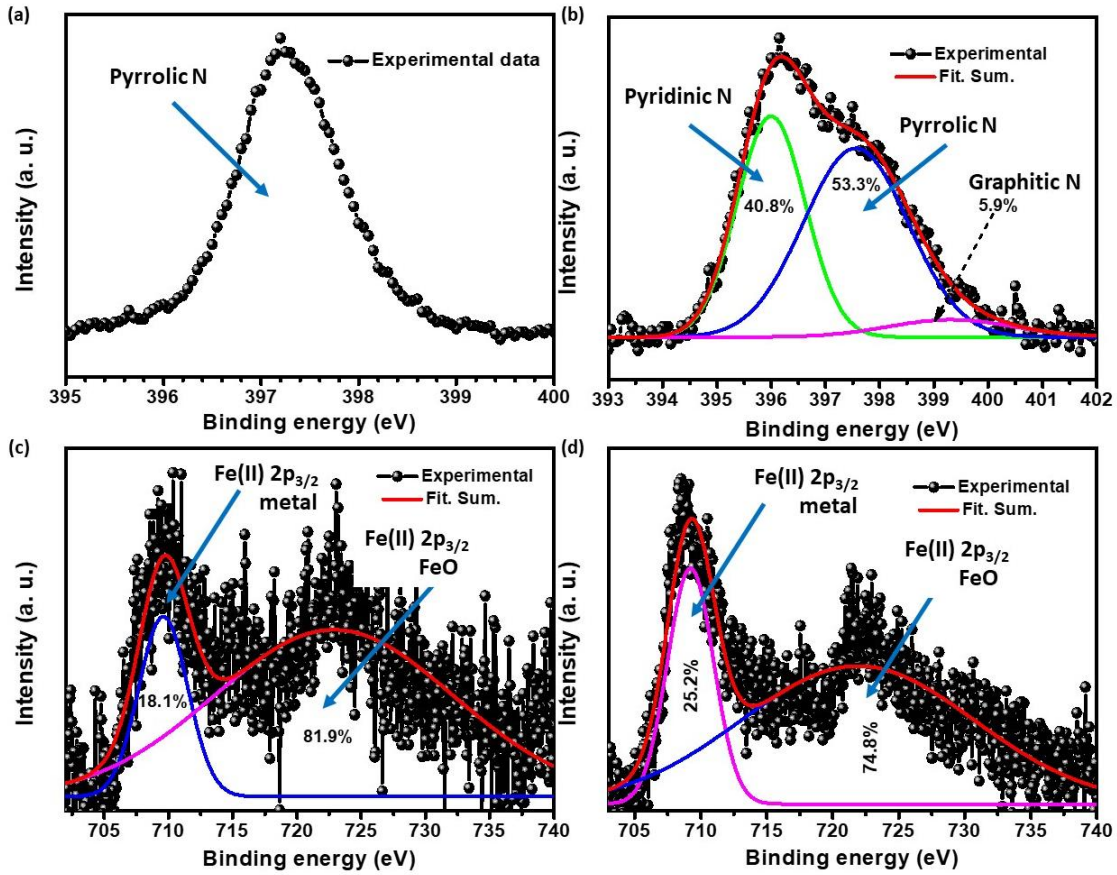

Figure 6.10 Comparative XPS spectrum of (a, c) as-electrospun FePc-PAN and (b, d) thermally-treated FeN_4-CMF for N 1s and Fe $2p_{3/2}$.

Thermogravimetric curves for phthalocyanine and its complexes are shown in figure 6.11. Initially no weight loss was observed for FePc-PAN up to 300 °C. A major decomposition reaction occurred between 360 and 580 °C due to the pyrolytic reactions in the fibre. On the other hand, FeN_4-CMF initial weight loss was detected between 100-352 °C due to loss of moisture and partial evaporation of surface adsorbed gases. The further gradual decline on weight was overall estimated to be approx.10 wt.% and was attributed to the actual pyrolysis by a minor decomposition reaction. Generally, the metal complexes need thermal energy less than that of ligand resulting in weaker bonding force between the metal and ligand. Evidently, FeN_4-CMF has a higher major decomposition temperature compared to FePc-PAN. This may be due to its highest bonding energy such that the metal has full outer orbitals. Finally, there is a steady decrease in weight with a total loss

of 90 and 85 % for FePc-PAN and Fe-N_4-CMF, respectively. Indicating a complete evaporation of any polymer chain fragments from PAN fibres.

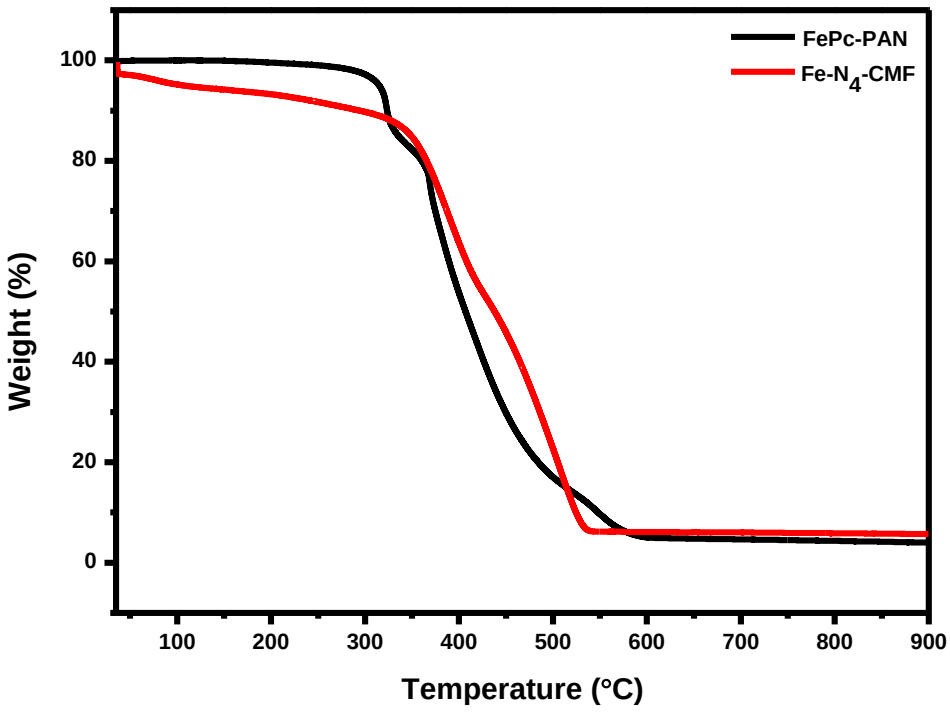

Figure 6.11 TGA analysis of FePc-PAN (a), and FeN_4-CMF (b).

6.2.2 Electrochemical performance

The initial electrochemical performance of the electrospun fibres was studied in a three-electrode system. Figure 6.12 shows CV curves of the (a) FePc-PAN and (b) Fe-N_4-CMF at various scan rates ranging from 5-200 mV s^{-1} in 1M Na_2SO_4 electrolyte solution. The shapes of the curves do not resemble those of typical EDLCs but rather demonstrate pseudocapacitive properties and remain unchanged up to 200 mV s^{-1}. FePc-PAN optimum voltage window is between the potential range of 0 and 0.8 V. For the purpose of comparison, the FeN_4-CMF electrodes were also analyzed at a similar potential window. The curves for FeN_4-CMF maintained a similar shape even at higher scan rates, demonstrating excellent rate capability. In figure 6.12 (c and d), a scan rate of 25 mV s^{-1} was kept constant while varying the potential window between 0.6 and 1.8 V. In the case of FeN_4-CMF (figure 6.12 c), the CV curves seem stable up to 1.6 V which is much better than the 1.0 V range provided by the FePc-PAN electrodes in figure 6.12 d. This suggests

the porous structure of FeN_4-CMF coupled with physicochemical properties of the material have a positive effect on the accessibility of ions by the electrolyte solution.

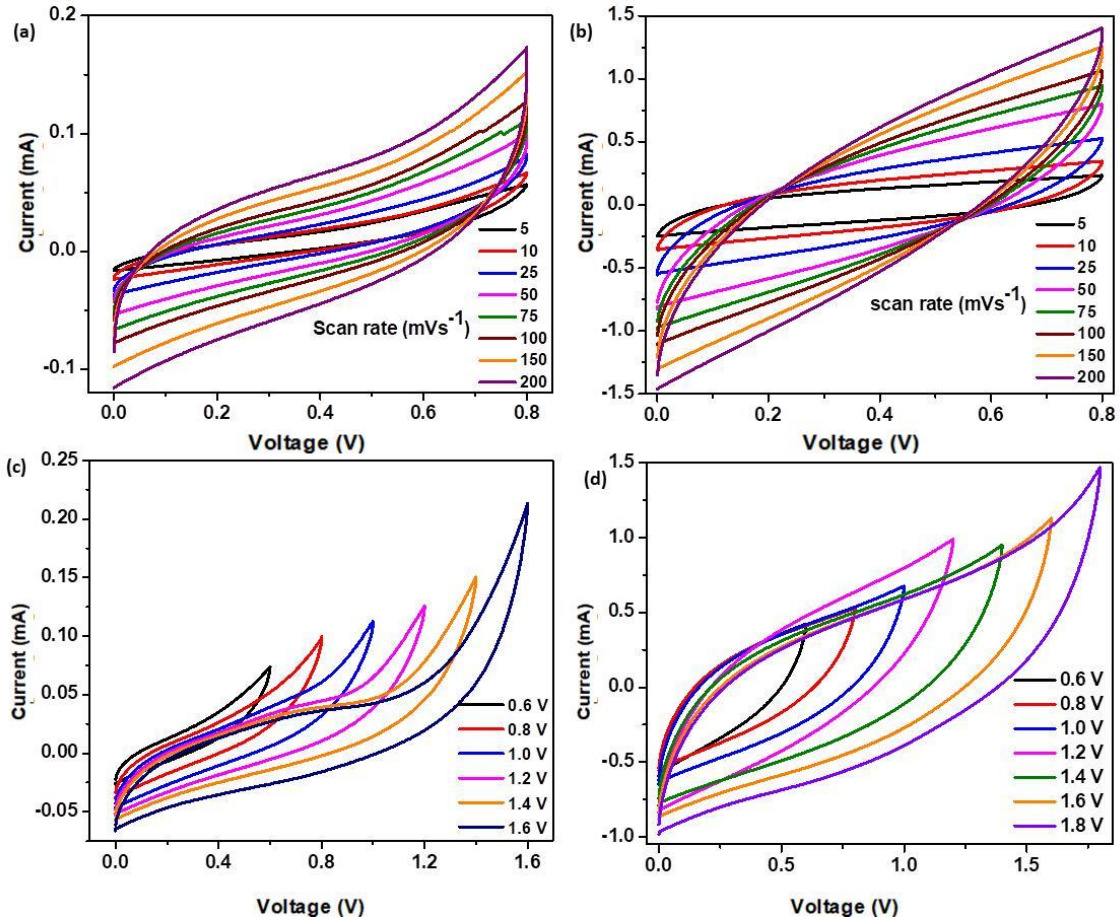

Figure 6.12 (a and b) CV between 5-200 mV s^{-1}, and (c and d) CV at 25 mV s^{-1} between 0.6- 1.8 V of FePc-PAN and FeN_4-CMF, respectively, in 1M Na_2SO_4 electrolyte using a three-electrode SPCEs.

Figure 6.13 demonstrates the comparative CV plots at 25 mV s^{-1} for both FePc-PAN and FeN_4-CMF using the T-type cells. The potential window for FePc-PAN was within 0.5 to -1.0 V and within 0 V to 1.2 V for FeN_4-CMF, respectively. The larger area under the curve shown by the FeN_4-CMF electrodes indicates better response with regards to electrochemical activity. The galvonastatic charge-discharge curves in figure 6.14 are pseudocapacitive. The deviation observed for FePc-PAN electrodes during a discharge cycle indicates possible confinement of redox reactions on the electrode surface. The

extended discharge cycle time for FeN_4-CMF is indicative of better supercapacitive performance.

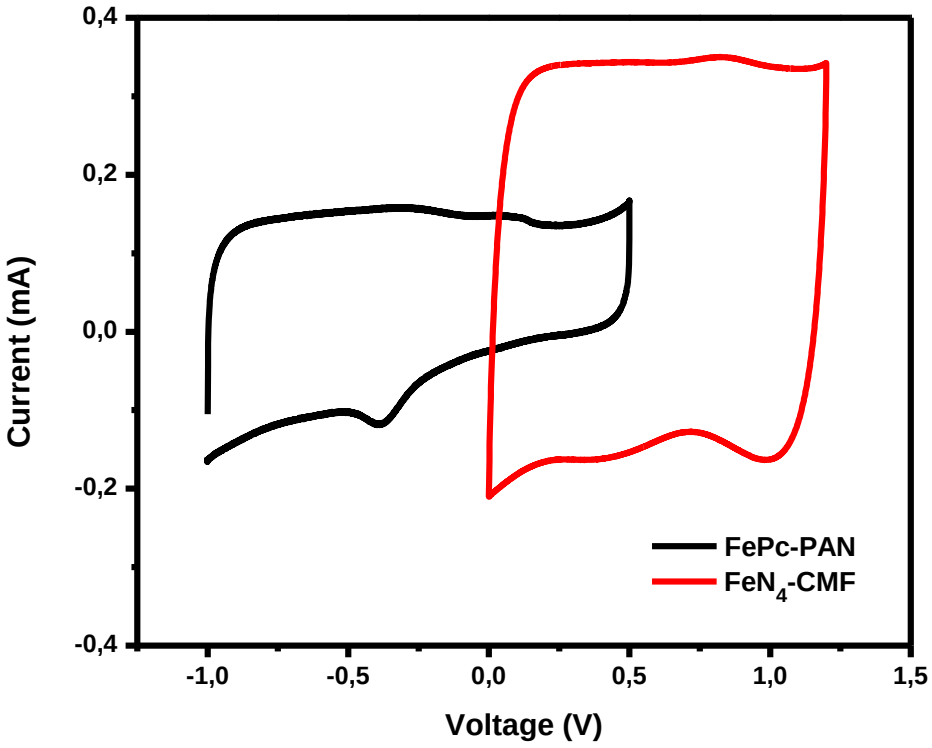

Figure 6.13 Shows CV at 25 mV s^{-1} for the electrospun FePc-PAN and FeN_4-CMF.

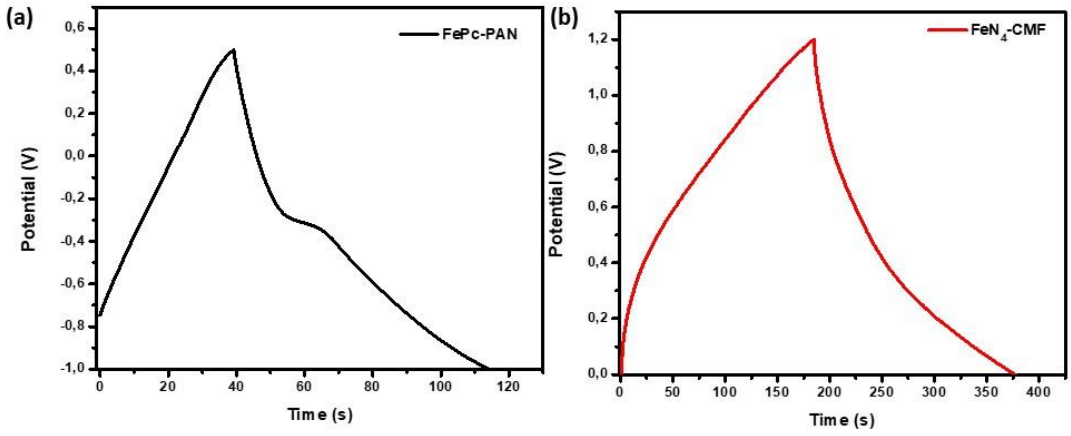

Figure 6.14 Galvanostatic charge-discharge curves at current densities 0.1 A g^{-1} for the electrospun (a) FePc-PAN and (b) FeN_4-CMF, respectively.

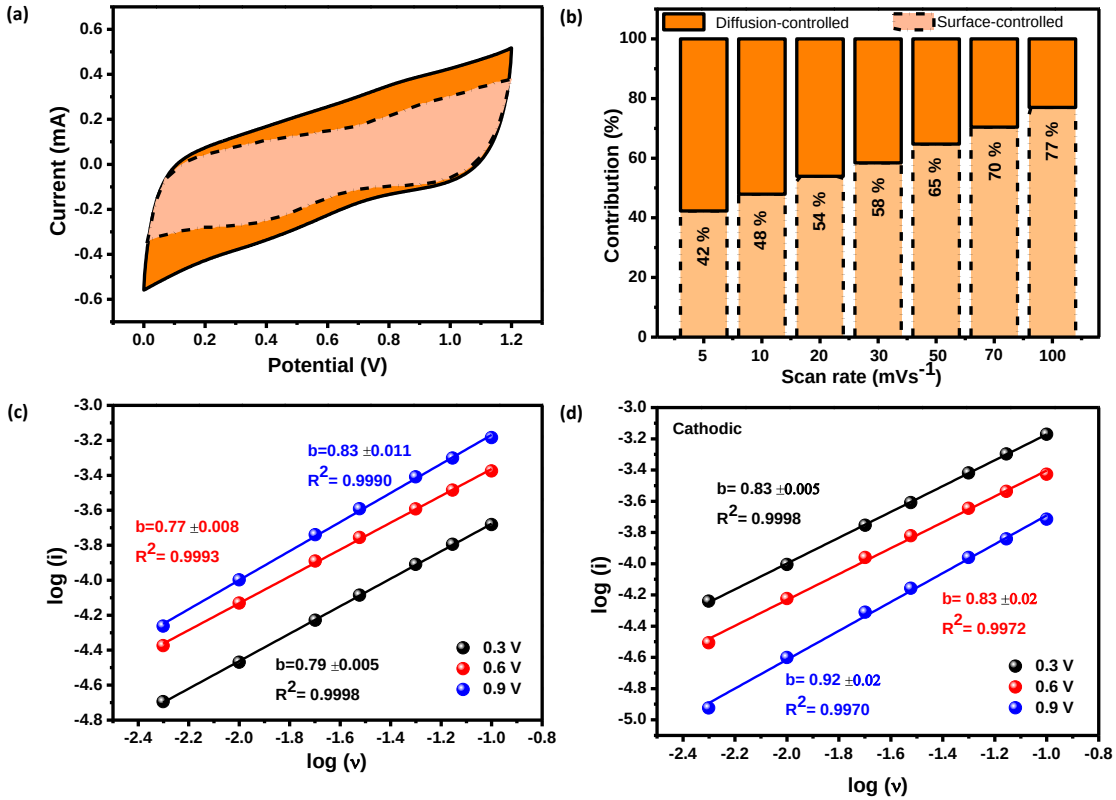

Figure 6.15 Supercapacitive study of FeN_4-CMF electrodes based on a three-electrode system.

The results from two electrode configuration for FeN_4-CMF are plotted in figure 6.16. The experiments were cried out in symmetrical configuration in 1 M Na_2SO_4 aqueous electrolyte solution. The CV curves demonstrated in figure 6.16 a are rectangular in shape, typical for a supercapacitor with electrochemical features of a pseudocapacitor. The current response gradually increased with higher scan rates resulting in a maximum capacitance 105 F g^{-1} at 100 mV s^{-1}. On the basis of galvanostatic charge-discharge curves (see figure 6.16 b), the presence of large gradient in the curves corresponding to FeN_4-CMF indicates a largely capacitive behaviour. The specific capacitance reached a maximum of 140 F g^{-1} at a current density of 0.1 A g^{-1}, and rapidly reduced with increasing current density as seen in figure 6.16 c. Figure 6.16 d shows the power density versus the energy density of FeN_4-CMF in the range of 0.1 -10 A g^{-1}.

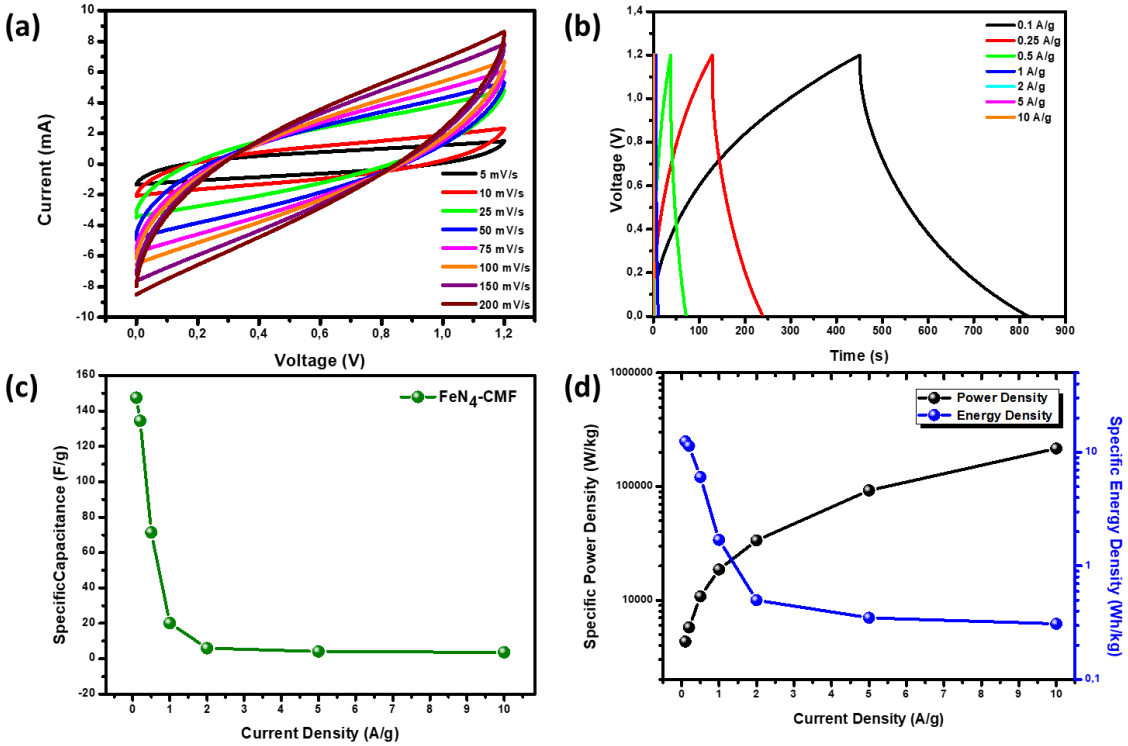

Figure 6.16 (a) CV, (b) galvonstatic charge-discharge curves, (c) specific capacitance at various current densities, and (d) the Ragone plot of FeN_4-CMF electrodes.

The cycling stability data of the FeN_4-CMF electrodes is provided in figure 6.17. The capacitance retention was 96% after 2000 cycles. The plot demonstrates that the potential window for the FeN_4-CMF electrodes was 1.2 V during cycling. The cycling performance shows good reversibility of the Fe^{3+} and Fe^{2+} redox reactions and successful integration of FeN_4 with a conductive CMF network.

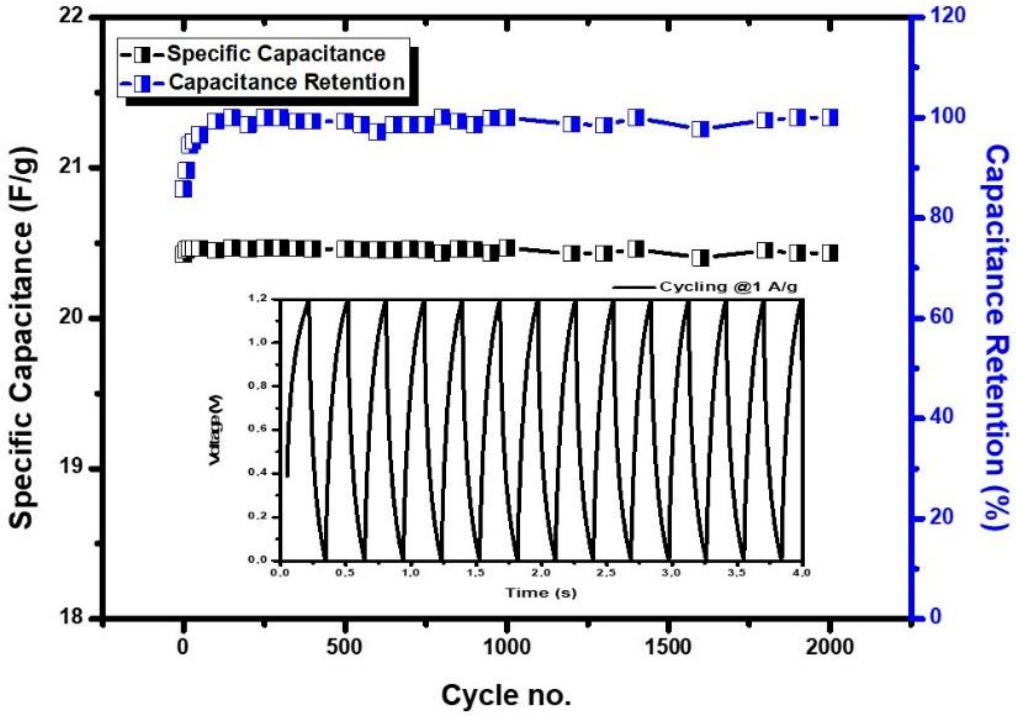

Figure 6.17 FeN_4-CMF specific capacitance and capacitance retention during cycling stability test at 1 A g^{-1} in 1M Na_2SO_4 aqueous electrolyte for 2000 cycles.

Electrochemical impedance spectroscopy was used to further understand the electron transfer processes occurring at the electrode-electrolyte interface. Figure 6.18 demonstrates the Nyquist plot for FePc-PAN and FeN_4-CMF fibres. Subsequently the spectra were fitted with modified Randles equivalent electrical cicuits. The fitting parameters involve the electrolyte resistance (Rs) electron-transfer resistance (Rct), constant phase element (CPE), double layer capacitance (Cdl) and Warburg-type impedance (Zw) which is associated with the diffusion of the ions of the redox probe, represented by the Randles circuit in figure 6.18c.

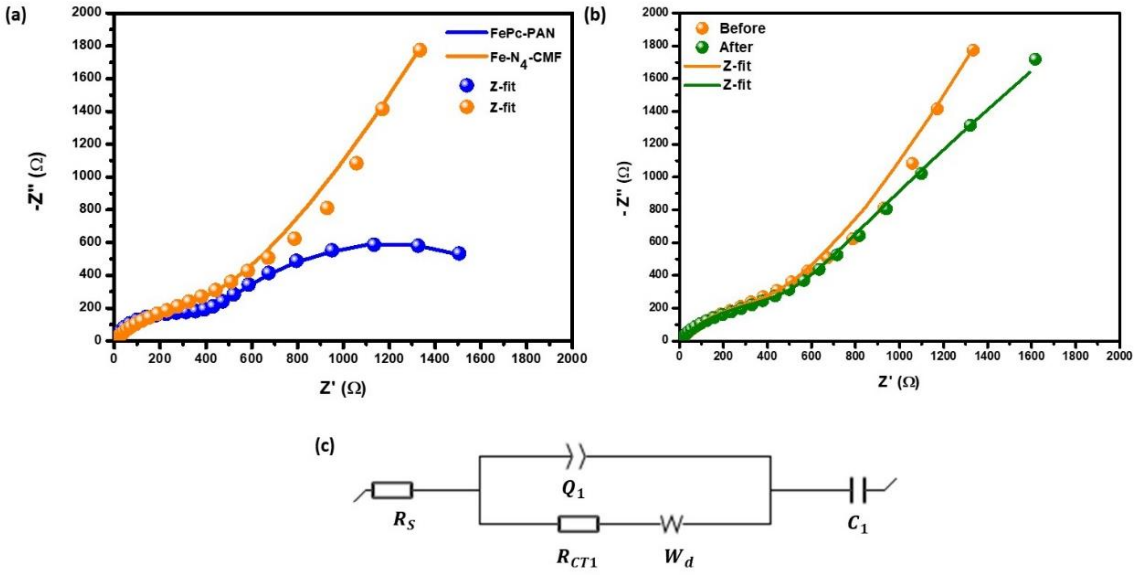

Figure 6.18 (a) Comparative EIS analysis of FePc-PAN and FeN_4-CMF, (b) EIS of FeN_4-CMF before and after cycling, and (c) electrical equivalent circuit used in fitting the FeN_4-CMF electrode Nyquist plots.

Figure 6.19 a is a photograph of the pouch cells connected in series. The cells were charged and discharged at 1 A g^{-1} as demonstrated by the curves in figure 6.19 b. The electrical circuit in figure 6.19 c reflects how the electrodes were connected.

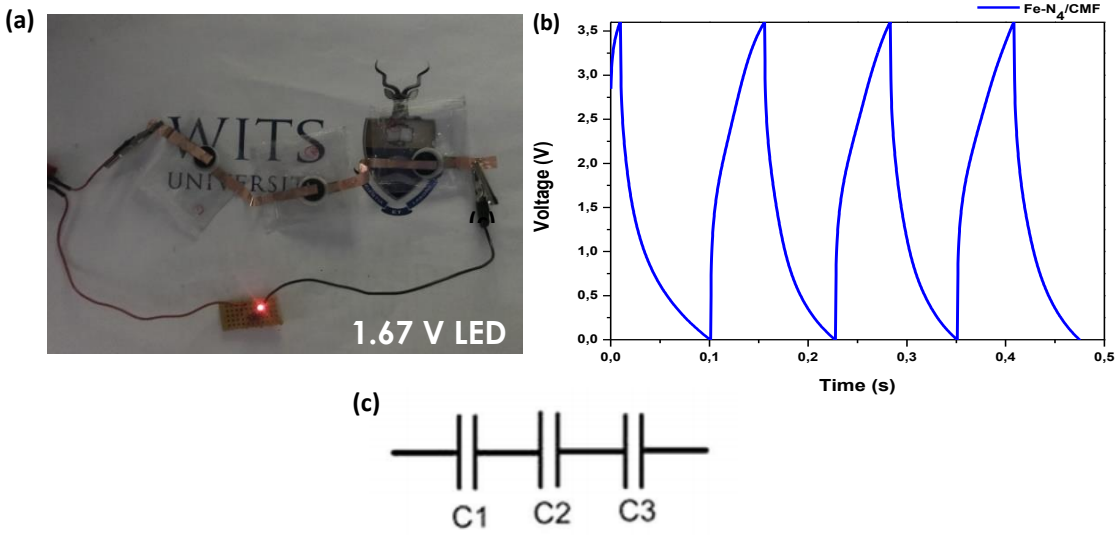

Figure 6.19 (a) Flexible supercapacitor based on FeN_4-CMF electrodes connected in series and lighting up a 1.67 V LED at a 0° bending angle, (b) charge-discharge curves from the electrodes with a 3.6 V window, and (c) the electrical circuit.

6.3 Conclusion

Successful encapsulation of FePc in electrospun PAN fibres was achieved during electrospinning. High surface area defect-rich FeN_4-CMF was obtained from multi-step heat treatment. FeN_4-CMF composite exhibited higher specific capacitance (147 F g^{-1}) than its counterpart, FePc-PAN. The performance was accredited to the redox processes involving the complex ion species on the electrode surface and porous nature of the fibres after heat treatments. Better conductivity and improved cycling stability were attributed to the full encapsulation of the Fe-N_4 particles within the highly conductive CMF matrix, which prevented the particles from detachment during cycles.

6.4 References

[1] Agboola, B.; Ozoemena, K. I.; Nyokong, T. Comparative efficiency of immobilized non-transition metal phthalocyanine photosensitizers for the visible light transformation of chlorophenols, *J. Mol. Catal. A Chem.* **2006**, 248, 84.

[2] Ozoemena, K. I.; Nyokong, T. Surface electrochemistry of iron phthalocyanine axially ligated to 4-mercaptopyridine self-assembled monolayers at gold electrode: applications to electrocatalytic oxidation and detection of thiocyanate, *J. Electroanal. Chem.* **2005**, 579, 283.

[3] Ozoemena, K. I.; Nkosi, D.; Pillay, J. Influence of solution pH on the electron transport of the self-assembled nanoarrays of single-walled carbon nanotube-cobalt tetra-aminophthalocyanine on gold electrodes: electrocatalytic detection of epinephoursine, *Electrochim. Acta*. **2008**, 53, 2844.

[4] Chidembo, A. T.; Ozoemena, K. I.; Agboola, B. O.; Gupta, V.; Wildgoose, G. G.; Compton, R. G. Nickel (II) tetra-aminophthalocyanine modified MWCNTs as potential nanocomposite materials for the development of supercapacitors, *Energy Environ. Sci.* **2010**, 3, 228.

[5] Sehlotho, N.; Nyokong, T. Effects of ring substituents on electrocatalytic activity of manganese phthalocyanines towards the reduction of molecular oxygen. *J. Electroanal. Chem*. **2006**, 595, 161-167.

[6] Yamaki, J.; Yamaji, A. Phthalocyanine Cathode Materials for Secondary Lithium Cells. *J. Electrochem. Soc.* **1982**, 129, 5-9.

[7] Sakamoto, K.; Ohno-Okumura, E. Syntheses and Functional Properties of

Phthalocyanines. *Materials*. **2009**, 2, 1127-1179.

[8] Samanta, M.; Howli, P.; Ghorai, U. K.; Mukherjee, M.; Bose, C.; Chattopadhyay, K. K. Solution processed Copper Phthalocyanine nanowires: A promising supercapacitor anode material. *Physica E Low Dimens. Syst. Nanostruct.* **2019**, 114, 113654.

[9] Sakamoto, K.; Ohno-Okumura, E. Synthesis and functional properties of phthalocyanines. *Materials*. **2019**, 2, 1127-1179.

[10] Sorokin, A. B. Phthalocyanine Metal Complexes in Catalysis. *Chem. Rev.* **2013**, 113, 8152-8191.

[11] Chen, G.; Jang, B. Z.; Zhamu, A. Encapsulated phthalocyanine particles, high-capacity cathode containing these particles, and rechargeable lithium cell containing such a cathode. *US13/573,298* https://patents.google.com/patent/US20140072879.

[12] Jahnke, H.; Schönborn, M.; Zimmermann, G. Organic dyestuffs as catalysts for fuel cells. *Top. Curr. Chem.* **1976**, 61, 133-181.

[13] van Veen, J. A. R.; Colijn, H. A.; van Baar, J. F. On the effect of a heat treatment on the structure of carbon-supported metalloporphyrins and phthalocyanines. *Electrochim. Acta*, **1988**, 33, 801-804.

[14] Kovalenko, I.; Bucknall, D. G.; Yushin, G. Detonation Nanodiamond and Onion-like-Carbon-Embedded Polyaniline for Supercapacitors. *Adv. Funct. Mater*. **2010**, 20, 3979-3986.

[15] Borgohain, R.; Li, J.; Selegue, J. P.; Cheng, Y. T. Electrochemical Study of Functionalized Carbon Nano-Onions for High-Performance Supercapacitor Electrodes. *J. Mater. Chem. C*. **2012**, 116, 15068-15075.

[16] Miller, H. A.; Bevilacqua, M.; Filippi, J.; Lavacchi, A.; Marchionni, A.; Marelli, M.; Moneti, S.; Oberhauser, W.; Vesselli, E.; Innocenti, M.; Vizza, F. Nanostructured Fe-Ag electrocatalysts for the oxygen reduction reaction in alkaline media. *J. Mater. Chem. A*, **2013**, 1, 13337-13347.

[17] Gojkovic, S. L.; Gupta, S.; Savinell, R. F. Heat treated iron (III) tetraethoxy porphyrin chloride supported on high surface area carbon as an electrocatalyst for oxygen reduction: Part III Detecetion of oxygen peroxide during oxygen reduction. *Electrochim. Acta*. **1999**, 45, 889-897.

[18] Goue´rec, P.; Savy, M.; Riga, J. Oxygen reduction in acid media catalyzed by heat treated cobalt tetraazaannulene supported on an active charcoal. *Electrochim. Acta*.

1998, 43, 743.

[19] Scherson, D.; Tanaka, A. A.; Gupta, S. L.; Tryk, D.; Fierro, C.; Holze, R.; Yeager, E. B.; Lattimer, R. P. Transition metal macrocycles supported on high area carbon: pyrolysis-mass spectrometry studies. *Electrochim. Acta.* **1986**, 31, 1247.

[20] Lefèvre, M.; Dodelet, J. P.; Bertrand, P. O_2 Reduction in PEM Fuel Cells: Activity and Active Site Structural Information for Catalysts Obtained by the Pyrolysis at High Temperature of Fe Precursors. *J. Phys. Chem. B.* **2000**, 104, 11238-11247.

[21] Schulenburg, H.; Stankov, S.; Schu¨nemann, V.; Radnik, J.; Dorbandt, I.; Fiechter, S.; Bogdanoff, P.; Tributsch, H. Catalysts for the oxygen reduction from heat-treated iron (III)tetramethoxyphenylporphyrin chloride: structure and stability of active sites. *J. Phys. Chem. B.* **2003**, 107, 9034-9041.

[22] Sakamoto, K.; Ohno-Okumura, E. Syntheses and Functional Properties of Phthalocyanines. *Materials.* **2009**, 2, 1127-1179

[23] Yadav, V. K.; Bhardwaj, N. Introduction to Supercapacitors and Supercapacitor Assisted Engine Starting System International. *Int. J. Eng. Res.* **2013**, 4, 583-588

[24] Simon, P.; Gogotsi, Y.; Dunn, B. Where Do Batteries End and Supercapacitors Begin? *Science.* **2014**, 343, 1210-1211.

[25] Huang, K. J.; Wang, L.; Liu, Y. J.; Wang, H. B.; Liu, Y. M.; Wang, L. L. Synthesis of polyaniline/2-dimensional graphene analog MoS_2 composites for high-performance supercapacitor. *Electrochim. Acta*. **2013**, 109, 587-594.

[26] Simon, P.; Gogotsi, Y. Materials for electrochemical capacitors. *J. Nanosci. Nanotechnol*. **2010**, 320-329.

CHAPTER SEVEN

Structural modification of electrode materials through Fe^{2+} vacancies in OLC-CNF@MoS_2 composites for enhanced electrochemical energy storage

7.1 Introduction

Defects have been reported to positively tune the electrochemical properties of supercapacitor electrodes in one way or the other. [1-5] For instance, in the case of a vacancy defects, the open pores from the missing atom in the lattice site facilitate the mass transport of ions and in turn become an extra host site for alkali cation intercalation which ultimately provides more charge storage capacity. The local distortions around vacancies are said to be responsible for relieving electrochemical strains such that cycling stability of the electrode material improves. In light of these benefits, developing high performing defect rich charge storage materials has been a major focus for some researchers. [6]

MoS_2 electrodes are increasingly used in the energy storage field due to their layered structured nature which offers efficient intercalation for high capacitance potential. Recent research has focused on the synthesis of MoS_2 on carbon support for enhanced conductivity response as electrode materials in both batteries and supercapacitors. [7] MoS_2 structure is characterized by the covalently bonded Mo layer to two S layers, which are stacked and held together by Van Der Waals forces, enabling intercalation of electrolyte ions. From an energy storage perspective, the most advantageous property of this material is its center Mo atom that possess a range of oxidation states from +2 to +6, giving it an additional capacitance via pseudocapacitance. Moreover, changes in ion arrangements within the S-Mo-S lattice allows structural transformation between trigonal 1T, hexagonal 2H or rhombohedral 3R. [8-13] The anisotropy of d-band hybridization and the strong Mo-S p-d interaction are significant elements determining the structural phase transition and subsequently electrochemical properties. 1T MoS_2 phase is more conductive than the semiconducting 2H phase. [14]

To enhance the electrochemical storage capabilities of MoS_2, Chen et al. [15] suggests doping and using nano-sized MoS_2 which accelerates electronic transfer and controls phase transitions during charge and discharging. However, the electronic conductivity of MoS_2 is still lower compared to graphite, and the specific capacitance of MoS_2 is still very limited when used alone for energy storage applications. [16-21] As evident in several literature reports, there is a need to improve the capacitance of MoS_2 with conductive materials. To tackle the aforementioned, onion-like carbons (OLC) are an interesting choice, due to their high electrical conductivity, large external surface area, and nanoscopic size.[22-24] Previously it was recognized that, when MoS_2 is supported on a carbonaceous surface, the electrolyte needs to diffuse through the surface of carbon materials to react with the MoS_2 underneath, thus limiting the rate capability of the electrode. Secondly, these nanocomposites usually contain a significant amount (>30 wt. %) of barely active carbon materials, which not only decreases the mass loading of MoS_2 but also more seriously over confines the electrodes, thus causing mechanical strain again. [19] Thus, it is highly desirable to develop a better 1D structure of the MoS_2/carbon composite with high specific capacity and excellent cycling stability.

Herein, electrospun fibres consisting of FePc integrated with OLC nanoparticles were encapsulated with MoS_2 sheets and engineered with defects in order to alleviate the well-known bottlenecks associated with poor accessibility of carbon in the electrode material. The influence of the induced defects on the physicochemical properties of the electrospun fibre composite material have been investigated and correlated with the electrochemical behaviour of the electrodes. The defects were induced by the chemical etching process of the Fe atoms in the FeN_4-OLC-CNF@MoS_2 composite and resulted in its counterpart denoted, $(FeN_4)_d$-OLC-CNF@MoS_2 composite.

Their synthesis route is outlined in figure 7.1. The defects were used as a powerful tool for improving material intercalation capabilities resulting in a new paradigm of energy storage electrode material design. We report that the pseudocapacitive properties, particularly their cycling stability and electronic conductivity of $(FeN_4)_d$-OLC-CNF@MoS_2 are intrinsically linked with the deficient Fe^{2+} atoms in the composite coupled with the high electrical conductivity of MoS_2 sheets and accessibility of the carbon component.

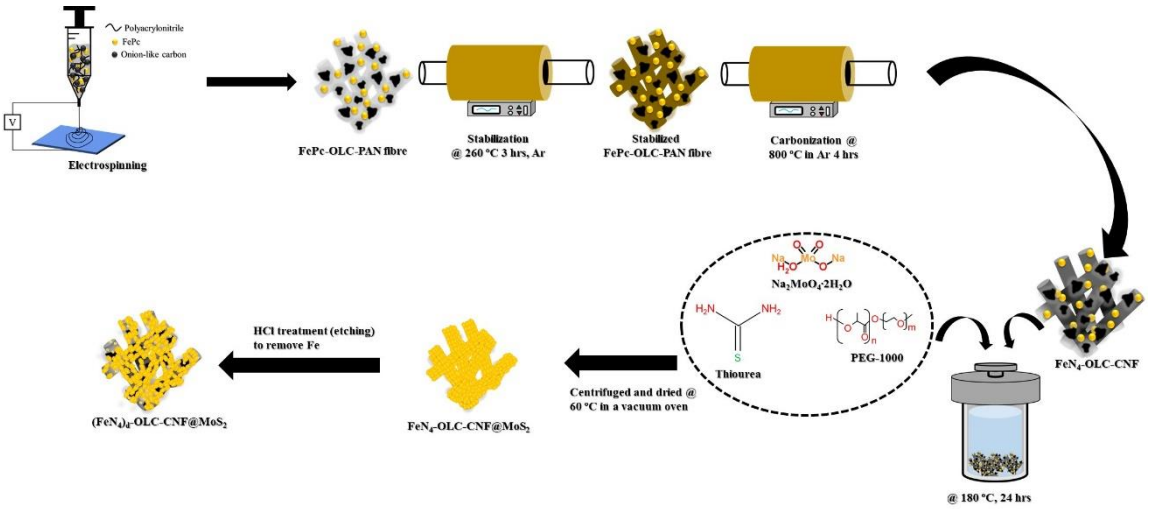

Figure 7.1 Schematic for synthesis of $(FeN_4)_d$-OLC-CNF@MoS_2 composite electrode material.

7.2 Results and discussions

7.2.1 Material Characteristics

Figure 7.2 shows SEM (on the left) and TEM (on the right) images of the original electrospun PAN fibre. The morphology of the fibres shows randomly oriented nanofibres with uniform diameter. When measured with the TEM, as shown below, the diameter was 670 nm.

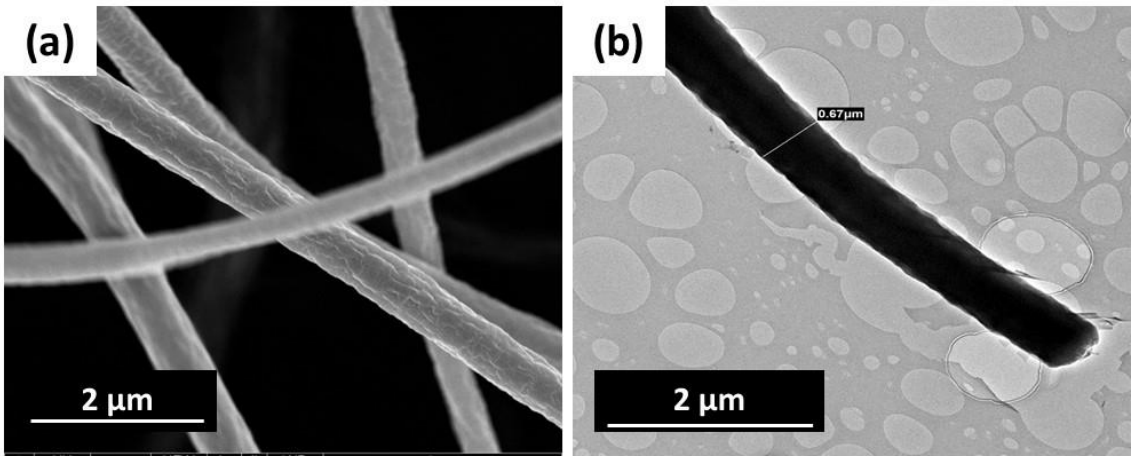

Figure 7.2 (a) SEM and (b) TEM micrographs of as electrospun PAN fibres.

In separate solutions, DMF solvent was saturated with OLC, FePc and PAN in a 1:1 stoichiometry. Once OLC and FePc had been added into the PAN solution slurry, the OLC-FePc-PAN composite fibre was produced via electrospinning method and the

resulting fibre morphology is shown in figure 7.3. It was noted that the addition of OLC and FePc compounds significantly altered the fibre morphology (i.e. diameter and surface roughness) from its original PAN counterpart depicted in figure 7.2. The diameter of OLC-FePc-PAN fibres ranged between 500 nm to 2 µm. Such high fibre diameter range was likely caused by the inhomogeneous distribution of particles in the polymer solution. Inhomogeneity had an adverse effect on the variability of the polymer solution properties during electrospinning.

The total molecular weight of the polymer solution ($Mw_{(FePc)}$= 568.4 g mol^{-1} + $Mw_{(OLC)}$= 12.011 g mol^{-1} + $Mw_{(PAN)}$= 53.062 g mol^{-1}) was relatively high in comparison to previous fibres from this study. However, the solution possessed a relatively high viscosity due to the solvent content. The effects of surface tension was restrained and this resulted in the fibre diameter variation. The rough nature of the surface morphology shown in figure 7.3 is due to the FePc and OLC agglomerates imbedded in a PAN fibre. The fibre composite diameters were unevenly distributed as a result of the phase separation with higher flow rate requirements followed by fast evaporation of the polymer solution during spinning process.

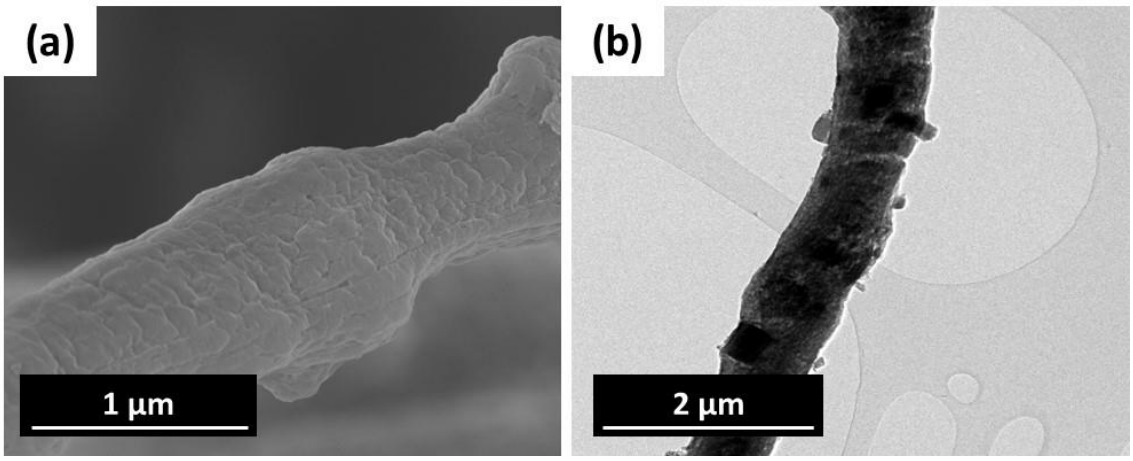

Figure 7.3 (a) SEM and (b) TEM micrographs of as electrospun OLC-FePc-PAN fibres.

Upon thermal treatment for stabilization and carbonization, the fibres maintained the 1D morphology, indicating a successful heat treatment process as shown in figure 7.4. As mentioned in the previous chapter (six), when FePc undergoes sufficient heat treatment in an inert environment, between 600 and 900 °C, various components are decomposed and thus molecular structural changes. [25] The centered iron bonded to four nitrogen atoms (Fe-N_4) originally bonded with Pc becomes bonded to the carbon fibre matrix. The non-carbon elements in PAN also decomposed during high temperature treatment resulting in weight loss, thus the fibre diameter reduced. The thermal treatment enabled the formation of a highly porous fibre with pores varying from micro-, meso- to macropores from inside and between the fibres.

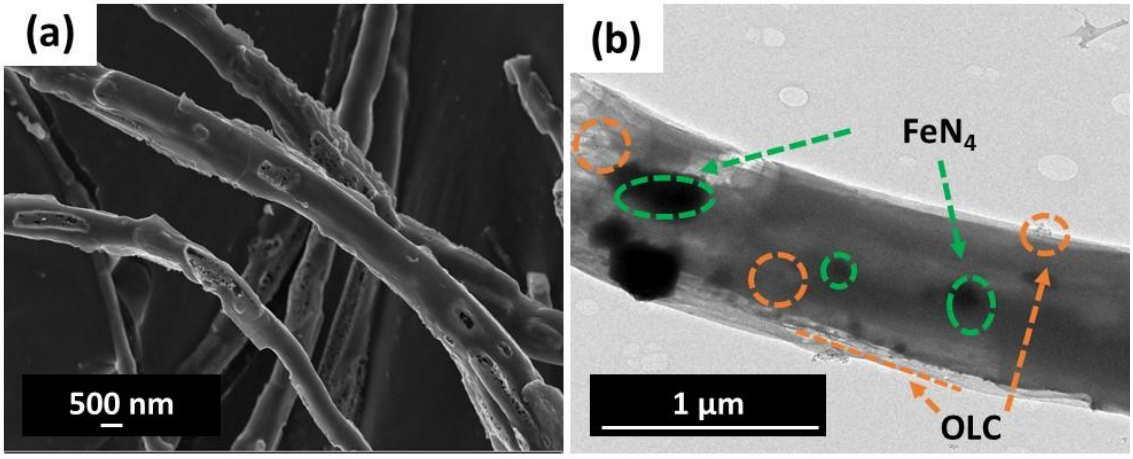

Figure 7.4 (a) SEM and (b) TEM micrographs of stabilized and carbonized FeN_4-OLC-CNF composites.

The stabilized and carbonized fibres were subjected to a hydrothermal treatment with MoS_2 reagents (i.e. $Na_2MoO_4{\cdot}2H_2O$ thiourea and PEG-1000), in which the fibre composites acted as nucleation sites for MoS_2 sheets to grow on and around its surface. The SEM micrograph of FeN_4-OLC-CNF@MoS_2 composites is illustrated in figure 7.5 (left) at lower magnifications. The morphology of the fibre composites was characterized by randomly oriented structural framework with visible hierarchical MoS_2 sheets on the surface of the fibres. Figure 7.5 (right) shows the subsequent fibre composites after removal of Fe^{2+} atoms in HCl, resulting in a fibre composites with deficient Fe atoms and its composites was denoted as $(FeN_4)_d$-OLC-CNF@MoS_2. The original encapsulated fibre composites showed fragmented MoS_2 sheets after etching.

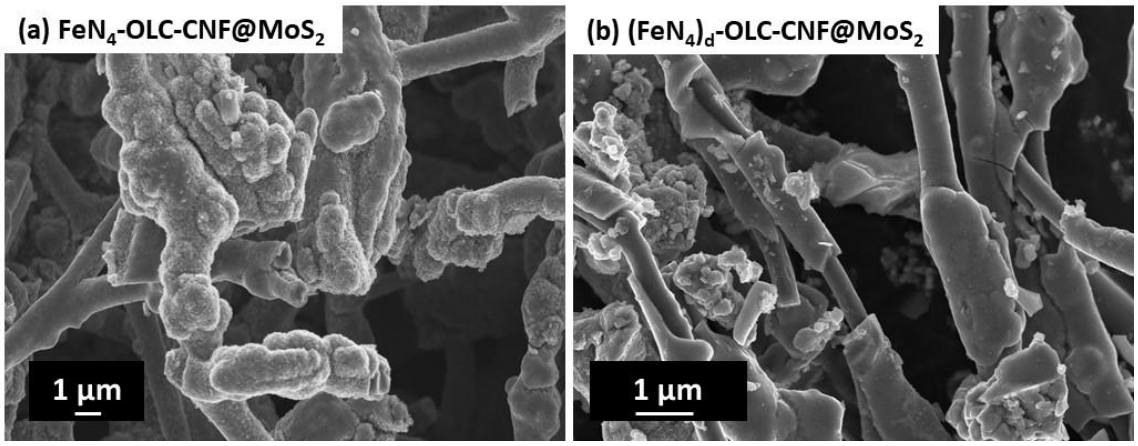

Figure 7.5 (a) SEM micrograph of MoS_2 encapsulated FeN_4-CNF composites; FeN_4-OLC-CNF@MoS_2 composite and (b) subsequent Fe removed composite $(FeN_4)_d$-OLC-CNF@MoS_2.

From the high-resolution SEM micrographs in figure 7.6 it is clear that the composite morphology of FeN_4-OLC-CNF@MoS_2 presents hierarchical porous MoS_2 encapsulated onto the fibres. The change in surface morphology of the fibres after HCl treatment was supported by the presence of pores and defects in the form of fractured pieces of MoS_2 layer. The modification of the morphology enables accessibility of the OLC embedded on the fibre and the carbon from the fibre itself. The easy access to the different components offering both EDLC and pseudocapacitors characteristics is of importance to maximize the electrochemical storage capacity.

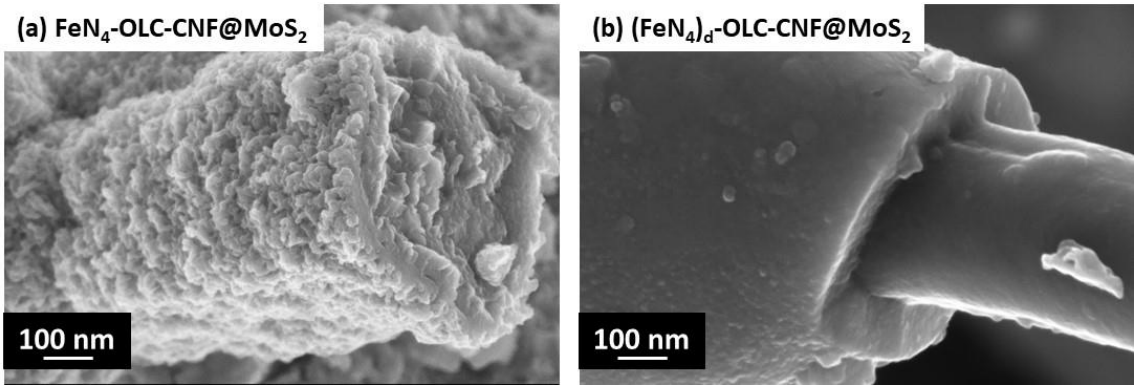

Figure 7.6 SEM micrographs of (a) FeN_4-OLC-CNF@MoS_2 and (b) $(FeN_4)_d$-OLC-CNF@MoS_2 fibre composites.

The surface elemental composition was investigated by EDS, firstly to verify the presence of main elements in the composite namely, C, Fe, Mo and S and secondly, to confirm the amount of Fe before and after removal via HCl treatment. A comparative summary on the weight percent of each element for the two composite materials obtained by mapping through SEM-EDS is shown in figure 7.7. Overall, the content of the elements changed from FeN_4-OLC-CNF@MoS_2 to (FeN_4)d-OLC-CNF@MoS_2 most notably that of Mo before and after Fe removal. It is likely linked to the high accessibility of Mo atoms in its various oxidation states as a results of defect creation in the structure. The significantly less N atoms in the (FeN_4)d-OLC-CNF@MoS_2 composite are also indicative of the breakdown of the FeN_4 component due to the extracted Fe. As can be seen from the spectra in figure 7.8, Mo and S have the highest content followed by C. Interestingly, Fe content before was up to 0.5 wt.% (figure 7.8a) and 0.2 wt.% (figure 7.8b) after removal, this confirms that the removal of some Fe^{2+} ions was successful although small traces may still be present in the final composite.

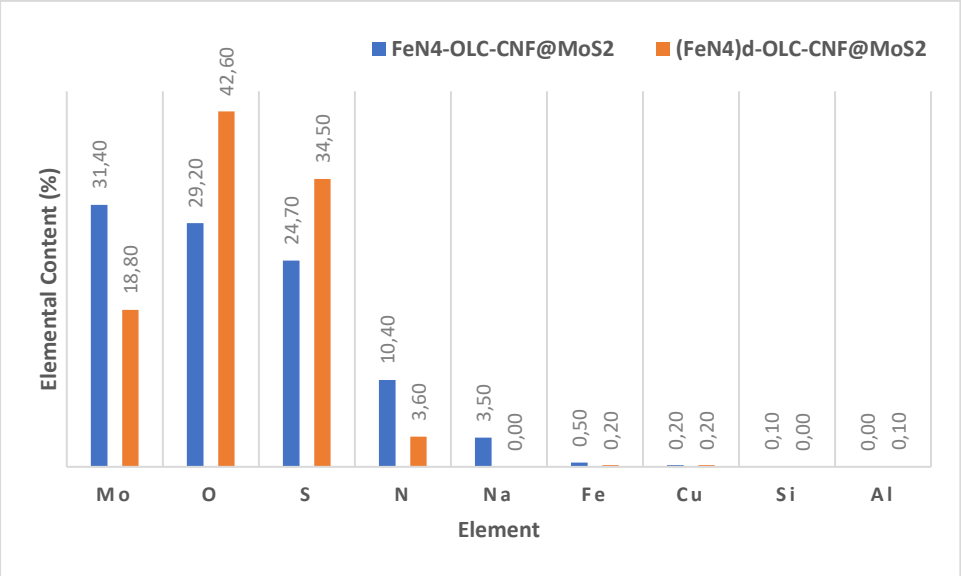

Figure 7.7 EDS Spectral images for FeN_4-OLC-CNF@MoS_2 versus $(FeN_4)_d$-OLC-CNF@MoS_2.

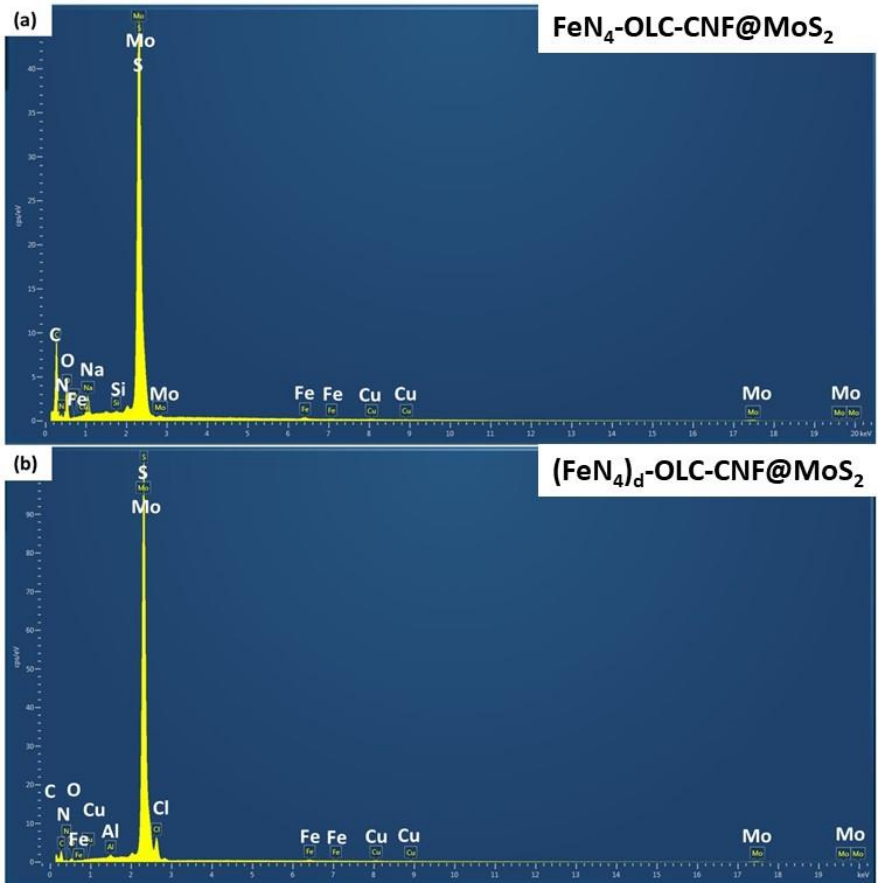

Figure 7.7 EDS Spectral images for (a) FeN_4-OLC-CNF@MoS_2 (b) $(FeN_4)_d$-OLC-CNF@MoS_2.

The BET surface area and pore size distribution (PSD) were tested using N_2 adsorption-desorption and the results are shown in figure 7.9. The plot in figure 7.9a displays an improvement in the N_2 uptake from FeN_4-OLC-CNF@MoS_2 to $(FeN_4)_d$-OLC-CNF@MoS_2, composite. On the other hand, the PSD in figure 7.9b shows additional peaks from 170 nm, suggesting more abundant nanopores formation from lattice distortion caused by the Fe^{2+} removal. Ideally an electrode material should have a high surface and pore size distribution as this is a direct correlation with better accessibility of surface area for either redox reactions and/or electrical double layer formation. Table 7.1 shows summarized values of the surface area parameters and it is clear that the final composite, $(FeN_4)_d$-OLC-CNF@MoS_2 with vacancies is three times larger than the FeN_4-OLC-CNF@MoS_2 counterparts. Furthermore, the pore size after the etching treatment has improved from its original 38.09 to 54.75 nm. This increase in both surface area and pore size of the composite structure is ideal for enhanced supercapacitor performance. In particular, the pore size expansion is likely to facilitate ion transportation into the intra pores of the vacant atomic sites of the fibres, thus improvement in the rate capability and power density of the electrodes.

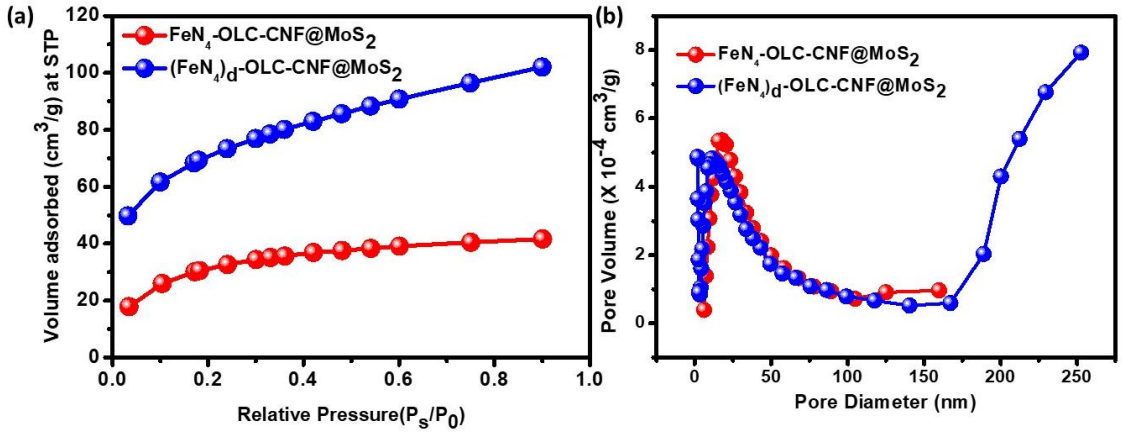

Figure 7.9 (a) N_2 adsorption-desorption isotherms, and (b) pore-size distribution, for FeN_4-OLC-CNF/MoS_2 and (FeN4)d-OLC-CNF@MoS_2 composite fibres, respectively.

Table 7.1 *BET surface area parameters for fibres.*

Sample	SSA (m^2/g)	Pore volume	Pore size (nm)
FeN_4-OLC-CNF@MoS_2	26.33	0.0718	38.09
$(FeN_4)_d$-OLC-CNF@MoS_2	80.41	0.0437	54.75

The difference in the elemental composition often results in different crystalline structures. Figure 7.10 shows the XRD patterns from FeN_4-OLC-CNF/MoS_2 and $(FeN_4)_d$-OLC-CNF@MoS_2 nanofibres. FeN_4-OLC-CNF/MoS_2 showed weak broad 2θ peaks at 26, 34, 41 and 59° which can be assigned to (002), (100), (103), (105) MoS_2 planes, respectively. The additional peaks at 9.7, 14 and 82 are typically observed in the presence of FePc species. On the other hand, $(FeN_4)_d$-OLC-CNF@MoS_2 nanofibres were characterized by the peaks at 2θ = 15.16, 33.56, 40.17, 59.13, 60.80 and 69.45 °, corresponding to the (002), (100), (103), (105), (110) and (200) planes and these are associated with the hexagonal structure of MoS_2. Considering the increase in the interlayer spacing of the (002) plane from previous 2θ= 26° to 2θ= 15° on the $(FeN_4)_d$-OLC-CNF@MoS_2 nanofibre and general peak intensity increase, re-stacking of the MoS_2 sheets may have occurred. This suggests that in addition to the removal of Fe atoms from the OLC@MoS_2 nanofibres structural framework, HCl aided into exfoliation of the MoS_2 sheets. Similar shifts were also observed with the remaining peaks of FeN_4-OLC-CNF@MoS_2 vs. $(FeN_4)_d$-OLC-CNF@MoS_2 nanofibres. Previous work by Forsberg at al., showed that MoS_2 sheets can be exfoliated in water through sonication without additives (i.e. DMF, DMSO and NMP). The results showed a reasonably good concentration of

exfoliated nanosheets from Atomic Force Microscopy (AFM) and TEM analysis and better feasibility for large scale production. [26]

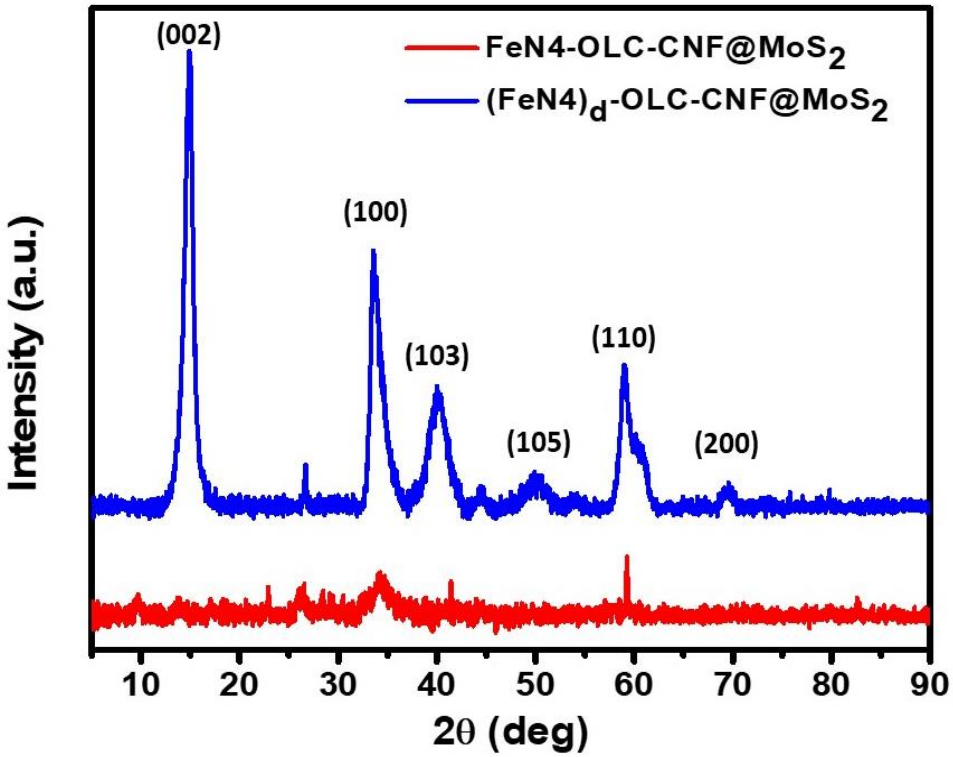

Figure 7.10 XRD patterns of FeN_4-OLC-CNF@MoS_2 and $(FeN_4)_d$-OLC-CNF@MoS_2 composites materials.

For this study, FT-IR was used to evaluate the presence and effect of MoS_2 and removal of the Fe atom from the atomic structure. The resulting spectra of the FeN_4-OLC-CNF@MoS_2 and $(FeN_4)_d$-OLC-CNF@MoS_2 nanofibres are shown in figure 7.11. Previous work in chapter six, showed that the FeN_4-CMF are characterized by stretching vibrations peaks at 2920, 2240 and 1450 cm^{-1} due to methylene and nitrile groups' coming from the original PAN and FePc, respectively. These were also observed in the composite materials in this work. Both spectra's appear quite similar except for a higher intensity for bands corresponding to Fe-N vibrations in the FeN_4-OLC-CNF@MoS_2 in comparison with $(FeN_4)_d$-OLC-CNF@MoS_2 fibre composite at 827 cm^{-1}. On the other hand, vibrational modes associated with the presence of MoS_2 in both composites were observed at 595 cm^{-1} and were indexed to vibrations of $Mo-S$ bonds. The intensity of MoS_2 related peaks were higher for the Fe-OLC/MoS_2 fibre composite, however the same was true for methylene related peaks in the $(FeN_4)_d$-OLC-CNF@MoS_2 fibre composite.

The interaction between MoS_2 with CNF was confirmed by the peaks at 921 and 723 cm^{-1}. For both variants, oxygen containing functionalities were present at 1073 cm^{-1} and were assigned to $C-O-H$ stretching, at 1655 cm^{-1} and were assigned to asymmetric and symmetric carboxylate groups namely, $C-O$ and finally, $C=O$ bending was detected at 1886 cm^{-1}. $O-H$ vibrations were observed at 1635 and 3300 cm^{-1}. Methylene groups, in particular $H-C-H$ were accounted for between 2600 and 2800 cm^{-1}, and finally between 3100 and 3300 cm^{-1} as $C=C$ symmetric and asymmetric stretching vibrations.

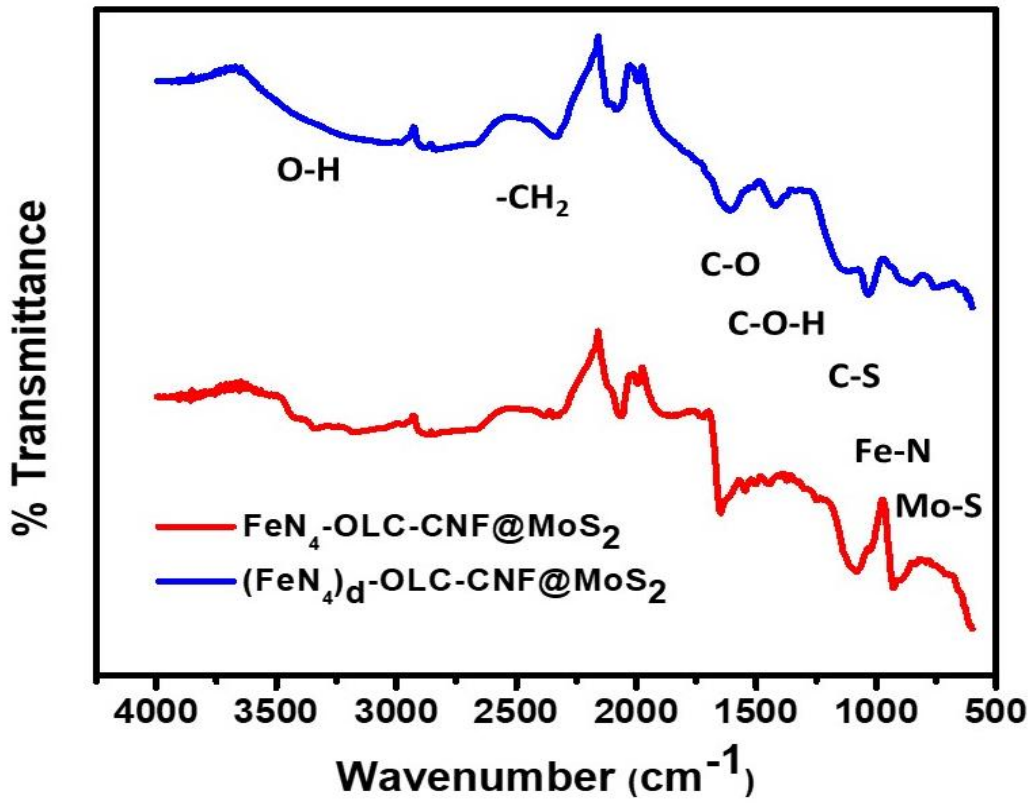

Figure 7.11 FT-IR spectra for FeN_4-OLC-CNF/MoS_2 and $(FeN_4)_d$-OLC-CNF@MoS_2 composite materials.

A comparative Raman spectra of FeN_4-OLC-CNF@MoS_2 and $(FeN_4)_d$-OLC-CNF@MoS_2 composite materials are shown in figure 7.12. Based on the differences in the Raman spectra, the removal of Fe atoms had effects on changes in the structural properties. Generally, MoS_2 is associated with atom vibrations between 300-500 cm^{-1}, where $E^1_{2g}$is ascribed to opposite vibration of two S atoms with repsect to Mo and A_{1g}peaks. Firstly, the Raman spectra for the FeN_4-OLC-CNF@MoS_2 composite has high

intensity peaks related to MoS_2 distortions in comparison to its $(FeN_4)_d$-OLC-CNF@MoS_2 counterpart, in agreement with FT-IR results. In Fe-OLC@MoS_2, the peaks at 377 and 403 cm^{-1} corresponding to E^1_{2g} and A_{1g} had left shifted to 376 and 402 cm^{-1} for $(FeN_4)_d$-OLC-CNF@MoS_2 composites. This phenomenon was explained by the defect induced vibrations as a result of Fe atom removal causing a drift in the electronic band structure. The typical D and G bands were observed at wave numbers 1340 and 1593 cm^{-1}, respectively for $(FeN_4)_d$-OLC-CNF@MoS_2. Interestingly, there were no D and G band peaks detected for the Fe-OLC@MoS_2. The limitations could be attributed to the encapsulation of the fibres and thus inability to detect through a surface analysis technique such as the Raman. In the case of $(FeN_4)_d$-OLC-CNF@MoS_2 composite material, the defect rich fibres enable the access to carbon containing elements embedded in the fibre. This agrees with previous observations from SEM. The calculated relative intensity ratio I_D/I_G for $(FeN_4)_d$-OLC-CNF@MoS_2 composite fibres is 1.47. The I_D/I_G ratio with defect rich $(FeN_4)_d$-OLC-CNF@MoS_2 indicates the transformation of disordered carbon into graphitic carbon which is known to enhance the electrochemical properties of an electrode.

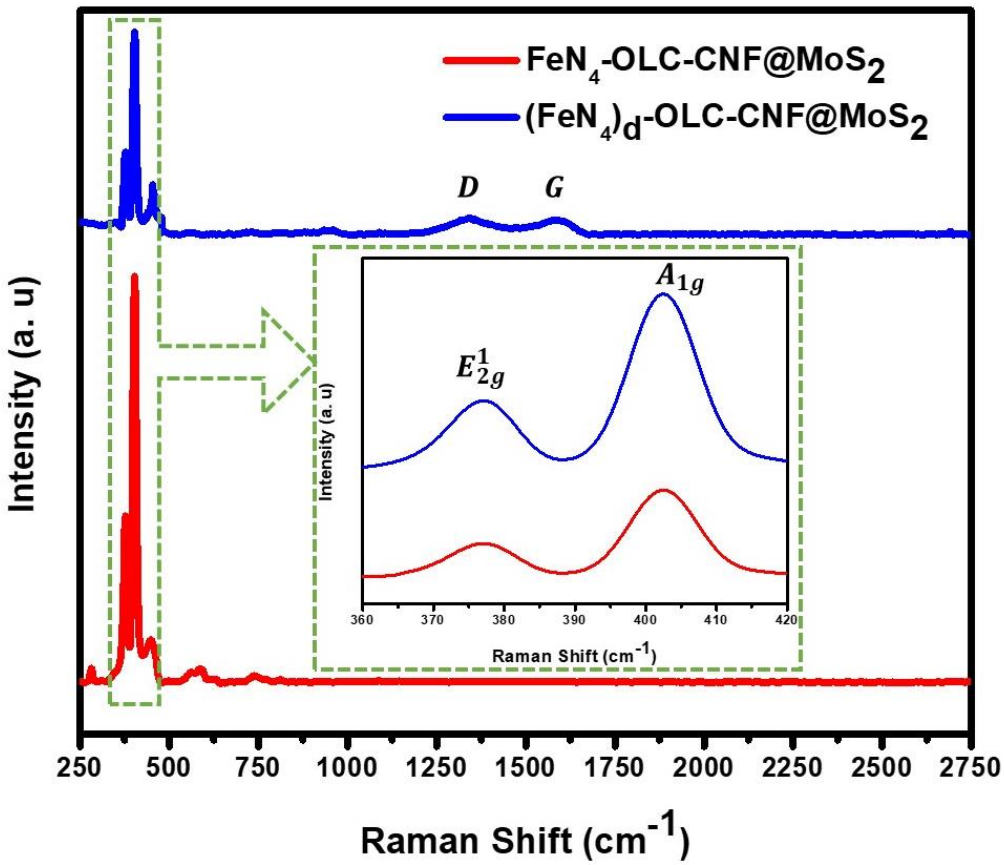

Figure 7.12 Raman spectra comparison of FeN_4-OLC-CNF@MoS_2 and $(FeN_4)_d$-OLC-CNF@MoS_2 fibres and a magnified view for the comparison of the MoS_2 related vibrations.

XPS analysis comparison was imperative in order to deduce whether the removal of Fe^{2+} ions resulted in changes to the chemistry of surfaces and the valence state of species of FeN_4-OLC-CNF/MoS_2 and $(FeN_4)_d$-OLC-CNF@MoS_2 composites. In table 7.2 the binding energies (E_b) and the atomic percentages of the elements are summarized. Seemingly, the vibration peak positions for all the elements remained constant however with regards to atomic content, a slight increase was observed for carbon, whilst oxygen reduced slightly after the removal of Fe^{2+} ions.

Table 7.2 *XPS data of FeN_4-OLC-CNF@MoS_2 and $(FeN_4)_d$-OLC-CNF@MoS_2 nanocomposite materials.*

	FeN_4-OLC-CNF@MoS_2		**$(FeN_4)_d$-OLC-CNF@MoS_2**	
Name	Peak BE	Atomic %	Peak BE	Atomic %
C1s	285.2	48.9	285.1	50.8
O1s	531.7	24.4	532.0	18.0
S2p	162.1	17.4	162.9	19.7
Mo3d	229.4	8.5	229.1	8.2
Na	1071.4	0.8		
Cl			197.9	3.2

High resolution XPS spectra for FeN_4-OLC-CNF@MoS_2 and $(FeN_4)_d$-OLC-CNF@MoS_2 composite fibres are shown in figure 7.13 and 7.14, respectively. It is worth noting that the Fe^{2+} removal process had no impact on the binding energy intensities or positions of critical elements.

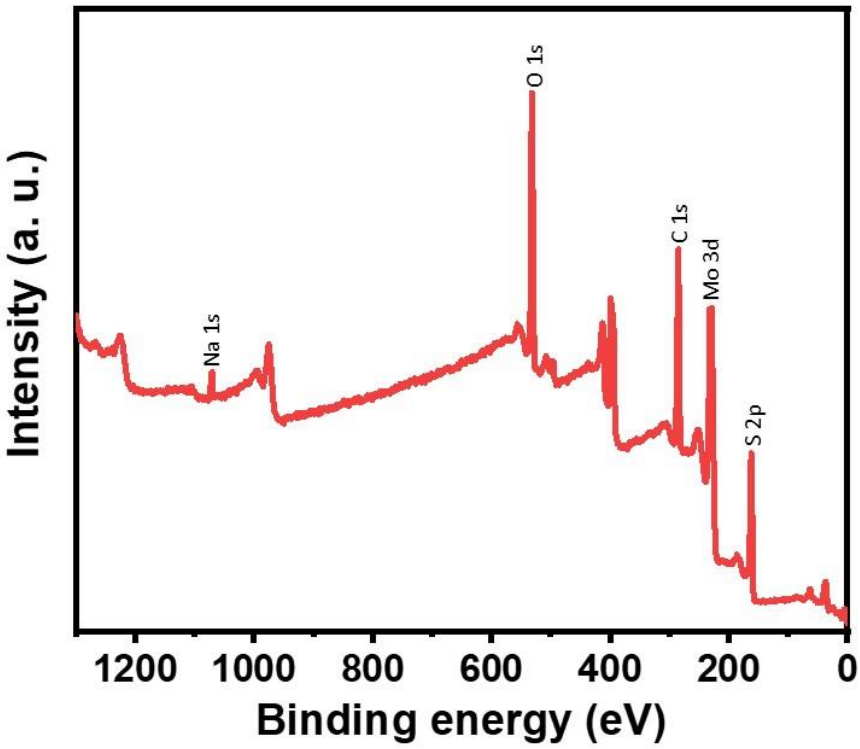

Figure 7.13 High resolution XPS spectra of FeN_4-OLC-CNF@MoS_2 composite material.

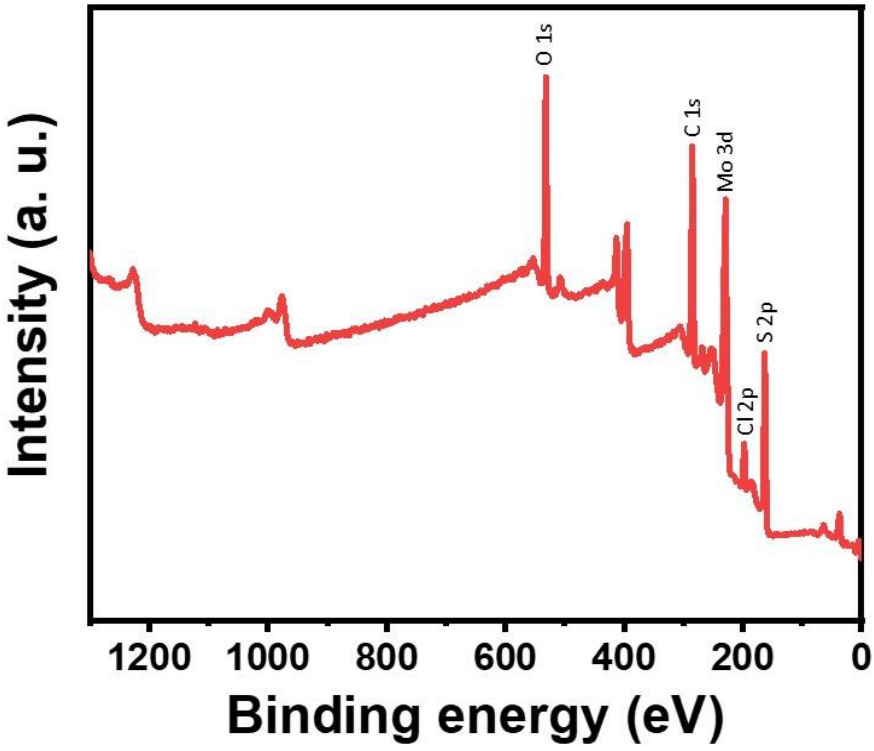

Figure 7.14 High resolution XPS spectra of $(FeN_4)_d$-OLC-CNF@MoS_2 composite material.

Figure 7.15 and 7.16 both show XPS spectra of Mo 3d of FeN_4-OLC-CNF@MoS_2 and $(FeN_4)_d$-OLC-CNF@MoS_2, respectively. In figure 7.15, Mo 3 d signals for Fe-OLC/MoS_2 show a two-peak structure derived from two overlapping doublets. Mo 3 d peaks were observed at binding energies at 228.1 eV and 231.3 eV for $Mo\ 3d_{\frac{5}{2}}$ and $Mo\ 3d_{\frac{3}{2}}$, respectively and indicating co-existence of 2H and 1T-MoS_2 phase in the fibre composite. MoO_3 related peaks were assigned at 229.3 eV and 232.4 eV binding energies. However, upon the Fe^{2+} removal process, two characteristic peaks attributed to $Mo\ 3d_{\frac{5}{2}}$ at 229.2 eV and $Mo\ 3d_{\frac{3}{2}}$ at 232.4 eV were observed with increased sharpness in figure.7.16. $(FeN4)_d$-OLC-CNF@MoS2 composite nanofibres showed a shift of about 1 eV towards a higher binding energy compared to that of FeN_4-OLC-CNF@MoS_2 sample, indicating presence of 2H phase in the synthesized $(FeN_4)_d$-OLC-CNF@MoS_2. The Mo 3 d deconvoluted doublet are evidence of Mo^{4+}, Mo^{5+} and Mo^{6+} species.

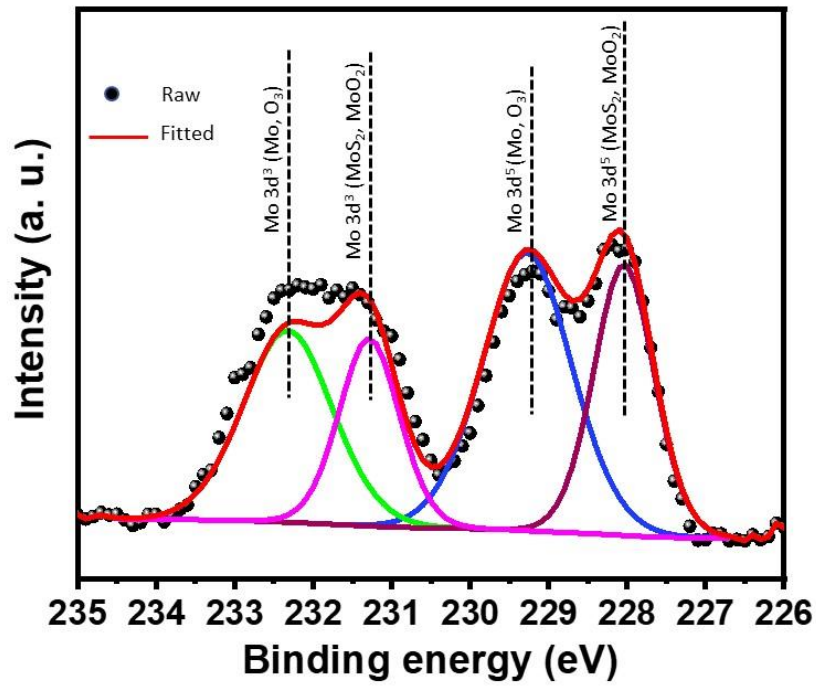

Figure 7.15 XPS spectrum of Mo 3d for FeN_4-OLC-CNF@MoS_2 composite material.

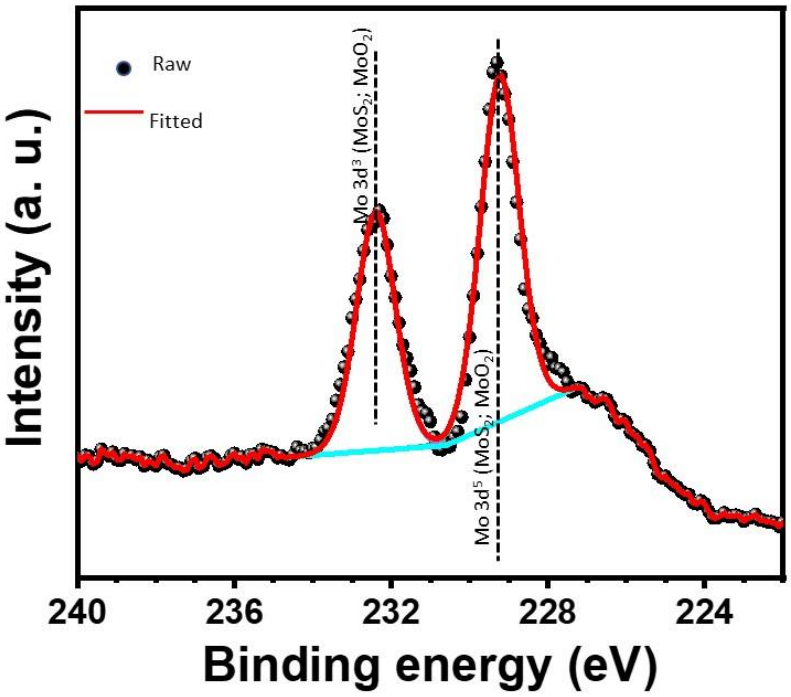

Figure 7.16 XPS spectrum of Mo 3d for $(FeN_4)_d$-OLC-CNF@MoS_2 composite material.

S 2p deconvoluted peaks with binding energy were observed at 170.9 eV 164.1 eV 162.4 eV S 2$p_{\frac{3}{2}}$ 168 eV 162.8 eV 161.2 eV for of FeN_4-OLC@MoS_2 composite fibre, as shown by figure 7.17. Analogous to Mo 3 d, S 2p also showed similar peak shifts, from Fe-OLC/MoS_2 to $(FeN_4)_d$-OLC-CNF@MoS_2 counterpart. In the latter, S 2p peaks were observed at binding energies, 164.1 eV 162.7 eV and 163 eV 161.6 eV for S 2$p_{\frac{3}{2}}$ as shown in figure 7.18.

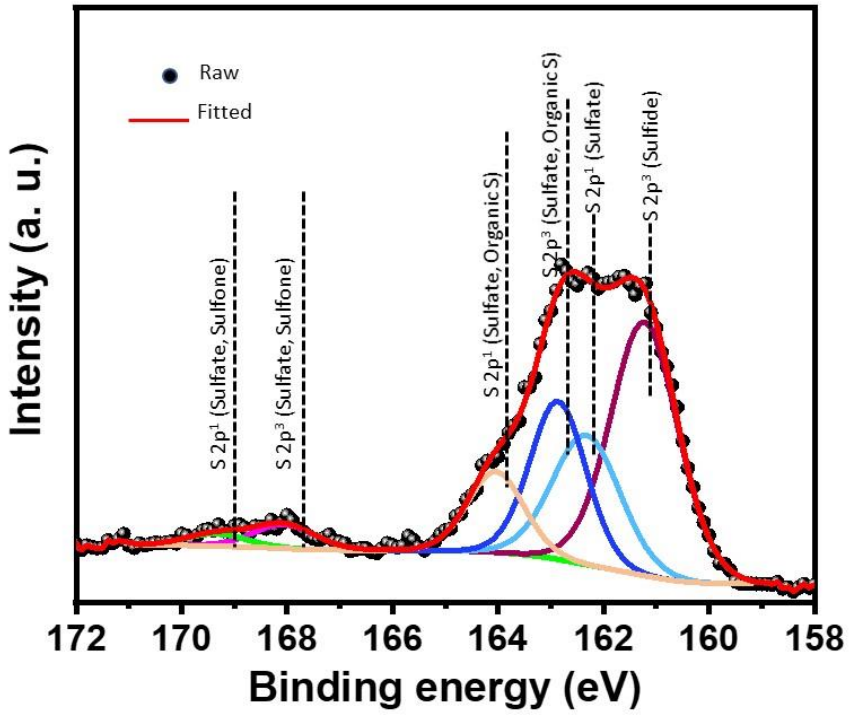

Figure 7.18 S 2p spectrum for FeN_4-OLC-CNF@MoS_2 composite material.

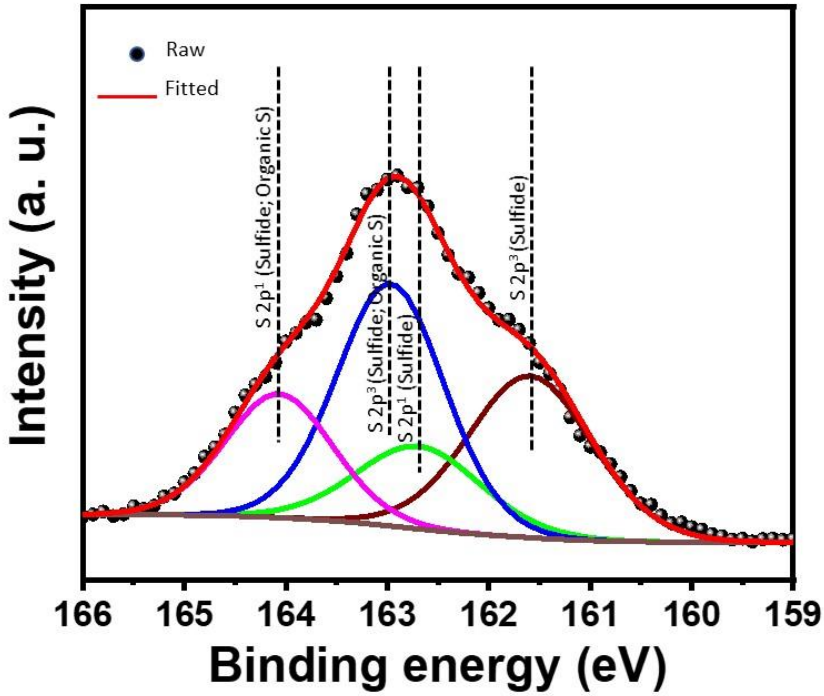

Figure 7.19 S 2p spectrum for $(FeN_4)_d$-OLC-CNF@MoS_2 composite material.

In figure 7.20, the deconvoluted peaks as a result of C 1s bonding interactions namely, $O-C=O, C=O, C-O, C-C$ were observed at binding energies 288.56 eV 287.25 eV 285.7 eV 284.2 eV, respectively for FeN_4-OLC-CNF@MoS_2 composite. Figure 7.21 Similar peaks were deconvoluted for the $(FeN_4)_d$-OLC-CNF@MoS_2 fibre composite.

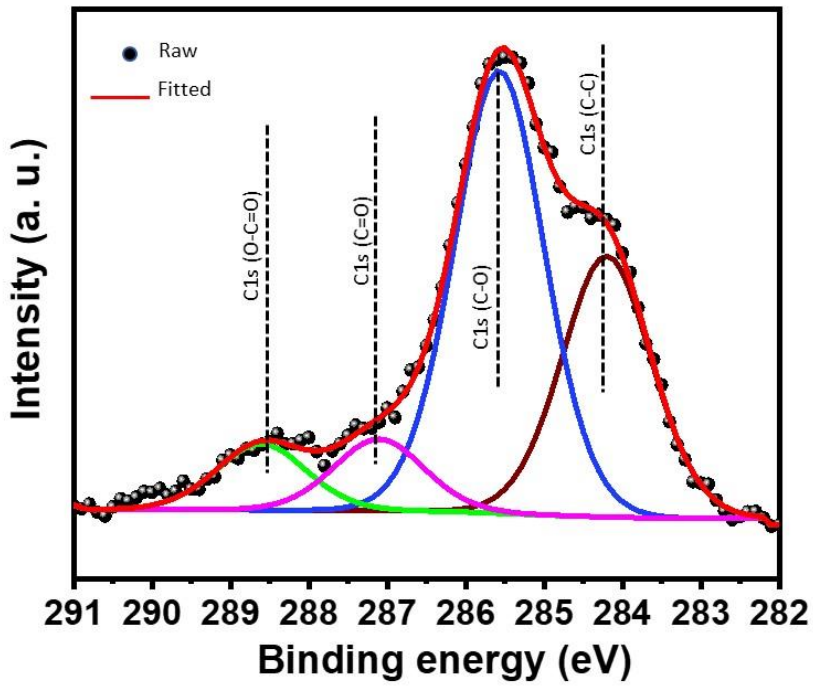

Figure 7.20 C 1*s* spectrum for FeN_4-OLC-CNF@MoS_2 composite material.

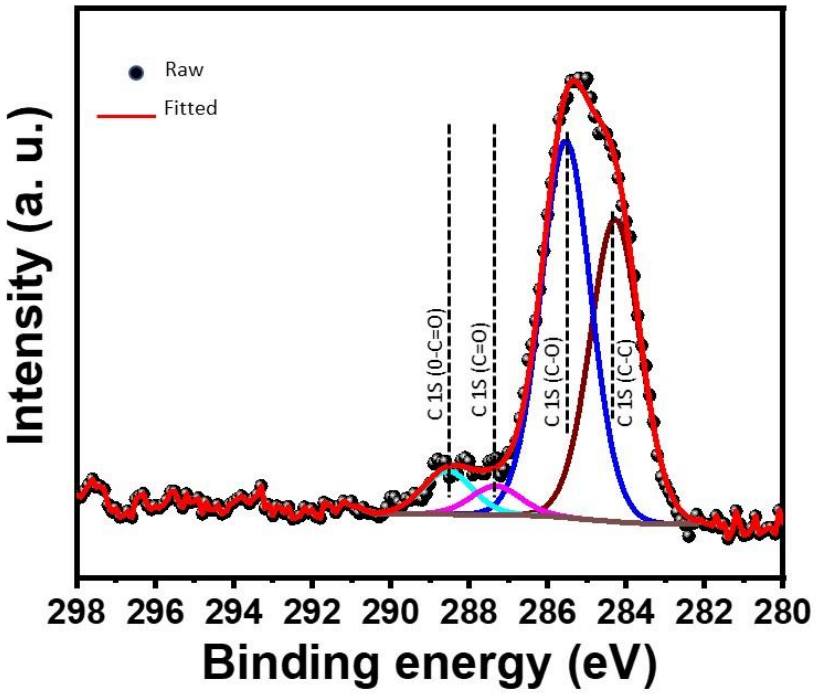

Figure 7.21 C 1*s* spectrum for $(FeN_4)_d$-OLC-CNF@MoS_2 composite material.

Figure 7.22 and figure 7.23. show a slight shift of the O 1s peak from 531.7 eV to 532 eV after Fe^{2+} removal was observed.

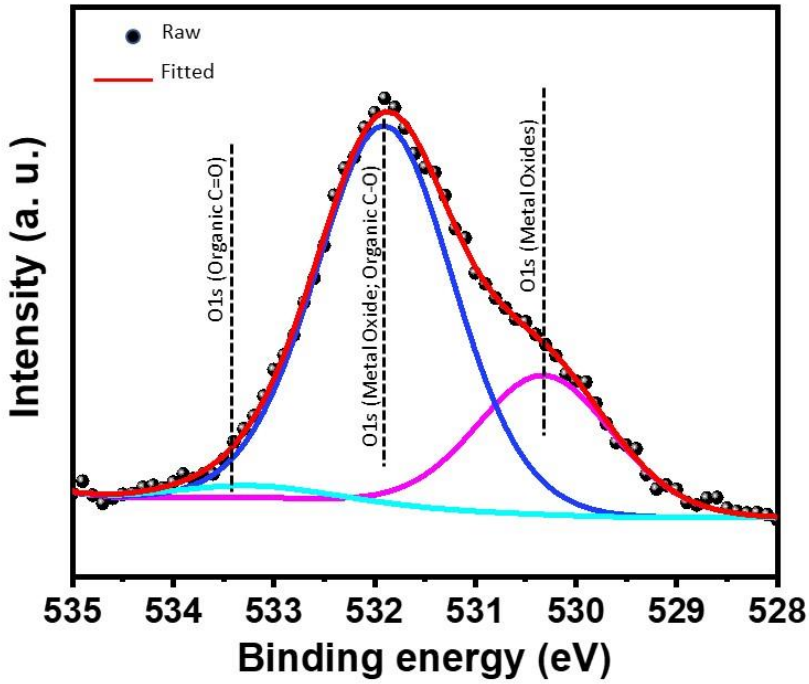

Figure 7.22 O 1*s* spectrum for FeN_4-OLC-CNF@MoS_2 composite material.

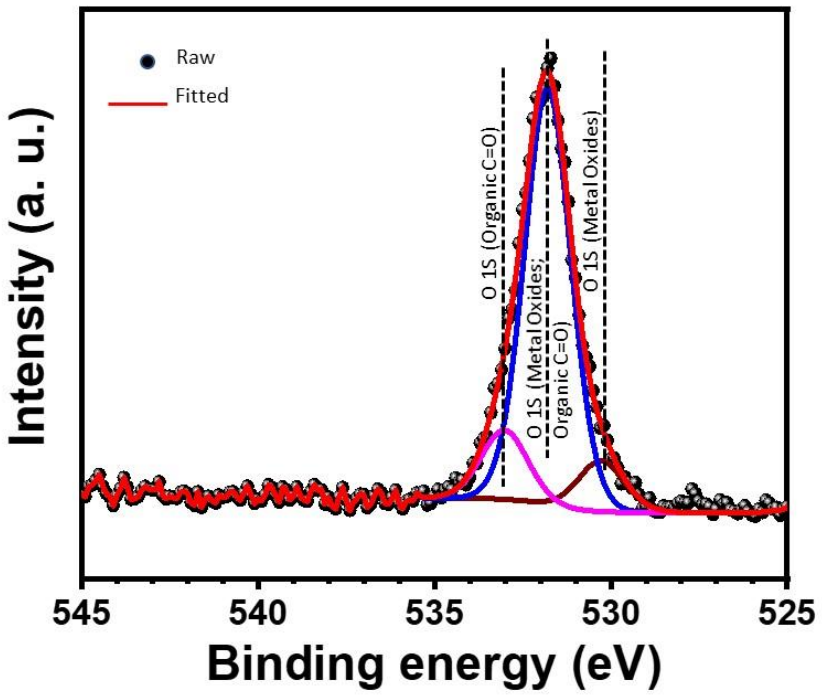

Figure 7.23 O 1*s* spectrum for $(FeN_4)_d$-OLC-CNF@MoS_2 composite material.

Additional elements analyzed include Na 1s for FeN_4-OLC-CNF@MoS_2 and the peak was observed at 1071.2 eV due to the contribution from the sodium molybdate dehydrate ($Na_2MoO_4 \bullet 2H_2O$) reagent for MoS_2 synthesis. In the case of $(FeN_4)_d$-OLC-CNF@MoS_2, Cl 1s at 197 eV was observed and is likely to have originated from the HCl used to remove the residual Fe^{2+} ions.

7.2.2 Electrochemical properties

The electrochemical reaction of these fibre materials is demonstrated with cyclic voltammograms displayed in figure 7.24 below first using three electrode configurations. The CV curves were characteristic of those observed in pseudocapacitors, as they deviated from a standard rectangular shape and showed redox peaks. Seemingly, $(FeN_4)_d$-OLC-CNF@MoS_2 in the absence of Fe species demonstrates better performance as the current response of the curve is relatively larger than its counterpart FeN_4-OLC-CNF@MoS_2. In the case of $(FeN_4)_d$-OLC-CNF@MoS_2, the redox active species present as demonstrated by the bulging curve were at -0.5 V for oxidation and -0.2 V during reduction. Thus, the CV curves of both FeN_4-OLC-CNF@MoS_2 and $(FeN_4)_d$-OLC-CNF@MoS_2 were captured between -0.7 V and 0.3 V.

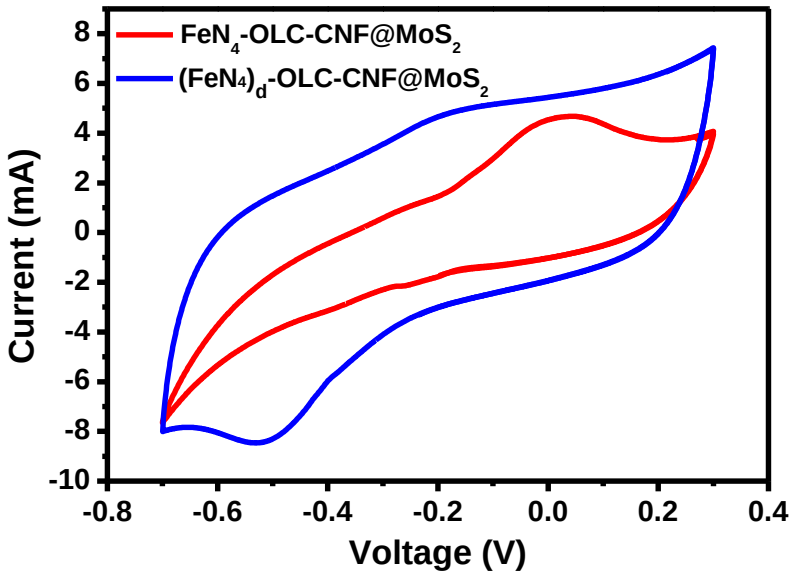

Figure 7.24 Three-electrode CV comparison for FeN_4-OLC-CNF@MoS_2 and $(FeN_4)_d$-OLC-CNF@MoS_2 at 50 mV s^{-1}.

The charge-discharge curves demonstrated in figure 7.25 also prove the superiority of the $(FeN_4)_d$-OLC-CNF@MoS_2 composite seeing that at similar current density, it discharged for longer periods than FeN_4-OLC-CNF@MoS_2 composite. The perception of defects has generally been negative in the past. However, this proves that the electrochemical activity has been improved by tapping into areas that were not previously available for charge storage.

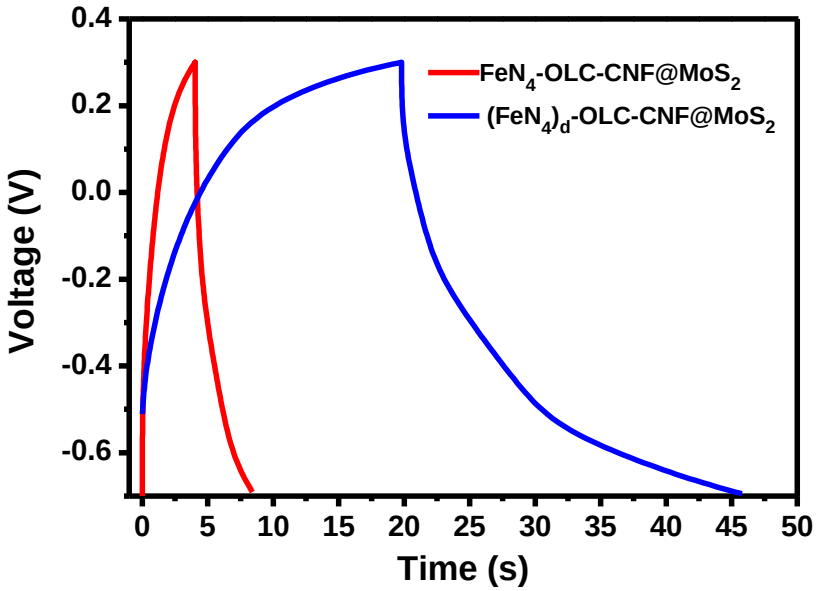

Figure 7.25 Charge-discharge curves of FeN_4-OLC-CNF@MoS_2 and $(FeN_4)_d$-OLC-CNF@MoS_2 fibres obtained via GCPL was obtained at 1 A g^{-1}.

To get an indication of the electrode's kinetics, EIS analysis was performed on the electrodes and are compared on a Nyquist plot in figure 7.26. Both electrodes show similar R_s of 0.93 and 1 Ω for FeN_4-OLC-CNF@MoS_2 and $(FeN_4)_d$-OLC-CNF@MoS_2, respectively. This suggests consistency with electrochemical set up of the experiments and the slight differences were possibly due to the electrode resistance. The high R_{CT} value for the FeN_4-OLC-CNF@MoS_2 electrodes corresponds to a slower reaction rate in comparison to the lower R_{CT} for the $(FeN_4)_d$-OLC-CNF@MoS_2 electrode materials. This is likely due to the morphological differences in $(FeN_4)_d$-OLC-CNF@MoS_2 and pseudocapacitive nature of charge storage. On the other hand, Fe-OLC/MoS_2 electrodes have large slope Z_ω suggesting better solid state diffusion of Na^{2+} ions into the OLC-CNF@MoS_2 nanofibre composite electrode due to the high porosity and larger surface area induced by removal of Fe^{2+} ions and MoS_2 sheets exfoliation.

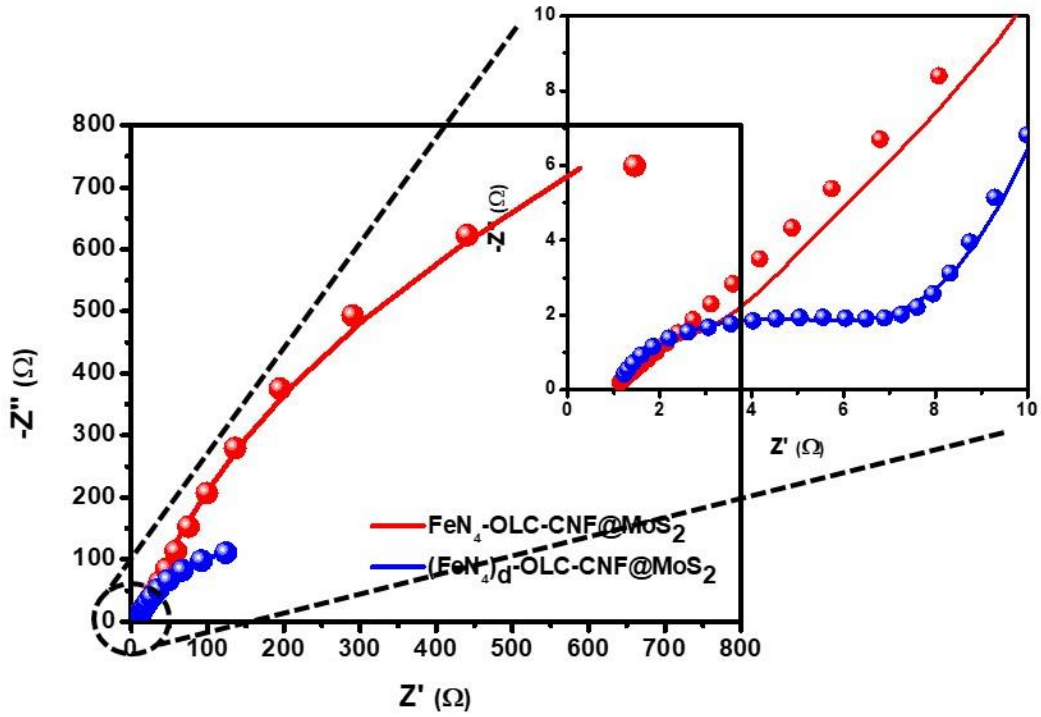

Figure 7.26 Nyquist plots between FeN_4-OLC-CNF@MoS_2 and $(FeN_4)_d$-OLC-CNF@MoS_2 electrode materials, acquired in a 1 M Na_2SO_4 aqueous electrolyte solution.

The capacitive study of the electrodes is displayed in figure 7.27. Importantly, $(FeN_4)_d$-OLC-CNF@MoS_2 electrodes are pseudocapacitive in nature as indicated by the a and b values.

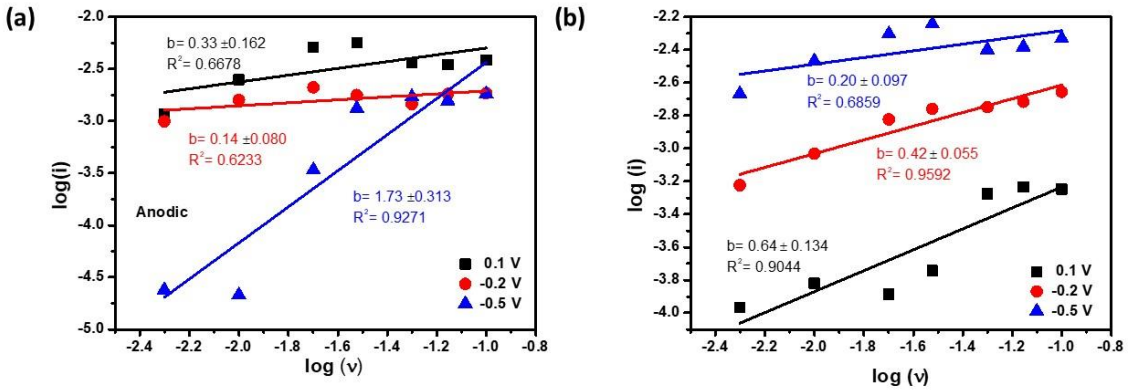

Figure 7.27 Log peak current vs log scan rate for $(FeN_4)_d$-OLC-CNF@MoS_2 (a) anodic and (b) cathodic plots.

In a two-electrode configuration the electrochemical properties of FeN_4-OLC-CNF@MoS_2 and $(FeN_4)_d$-OLC-CNF@MoS_2 were studied using a Swagelok full cell to investigate the effect of Fe^{2+} removal and as a result introducing defects into the structure. In figure 7.28a, the CV plots for FeN_4-OLC-CNF/MoS_2 are rectangular in nature reflecting capacitive behavior of the electrodes. Figure 7.28b represents the CV curve of $(FeN_4)_d$-OLC-CNF@MoS_2 electrodes and shows a higher voltage window of 1.0 V in comparison to the narrower voltage window of 0.8 V from its counterpart electrodes, FeN_4-OLC-CNF/MoS_2. Since there is a direct correlation between the square of the cell's voltage and energy density in supercapacitors, $E = \frac{CV^2}{2}$. It is likely that the improvement in voltage window observed for $(FeN_4)_d$-OLC-CNF@MoS_2 electrodes provides the much required high capacitance/energy density values for supercapacitors. A plateau for $(FeN_4)_d$-OLC-CNF@MoS_2 electrodes was observed at 0.5 V. However, the faradaic reactions taking place at the electrode-electrolyte interface are reversible since the shape of the CVs are symmetrical for both horizontal and vertical orientations. The surface area under the CV curve for $(FeN_4)_d$-OLC-CNF@MoS_2 electrodes showed improvement. This is because there are vacancies after Fe removal which makes the surface pores more accessible. The sonification process which aided the exfoliation process of MoS_2 sheets, has enhanced intercalation of electrolyte cations thus giving it's a higher current response. Capacitance, which is directly related to the current response also improved in $(FeN_4)_d$-OLC-CNF@MoS_2. As a new type of electrode material $(FeN_4)_d$-OLC-CNF@MoS_2 with defects, would give important insights in developing new generation of MoS_2 based electrodes with improved performance. Figure 7.28(c) and (d) represent charge-discharge curves for both fibre composites, carried out at various current densities from 0.1 up to 10 A g^{-1}. As with CV data, the GCD curves show close to ideal behavior with acceptable voltage drops at the start of the discharge cycle. The potential window for $(FeN_4)_d$-OLC-CNF@MoS_2 is 0.7 V, whereas it is 1.0 V for $(FeN_4)_d$-OLC-CNF@MoS_2, slightly higher due to higher affinity of the Na+ ions for charge accumulation in the electrodes.

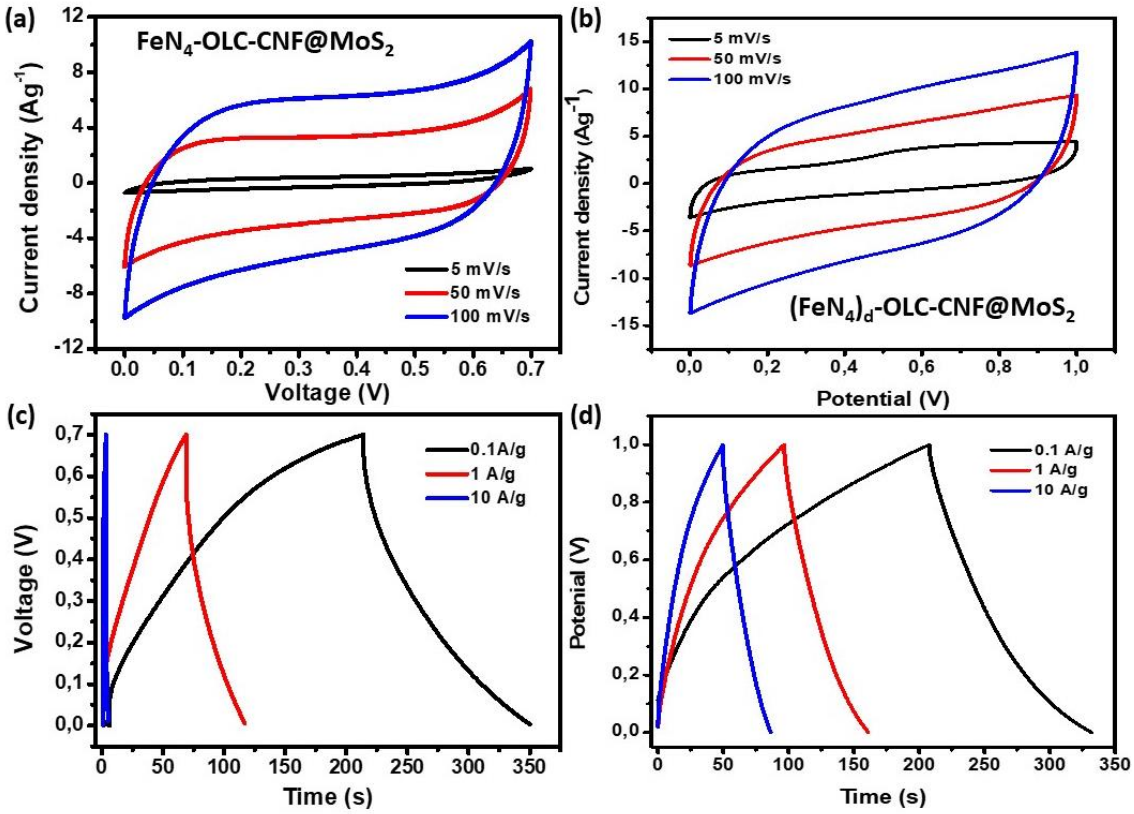

Figure 7.28 Two-electrode CV comparison of (a) FeN_4-OLC-CNF@MoS_2 and (b) $(FeN_4)_d$-OLC-CNF@MoS_2 fibre composites obtained at 5, 50 and 100 mV s^{-1}. Charge-discharge curves extracted at 0.1, 1 and 10 A g^{-1} for (c) FeN_4-OLC-CNF@MoS_2, and (d) $(FeN_4)_d$-OLC-CNF@MoS_2 composites, respectively.

Storage capabilities of these electrodes were calculated from the obtained GCD curves. Figure 7.29a shows specific capacitance values at increasing current density. Evidently the specific capacitance gradually decreased with increasing current density from 481 F g^{-1} at 0.1 A g^{-1} to 98 F g^{-1} at 10 A g^{-1} and 178 F g^{-1} at 0.1 A g^{-1} to 22 F g^{-1} at 10 A g^{-1} for FeN_4-OLC-CNF@MoS_2 and $(FeN_4)_d$-OLC-CNF@MoS_2, respectively. At low current densities the electrolyte ions have sufficient time to penetrate through the porous nanofibres for charge accumulation and thus greater capacitance values (the inverse is true for high current density cycles). Furthermore, a Ragone plot (i.e. energy vs power density) was deduced from the charge-discharge curves and has been illustrated in figure 7.29b. At current density 0.1 A g^{-1} the FeN_4-OLC-CNF@MoS_2 electrode showed a power and energy density of 33 W kg^{-1} and 1620 Wh kg^{-1}, respectively. Whereas for $(FeN_4)_d$-OLC-CNF@MoS_2, the energy and power density at 0.1 A g^{-1} where 76 W kg^{-1} and 5833 Wh kg^{-1}, respectively. In essence, the cation vacancies lower the activation energy for ion

diffusion through the lattice, the effect enhances the thermodynamic reactivity of the materials. This is displayed by the ease of the intercalation/de-intercalation process of the electrolyte ions which enhances the rate capability and the additional extra host sites for cation intercalation provides more charge storage.

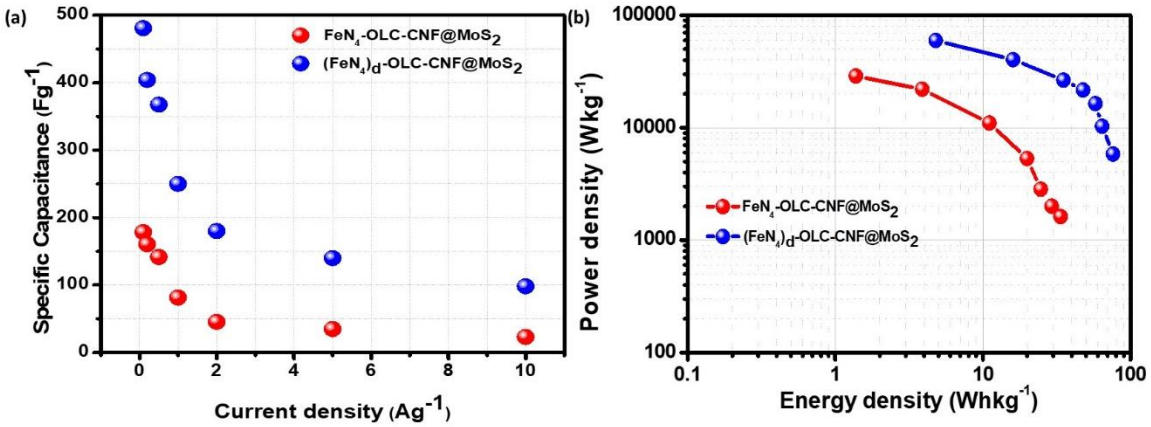

Figure 7.29 (a) Specific capacitance of FeN_4-OLC-CNF@MoS_2 and $(FeN_4)_d$-OLC-CNF@MoS_2 composite electrodes based on the charge-discharge cycles at various current densities, and (b) Ragone plot showing energy density vs power density.

Table 7.3 compares the specific capacitance, energy density and power density values at 1 A g^{-1} for the composite materials of this study. The maximum electrochemical performance was achieved by the $(FeN_4)_d$-OLC-CNF@MoS_2 composite electrodes.

Table 7.3 *Comparison of electrochemical performance of fibre composite materials*

Electrode Material	**C_{sp}/F g^{-1}**	**Energy density/ Wh kg^{-1}**	**Power density/ W kg^{-1}**	**Electrolyte**	**Type of device**
OLC-CNF@Mn_2O_3	200	1.63	3235	Aqueous 1.0 M Na_2SO_4	SSC
OLC-CNF/MoS_2@Mn_2O_3	345	18.42	5095	Aqueous 1.0 M Na_2SO_4	SSC
FeN_4-CMF	147	12.48	4320	Aqueous 1.0 M Na_2SO_4	SSC
$(FeN_4)_d$-OLC-CNF@MoS_2	481	76.02	5833	Aqueous 1.0 M Na_2SO_4	SSC

*C_{sp} is the specific capacitance
*SSC is the symmetrical supercapacitor configuration in a device

A stability test was done for both electrodes under constant current density of 1 A g^{-1} using the traditional charge-discharge cycling method as demonstrated in figure 7.30a

and b. $(FeN_4)_d$-OLC-CNF@MoS_2 electrodes in figure 7.30 b, showed the highest capacitance at a similar current density as FeN_4-OLC-CNF@MoS_2 electrode in figure 7.30 a. In addition, the electrodes had over 96 % (4 % loss of capacitance) specific capacitance retention after 5000 cycles from 141 F g^{-1} to 138 F g^{-1}. The initial capacitance of FeN_4-OLC-CNF@MoS_2 electrodes of the cycle was 70 F g^{-1} and gradually decreased to 61 F g^{-1} by the 2000^{th} cycle, which is about 12 % loss of capacitance.

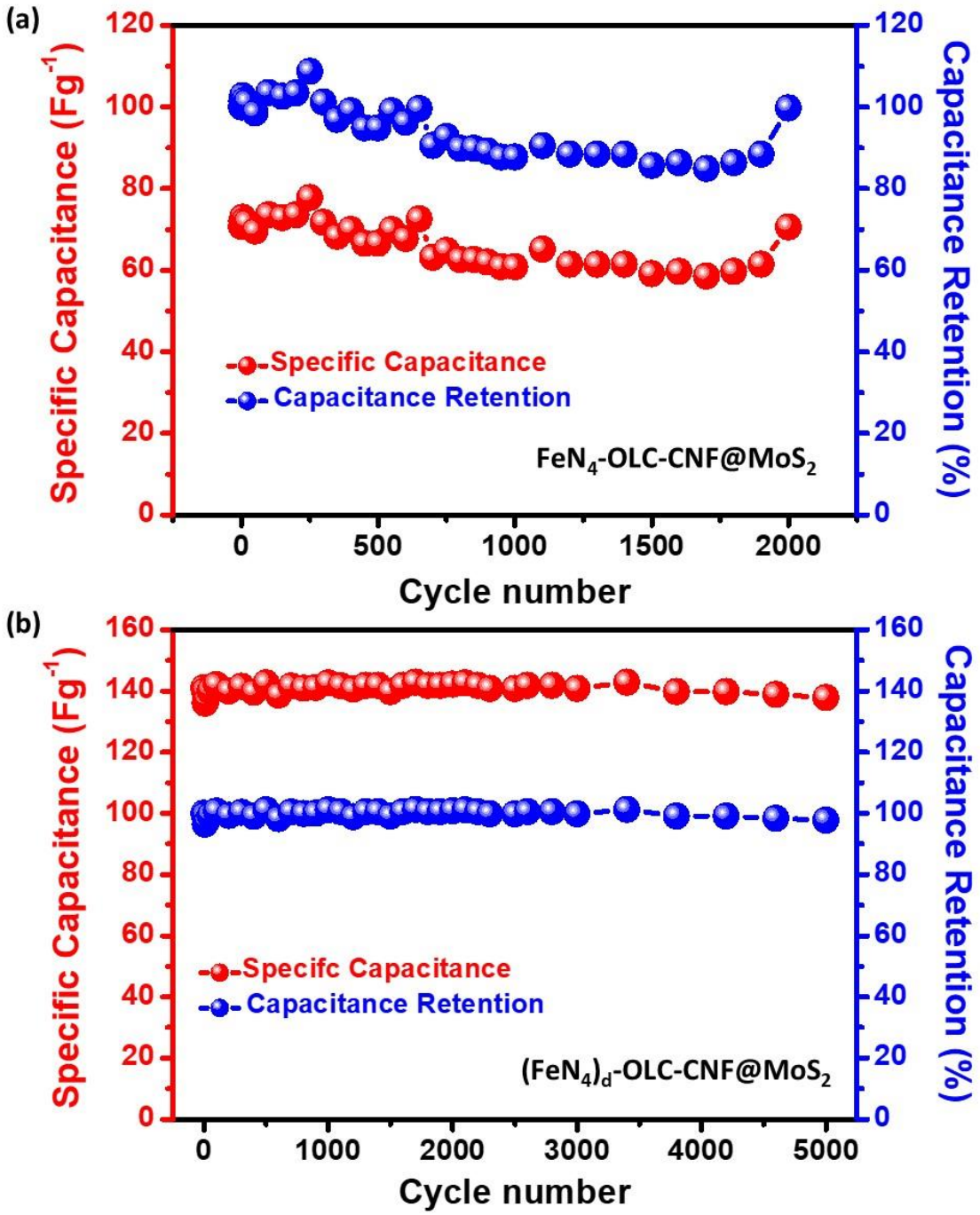

Figure 7.30 Cycling stability analysis of (a) FeN_4-OLC-CNF@MoS_2 and (b) $(FeN_4)_d$-OLC-CNF@MoS_2 composite electrodes.

Moreover, impedance was performed on the two-electrode systems of FeN_4-OLC-CNF@MoS_2 and $(FeN_4)_d$-OLC-CNF@MoS_2 electrodes to understand the effect of creating vacancies in the OLC-CNF@MoS_2 composite material. Similar observations as

with three- electrode were observed on the two-electrode system in figure 7.31a and b. The R_S and R_{CT} of the electrodes can be separated using Nyquist plot. EIS interpretation of the electrode behavior based on the electrical equivalent circuit obtained from the fitted data. FeN_4-OLC-CNF@MoS_2 showed evidence of a semi-circle, indicative of charge transfer resistance in comparison to $(FeN_4)_d$-OLC-CNF@MoS_2 electrodes which is only visible after cycling.

The $(FeN_4)_d$-OLC-CNF@MoS_2 electrodes still displayed non-linear behavior accompanied by R_S of 0.402 Ω with phase angle -50 °. From the Nyquist plots, the capacitance retardation in the fibre composite electrodes of FeN_4-OLC-CNF@MoS_2 was primarily due to possible high series resistance attributed to insufficient conductivity of the electrode, and large charge transfer resistance at the carbon fibre@MoS_2 interface that inhibits the Na^+ insertion/adsorption process in MoS_2. This resulted in a capacitance degradation at a high operation rate. These deficiencies were mitigated by the removal of Fe^{2+} ions from the CNF. In addition, the $(FeN_4)_d$-OLC-CNF@MoS_2 electrodes showed an almost linear shape in the Nyquist plot in the absence of an evident semicircle before the 5 000 cycles, which indicated a negligible charge transfer resistance. The electrodes benefited from the higher surface area defect rich $(FeN_4)_d$-OLC-CNF@MoS_2. The presence of vacancies in the framework structure enabled larger contact area with the electrolyte ions and the interfacial resistance between carbon fibre and MoS_2 was reduced, therefore the charge carriers could be more easily transferred.

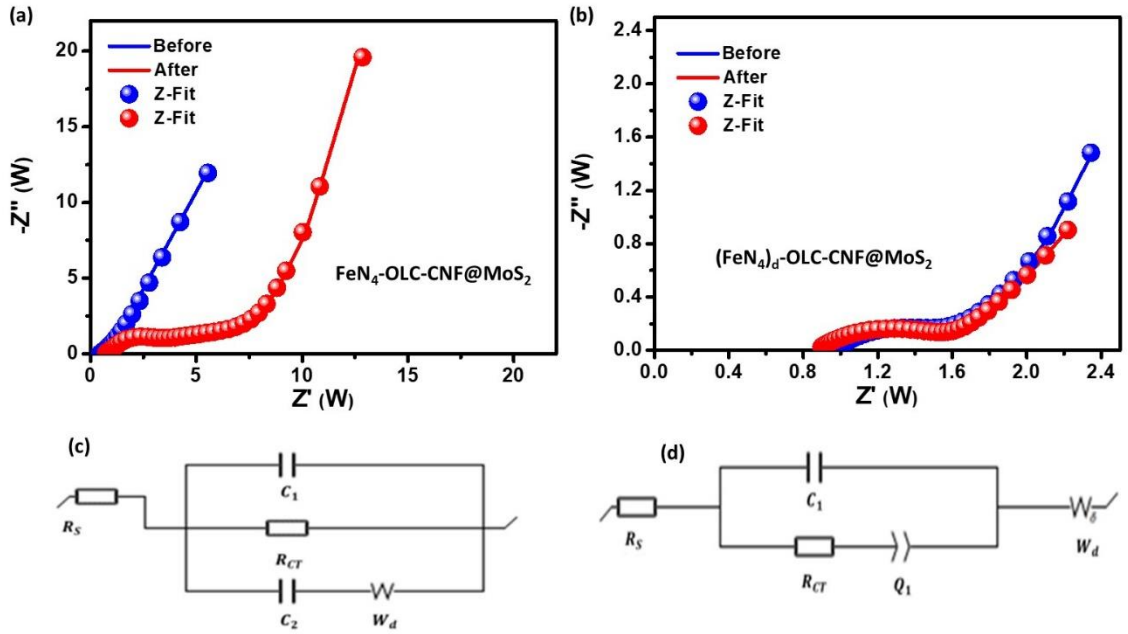

Figure 7.31 (a, b) Nyquist plots and (c, d) the electrical equivalent circuit used in fitting the Nyquist plots of FeN_4-OLC-CNF/MoS_2, and $(FeN_4)_d$-OLC-CNF@MoS_2 composite, respectively.

The relationship between phase angle and frequency was studied and is depicted in figure 7.32. The phase angle was observed at -50 ° and -38 ° for FeN_4-OLC-CNF@MoS_2 and $(FeN_4)_d$-OLC-CNF@MoS_2 electrodes, respectively. Although pseudocapacitive behavior is the dominating charge storage mechanism, the change from -50 ° to -38 ° suggests a shift to the double layer charge storage properties. It was observed that for frequencies between 10 and 1000 Hz electrodes, the phase angle for $(FeN_4)_d$-OLC-CNF@MoS_2 is above that of FeN_4-OLC-CNF@MoS_2 electrodes suggesting a small resistive loss in this frequency region. Which indicates that the $(FeN_4)_d$-OLC-CNF@MoS_2 electrodes have a quicker frequency response capability, as well as shorter ionic transport pathways that result in lower internal resistance and greater electrical conductivity.

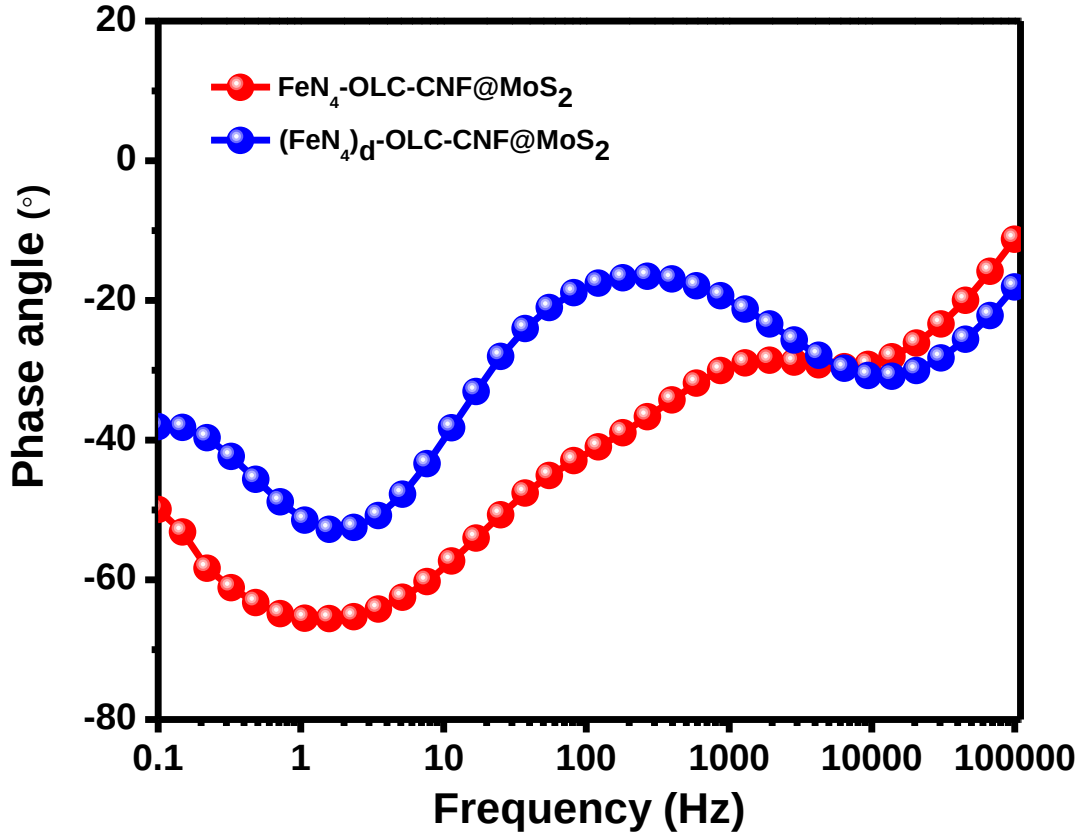

Figure 7.32 Comparative Bode plots of Phase angle vs frequency of FeN_4-OLC-CNF/MoS_2 and $(FeN_4)_d$-OLC-CNF@MoS_2 composite materials.

The efficiency of the supercapacitor device made from the $(FeN_4)_d$-OLC-CNF@MoS_2 composite material electrodes was examined with a commercially available LED bulb test. As shown in figure 7.33 three cells were connected in series and charged at 1 A g^{-1} with the BioLogic equipment. During the discharge cycle, the cells were connected to the LED bulb and were able to power the bulb for about 5 minutes before the light began to fade.

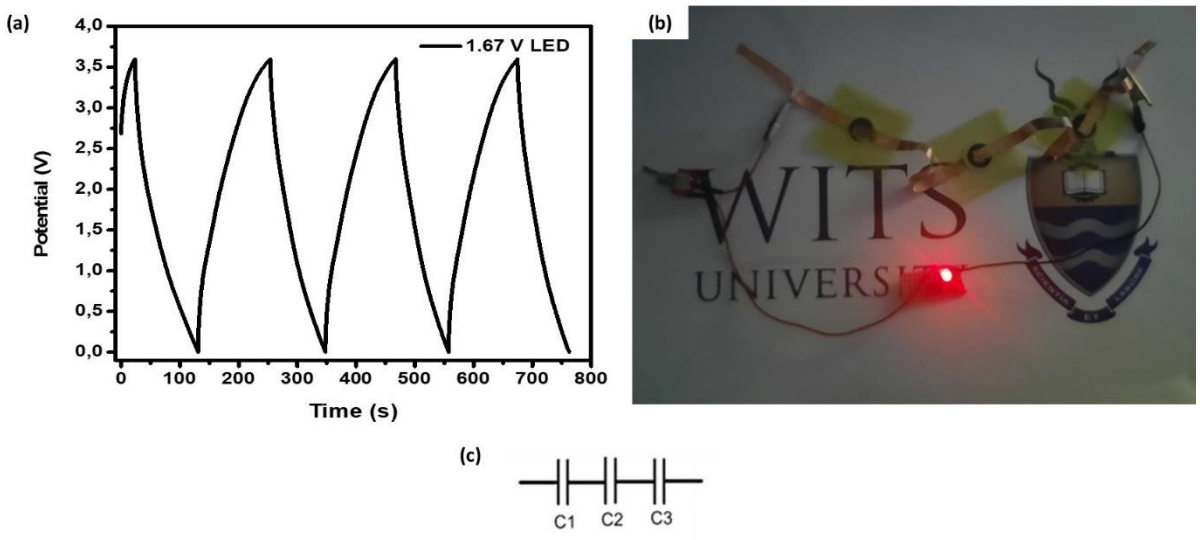

Figure 7.33 (a) charge-discharge profiles of $(FeN_4)_d$-OLC-CNF@MoS_2 composite electrodes giving 3.6 V, (b) a photograph of $(FeN_4)_d$-OLC-CNF@MoS_2 electrodes lighting up a 1.67 V LED at a 0° bending angle, and (c) electrical circuit representative of the electrodes connected in series.

7.3 Conclusion

In this study, we have successfully electrospun the highly conductive OLC-FePc based fibres and employed a simple hydrothermal method to encapsulate the fibres with MoS_2 and finally created vacancies by the removal of the Fe atoms from the composite structure. The synthesized $(FeN_4)_d$-OLC-CNF@MoS_2 composite showed improved crystallographic properties with regards to stacking of the MoS_2 sheets, likely due to the exfoliation during the sonification process in HCl that aided the Fe removal. The measured surface area had increased and had porosity varying from nano to macro ranges, making the electroactive species for energy storage a lot more accessible. The fragmented MoS_2 layer on the surface of the fibres exposed the underlying carbonaceous active material, which enhanced the conductivity of the electrodes. As a result of the above-mentioned advantages, their assembled electrodes exhibited high capacitance values, superior rate capability and better cycling stability. The composite prior to vacancies in the fibres (i.e. FeN_4-OLC-CNF@MoS_2) had restricted diffusion of the electrolyte ions in the fibre, and thus the same specific capacitance, energy density and power density were 178 F g^{-1}, 33 Wh kg^{-1} 1620 W $kg^{-1,}$ respectively. For $(FeN_4)_d$-OLC-CNF@MoS_2 at 0.1 A g^{-1} their specific capacitance, energy density and power density were 481 F g^{-1}, 76 W kg^{-}

[1] 5833 W $kg^{-1,}$ respectively. The cycling stability analysis of the electrodes also demonstrated excellent capacitance retention from the defective $(FeN_4)_d$-OLC-CNF@MoS_2 approx. 96 % as opposed to that of FeN_4-OLC-CNF@MoS_2 at 88 %.

7.4 References

[1] Zhang, X.; Liu, X.; Zeng, Y. Oxygen Defects in Promoting the Electrochemical Performance of Metal Oxides for Supercapacitors: Recent Advances and Challenges. *Small Methods.* **2020**, 4, 1900823.

[2] Lee, W.; Suzuki, S.; Miyayama, M. Electrode properties of defect-introduced graphene sheets for electrochemical capacitors using aqueous electrolyte. *Electrochim. Acta*. **2014**, 142, 240-246.

[3] Bi, W.; Jahrman, E.; Seidler, G. Tailoring Energy and Power Density through Controlling the Concentration of Oxygen Vacancies in V_2O_5/PEDOT Nanocable-Based Supercapacitors. *ACS Appl. Mater. Interfaces*. **2019**, 11, 16647-16655.

[4] Singal, S.; Joshi, A.; Tomar, K. A. Vacancies and edges: Enhancing supercapacitive performance metrics of electrode materials. *J. Energy Storage*. **2020**, 31, 101614.

[5] Wang, L.; Liu, R.; Li, X. Tailoring electrochemically active sites in carbon fibre by edge oxygen functionalized strategy for high performance yarn energy storage. *J. Power Sources*, **2021**, 491, 229579.

[6] Gao, P.; Chen, Z.; Gong, Y. The Role of Cation Vacancies in Electrode Materials for Enhanced Electrochemical Energy Storage: Synthesis, Advanced Characterization, and Fundamentals. *Adv. Energy Mater.* **2020**, 10, 1903780.

[7] Soon, J. M.; Lohz K. P. Electrochemical Double-Layer Capacitance of MoS_2 Nanowall Films. *Electrochem. Solid-State Lett.* **2007**, 10, A250-A254.

[8] Huang, K. J.; Wang, L.; Liu, Y-L; Wang, H-B.; Liu, Y-M.; Wang, L. L. Synthesis of polyaniline/2-dimensional graphene analogue MoS_2 composites for high-performance supercapacitor. *Electrochim. Acta.* **2013**, 109, 587-594.

[9] Nanjundan, A. K.; Mushtaq, A. D.; Rukhsana, G.; Jong-Boem, B. Graphene and molybdenum disulfide hybrids: synthesis and applications. *Mater. Today*. **2015**, 18, 286-298.

[10] Wang, T.; Chen, S.; Pang, H.; Xue, H.; Yu, Y. MoS_2-Based Nanocomposites for Electrochemical Energy Storage. *Adv. Sci*. **2017**, 4, 1600289.

[11] Li, X.; Zhu, H. Two-dimensional MoS_2: Properties, preparation, and applications. *J. Materiomics*, **2015**, 1, 33-44.

[12] Pan, Q.; Zhang, Q.; Zheng, F.; Liu, Y.; Li, Y.; Ou, X.; Xiong, X.; Yang, C. Liu, M. Construction of MoS_2/C Hierarchical Tubular Heterostructures for High-Performance Sodium Ion Batteries. *ACS Nano.* **2018**, 12, 12578-12586.

[13] Tongay, S.; Zhou, J.; Ataca, C.; Lo, K.; Mattews, T. S.; Li, J.; Grossman, J. C.; Wu, J. Thermally Driven Crossover from Indirect toward Direct Bandgap in 2D Semiconductors: $MoSe_2$ versus MoS_2. *Nano Letters*. **2012**, 12, 5576-5580.

[14] Toh, R. J.; Sofer, Z.; Luxa, J.; Sedmidubsky, D.; Pumera, M. 3R phase of MoS_2 and WS_2 outperforms the corresponding 2H phase for hydrogen evolution. *Chem. Commun*. **2017**, 53, 3054-3057.

[15] Chen, X.; Chen, Z. L.; Li, J. Critical electronic structures controlling phase transitions induced by lithium ion intercalation in molybdenum disulphide. *Chin. Sci. Bull.* **2013**, 58, 1632-1641.

[16] Khawula, T. N. Y.; Raju, K.; Franklyn P. J.; Sigalas, I.; Ozoemena, K. I. Symmetric pseudocapacitors based on molybdenum disulfide (MoS_2)-modified carbon nanospheres: Correlating physico-chemistry and synergistic interaction on energy storage. *J. Mater. Chem. A.* **2016**, 4, 6411-6425.

[17] Wang, T.; Chen, S.; Pang, H.; Xue, H.; Yu, Yan. MoS_2-Based Nanocomposites for Electrochemical Energy Storage. *Adv. Sci.* **2017**, 4, 1600289.

[18] Zhao, C.; Zhou, Y.; Ge, Z.; Zhao, C.; Qian, X. Facile construction of MoS_2/RCF electrode for high-performance supercapacitor. *Carbon.* **2018**, 127, 699-706.

[19] Chen, Y. M.; Yu, X. Y.; Li, Z.; Paik, U.; Lou, X. W. Hierarchical MoS_2 tubular structures internally wired by carbon nanotubes as a highly stable anode material for lithium-ion batteries. *Sci. Adv.* **2016**, 2, 1-8.

[20] Chen, M.; Dai, Y.; Wang, J.; Wang, Q.; Wang, Y.; Cheng, X.; Yan, X. Smart combination of three-dimensional-flower-like MoS_2 nanospheres/interconnected carbon nanotubes for application in supercapacitor with enhanced electrochemical performance. *J. Alloys Compd.* **2017**, 696, 900-906.

[21] Li, H.; Yu, K.; Fu, H.; Guo, B.; Lei, X.; Zhu, Z. MoS_2/Graphene Hybrid Nanoflowers with Enhanced Electrochemical Performances as Anode for Lithium-Ion Batteries. *J. Phys. Chem. C*. **2015**, 119, 7959-7968.

[22] Zeiger, M.; Jäckel, N.; Mochalin, V. N.; Presser, V. Review: carbon onions for electrochemical energy storage. *J. Mater. Chem. A*, **2016**, 4, 3172-3196.

[23] Zheng, Z.; Qi, S.; Zhang, Q. Onion-like carbon microspheres as long-life anodes materials for Na-ion batteries, *J. Mater. Sci.* **2018**, 53, 12421-12431.

[24] Makgopa, K.; Ejikeme, P. M.; Jafta, C. J.; Raju, K.; Zeiger, M.; Presser, V.; Ozoemena, K. I. A high-rate aqueous symmetric pseudocapacitor based on highly graphitized onion-like carbon/birnessite-type manganese oxide nanohybrids. *J. Mater. Chem. A.* **2015**, 3, 3480-3490.

[25] Miller, H. A., Bevilacqua, M., Filippi, J.Lavacchi, A.; Marchionni, A.; Marelli, M.; Moneti, S.; Oberhauser, W.; Vesselli, E.; Innoventi, M.; Vizza, F. Nanostructured Fe-Ag electrocatalysts for the oxygen reduction reaction in alkaline media. *J. Mater. Chem. A.* **2013**, 1, 13337-13347.

[26] Forsberg, V.; Zhang, R.; Bäckström, J. Dahlström, C.; Andres, B.; Norgren, M.; Andersson, M.; Hummelgärd, M.; Olin, H. Exfoliated MoS_2 in Water without Additives. *PLoS One*. **2016**, 11, 0154522.

CHAPTER EIGHT

8.1 Conclusions

The supercapacitive performance of the novel electrode materials prepared, was evaluated and surpassed the performance/energy storage capacity of some of the existing electrode materials. The enhanced performance is attributed to the synthesis of composite materials; wherein the different energy storage mechanisms of the constituents were mutually beneficial.

1. The advantages of physico-chemical properties, in particular an increase in specific surface area (SSA) as a function of chemical composition was observed in cases where the fibre composite (e.g. OLC-PAN, FePc-PAN) was thermally treated and/or integrated with a highly capacitive metal component (e.g. Mn_2O_3, MoS_2).
2. Synergistic effects; stemming from the interaction of a highly conductive material with a capacitive one to form a composite, had a significant influence on the charge transport and thus the energy storage capabilities of the composite materials prepared.
3. Encapsulation of the nano-carbon fibres with MoS_2 afforded additional capacitance and overcame the structural deficiencies associated with electrospun fibres and FePc based electrode materials. These benefits were quantified through cycling stability and rate capability analysis of the electrodes and was a 5-fold improvement over existing electrodes.
4. Engineering defects in the form of cation vacancies on the fibre composites reduced barriers for the electrolyte ion diffusion.
5. Lastly, it has been shown that an appropriate cell configuration with an optimized electrode-electrolyte interface for rapid charge transfer reaction, benefited the capacitive performance of the composite electrodes.

- OLC-CNF@Mn_2O_3 composite electrodes presented in chapter four exhibit a 10x increase in charge storage capacity compared to the electrospun OLC-PAN fibres and 2x that of OLC-CNF. The enhanced specific capacitance of the OLC-CNF@Mn_2O_3 composite electrodes is attributed to the combination of graphite nano-fibres with the improved ion mobilities of Mn_2O_3 nanoparticles.

- OLC/MoS_2@Mn_2O_3 supercapacitor electrodes discussed in chapter five displayed an improvement in all the critical parameters, i.e. specific capacitance, energy and power density, that were not shown by the OLC-CNF@Mn_2O_3 composite. Determination of the specific capacitance, energy and power density were 348 F g^{-1}, 18.42 Wh kg^{-1} and 5 095 W kg^{-1}, showed a 2-fold improvement over that of OLC-CNF@Mn_2O_3. The encapsulation of the fibres with MoS_2 reduced the resistivity of the electrodes resulting in greater capacitance retention over prolonged cycling and optimized the overall energy density significantly.
- The simplified porous FeN_4-CMF electrode developed in chapter six, was tested as an electrode material and exhibited a specific capacitance, energy and power density 147 F g^{-1}, 12.48 Wh kg^{-1} and 4320 W kg^{-1}, respectively. The poor rate capability of this electrode will limit its deployment/use in application.
- In chapter seven, the vacancy-rich $(FeN_4)_d$-OLC-CNF@MoS_2 composite obtained by removal of Fe^{2+} atoms from the starting FeN_4-OLC-CNF@MoS_2, showed superior specific capacitance, energy density and power density values of 481 F g^{-1}, 76 Wh kg^{-1} 5 833 W kg^{-1}, to the other materials prepared. This performance was achieved by encapsulating the FeN_4-CMF (chapter six) with MoS_2 and the subsequent removal of Fe^{2+} atoms to create vacancies in the fibre composite matrix.

In conclusion, electrode materials have been synthesized using the electrospinning method to address the primary limitation of supercapacitors, i.e. energy density. Novel methods of tuning their surface morphology were developed for improved electronic transport properties. The current study indicates crucial links between supercapacitor material characteristics and synthesis techniques. Designing porous, conductive and capacitive electrode materials is a key factor in pushing the envelope for supercapacitors as energy storage devices in application.

8.2 Future work

- Although capacitance was improved through carbonization at 600 °C and integrated with pseudocapacitive materials to form composites, more work is required to explore higher carbonization temperatures. Temperature is the main driving force for transformation of dangling bonds on carbon atoms to form π-bonds of graphite. Thus, at 800 °C the PAN-based electrospun fibres are likely to

fully graphitize. Additional time could enable the partially graphitized fibres to fully transform into ordered graphitic layers for the additional surface chemistry effect critical for electrolyte ion diffusion.

- Study the effect of concentration of etchant and the time on the formation of defects in the $(FeN_4)_d$-OLC-CNF@MoS_2 composite and microstructural evolution.
- Investigate asymmetric type configurations, including different carbons electrodes optimized for negative and positive ions. Supercapacitor hybrids may expand energy densities and voltage windows of the energy storage device.
- Most supercapacitor research focuses on improving the energy density of the electrode. However, more work is required to look into the environmental impact and sustainability of the synthesis methods for the new electrode materials in comparison to the current source i.e. fossil fuels.